

REPORT DOCUMENTATION PAGE

AFRL-SR-BL-TR-00
0555

Public reporting burden for this collection of information is estimated to average 1 hour per response, including the gathering and maintaining the data needed, and completing and reviewing the collection of information. Send comments concerning this collection of information, including suggestions for reducing this burden, to Washington Headquarters Services, Directorate for Information Operations and Infrastructure, Division of Defense Program Assessment, 8th Floor, 1215 Jefferson Davis Highway, Suite 1204, Arlington, VA 22202-4302, and to the Office of Management and Budget, Paperwork Reduction Project 0704-0188.

1. AGENCY USE ONLY (Leave blank)	2. REPORT DATE	3. REPORT TYPE	
	10/13/00	Final Report - 01 Feb 96 To 31 May 99	
4. TITLE AND SUBTITLE FUNDAMENTAL RESEARCH ON THE MECHANICS OF FLUID FLOW THROUGH POROUS MEDIA			5. FUNDING NUMBERS F49620-96-1-0020
6. AUTHOR(S) Fox, P. J., Zhu, Y., & Morris, J. P.			
7. PERFORMING ORGANIZATION NAME(S) AND ADDRESS(ES) School Of Civil Engineering Purdue University West Lafayette, IN 47907			8. PERFORMING ORGANIZATION REPORT NUMBER
9. SPONSORING/MONITORING AGENCY NAME(S) AND ADDRESS(ES) AFOSR/NA 801 N. Randolph St. Room 732 Arlington VA 22203-1977			10. SPONSORING/MONITORING AGENCY REPORT NUMBER
11. SUPPLEMENTARY NOTES			
12a. DISTRIBUTION AVAILABILITY STATEMENT Unclassified Unlimited Distribution		12b. DISTRIBUTION CODE	
13. ABSTRACT (Maximum 200 words) This report presents a pore-scale numerical model for flow and transport phenomena in spatially periodic porous media using Smoothed Particle Hydrodynamics (SPH). SPH is a fully Lagrangian computational fluid dynamics technique in which the numerical solution is achieved without a grid. Originally developed for astrophysical applications, SPH is extended to model low Reynolds number single-phase flow and tracer transport in porous media. In this report, a review of literature related to the current research is first provided. The development, verification, and application of the numerical model are then presented for pore-scale flow, diffusion, tracer convection, and hydrodynamic dispersion. Simulations using SPH were used to calculate permeability, diffusivity, dispersivity, and tortuosity of porous media. Simulations indicated that pure tracer convection through two-dimensional spatially periodic porous media cannot be described as an asymptotic Fickian-type process, even for large times, if body force F is parallel to a line of media symmetry. If F is not parallel to a line of media symmetry, Fickian-type mixing is possible for pure tracer convection. An asymptotic Fickian approximation is also valid for tracer hydrodynamic dispersion through spatially periodic porous media. Finally, conclusions and future research needs using the numerical model are provided.			
14. SUBJECT TERMS Flow and transport phenomena, spatially periodic porous media, smoothed particle, Hydrodynamics			15. NUMBER OF PAGES
			16. PRICE CODE
17. SECURITY CLASSIFICATION OF REPORT UNCLASS	18. SECURITY CLASSIFICATION OF THIS PAGE UNCLASS	19. SECURITY CLASSIFICATION OF ABSTRACT UNCLASS	20. LIMITATION OF ABSTRACT UL

**FUNDAMENTAL RESEARCH
ON THE MECHANICS OF FLUID FLOW
THROUGH POROUS MEDIA**

FINAL PROJECT REPORT

for

AFOSR Grant Number F49620-96-1-0020

by

Patrick J. Fox, Associate Professor (PI)

Yi Zhu, Graduate Research Assistant

Joseph P. Morris, Postdoctoral Researcher

submitted to the

Air Force Office of Scientific Research

Period of Support: Feb. 1, 1996 – May 31, 1999

School of Civil Engineering
Purdue University
West Lafayette, IN 47907

July 9, 1999

EMIC QUALITY INSPECTED 4

20001101 114

TABLE OF CONTENTS

	Page
TABLE OF CONTENTS	iii
LIST OF TABLES	vii
LIST OF FIGURES	viii
LIST OF SYMBOLS	xv
1 INTRODUCTION	1
1.1 What is a Porous Medium?	1
1.2 Problem Statement	1
1.3 Objectives of Research	3
1.4 Outline of Report	4
2 LITERATURE REVIEW	5
2.1 Models of Porous Media	5
2.1.1 Spatially Periodic Model	5
2.1.2 Network Model	8
2.1.3 Fractal Model	9
2.1.4 Reconstructed Porous Media	10
2.2 Single-Phase Flow Through Porous Media	10
2.2.1 Introduction	10
2.2.2 Conduit Flow Model	12
2.2.2.1 Kozeny-Carman Model	12
2.2.2.2 Capillary Model	15
2.2.3 Drag Flow Model	17
2.2.4 Anisotropic Porous Media and Permeability Tensor	19
2.2.5 Limitations of Darcy's Law	24

2.3	Hydrodynamic Dispersion in Porous Media	26
2.3.1	Introduction and Convection-Dispersion Equation	26
2.3.1.1	Molecular Diffusion	27
2.3.1.2	Mechanical Dispersion	29
2.3.2	Hydrodynamic Dispersion Tensor and Its Determination	32
2.3.3	Geometric Model	36
2.3.4	Random Network Model	38
2.3.5	Statistically Geometric Model	39
2.3.6	Statistical Model	42
2.3.7	Problem of Scale and Fickian Approximation	43
2.4	Transport Through Spatially Periodic Porous Media	46
2.4.1	Single-Phase Flow	47
2.4.2	Hydrodynamic Dispersion	53
2.4.3	Spatially Periodic versus Real Porous Media	58
2.5	Computational Fluid Dynamics Techniques	59
2.5.1	Lattice-gas Method	59
2.5.2	Lattice-Boltzmann Method	61
2.5.3	Smoothed Particle Hydrodynamics (SPH)	62
2.6	Summary	63
3	DEVELOPMENT AND VERIFICATION OF A PORE-SCALE FLOW MODEL USING SMOOTHED PARTICLE HYDRODYNAMICS	64
3.1	Overview of SPH	64
3.2	Model Establishment for Pore-Scale Flow Problem	68
3.2.1	Equation of State	68
3.2.2	Evolution of Density	71
3.2.3	Evaluation of Acceleration	72
3.2.3.1	Pressure Gradient Acceleration	72
3.2.3.2	Viscosity	73
3.2.4	Dynamic Pressure	74

3.2.5	Boundary Conditions	75
3.2.6	Interpolation Kernel	78
3.2.7	Locating the Nearest Neighboring Particles	80
3.2.8	Time Integration	82
3.3	Model Initialization and Execution	84
3.3.1	Initialization	84
3.3.2	Execution	85
3.4	Flow Model Verification	87
3.4.1	Simulations of Couette and Poiseuille Flows	88
3.4.1.1	Couette Flow	88
3.4.1.2	Poiseuille Flow	89
3.4.2	Simulations of Flow Through Periodic Lattices of Obstacles	90
3.4.2.1	Square, Staggered, and Hexagonal Arrays of Obstacles	91
3.4.2.2	Flow Through a Periodic Square Lattice of Circular Cylinders	92
3.4.2.3	Flow Through a Periodic Square Lattice of Elliptical Cylinders	104
3.4.2.4	Flow Through Periodic Square and Hexagonal Lattices of Circular Cylinders	106
3.5	Summary	115
4	DEVELOPMENT, VERIFICATION, AND APPLICATION OF A PORE-SCALE DIFFUSION MODEL USING SMOOTHED PARTICLE HYDRODYNAMICS	121
4.1	Model Establishment for Pore-Scale Diffusion Problem	121
4.2	Calculation of Diffusion Coefficients of Porous Media Using SPH	122
4.3	Model Initialization and Execution	127
4.3.1	Initialization	127
4.3.2	Execution	128
4.4	Diffusion Model Verification	128

4.4.1	Simulations of Diffusion in Aqueous Solution	128
4.4.2	Simulations of Diffusion Through Periodic Lattices of Obstacles	131
4.4.3	Simulations of Diffusion Through Composite Media	134
4.5	Diffusion Model Application	135
4.5.1	Effect of Specific Surface Area	142
4.5.2	Effect of Porosity	142
4.5.3	Effect of Anisotropy	143
4.5.4	Effect of Cylinder Arrangement	148
4.6	Summary	148
5	PORE-SCALE TRACER CONVECTION AND HYDRODYNAMIC DISPERSION SIMULATIONS	151
5.1	Pore-Scale Tracer Convection Model	151
5.2	Pore-Scale Hydrodynamic Dispersion Model	152
5.3	Method of Moments	158
5.4	Interpretation of Tracer Diffusion Using Method of Moments	160
5.5	Simulations of Taylor Dispersion	161
5.6	Simulations of Tracer Convection	173
5.6.1	Tortuosity of Porous Media	189
5.6.2	Seepage Velocity and Effective Porosity of Porous Media . . .	195
5.6.3	Mechanical Dispersion Coefficient of Porous Media	196
5.7	Simulations of Tracer Hydrodynamic Dispersion	206
5.8	Summary	214
6	CONCLUSIONS AND RECOMMENDATIONS FOR FUTURE WORK .	215
6.1	Conclusions	215
6.2	Recommendations for Future Work	216
	LIST OF REFERENCES	218

LIST OF TABLES

Table	Page
3.1 Summary of results for flow simulations through square lattice.	117
3.2 Summary of results for flow simulations through hexagonal lattice.	118
3.3 Check of results for flow simulations through square lattice using Equation 3.70.	119
3.4 Check of results for flow simulations through hexagonal lattice using Equa- tion 3.70.	120
4.1 Values of d^* for composite media.	135
4.2 Summary of results for diffusion simulations with circular cylinders. . . .	136
4.3 Summary of results for diffusion simulations with elliptical cylinders. . .	138
5.1 Summary of results for Taylor dispersion simulations.	172
5.2 Summary of information for tracer convection simulations.	174
5.3 Summary of results for tracer convection simulation analysis.	174

LIST OF FIGURES

Figure	Page
2.1 Unit cell of a spatially periodic structure.	6
2.2 A spatially periodic porous medium.	7
2.3 Kozeny-Carman flow model.	13
2.4 Straight parallel capillary model.	15
2.5 Serial capillary model.	17
2.6 Graphical determination of the direction of the pressure gradient based on a given velocity and the permeability tensor ellipse.	22
2.7 Graphical determination of the direction of the velocity based on a given pressure gradient and the permeability tensor ellipse.	22
2.8 x - y Cartesian coordinate system and principal tensor axes.	24
2.9 Components of mechanical dispersion at the microscopic level: (1) the velocity distribution across each pore channel; (2) variations in velocity as a result of the distribution of pore channel size; and (3) tortuosity of individual flow paths.	31
2.10 A generic relation between D_L and Pe	35
2.11 Taylor dispersion problem.	37
2.12 Porosity n versus its averaging volume V in a porous medium.	40
2.13 Representative elementary volume (REV).	41
3.1 Sphere of influence for SPH particle a	65
3.2 Construction of no-slip fluid-solid boundary for a curved surface.	77
3.3 Initial hexagonal configuration of SPH fluid particles.	78
3.4 Wh^2 versus s for quintic spline kernel.	79
3.5 Construction of image particles to simulate a periodic porous medium. .	86

3.6 Wrapping fluid particles around unit cell.	87
3.7 Couette flow.	88
3.8 Comparison of SPH and series solutions for Couette flow ($Re = 0.0125$).	89
3.9 Poiseuille flow.	89
3.10 Comparison of SPH and series solutions for Poiseuille flow ($Re = 0.0125$).	90
3.11 Two-dimensional cross sectional representations of unit cell geometry for square array with circular and elliptical inclusions.	91
3.12 Two-dimensional cross sectional representations of unit cell geometry for staggered array with circular and elliptical inclusions.	92
3.13 Two-dimensional cross sectional representations of unit cell geometry for hexagonal array with circular and elliptical inclusions.	93
3.14 Paths for comparison of SPH and FEM solutions for flow through a periodic square lattice of circular cylinders.	94
3.15 Comparison of SPH and FEM velocity profiles along paths 1 and 2 in Figure 3.14 for $Re = 1$	96
3.16 Contour plots of velocity magnitude using (a) FEM, and (b) SPH for $Re = 1$ (contour lines are labeled in unit of $10^{-4} \frac{m}{s}$).	97
3.17 Comparison of SPH and FEM pressure profiles along paths 3 and 4 in Figure 3.14 for $Re = 1$	98
3.18 Contour plots of pressure using (a) FEM, and (b) SPH for $Re = 1$ (contour lines are labeled in unit of $10^{-6} Pa$).	99
3.19 Comparison of SPH and FEM velocity profiles along paths 1 and 2 in Figure 3.14 for $Re = 0.03$	100
3.20 Contour plots of velocity magnitude using (a) FEM, and (b) SPH for $Re = 0.03$ (contour lines are labeled in unit of $10^{-4} \frac{m}{s}$).	101
3.21 Comparison of SPH and FEM pressure profiles along paths 3 and 4 in Figure 3.14 for $Re = 0.03$	102
3.22 Contour plots of pressure using (a) FEM, and (b) SPH for $Re = 0.03$ (contour lines are labeled in unit of $10^{-3} Pa$).	103

3.23 Paths for comparison of SPH and FEM solutions for flow through a periodic square lattice of elliptical cylinders.	104
3.24 Comparison of SPH and FEM velocity profiles along paths 1 and 2 in Figure 3.23.	105
3.25 Comparison of SPH and FEM pressure profiles along paths 3 and 4 in Figure 3.23.	105
3.26 Paths for comparison of SPH and FEM solutions for flow through a periodic (a) square lattice, and (b) hexagonal lattice of circular cylinders.	107
3.27 Particle positions for square lattice with $n = 0.5$ and $F = 0.049 \frac{m}{s^2}$ (a) initial positions, and (b) final positions. Fluid and boundary particles are shown in black and grey, respectively.	108
3.28 Particle positions for hexagonal lattice with $n = 0.5$ and $F = 0.049 \frac{m}{s^2}$ (a) initial positions, and (b) final positions. Fluid and boundary particles are shown in black and grey, respectively.	109
3.29 Maximum fluid velocity and dimensionless cylinder drag force versus time for square and hexagonal lattices ($n = 0.5, F = 0.049 \frac{m}{s^2}$).	110
3.30 Darcy velocity versus time for square and hexagonal lattices ($n = 0.5, F = 0.049 \frac{m}{s^2}$).	111
3.31 Comparison of SPH and FEM results for square lattice (a) velocity profile for path A, and (b) dynamic pressure profile for path B ($n = 0.5, F = 0.049 \frac{m}{s^2}$).	112
3.32 Comparison of SPH and FEM results for hexagonal lattice (a) velocity profile for path C, and (b) dynamic pressure profile for path D ($n = 0.5, F = 0.049 \frac{m}{s^2}$).	113
3.33 Darcy velocity versus hydraulic gradient for square and hexagonal lattices ($n = 0.5$).	114
3.34 Hydraulic conductivity versus porosity for square and hexagonal lattices.	115
3.35 $\frac{k_x}{R^2}$ and dimensionless cylinder drag force versus porosity for square and hexagonal lattices (a) $\frac{k_x}{R^2}$, and (b) dimensionless cylinder drag force.	116

4.1 Steady state diffusion through a spatially periodic porous medium.	123
4.2 Problem geometries to determine diffusion coefficients of an anisotropic porous medium (a) a concentration gradient is imposed in the x direction, and (b) a concentration gradient is imposed in the y direction.	126
4.3 Geometry for one-dimensional diffusion in an aqueous solution.	129
4.4 Normalized concentration versus distance for one-dimensional diffusion in an aqueous solution.	130
4.5 Geometry for two-dimensional diffusion in an aqueous solution.	130
4.6 Normalized concentration versus distance for an instantaneous cylindrical diffusion source.	131
4.7 Contour plots of concentration using (a) FEM, and (b) SPH for a square array of circular cylinders.	132
4.8 Contour plots of concentration using (a) FEM, and (b) SPH for a square array of elliptical cylinders.	133
4.9 Unit cell of a square array of circular cylinders. The interstitial phase has a diffusion coefficient of d_0 and the cylinder has a diffusion coefficient of βd_0	134
4.10 Nondimensional diffusivity versus porosity for square, staggered, and hexagonal circular cylinder arrays.	143
4.11 Normalized principal nondimensional diffusivity (a) $\frac{d_1^*}{d^*}$, and (b) $\frac{d_2^*}{d^*}$ versus aspect ratio $\frac{a}{b}$ for elliptical cylinder arrays having $n = 0.8$ (SQ = square array, ST = staggered array, HX = hexagonal array).	145
4.12 Normalized principal nondimensional diffusivity (a) $\frac{d_1^*}{d^*}$, and (b) $\frac{d_2^*}{d^*}$ versus α for elliptical cylinder arrays having $n = 0.8$	146
4.13 Normalized principal nondimensional diffusivity (a) $\frac{d_1^*}{d^*}$, and (b) $\frac{d_2^*}{d^*}$ versus aspect ratio $\frac{a}{b}$ for staggered elliptical cylinder arrays having $n = 0.5$ and 0.8.	147
4.14 θ versus α for elliptical cylinder arrays having $n = 0.8$	148
4.15 θ versus α for staggered elliptical cylinder arrays having $n = 0.5$ and 0.8.	149

5.1 Tracer particle positions (a) within the unit cell, and (b) within the corresponding spatially periodic porous medium.	153
5.2 Tracer plumes for the problem of tracer hydrodynamic dispersion: (a) initial tracer plume, and (b) tracer plume at time t	154
5.3 Initial concentration field for a problem of tracer hydrodynamic dispersion in a spatially periodic porous medium.	156
5.4 Unit cell (1, 1) for the problem in Figure 5.3.	156
5.5 Wrapping fluid particles and creating image particles to simulate tracer dispersion in a spatially periodic porous medium.	157
5.6 Initial condition for a tracer diffusion through a square array of circular cylinders.	160
5.7 Nondimensional diffusivity versus time for diffusion through a square array of circular cylinders.	161
5.8 Initial condition ($t = 0$) for Taylor dispersion between two infinite plates. .	162
5.9 Tracer concentration fields for Taylor dispersion between two infinite plates at elapsed times of (a) 0.01140 s, (b) 0.16342 s, (c) 0.35344 s, and (d) 0.52448 s.	165
5.10 The zeroth moment of tracer distribution versus time for Taylor dispersion between two infinite plates.	167
5.11 The first moment in the x direction of tracer distribution versus time for Taylor dispersion between two infinite plates.	168
5.12 Average channel velocity versus time for Taylor dispersion between two infinite plates.	169
5.13 Centered second moment in the x direction of tracer distribution versus time for Taylor dispersion between two infinite plates.	170
5.14 Hydrodynamic dispersion coefficient in the x direction versus time for Taylor dispersion between two infinite plates.	171
5.15 Body force F direction L and perpendicular direction T	173

5.16 Tracer convection through a square array of circular cylinders ($\gamma = 0^0$). Tracer particles are shown in black.	175
5.17 Tracer convection through a staggered array of circular cylinders ($\gamma = 0^0$). Tracer particles are shown in black.	177
5.18 Tracer convection through a staggered array of circular cylinders ($\gamma = 30^0$). Tracer particles are shown in black.	179
5.19 Tracer convection through a hexagonal array of circular cylinders ($\gamma = 0^0$). Tracer particles are shown in black.	181
5.20 Tracer convection through a hexagonal array of circular cylinders ($\gamma = 45^0$). Tracer particles are shown in black.	185
5.21 Trajectory $L_{e,z}$ and straight-line distance L traveled by tracer particle z	189
5.22 Trajectories of tracer particles in a square array of circular cylinders ($\gamma = 0^0$).	190
5.23 Trajectories of tracer particles in a staggered array of circular cylinders ($\gamma = 0^0$).	190
5.24 Trajectories of tracer particles in a staggered array of circular cylinders ($\gamma = 30^0$).	191
5.25 Trajectories of tracer particles in a hexagonal array of circular cylinders ($\gamma = 0^0$).	192
5.26 Trajectories of tracer particles in a hexagonal array of circular cylinders ($\gamma = 45^0$).	193
5.27 Tortuosity versus time for simulations in Table 5.2.	194
5.28 Seepage velocity versus time for simulation 1 in Table 5.2.	196
5.29 (a) Centered second moment, and (b) mechanical dispersion coefficient versus time for tracer convection through a square array of circular cylinders ($\gamma = 0^0$).	197
5.30 (a) Centered second moment, and (b) mechanical dispersion coefficient versus time for tracer convection through a staggered array of circular cylinders ($\gamma = 0^0$).	198

5.31 (a) Centered second moment, and (b) mechanical dispersion coefficient versus time for tracer convection through a staggered array of circular cylinders ($\gamma = 30^0$)	199
5.32 (a) Centered second moment, and (b) mechanical dispersion coefficient versus time for tracer convection through a hexagonal array of circular cylinders ($\gamma = 0^0$).	200
5.33 (a) Centered second moment, and (b) mechanical dispersion coefficient versus time for tracer convection through a hexagonal array of circular cylinders ($\gamma = 45^0$).	201
5.34 $\log(M_{2L})$ versus $\log(t)$ for tracer convection through a square array of circular cylinders ($\gamma = 0^0$).	203
5.35 $\log(M_{2L})$ versus $\log(t)$ for tracer convection through a staggered array of circular cylinders ($\gamma = 0^0$).	203
5.36 $\log(M_2)$ versus $\log(t)$ for tracer convection through a staggered array of circular cylinders ($\gamma = 30^0$).	204
5.37 $\log(M_{2L})$ versus $\log(t)$ for tracer convection through a hexagonal array of circular cylinders ($\gamma = 0^0$).	204
5.38 $\log(M_2)$ versus $\log(t)$ for tracer convection through a hexagonal array of circular cylinders ($\gamma = 45^0$).	205
5.39 Tracer concentration fields for dispersion through a square array of circular cylinders ($d_0 = 10^{-10} \frac{m^2}{s}$) at elapsed times of (a) 0 s, (b) 33.166 s, (c) 65.942 s, (d) 94.038 s.	208
5.40 Tracer concentration fields for dispersion through a square array of circular cylinders ($d_0 = 10^{-8} \frac{m^2}{s}$) at elapsed times of (a) 0 s, (b) 33.166 s, (c) 65.942 s, (d) 94.038 s.	210
5.41 Centered second moment in the L direction of tracer distribution versus time for tracer transport through a square array of circular cylinders.	212
5.42 Dispersion coefficient in the L direction of tracer distribution versus time for tracer transport through a square array of circular cylinders.	213

LIST OF SYMBOLS

Bold face letters:

B	vector field in Brenner's theory
B̄	vector field in Brenner's theory
D	hydrodynamic dispersion tensor
D_m	mechanical dispersion tensor
F	a field, body force
F_n	force in Equation 2.97
G	concentration gradient vector
I₁, I₂, I₃	three basic vectors defining unit cell of a spatially periodic porous medium
Î₁, Î₂, Î₃	three basic vectors defining the reciprocal cell of unit cell of a spatially periodic porous medium
J	total mass flux vector of a non-reactive tracer,
	probability flux vector of a Brownian particle
J_d	total dispersive mass flux vector of a non-reactive tracer
J_m	mass flux vector of a non-reactive tracer due to mechanical dispersion
M_m ($m = 0, 1, 2, \dots$)	moments of probability density, moments of tracer distribution
R	global position vector in a spatially periodic porous medium
R'	initial position vector in a spatially periodic porous medium

$\bar{\mathbf{R}}$	mean displacement of a Brownian particle
\mathbf{R}_n	centroid of unit cell of a spatially periodic porous medium
$\hat{\mathbf{R}}_n$	centroid of the reciprocal cell of unit cell of a spatially periodic porous medium
\mathbf{d}	diffusion tensor
\mathbf{d}^*	nondimensional diffusivity tensor
\mathbf{f}	a field
\mathbf{g}	gravitational acceleration
\mathbf{h}	total head vector
\mathbf{i}	hydraulic gradient vector
\mathbf{i}_x	unit vector in positive x direction
\mathbf{j}	mass flux vector of a non-reactive tracer due to molecular diffusion in anisotropic porous media
\mathbf{k}	specific, absolute, or intrinsic permeability tensor, permeability tensor
\mathbf{k}^{-1}	inverse of \mathbf{k}
$\hat{\mathbf{n}}$	a direction, unit vector normal to a surface
\mathbf{r}	local position vector in a spatially periodic porous medium, position vector in SPH
\mathbf{r}'	position vector in SPH
\mathbf{u}	fluid velocity vector
\mathbf{v}	filter velocity, Darcy velocity, discharge velocity, or specific discharge vector
\mathbf{v}_s	average pore, interstitial, or seepage velocity vector

Calligraphy letters:

\mathcal{C}	correction factor for local concentration gradient in SPH
\mathcal{F}	effective viscosity in Lundgren's generalized Brinkman equation
\mathcal{L}	macroscopic length scale of a spatially periodic porous medium, a characteristic length in defining the Reynolds and Peclet numbers, a typical length scale of a problem
\mathcal{L}_D	Darcy length scale of a spatially periodic porous medium
\mathcal{L}_m	microscopic length scale of a spatially periodic porous medium
\mathcal{M}	solute mass associated with SPH tracer particle
\mathcal{T}	tortuosity
\mathcal{U}	a typical fluid velocity scale of a problem
\mathcal{V}	a characteristic velocity in defining the Reynolds and Peclet numbers

Italic letters:

A	averaging surface, a scalar field
A_i	integral interpolant of A
A_s	summation interpolant of A
$A_{solid-fluid}$	solid-fluid interfacial area
$A_{unit\ cell}$	area of unit cell of a spatially periodic porous medium
C	tracer concentration

\check{C}	spatially periodic component of C
C_m	empirical parameter in Hazen equation
C_s	shape factor in Kozeny-Carman model
D	diameter of flow channels, capillaries, cylinders, or spheres, dispersion coefficient
D_{10}	effective grain size
D_{Aris}	Aris dispersion coefficient
D_L	longitudinal dispersion coefficient
$D_{Saffman,L}$	Saffman longitudinal dispersion coefficient
$D_{Saffman,T}$	Saffman transverse dispersion coefficient
D_T	transverse dispersion coefficient
D_{Taylor}	Taylor dispersion coefficient
D_{ij} ($i, j = x, y, z$)	components of hydrodynamic dispersion tensor in a $x-y-z$ Cartesian coordinate system
D_{mL}	longitudinal mechanical dispersion coefficient
D_{mT}	transverse mechanical dispersion coefficient
D_x	dispersion coefficient in the x direction
F	a function, magnitude of body force
F_d	drag force acting on the solid in mean flow direction in a spatially periodic porous medium
\bar{F}_d	dimensionless drag force
I_0	modified Bessel function of the first kind of order zero
K	permeability
L	path length of flow in Kozeny-Carman model, direction of regional flow, a length, side length of unit cell of a spatially periodic porous medium, direction of body force, straight-line distance in defining \mathcal{T}

L_1, L_2	side lengths of unit cell of a spatially periodic porous medium
L_e	effective path length of flow in Kozeny-Carman model, length of trajectory in defining \mathcal{T}
M_0	zeroth moment
M_{1x}	first moment in the x direction
M_{2L}	centered second moment in the L direction
M_{2T}	centered second moment in the T direction
M_{2x}	centered second moment in the x direction
Ma	Mach number
N_{part}	number of SPH particles
N_{tracer}	number of SPH tracer particles
P	total pressure
Pe	Peclet number
Q	volume flow rate
R	radius of flow channels, capillaries, cylinders, or spheres, characteristic dimension of cross section in Equation 2.86, regression coefficient
Re	Reynolds number
S_0	specific surface area
S_c	Schmidt number
S_p	surface of solid phase
T	direction perpendicular to regional flow, direction perpendicular to body force
V	averaging volume, SPH particle volume
V_{fluid}	fluid volume
V_{fluid}^∞	fluid volumes in all unit cells of a spatially periodic porous medium
V_{solid}	solid volume

$V_{\text{unit cell}}$	volume of unit cell of a spatially periodic porous medium
W	SPH kernel function
a	half of the major axis of an ellipse
a_1, a_2, a_3	constants in Forchheimer equation
a_L	longitudinal geometrical dispersivity
a_T	transverse geometrical dispersivity
a_{ijkm} ($i, j, k, m = x, y, z$)	components of geometrical dispersivity tensor in a x - y - z Cartesian coordinate system
b	half of the minor axis of an ellipse
c	speed of sound
d	coefficient of molecular diffusion in isotropic porous media, normal distance to boundary
d_0	coefficient of molecular diffusion in aqueous solution
d_i ($i = 1, 2, 3$)	principal components of diffusion tensor
d_{ij} ($i, j = x, y, z$)	components of diffusion tensor in a x - y - z Cartesian coordinate system
d_n	directional diffusion coefficient
d_x	diffusion coefficient in the x direction
d^*	nondimensional diffusivity of an isotropic porous medium
d_i^* ($i = 1, 2, 3$)	principal components of nondimensional diffusivity tensor
d_{ij}^* ($i, j = x, y, z$)	components of nondimensional diffusivity tensor in a x - y - z Cartesian coordinate system
d_x^*	nondimensional diffusivity in the x direction
erf	error function
f	a function

f_C	rate of change of concentration
f_a	magnitude of particle acceleration
f_ρ	rate of change of density
g	gravitational constant
h	total head, smoothing length in SPH, a distance
i	hydraulic gradient, unit cell coordinate in dispersion model
j	unit cell coordinate in dispersion model
j_0	mass flux of a non-reactive tracer due to molecular diffusion in aqueous solution
j_i ($i = 1, 2, 3$)	mass fluxes in principal directions of the diffusion tensor of a non-reactive tracer due to molecular diffusion
j_i ($i = x, y, z$)	mass fluxes in a x - y - z Cartesian coordinate system of a non-reactive tracer due to molecular diffusion
k	specific, absolute, or intrinsic permeability, permeability
k_H	hydraulic conductivity
k_i ($i = 1, 2, 3$)	principal components of permeability tensor
k_{ij} ($i, j = x, y, z$)	components of permeability tensor in a x - y - z Cartesian coordinate system
k_n	directional permeability
k'	Kozeny-Carman constant
m	number of capillaries per unit area of cross section in straight capillary model, SPH particle mass
m_1, m_2	empirical constants in Equations 2.76 and 2.77
n	porosity, a direction, a number
n_1, n_2, n_3	trio of integers
n_{eff}	effective porosity

n_s	number of solid obstacles in unit cell of a spatially periodic porous medium
p	hydrostatic pressure, probability density, dynamic pressure
p_0	reference pressure
p_d	dynamic pressure
p_h	hydrostatic pressure
p_t	total pressure
r	coordinate
s	kernel index, a variable in Equation 5.18
t	time
t_c	characteristic time for transverse diffusion, characteristic time for tracers to sample all interstitial space of unit cells
u_0	magnitude of fluid velocity
u_i ($i = 1, 2, 3$)	components of fluid velocity in a x_1 - x_2 - x_3 Cartesian coordinate system
u_i ($i = x, y, z$)	components of fluid velocity in a x - y - z Cartesian coordinate system
u_{max}	maximum magnitude of fluid velocity
$u_{x,max}$	maximum fluid velocity in the x direction
v	filter velocity, Darcy velocity, discharge velocity, or specific discharge
v_i ($i = 1, 2, 3$)	Darcy velocities in principal directions of permeability tensor
v_i ($i = x, y, z$)	Darcy velocities in a x - y - z Cartesian coordinate system
v_n	directional filter velocity, Darcy velocity, discharge velocity, or specific discharge

v_s	average pore, interstitial, or seepage velocity, average channel velocity in Poiseuille flow
v_{sL}	seepage velocity in the L direction
v_{sT}	seepage velocity in the T direction
x	coordinate, a distance in Equation 2.92
y	coordinate
z	elevation head, coordinate

Greeks and Mathematical Operators:

Π	artificial viscosity in SPH
α	pore size distribution function, an angle, empirical constant in Equation 2.83, dimensionless number in Equation 2.86, angle between the direction of the major axis of an ellipse and the positive x direction
β	an angle, empirical constant in Equation 2.83, ratio of the two diffusion coefficients in Figure 4.9
δ	Dirac delta function
ϵ	ordering parameter in homogenization analysis, a variable
ϕ	solid fraction
γ	an angle, a variable
λ	a variable
μ	fluid dynamic viscosity
ν	fluid kinematic viscosity
θ	angle in Figure 2.8
ρ	fluid density
ρ_0	reference density

σ	number of dimensions
σ_L^2	variance of longitudinal spreading of tracer plume
σ_T^2	variance of transverse spreading of tracer plume
τ	time step
ψ	a scalar, vector, or second-order tensor
Δ	difference operator
ΔL	distance in the direction of applied body force between locations of minimum and maximum fluid density
Δx	initial nearest neighbor distance of SPH fluid particles
$\Delta\rho$	maximum allowable density difference
∇	gradient operator
∇^2	Laplacian operator
∇_T^2	Laplacian in transverse directions
$\langle \quad \rangle$	an average quantity, unit cell jump operator

Subscripts:

0	initial quantity
B	quantity associated with SPH boundary particle B
a	quantity associated with SPH fluid particle a
b	quantity associated with SPH fluid particle b
z	quantity associated with SPH tracer particle z

CHAPTER 1 INTRODUCTION

1.1 What is a Porous Medium?

Almost anything can be considered as porous depending on the observation scale (Cushman 1997). In our daily life, we usually think of porous media as the heterogeneous systems consisting of a solid matrix with fluid-filled voids. Dullien (1992) proposed two criteria that a material must satisfy in order to qualify as a porous medium:

1. It must contain relatively small spaces, so-called pores or voids, free of solids, embedded in the solid or semi-solid matrix. The pores usually contain a fluid, such as air, water, oil, etc., or a mixture of different fluids;
2. It must be permeable to a variety of fluids, i.e., fluids should be able to penetrate through one face of a septum made of the material and emerge on the other side. In this case one refers to a "permeable porous material".

Porous media are ubiquitous throughout nature. Artificial (man-made) porous media include fabric, paper, concrete, cement, and brick. Vegetal and animal biological media, such as arteries and lungs, must convey fluids to transport oxygen, nutrients, and wastes. Geological porous media are of interest in this report because of their practical importance in oil recovery, groundwater flow, and contaminant transport in the subsurface.

1.2 Problem Statement

Analysis of flow and transport processes through porous media has many applications in engineering systems, science, and technology. Such applications include the

problem of seepage, intrusion of sea water in coastal areas, contaminant transport through the subsurface, enhanced oil recovery, lubrication, filtration of suspended solids, geothermal energy management, and nutrition supply in soils. These applications are typically interdisciplinary and involve the areas of civil, environmental, petroleum, chemical, mechanical, and agricultural engineering; geology and groundwater hydrology; food, soil and biochemical sciences.

With the increasing sense of environmental awareness, people have interest in the mechanisms responsible for contaminant transport through groundwater systems. Much of the interest has resulted from the enactment of new legislation which address the disposal of solid and hazardous wastes (RCRA) and the cleanup of previously contaminated sites (CERCLA). The EPA Superfund Innovative Technology Evaluation (SITE) Program is working to expedite environmental remediation by developing promising new technologies for the cost-effective cleanup of contaminated soil and groundwater (Nyer 1992). Successful implementation of these technologies—such as in situ bioremediation, air sparging, soil vapor extraction, surfactant flushing, and electrokinetic remediation—requires a clear understanding of subsurface contaminant transport processes. To prevent the deterioration of groundwater quality and evaluate remediation technologies, considerable efforts have been made toward the development of mass transport models for monitoring, analyzing, and predicting the transport of contaminants through the subsurface.

The ability to model transport through porous media has, however, been limited by an insufficient understanding of physical processes at the particulate level. Although the geometry of voids and solids in porous media is inherently discrete at the microscale, transport through porous media has been traditionally characterized using a macroscopic continuum approach based on Darcy's law and Fick's law (Ogata 1970; Bear 1972; Freeze and Cherry 1979). Numerous theoretical and experimental studies have attempted to predict macroscopic transport from known media properties, but knowledge of flow paths and mixing processes that occur within the individual pores remains unsatisfactory. To improve available continuum models, a

better understanding of the fundamental physics which govern the flow and transport processes at the pore-scale is required. One means by which this understanding can be achieved is through the development of pore-scale models that more accurately represent the geometry of fluid and solid phases within porous media. Development of such models permits detailed study of flow and transport phenomena in assemblages of particles with varying shape, angularity, orientation, void ratio, and size distribution. This could lead to important discoveries regarding the nature and interrelationships of permeability and hydrodynamic dispersion tensors used in current mass transport models.

In addition, better knowledge of pore-scale flow and transport processes could significantly improve our ability to predict in situ liquid-liquid chemical and biological reaction rates (surfactant flushing, bioremediation), and liquid-solid partitioning (adsorption, retardation). Such knowledge would aid our understanding of the migration behavior of light and dense non-aqueous phase liquids (LNAPLs and DNAPLs) through the subsurface, the mobility of which are largely governed by surface tension and pore geometry considerations.

1.3 Objectives of Research

The principal objective of this research is to simulate microscopic (pore-scale) single-phase flow and tracer transport processes through porous media, and thereby gain insight with regard to macroscopic flow and transport behavior. Rather than employ a continuum approach, Smoothed Particle Hydrodynamics (SPH) will be used to simulate fluid flow and solute transport processes within a periodic pore network. SPH is well suited for this study because it is a fully Lagrangian technique in which the numerical solution is achieved without a grid. Using this approach, fluid velocity, pressure, contaminant distributions, and volumetric flow rates can be computed. In addition, the flow paths of individual fluid masses can be monitored as they travel through the void system of the medium. Detailed information about transport processes obtained by this approach would be difficult or impossible to

observe experimentally or with many other numerical techniques. Another advantage of SPH is the relative ease with which new physics may be incorporated into the formulation. For example, surface tension can be implemented into the model to simulate multiphase transport (Morris 1999).

1.4 Outline of Report

Chapter 2 of this report reviews literature related to the current research. Chapters 3 to 5 present the development, verification, and application of the numerical model for pore-scale flow, diffusion, tracer convection and hydrodynamic dispersion, respectively. Chapter 6 presents the conclusions and expected future research using the numerical model.

CHAPTER 2 LITERATURE REVIEW

Although practical hydraulics had its origins in antiquity, scientific attention to transport in particulate media began about one hundred and fifty years ago. An enormous and still rapidly growing literature, including thousands of articles and many monographs, has since been devoted to the topic of flow and transport through porous media. It is not intended herein to provide a comprehensive review of these works, rather, it is the purpose of this chapter to address the literature specifically related to the current research.

2.1 Models of Porous Media

A model represents a useful simplification of complex reality. As the detailed structure of natural porous media is too complicated to describe mathematically, for years these materials have been represented using simplified hypothetical models which can be analytically treated. Actually, any modeling of flow and transport phenomena in a porous medium has to include a realistic model of the medium itself. There have been efforts to describe pore-scale transport through spatially periodic porous media, network models, fractal porous media, and reconstructed porous media. The following sections outline the progress which has been made in these areas.

2.1.1 Spatially Periodic Model

A spatially periodic model views the porous medium as having a spatially periodic structure. This is based on translational symmetry, which is a classical concept that many materials look much the same at different locations. Spatially periodic structure is the simplest structure that can be seen in nature and was historically the first to be studied. Spatially periodic media are generated by infinite sequences of

repeating unit cells in one, two, or three dimensions. For a three-dimensional problem, periodic media can be constructed following the work of Adler (1992). Consider a

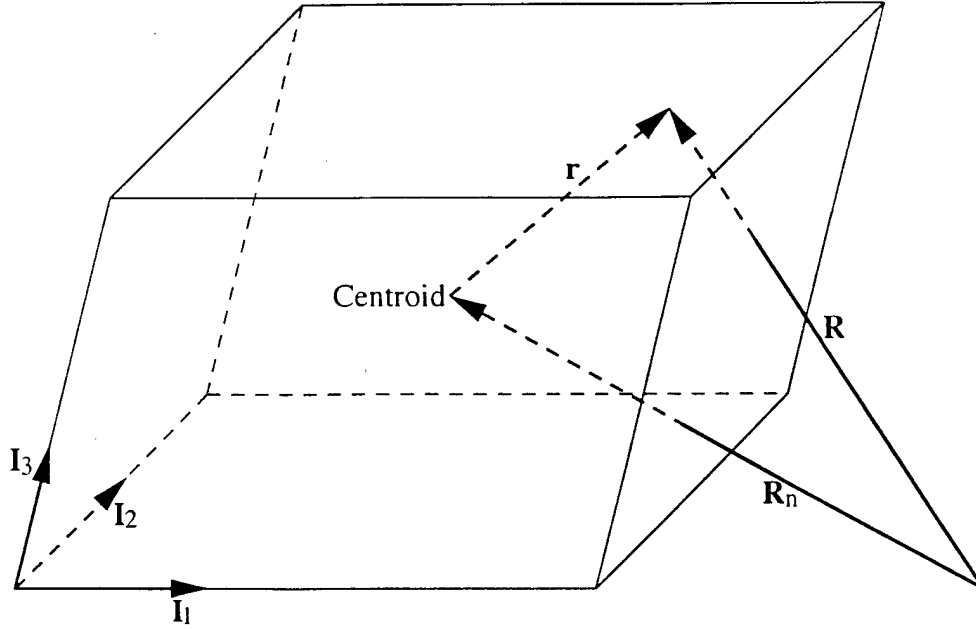


Figure 2.1: Unit cell of a spatially periodic structure.

parallelepiped unit cell whose sides are characterized by three vectors \mathbf{I}_1 , \mathbf{I}_2 , and \mathbf{I}_3 (Figure 2.1). The content of this cell is arbitrary. It can be composed of particles, of a network of capillary tubes, or of any other solid or void organization. Its volume $V_{\text{unit cell}}$ is assumed to be strictly positive,

$$V_{\text{unit cell}} = |\mathbf{I}_1 \cdot \mathbf{I}_2 \times \mathbf{I}_3|, \quad (2.1)$$

which is equivalent to assuming that these three vectors are linearly independent. An infinite spatially periodic medium is obtained by translating this unit cell by all linear combinations \mathbf{R}_n of the three vectors \mathbf{I}_1 , \mathbf{I}_2 , and \mathbf{I}_3 ,

$$\mathbf{R}_n = n_1 \mathbf{I}_1 + n_2 \mathbf{I}_2 + n_3 \mathbf{I}_3, \quad (2.2)$$

where the trio (n_1, n_2, n_3) are integers. By doing this, infinite unit cells are simply juxtaposed to one another to form a spatially periodic medium. If \mathbf{R}_n is defined as the

centroid of each unit cell, the global position vector \mathbf{R} anywhere within the infinite medium may be identified as.

$$\mathbf{R} = \mathbf{R}_n + \mathbf{r}. \quad (2.3)$$

where \mathbf{r} is the local position vector originating at the centroid of each unit cell (Figure 2.1). Figure 2.2 depicts an irregular but spatially periodic porous medium in two dimensions.

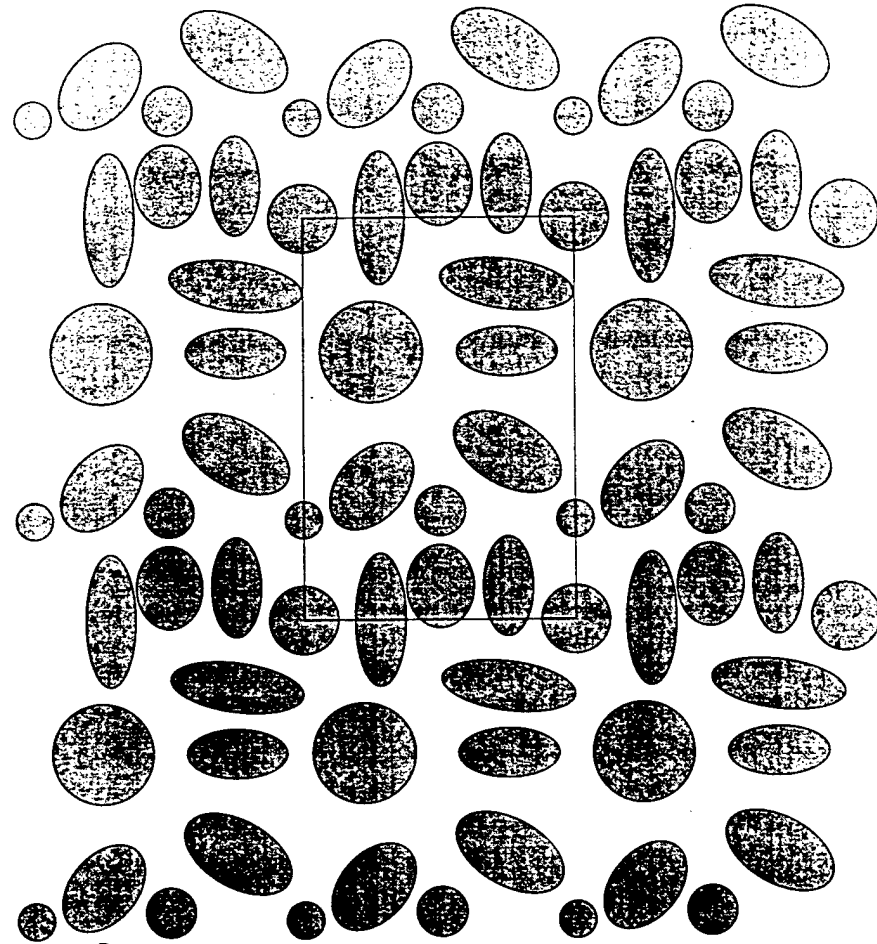


Figure 2.2: A spatially periodic porous medium.

A spatially periodic medium is characterized by three physical length scales. The first is the microscopic length scale \mathcal{L}_m of the characteristic size of the particles over which the local interstitial fields (e.g., velocity field) vary due to the local boundary

conditions satisfied on the particle surfaces. The second is the Darcy scale \mathcal{L}_D of the order of the size of the unit cell over which the mean or average fields vary sensibly. People are usually interested in physically describing the gross or average transport process occurring at the Darcy scale. Quantities defined at the Darcy scale represent, in some sense, averages of comparable quantities defined at each point of the interstices. It is necessary to require.

$$\mathcal{L}_D \gg \mathcal{L}_m, \quad (2.4)$$

such that a volume element of $O(\mathcal{L}_D^3)$ contains a representative number of particles and encapsulates enough degree of heterogeneity to render the various meaningful averages formed from integration of the local interstitial fields. The last is the macroscopic length scale \mathcal{L} which corresponds to a characteristic linear dimension of the external boundaries of the porous medium under consideration. For example, the dimension of a specimen of porous media upon which an experiment is being performed. In order to model a porous medium as spatially periodic, it is assumed that,

$$\mathcal{L} = \infty \quad \text{and} \quad \mathcal{L} \gg \mathcal{L}_D, \quad (2.5)$$

so that some average fields defined on the Darcy scale remain sensibly constant, such as pressure gradient and the resulting average discharge velocity. Similarly, the average concentration gradient and the corresponding mass flux are sensibly constant over \mathcal{L}_D .

Some theoretical and numerical research has been devoted to transport through spatially periodic porous media. By assigning a given solid configuration to the unit cell, it is possible to study the problem at the pore-scale. As this report also assumes a porous medium has spatial periodicity, the related literature will be reviewed in detail in section 2.4.

2.1.2 Network Model

The use of networks of capillary tubes to model porous media was first suggested by Fatt (1956). The work was based on the idea that pore space may be represented

as an interconnected network of capillary tubes whose radii represent the dimensions of the pores within a porous medium. The premise of the network model is that the void space of a porous medium can be represented by a graph of connected nodes. The nodes in the graph correspond to pore bodies and the links that connect the nodes correspond to pore throats. Such a graph preserves the essential topology of the pore spaces. In addition, sizes can be assigned to the nodes and links according to a chosen size distribution of pore bodies and throats (Bryant et al. 1993).

The pore-scale network approach for investigating the nature of fluid flow has been developed extensively in the petroleum engineering (Chatzis and Dullien 1977; Larson et al. 1981), and also recently in the fields of hydrology and soil physics (Ferrand and Celia 1992; Reeves and Celia 1996; Rajaram et al. 1997). Although network models can replicate highly disordered geometry of fluid phases in principal, in practice, they have been constructed using various assumptions concerning pore structure. Mathematical network models are used in computer simulations while physical network models have been developed for flow visualization studies (Wan et al. 1996).

2.1.3 Fractal Model

Mandelbrot (1982) coined the name “fractal” from the Latin *fractus* which describes the appearance of a broken stone and popularized the concept of fractals. It has been found in many fields that fractals could mimic the geometry of the real world better than classic geometry. Fractals provide a powerful concept for physicists to solve problems characterized by the simultaneous existence of very different scales. In recent years, many complex behaviors of a wide variety of phenomena have been quantitatively characterized using the concept of fractals.

A number of authors have studied the fractal character of porous media (Avnir et al. 1985; Wong et al. 1986; Jacquin and Adler 1987; Thompson et al. 1987). Fractal porous media are highly self-organized in that many static and dynamic properties have infinite correlation lengths. The problem scale of fractal porous media evolves

continuously from pore to reservoir. Constitutive variables in such a system are wave vector and frequency dependent, and result from non-local theories (Cushman 1990; Cushman and Ginn 1993; Cushman et al. 1994; Cushman 1997).

2.1.4 Reconstructed Porous Media

Reconstruction of actual porous media has been done using computer microtomography (CMT) (Spanne et al. 1994; Peyton et al. 1994; Schwartz et al. 1994) and digital image processing (Koplik et al. 1984). Spanne et al. (1994) applied computer microtomography to sandstone to determine the geometrical structure of the pores to a resolution of $10 \mu m$. Reconstructed porous media may mimic more closely the geometry of real media and generate numerical samples with desired properties.

Adler (1992) presented three steps for the study of transport in reconstructed porous media. The first involves the measurement of any salient geometric features. The second step is the reconstruction process. Samples of porous media are generated in such a way that, on average, they possess the same statistical properties as the real samples that they are intended to mimic. For the last step, all transport phenomena are studied analytically or numerically. Reconstruction of porous media can be done on pore- or field-scale, depending on the problem.

2.2 Single-Phase Flow Through Porous Media

2.2.1 Introduction

Henry P. G. Darcy published studies on the development of the water supply systems of Dijon in 1856. The law he discovered, namely, that the rate of flow is proportional to the total head drop through a bed of fine particles, bears his name and is widely employed for investigating the behavior of all types of fluid flow through porous media.

For isotropic media, Darcy's law is written in differential form as,

$$\mathbf{v} = -K \nabla P = -K(\nabla p + \rho \mathbf{g}), \quad (2.6)$$

where \mathbf{v} denotes the filter velocity (i.e., Darcy velocity, discharge velocity, or specific discharge) and ∇P is the pressure gradient vector. K is the permeability, p is the hydrostatic pressure, ρ is the fluid density, \mathbf{g} is the gravitational acceleration, and the total pressure P is defined as,

$$P = p + \rho g z, \quad (2.7)$$

where z is the distance measured vertically upward from an arbitrarily chosen datum level, and g is the gravitational constant. Usually, P is measured by a piezometer and is indicated as the "piezometric head" or "total head" h .

$$h = \frac{P}{\rho g} = \frac{p}{\rho g} + z, \quad (2.8)$$

which is the sum of the elevation head z and the pressure head $\frac{p}{\rho g}$.

The permeability K depends on both the medium and the fluid. Nutting (1930) separated the influence of the porous medium from that of the fluid and stated that,

$$K = \frac{k}{\mu}, \quad (2.9)$$

where μ is the dynamic viscosity of the fluid and k is called the specific, absolute, or intrinsic permeability of the medium which has dimensions of length squared. This concept was popularized by Wyckoff et al. (1933). For simplicity, k will be called permeability in this report.

Flow in porous media takes place through flow channels, each having a local distribution of pore velocity. The average pore velocity, on the whole, must be larger than the Darcy velocity owing to the reduced space available for flow, as compared with the bulk volume of the porous medium on which the Darcy velocity is defined. A commonly accepted hypothesis for the connection between pore velocity and Darcy velocity is the Dupuit-Forchheimer assumption (Scheidegger 1974),

$$\mathbf{v} = \mathbf{v}_s n, \quad (2.10)$$

where \mathbf{v}_s is the pore or seepage velocity and n is the porosity of the medium. It should be noted that the seepage velocity, like Darcy velocity, is not a true physical

velocity because the actual velocity of the fluid must be expected to fluctuate grossly within one flow channel and from one flow channel to another, and because of the tortuosity of the channels.

In groundwater hydrology and soil mechanics, the fluid of interest is usually water. Therefore, a “hydraulic conductivity” k_H is defined as.

$$k_H = \frac{k\rho g}{\mu}, \quad (2.11)$$

and Darcy's law is written as,

$$\mathbf{v} = -k_H \nabla h = -k_H \mathbf{i}, \quad (2.12)$$

where $\mathbf{i} = \nabla h$ is the hydraulic gradient.

The concept of permeability permits a phenomenological description of flow through porous media. However, an actual understanding of the phenomena can be obtained only if the concept of permeability can be reduced to more fundamental physical principles. It is intuitively clear that permeability is linked with other properties of porous media. Many attempts have been made to establish correlations between permeability and other properties of porous media with the help of various models. These approaches may be categorized in several different ways. Here, two fundamentally different approaches are distinguished: in one, the flow inside conduits is analyzed; in the other, the flow around solid objects immersed in the fluid is considered.

2.2.2 Conduit Flow Model

Conduit flow does not account for the fact that different pores are interconnected with each other, so conduit flow models are inherently one-dimensional models. Among them, the Kozeny-Carman model is generally more popular than the rest.

2.2.2.1 Kozeny-Carman Model

The Kozeny-Carman approach is also called the “hydraulic radius theory” and was developed for creeping flow. In the Kozeny-Carman theory (Kozeny 1927; Carman 1937; Carman 1938a; Carman 1938b; Carman 1939; Carman 1956), the porous

medium is assumed to be equivalent to a conduit, the cross section of which may have a complicated shape but, on an average, a constant area.

A Hagen-Poiseuille type equation is assumed to give the average seepage velocity in the flow channels.

$$v_s = -\frac{\Delta P}{L_e} \frac{D^2}{C_s 16\mu}, \quad (2.13)$$

where L_e is the effective path length of flow, D is the flow channel diameter, and C_s is a shape factor.

In addition to the Dupuit-Forchheimer assumption in Equation 2.10, Carman related Darcy velocity with the seepage velocity as.

$$v_s = \frac{v}{n} \frac{L_e}{L}, \quad (2.14)$$

which corrects for the fact that a hypothetical fluid particle used in macroscopic flow equations and flowing with velocity v covers a path length L in the same time as an actual fluid particle flowing with velocity v_s covers an average effective path length L_e , as shown in Figure 2.3.

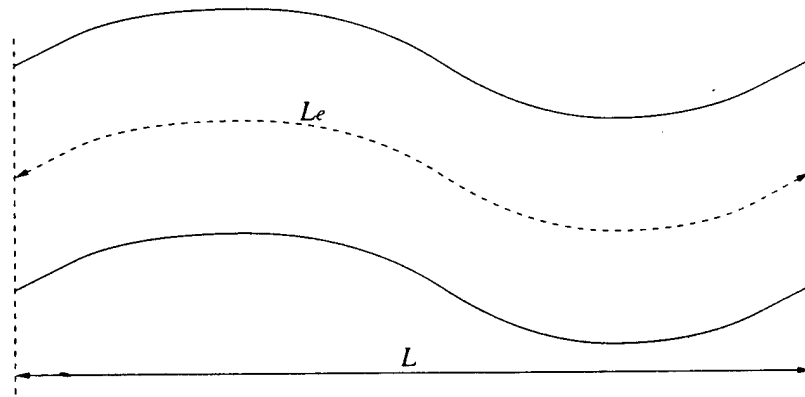


Figure 2.3: Kozeny-Carman flow model.

Combination of Equations 2.13 and 2.14 gives,

$$k = \frac{nD^2}{16C_s \left(\frac{L_e}{L}\right)^2}, \quad (2.15)$$

where D is assumed to be four times the hydraulic radius,

$$D = 4 \frac{\text{void volume of medium}}{\text{surface area of channels in medium}} = \frac{4n}{S_0(1-n)}, \quad (2.16)$$

and S_0 is the specific surface area based on the solid volume. By combining Equations 2.15 and 2.16, the usual form of the Kozeny-Carman equation for permeability is,

$$k = \frac{n^3}{C_s \left(\frac{L_e}{L}\right)^2 (1-n)^2 S_0^2}, \quad (2.17)$$

where $\frac{L_e}{L}$ is the tortuosity factor \mathcal{T} . A combined factor $k' = C_s \mathcal{T}^2 = C_s \left(\frac{L_e}{L}\right)^2$ is the Kozeny-Carman constant. The Kozeny-Carman equation indicates the overwhelming importance of pore size (through the S_0 term) in determining the permeability of a porous medium.

According to Carman, C_s lies within the range 2.0 to 3.0 with a likely average value of 2.5. He also suggested that \mathcal{T}^2 has a value of about 2.0 in all unconsolidated porous aggregates like packed beds, which results in $k' = 5.0$. Much evidence that is now available certainly suggests that for unoriented particle aggregates in the porosity range of 0.35 to 0.70, $k' = 5.0 \pm 10\%$ according to Wyllie and Spangler (1952) and Wyllie and Gregory (1955). They also found k' is dependent on the porosity, particle shape, and particle orientation. For aggregates of fibers at very large porosities ($n > 0.84$), k' was found to increase rapidly with the porosity.

Although Scheidegger (1974) has strong criticism of the Kozeny-Carman equation, some scholars consider the equation to be approximately valid for certain soil types (Dullien 1992; Mitchell 1993). The Kozeny-Carman equation can be applied to uniformly graded sands and some silts, although serious discrepancies are found when the equation is applied to clays. The main reason of the discrepancy is that clays do not contain approximately uniform pore sizes. Particles in clays are grouped in clusters or aggregates that produce large intercluster pores and small intracluster pores. It is implicit in the derivation of the Kozeny-Carman equation that there shall be no large and small pores in parallel contributing to flow. If such a condition exists, the contribution to flow made by the larger pores is disproportional to the corresponding

effect on specific surface area. The latter quantity is dominated by the dimensions of the small pores.

2.2.2.2 Capillary Model

The capillary permeability model is the simplest approach based on the idea of conduit flow. Scheidegger (1974) distinguished among straight, parallel, and serial type capillary models.

The straight capillary model (Figure 2.4) represents a porous medium as a bundle of identical and parallel straight capillaries of uniform diameter D . The total volume

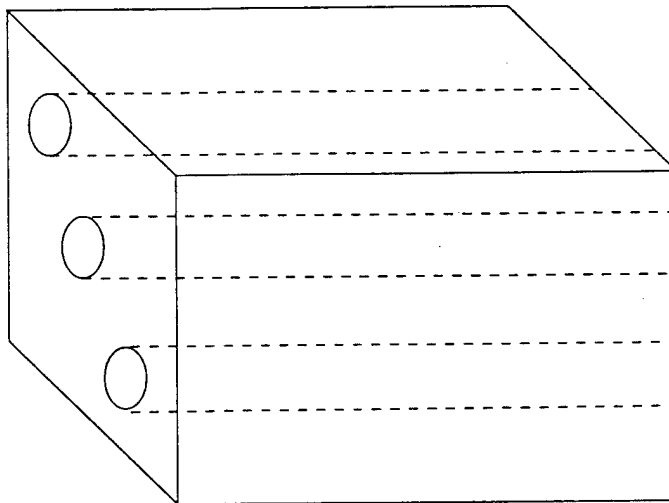


Figure 2.4: Straight parallel capillary model.

flow rate Q through a capillary is given by the law of Hagen-Poiseuille,

$$Q = -\frac{\pi D^4}{128\mu} \frac{dP}{dx}. \quad (2.18)$$

If there are m such capillaries per unit area of cross section of the model, the Darcy velocity will be,

$$v = -\frac{m\pi D^4}{128\mu} \frac{dP}{dx}, \quad (2.19)$$

and,

$$k = \frac{m\pi D^4}{128}. \quad (2.20)$$

As the model has a porosity of,

$$n = \frac{1}{4}m\pi D^2, \quad (2.21)$$

the permeability is,

$$k = \frac{nD^2}{32}, \quad (2.22)$$

which is a variant of Kozeny-Carman equation. Equation 2.22 also bears similarity to the empirical Hazen equation,

$$k = C_m D_{10}^2, \quad (2.23)$$

where C_m is an empirical parameter and D_{10} is the effective grain size of a loose clean sand.

In the straight capillary model, there is no flow orthogonal to the capillaries. A general parallel model of capillaries with different diameters has one-third of the capillaries in each of three spatial dimensions and arrives at the permeability as,

$$k = \frac{n}{96} \int_0^\infty D^2 \alpha(D) dD. \quad (2.24)$$

The mean square diameter is evaluated according to a pore size distribution function $\alpha(D)$ and 96 is substituted for 32 in Equation 2.22 because only $\frac{1}{3}$ of the capillaries are oriented in each direction. Equation 2.24 is sensitive to error at the extrema of the pore size distribution function corresponding to the largest pore sizes (Scheidegger 1974).

In the serial type capillary model (Figure 2.5), the pore network is approximated by three identical sets of tortuous channels. Each channel is assumed to consist of segments having different diameters distributed according to a pore size distribution function $\alpha(D)$. The permeability of this model is,

$$k = \frac{n}{96} \frac{\left(\int \frac{\alpha(D)}{D^2} dD \right)^2}{\int \frac{\alpha(D)}{D^6} dD}. \quad (2.25)$$

The serial type model tends to underestimate permeabilities and is very sensitive to uncertainties at the extrema of the pore size distribution function corresponding to the smallest pores (Dullien 1992).

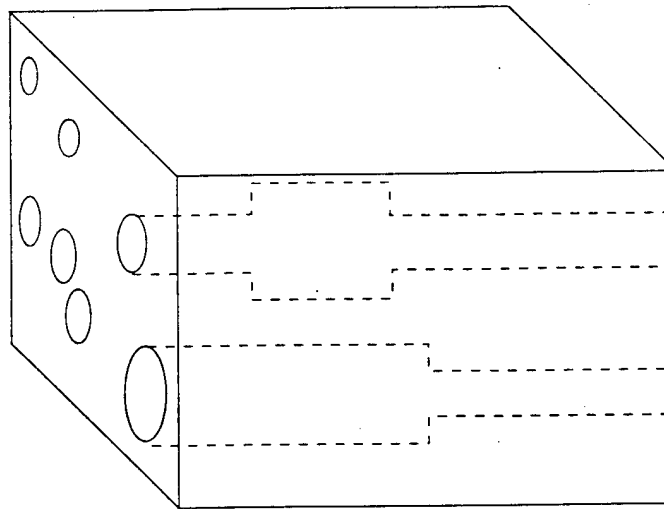


Figure 2.5: Serial capillary model.

2.2.3 Drag Flow Model

As discussed by Scheidegger (1974), Emersleben (1925) first proposed the “drag theory of permeability”, which was different from the theory of Kozeny. This approach considers flow around submerged objects. The walls of the pores are modeled as obstacles in an otherwise straight flow of viscous fluid. Fluid drag forces are estimated from the Navier-Stokes equations, and the sum of drag forces is assumed to give the resistance of porous medium to flow. The subject of low Reynolds number flow around submerged objects is discussed in detail by Happel and Brenner (1965).

Iberall (1950) specified the obstacles as cylinders. He considered the permeability of a random distribution of circular cylinders and showed for low Reynolds number Re that,

$$k = \frac{3}{16} \frac{nD^2}{1-n} \frac{2 - \ln Re}{4 - \ln Re}, \quad (2.26)$$

where,

$$Re = \frac{\rho v_s D}{\mu}, \quad (2.27)$$

D is the diameter of the cylinders, and v_s is the average pore velocity (i.e., seepage velocity). It is noted from Equation 2.26 that permeability is not constant but varies with the Reynolds number, i.e., the flow velocity, although the derivation was actually based on the assumption of low Reynolds number flow. This slow variation of permeability with flow is quite characteristic of many instances in which the flow is nominally viscous.

Brinkman (1947, 1948) assumed the obstacles in the fluid were spheres of diameter D held in position by external forces. He extended the Stokes drag force on a sphere (a sphere placed in an infinite flow domain) to include the effect of neighboring spheres and superimposed Stokes and Darcy flow to obtain,

$$\nabla P = -\frac{\mu}{k} \mathbf{v} + \mu \nabla^2 \mathbf{v}. \quad (2.28)$$

The relationship derived by Brinkman for the permeability is,

$$k = \frac{D^2}{72} \left(3 + \frac{4}{1-n} - 3 \sqrt{\frac{8}{1-n} - 3} \right). \quad (2.29)$$

This equation gives $k = 0$ for $n = \frac{1}{3}$, which makes it unsuitable for relatively low porosities (Happel and Brenner 1965). Lundgren (1972) proposed a generalized Brinkman equation,

$$k = \frac{D^2}{72\mathcal{F}(n)} \left(3 + \frac{4}{1-n} - 3 \sqrt{\frac{8}{1-n} - 3} \right). \quad (2.30)$$

Equation 2.30 includes an “effective viscosity” $\mathcal{F}(n)$ defined as,

$$\mathcal{F}(n) = \frac{4\pi}{3} \frac{\alpha^2 R^2}{(1-n) F(\alpha^2 R^2, \alpha R)}, \quad (2.31)$$

where,

$$\alpha R = \frac{3}{4} \frac{3 + \sqrt{\frac{8}{1-n} - 3}}{\frac{1}{1-n} - \frac{3}{2}}, \quad (2.32)$$

$R = \frac{D}{2}$, and $F(\alpha^2 R^2, \alpha R)$ is a complicated expression involving Bessel functions and Legendre polynomials. However, the modified Brinkman equation behaves much differently from other predictions for $n < 0.7$ (Dullien 1992).

The resistance of arbitrarily shaped objects in a steady state stream of a viscous fluid can be calculated by solving the Navier-Stokes equations for the appropriate boundary conditions. However, analytical solutions for such problems are very limited.

2.2.4 Anisotropic Porous Media and Permeability Tensor

Most porous media are anisotropic. Anisotropic permeability can result from both preferred orientation of elongated or platy particles and stratification of soil deposits (Mitchell 1993). While the pressure gradient and Darcy velocity vectors are parallel in isotropic media, their directions are generally non-parallel in anisotropic media. Consequently, the value of permeability depends on the direction of measurement in an anisotropic porous medium.

In anisotropic media, Darcy's law is written as,

$$\mathbf{v} = -\frac{\mathbf{k}}{\mu} \nabla P, \quad (2.33)$$

where the permeability \mathbf{k} takes the form of a second-order tensor in a x - y - z Cartesian coordinate system,

$$\mathbf{k} = \begin{bmatrix} k_{xx} & k_{xy} & k_{xz} \\ k_{yx} & k_{yy} & k_{yz} \\ k_{zx} & k_{zy} & k_{zz} \end{bmatrix}. \quad (2.34)$$

Considerable effort has been expended to prove the \mathbf{k} tensor is symmetric, i.e., $k_{xy} = k_{yx}$, etc. (Szabo 1968; Whitaker 1969; Guin et al. 1971; Case and Cochran 1972). The physical meaning of these equalities is that the permeability values in opposite directions in the medium are the same, so that the \mathbf{k} tensor changes the axes without deformation of the system. In exceptional cases, where the pores of a medium form a symmetric helicoidal arrangement and the velocity field is forced to have rotation, the

tensor is not symmetric (Liakopoulos 1965). It is generally assumed that anisotropic porous media are “orthotropic”, i.e., they have three mutually orthogonal principal axes. For an orthotropic medium, rotation of the coordinate system will produce a diagonal \mathbf{k} matrix when the coordinate axes are aligned with the principal axes of the medium. In this case, ∇P and \mathbf{v} are parallel and Darcy’s law becomes.

$$v_1 = -\frac{k_1}{\mu} \frac{\partial P}{\partial 1}, \quad (2.35)$$

$$v_2 = -\frac{k_2}{\mu} \frac{\partial P}{\partial 2}, \quad (2.36)$$

$$v_3 = -\frac{k_3}{\mu} \frac{\partial P}{\partial 3}, \quad (2.37)$$

where 1, 2, and 3 denote the three principal directions of the permeability tensor, and v_i and k_i ($i = 1, 2, 3$) are the Darcy velocities and permeabilities in the three principal directions, respectively.

In practice, the permeability is usually measured along a direction $\hat{\mathbf{n}}$, which may not necessarily coincide with the principal permeability directions. Darcy’s law in this direction is written as,

$$v_n = -\frac{k_n}{\mu} \frac{\partial P}{\partial n}, \quad (2.38)$$

where v_n and $\frac{\partial P}{\partial n}$ are the projections of \mathbf{v} and ∇P in the $\hat{\mathbf{n}}$ direction, respectively, i.e.,

$$v_n = \hat{\mathbf{n}} \cdot \mathbf{v}, \quad (2.39)$$

$$\frac{\partial P}{\partial n} = \hat{\mathbf{n}} \cdot \nabla P, \quad (2.40)$$

and k_n is called the directional permeability. The directional permeability may not necessarily be equal to the projection of \mathbf{k} in the $\hat{\mathbf{n}}$ direction (Case 1971).

Scheidegger (1974) investigated the relation between directional permeability and permeability tensor. He distinguished two possible cases. Case 1: the velocity is measured directly and the component of the pressure gradient in the direction of the

velocity is used in Darcy's law; Case 2: the velocity in the direction of the pressure gradient is measured and used in Darcy's law.

In the first case, from Equations 2.38, 2.39 and 2.40.

$$k_n = -\mu \frac{\hat{\mathbf{n}} \cdot \mathbf{v}}{\hat{\mathbf{n}} \cdot \nabla P}. \quad (2.41)$$

Operating on the tensor form of Darcy's law in Equation 2.33 leads to.

$$-\nabla P = \mu \mathbf{k}^{-1} \cdot \mathbf{v}, \quad (2.42)$$

where \mathbf{k}^{-1} is the inverse of \mathbf{k} . Combining Equations 2.41 and 2.42 gives.

$$k_n = \frac{\hat{\mathbf{n}} \cdot \mathbf{v}}{\hat{\mathbf{n}} \cdot \mathbf{k}^{-1} \cdot \mathbf{v}} = \frac{1}{\hat{\mathbf{n}} \cdot \mathbf{k}^{-1} \cdot \hat{\mathbf{n}}}. \quad (2.43)$$

If the principal axes of the permeability tensor are chosen as coordinate axes and the $\hat{\mathbf{n}}$ direction makes angles α , β , and γ with the principal axes. Equation 2.43 becomes,

$$\frac{1}{k_n} = \frac{\cos^2 \alpha}{k_1} + \frac{\cos^2 \beta}{k_2} + \frac{\cos^2 \gamma}{k_3}. \quad (2.44)$$

In two dimensions, according to Equation 2.44, the plot of $k_n^{\frac{1}{2}}$ produces an ellipse whose axes are in the principal directions of permeability with lengths of axes equal to twice the square root of the principal permeability values (Figure 2.6).

In the second case, however, pressure gradient is in the $\hat{\mathbf{n}}$ direction. i.e..

$$\nabla P = \frac{\partial P}{\partial n} \hat{\mathbf{n}}, \quad (2.45)$$

and.

$$v_n = \hat{\mathbf{n}} \cdot \mathbf{v} = -\frac{1}{\mu} \hat{\mathbf{n}} \cdot \mathbf{k} \nabla P = -\frac{1}{\mu} \hat{\mathbf{n}} \cdot \mathbf{k} \frac{\partial P}{\partial n} \hat{\mathbf{n}}. \quad (2.46)$$

Comparison of Equations 2.46 and 2.38 yields,

$$k_n = \hat{\mathbf{n}} \cdot \mathbf{k} \cdot \hat{\mathbf{n}}. \quad (2.47)$$

If the principal axes of the permeability tensor are coordinate axes. a similar treatment as that used in Case 1 results in following expression,

$$k_n = k_1 \cos^2 \alpha + k_2 \cos^2 \beta + k_3 \cos^2 \gamma. \quad (2.48)$$

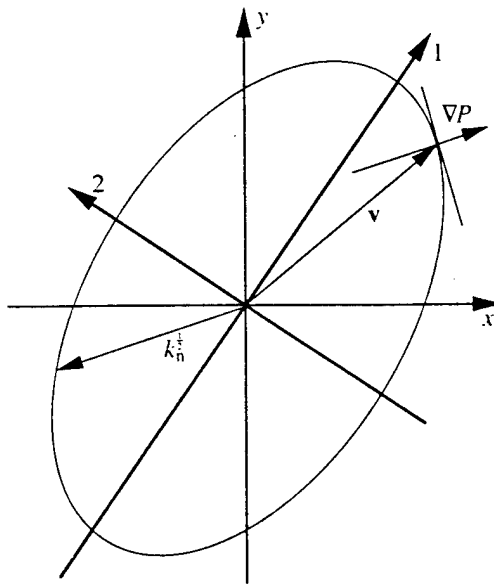


Figure 2.6: Graphical determination of the direction of the pressure gradient based on a given velocity and the permeability tensor ellipse.

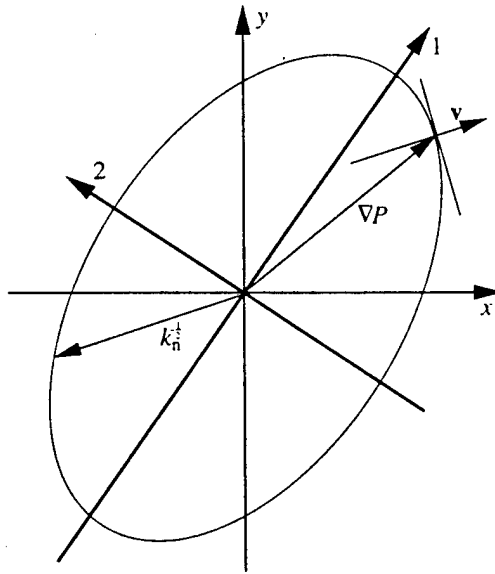


Figure 2.7: Graphical determination of the direction of the velocity based on a given pressure gradient and the permeability tensor ellipse.

Equation 2.48 defines an ellipse if $k_n^{-\frac{1}{2}}$ is plotted for various \hat{n} directions in two dimensions (Figure 2.7).

Given the first ellipse of permeability, the direction of pressure gradient can be graphically determined for a given velocity, while the direction of velocity for a given pressure gradient can be determined from the second ellipse of permeability (Liakopoulos 1965; Case and Cochran 1972). The construction procedure for obtaining the direction of the velocity vector for a known direction of pressure gradient is (Liakopoulos 1965):

1. Construct the permeability ellipse in the directions of its principal axes with semi-axes equal to the inverse square root of the principal permeabilities, i.e., the second ellipse of permeability;
2. Draw the direction of the pressure gradient vector passing through the center of the ellipse;
3. Draw the tangent plane at the point where the pressure gradient vector penetrates the surface of the ellipse;
4. Draw the normal to the tangent plane at the penetration point. This is the direction at which the flow will take place (Figure 2.7).

A similar procedure can be followed to determine the direction of pressure gradient using the first ellipse of permeability (Figure 2.6). More details can be found in Liakopoulos (1965).

There is a standard method for the transformation of a symmetric tensor in any arbitrary Cartesian coordinate system to one in which the tensor is diagonal. For a two-dimensional anisotropic porous medium, if k_{xx} , k_{yy} , and k_{xy} are known in the x - y Cartesian coordinate system (Figure 2.8), the values of the principal permeabilities k_1 and k_2 and the angle θ ($0^0 \leq \theta \leq 180^0$) between the direction of k_1 and the positive x direction can be determined by (Szabo 1968),

$$\theta = \begin{cases} \frac{1}{2} \arctan\left(\frac{2k_{xy}}{k_{xx} - k_{yy}}\right) & \text{if } k_{xx} > k_{yy} \text{ and } k_{xy} \geq 0; \\ 45^0 & \text{if } k_{xx} = k_{yy} \text{ and } k_{xy} \geq 0; \\ \frac{1}{2} \arctan\left(\frac{2k_{xy}}{k_{xx} - k_{yy}}\right) + \frac{\pi}{2} & \text{if } k_{xx} < k_{yy}; \\ 135^0 & \text{if } k_{xx} = k_{yy} \text{ and } k_{xy} \leq 0; \\ \frac{1}{2} \arctan\left(\frac{2k_{xy}}{k_{xx} - k_{yy}}\right) + \pi & \text{if } k_{xx} > k_{yy} \text{ and } k_{xy} \leq 0. \end{cases} \quad (2.49)$$

$$k_{1,2} = \frac{k_{xx} + k_{yy}}{2} \pm \frac{1}{2} \sqrt{(k_{xx} - k_{yy})^2 + 4k_{xy}^2}. \quad (2.50)$$

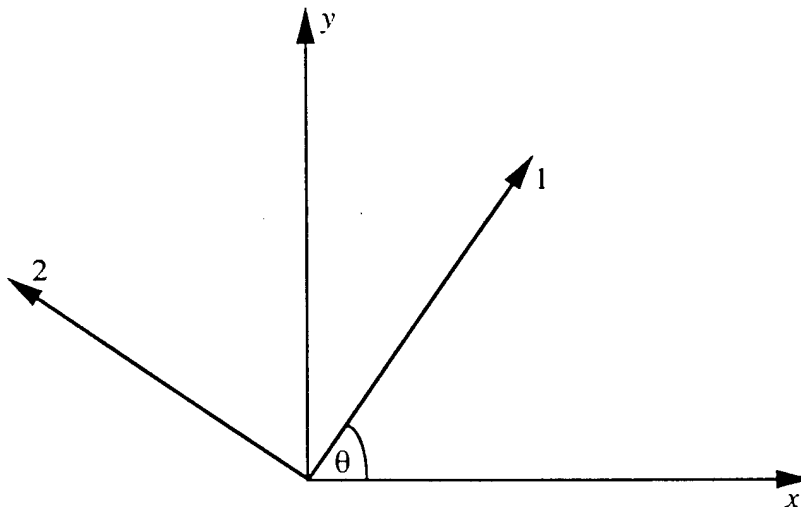


Figure 2.8: x - y Cartesian coordinate system and principal tensor axes.

2.2.5 Limitations of Darcy's Law

Non-Darcy flow behavior was reported as early as 1898 (Mitchell 1993). The following hypotheses have been proposed to account for non-linearity between flow velocity and gradient (Scheidegger 1974; Mitchell 1993): (1) non-Newtonian behavior

of the fluid itself; (2) particle migrations that cause blocking and unblocking of pores; (3) local consolidation and swelling of the soil; (4) molecular or ionic effects; and (5) turbulent effects associated with high flow rates.

The linearity of Darcy's law can be derived from the Navier-Stokes equations if the inertial and unsteady terms are neglected. Ignoring the inertial term restricts the analysis to creeping (laminar) flow where viscous forces dominate in the flow regime. The range of validity of Darcy's law is expressed in terms of Re .

$$Re = \frac{\rho V \mathcal{L}}{\mu}. \quad (2.51)$$

where \mathcal{L} is a characteristic length and V is a characteristic velocity of the flow system. \mathcal{L} is generally the mean pore size, mean grain size, or \sqrt{k} . Re is a measure of the ratio between the inertial and viscous forces of the flow. In any event, it is generally believed that Darcy's law is valid as long as $Re \leq 5$.

Darcy's law can be modified to account for non-linear flow behavior at high velocities. According to Scheidegger (1974), Forchheimer (1901) suggested that Darcy's law include a second-order velocity term,

$$\left| \frac{dP}{dx} \right| = a_1 v + a_2 v^2, \quad (2.52)$$

where a_1 and a_2 are constants. To obtain a better representation of experimental data, a cubic term was added later (Scheidegger 1974),

$$\left| \frac{dP}{dx} \right| = a_1 v + a_2 v^2 + a_3 v^3. \quad (2.53)$$

At low velocities, v^2 and v^3 are much less than v and Equation 2.53 reduces to Darcy's law. The Forchheimer Equation has been generalized further to contain a time-dependent term (Polubarinova-Kochina 1952),

$$\left| \frac{dP}{dx} \right| = a_1 v + a_2 v^2 + a_3 \frac{\partial v}{\partial t}. \quad (2.54)$$

Other heuristic corrections to Darcy's law can be found in Scheidegger (1974) and Dullien (1992).

2.3 Hydrodynamic Dispersion in Porous Media

2.3.1 Introduction and Convection-Dispersion Equation

According to Bear (1972), one of the earliest observations of dispersion was reported by Slichter in 1905 who used an electrolyte as a tracer in studying the movement of groundwater. A tracer is a chemical compound that does not affect the density or the viscosity of the fluid phase in which it is diluted and does not sorb to the solid phase of the porous medium during transport. Slichter observed that at an observation well downstream of the injection point, the tracer concentration increased gradually with time. It was also observed that in an uniform flow field the tracer advanced in the direction of the flow in a pear-like shape that became longer and wider as it advanced. Slichter explained this phenomena by noting that, for flow through capillary tubes, fluid velocity varies across the cross section of each tube and that, because a porous medium is composed of a great number of these tubes, the combined effect is likely to cause the mixing that he observed. This tracer spreading phenomenon is called hydrodynamic dispersion in porous media. It is a nonsteady, irreversible process in which the tracer mass mixes with progressively larger volumes of fluid. If the tracer initially occupies a separate region in the flow field, an ever-widening transition zone is created due to dispersion, across which the tracer concentration varies from that of the tracer liquid to that of the carrier liquid. In practice, the displacement of two miscible fluids may be considered as tracer flow when the fluids have the same densities and viscosities, and there is no volume change associated with mixing.

Contaminant transport in the subsurface is generally viewed as the net effect of two processes, convection and dispersion. Convection is transport by the average motion of the fluid and is the primary mechanism responsible for contaminant migration in many aquifers. Dispersion is spreading of the convective contaminant front due to the movements of individual contaminant particles through the pores and the various physical and chemical phenomena that take place within the pores. Mechanisms that

contribute to dispersion include molecular diffusion, mechanical dispersion, boundary layer or film diffusion, and intraparticle diffusion. Currently, one of the most widely held tenets is the assumption that hydrodynamic dispersion, which results from molecular diffusion and mechanical dispersion, constitutes the total dispersion.

2.3.1.1 Molecular Diffusion

The first quantitative study of diffusion was made by Fick in 1855, who found an analogy between molecular diffusion and heat conduction. He adapted Fourier's heat equation to describe the diffusion process by stating that mass flux of a diffusing substance is proportional to the concentration gradient,

$$j_0 = -d_0 \nabla C, \quad (2.55)$$

where j_0 is the mass flux, i.e., the rate of mass transfer per unit area of cross section, of a diffusive non-reactive tracer. d_0 is the coefficient of molecular diffusion, which is a scalar in aqueous solution, and C is the tracer concentration, usually defined as the mass of tracer per unit volume of solution. In the absence of convection, conservation of mass and Equation 2.55 lead to the well-known Fickian diffusion equation for transient tracer concentration,

$$\frac{\partial C}{\partial t} = d_0 \nabla^2 C, \quad (2.56)$$

where t is time and ∇^2 is the Laplacian operator. If diffusion occurs within a fluid in motion, the following convection-diffusion equation governs the evolution of tracer concentration,

$$\frac{dC}{dt} = \frac{\partial C}{\partial t} + \mathbf{u} \cdot \nabla C = d_0 \nabla^2 C, \quad (2.57)$$

where $\frac{d}{dt} = \frac{\partial}{\partial t} + \mathbf{u} \cdot \nabla$ is the Lagrangian or material derivative and \mathbf{u} is the fluid velocity vector.

Albert Einstein in 1905 was the first to derive an expression for d_0 of a colloidal suspension in an aqueous solution (Einstein 1956). His derivation was based on the

assumptions that colloidal molecules are approximately spherical and are large in comparison with the molecules of the aqueous solution. The successive displacements of the colloidal molecules by collision with liquid molecules were independent giving rise to a random walk or Brownian motion. Molecular diffusion (or simply diffusion) in solids, liquids, and gases is primarily due to Brownian motion. It is also caused by osmotic forces, thermal diffusion, and electro-osmosis. Due to Brownian motion, molecularly dispersed contaminants tend to move from a volume element with a higher concentration or specific heat toward any neighboring element with a lower concentration or specific heat content. This process is independent of convection.

As a consequence of the tortuous diffusive pathways within porous media and the presence of fluid-solid interfaces, the diffusion coefficient in an isotropic porous medium d is less than the diffusion coefficient in aqueous solution d_0 ,

$$d = d_0 d^*, \quad (2.58)$$

where d^* is the nondimensional diffusivity of the medium. From a review of data on consolidated granular media obtained by several investigators, Perkins and Johnston (1963) suggested that the value of d^* is approximately 0.7 while Fried and Combarous (1971) reported values of 0.4 to 0.8. Bhattacharya and Gupta (1990) derived a formula for d^* using central limit theorem applied to ergodic Markov processes, which provides a theoretical basis for the values of d^* observed in experiments.

Anisotropic porous media have different diffusion properties in different directions. As such, the direction of flow of diffusing substance at any point in such media may not be normal to the surface of constant concentration through the point. In an anisotropic medium, the vector of the mass flux \mathbf{j} is written as,

$$\mathbf{j} = -\mathbf{d}\nabla C, \quad (2.59)$$

where the diffusion coefficient \mathbf{d} is a symmetric second-order tensor in a x - y - z Cartesian coordinate system,

$$\mathbf{d} = \begin{bmatrix} d_{xx} & d_{xy} & d_{xz} \\ d_{xy} & d_{yy} & d_{yz} \\ d_{xz} & d_{yz} & d_{zz} \end{bmatrix}. \quad (2.60)$$

Accordingly, the nondimensional diffusivity \mathbf{d}^* is also a symmetric second-order tensor in the coordinate system.

$$\mathbf{d}^* = \frac{\mathbf{d}}{d_0} = \begin{bmatrix} d_{xx}^* & d_{xy}^* & d_{xz}^* \\ d_{xy}^* & d_{yy}^* & d_{yz}^* \\ d_{xz}^* & d_{yz}^* & d_{zz}^* \end{bmatrix}. \quad (2.61)$$

Like for the permeability tensor, rotation of the coordinate system will produce a diagonal \mathbf{d} tensor when the coordinate axes are aligned with the principal axes of diffusion for the medium. Vectors ∇C and \mathbf{j} are parallel in such cases and,

$$j_1 = -d_1 \frac{\partial C}{\partial 1}, \quad (2.62)$$

$$j_2 = -d_2 \frac{\partial C}{\partial 2}, \quad (2.63)$$

$$j_3 = -d_3 \frac{\partial C}{\partial 3}, \quad (2.64)$$

where 1, 2, and 3 denote the three principal directions of the diffusion tensor, j_i and d_i ($i = 1, 2, 3$) are the mass fluxes and diffusion coefficients along the three principal directions, respectively. If the normal of a surface makes angles α , β , and γ with the three principal axes of diffusion, the diffusion coefficient d_n in the direction of this normal is (Carslaw and Jaeger 1959),

$$d_n = d_1 \cos^2 \alpha + d_2 \cos^2 \beta + d_3 \cos^2 \gamma. \quad (2.65)$$

2.3.1.2 Mechanical Dispersion

Mechanical dispersion results from velocity variations within the porous media. Three mechanisms, shown schematically in Figure 2.9, operate at the microscopic level to give rise to such variations:

- (1) the velocity distribution across each pore channel;
- (2) variations in velocity as a result of the distribution of pore channel size; and
- (3) tortuosity of individual flow paths.

These processes combine to give two geometrical aspects of dispersion: (1) a longitudinal effect due to the differences between the velocity components along the mean velocity direction, and (2) a transverse effect due to the differences between the velocity components orthogonal to the mean velocity direction. Mechanical dispersion is attributed to convection. When convection is weak, mechanical dispersion may be negligible relative to molecular diffusion.

In most dispersion theories, mechanical dispersion is generally considered to be mathematically analogous to diffusion because spreading of the contaminant results from velocity variations across a concentration gradient. Consequently, the mechanical dispersion component of tracer flux is commonly represented mathematically by a "Fickian type" equation analogous to Equation 2.59,

$$\mathbf{J}_m = -\mathbf{D}_m \nabla C, \quad (2.66)$$

where \mathbf{J}_m is the mass flux vector due to mechanical dispersion and \mathbf{D}_m is the coefficient of mechanical dispersion. The characterization of mechanical dispersion as a Fickian process remains a subject of continuing debate which will be discussed in detail in section 2.3.7. Adding Equations 2.59 and 2.66 gives the total dispersive mass flux vector \mathbf{J}_d of a tracer as,

$$\mathbf{J}_d = -\mathbf{D} \nabla C, \quad (2.67)$$

where \mathbf{D} is the coefficient of hydrodynamic dispersion and,

$$\mathbf{D} = \mathbf{d} + \mathbf{D}_m. \quad (2.68)$$

The total mass flux vector \mathbf{J} due to both convection and dispersion is,

$$\mathbf{J} = \mathbf{u}C - \mathbf{D} \nabla C. \quad (2.69)$$

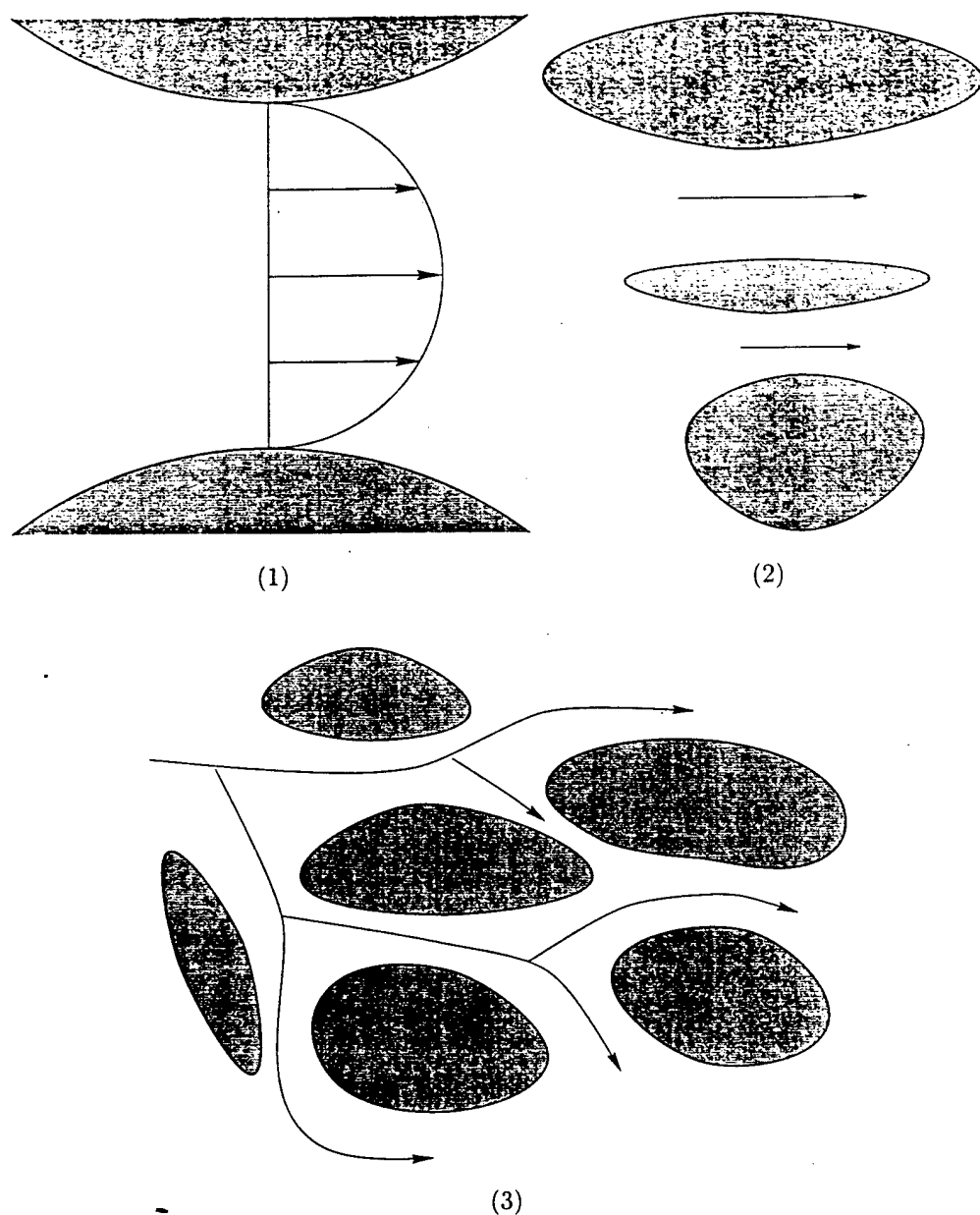


Figure 2.9: Components of mechanical dispersion at the microscopic level: (1) the velocity distribution across each pore channel; (2) variations in velocity as a result of the distribution of pore channel size; and (3) tortuosity of individual flow paths.

Conservation of mass and Equation 2.69 lead to the widely used convection-dispersion equation for solute transport (Ogata 1970; Bear 1972; Freeze and Cherry 1979).

$$\frac{dC}{dt} = \frac{\partial C}{\partial t} + \mathbf{u} \cdot \nabla C = \mathbf{D} \nabla^2 C. \quad (2.70)$$

The convection-dispersion equation models the process of dispersion as a diffusional process and predicts that, in an uniform flow field, a set of tracer particles will be normally distributed about a center moving with the average convective velocity.

From the viewpoint of classical statistics, if the travel time for an individual tracer particle becomes much larger than the time interval during which its successive velocities are positively correlated, its total displacement may be considered as a sum of a large number of elementary displacements which are statistically independent of one another. Then, the probability distribution of the particle's total displacement should be normal according to the central limit theorem (Bear 1972). In view of the ergodic principle (in an ergodic system, the ensemble averages and time averages are equivalent), this distribution also represents the spatial distribution of displacements of a cloud of initially close particles. It is this tendency for the cloud of tracer particles to converge to a normal distribution and to spread with a variance that is proportional to time that makes it possible to model mass transport as a diffusional process.

2.3.2 Hydrodynamic Dispersion Tensor and Its Determination

The coefficient of hydrodynamic dispersion \mathbf{D} (Equation 2.67) is a second-rank symmetric tensor (Bear 1972; Koch and Brady 1985; Plumb and Whitaker 1988). The principal axes of \mathbf{D} are believed to be oriented parallel and transverse to the mean direction of the regional flow. This indicates that mass transport can be defined by two characteristic dispersion components that are defined once the mean direction of regional flow is known. If the dispersion coefficient in the direction of the flow L (i.e., the longitudinal dispersion coefficient) and the dispersion coefficient in the direction perpendicular to the flow T (i.e., the transverse dispersion coefficient) are denoted as D_L and D_T , respectively, the convection-dispersion equation becomes,

$$\frac{\partial C}{\partial t} + \mathbf{u} \cdot \nabla C = D_L \frac{\partial^2 C}{\partial L^2} + D_T \nabla_T^2 C, \quad (2.71)$$

where ∇_T^2 is the Laplacian in transverse directions.

Bear (1961) studied the relationship between \mathbf{D} and \mathbf{u} . After assuming that only part of each velocity component is significant, which is either parallel or normal to the mean flow direction, he showed,

$$D_{km} = a_{ijkl} \frac{u_i u_j}{u_0} \quad (i, j, k, m = x, y, z), \quad (2.72)$$

where u_0 is the magnitude of the fluid velocity, u_i is the component of the fluid velocity in i direction, and a_{ijkl} is called the media's geometrical dispersivity (a fourth-rank symmetric tensor). In general, a_{ijkl} contains 81 components. Scheidegger (1961) studied the symmetry properties of a_{ijkl} and wrote the following equation for isotropic media,

$$a_{ijkl} = a_T \delta_{ij} \delta_{km} + \frac{a_L - a_T}{2} (\delta_{ik} \delta_{jm} + \delta_{im} \delta_{jk}), \quad (2.73)$$

where a_L and a_T are the longitudinal and transverse dispersivities of the media, respectively, and δ is the Dirac delta function,

$$\delta_{ij} = \begin{cases} 1 & \text{if } i = j; \\ 0 & \text{if } i \neq j. \end{cases} \quad (2.74)$$

By substituting Equation 2.73 into 2.72, the following equation is obtained,

$$D_{ij} = a_T u_0 \delta_{ij} + (a_L - a_T) \frac{u_i u_j}{u_0}, \quad (2.75)$$

which provides a theoretical basis for the relation between \mathbf{D} and \mathbf{u} for isotropic media.

In practice, the longitudinal and transverse mechanical dispersion coefficients are generally expressed in terms of the seepage velocity v_s in the flow direction L ,

$$D_{mL} = (a_L v_s)^{m_1}, \quad (2.76)$$

$$D_{mT} = (a_T v_s)^{m_2}, \quad (2.77)$$

where m_1 and m_2 are empirical constants between 1 and 2. Laboratory studies have indicated that for practical purposes, m_1 and m_2 can be generally taken as unity for granular materials (Bedient et al. 1994). For isotropic media, from Equations 2.68, 2.58, 2.76, and 2.77,

$$D_L = d_0 d^* + (a_L v_s)^{m_1}, \quad (2.78)$$

$$D_T = d_0 d^* + (a_T v_s)^{m_2}. \quad (2.79)$$

As most chemical species have d_0 on the order of 10^{-9} to $10^{-10} \frac{m^2}{s}$ at 20°C , the contribution of diffusion to hydrodynamic dispersion is typically very small and is neglected in most models of groundwater contamination. One exception would be in geologic formations where convective transport is essentially zero, such as in very low permeability clays or very deep aquifers where the flow rate may be on the order of a few centimeters in a hundred years.

D_L and D_T are also defined in terms of the spreading of an initial plume (Fetter 1993),

$$D_L = \frac{\sigma_L^2}{2t}, \quad (2.80)$$

$$D_T = \frac{\sigma_T^2}{2t}, \quad (2.81)$$

where σ_L^2 and σ_T^2 are the variance of the longitudinal and transverse spreading of the plume, respectively. In the asymptotic limit ($t \rightarrow \infty$), D_L in Equation 2.80 and D_T in Equation 2.81 are equivalent to those defined in Equation 2.71 (Brenner 1980a).

Many experimental studies have been performed to evaluate the influence on dispersion of the characteristics of miscible fluids, of the flow field, and of media properties. Conclusions have been drawn primarily based on comparisons between experimental results and solutions of Equation 2.71. The studies usually lead to relationships between D_L , D_T , and the Peclet number Pe . Dimensional analysis shows that \mathbf{D} is a function of Pe , which defines the ratio between rate of transport by convection and the rate of transport by molecular diffusion,

$$Pe = \frac{vL}{d_0}. \quad (2.82)$$

Fried and Combarous (1971), Bear (1972), and Fried (1975) have summarized many of the experimental results. The available data show that dispersion phenomena exists in several distinguishable domains according to the value of Pe (Figure 2.10). When Pe is very small, molecular diffusion predominates; in the next domain, the

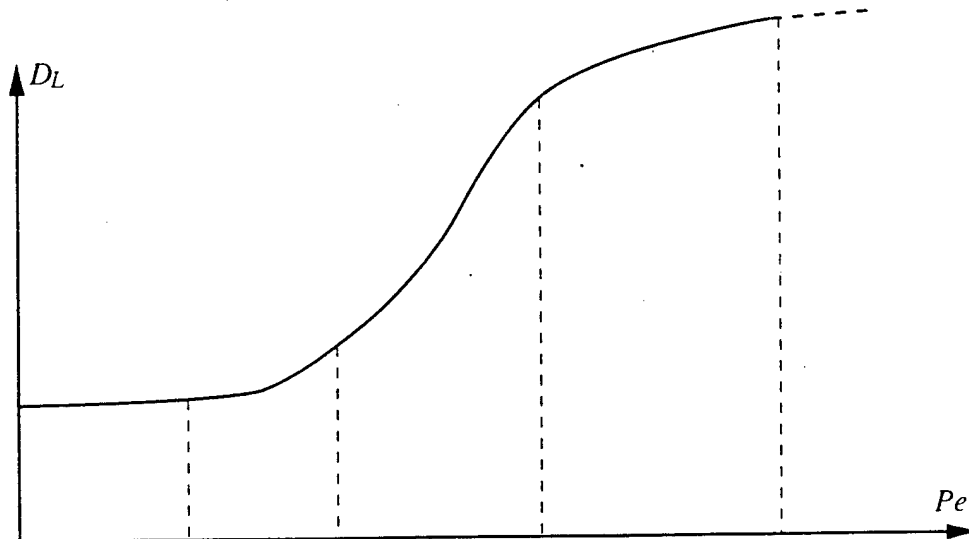


Figure 2.10: A generic relation between D_L and Pe .

effect of molecular diffusion and mechanical dispersion are of the same order; in the third domain, while the longitudinal molecular diffusion is negligible, the transversal molecular diffusion tends to reduce the longitudinal spreading; in the fourth domain, mechanical dispersion predominates; and when Pe is very large, while mechanical dispersion also dominates, the effects of inertia and turbulence can no longer be neglected. A regressive analysis usually leads to the following relation between D_L and Pe ,

$$\frac{D_L}{d_0} = \alpha Pe^\beta, \quad (2.83)$$

where α and β are empirical constants that change with Pe .

In a comprehensive study of dispersion phenomenon, Klotz and Moser (1974) performed 2500 laboratory column tests using radioactive, salt, and dye tracers to determine the dependence of D_L on the characteristics of the permeant and porous

media. Granular materials were tested with differing void ratio, uniformity coefficient, and grain properties (size, shape, and angularity). Their study generally confirms an approximate linear relation between D_L and v_s as suggested by Equation 2.78 with $m_1 = 1$. In addition, the effective grain size and uniformity coefficient substantially affect the value of D_L . The influence of the grain shape and the grain roughness as well as the water temperature are of minor importance. In the study on transverse dispersion in column tests by Klotz et al. (1980), they evaluated the width of the tracer cloud by measuring the concentration-time distributions perpendicular to the flow direction. In general, the transverse dispersion was difficult to determine. They found no dependence of the width on the flow velocity within the low measuring accuracy. On the other hand, they found the width increased with increasing grain size of the porous media. The tests confirmed that D_T is 6–20 times smaller than D_L and anisotropic mixing occurs even in isotropic porous media.

Dispersion theory is concerned with the asymptotic time-dependent, spatial distribution of non-reactive (passive) tracer particles introduced into a fluid flowing through the interstices of a porous medium under the influence of an externally applied pressure gradient. Research on dispersion has covered numerous aspects and involved many approaches. Various models have been developed to provide a mathematical description of this process. These models can be classified into four groups: geometric, random network, statistically geometric, and statistical models.

2.3.3 Geometric Model

Taylor dispersion problem is probably the best example of a geometric model. Taylor (1953, 1954) considered the dispersion in a cylindrical straight tube (Figure 2.11). Laminar, steady, one-dimensional flow of a fluid (i.e., Poiseuille flow) takes place in the tube. The velocity distribution is parabolic across the tube with an average velocity of v_s . At $t = 0$, a tracer is introduced at the origin $x = 0$, simulating a pulse of constant concentration C_0 . The tracer particles are then carried away by the flow. Because of the parabolic velocity profile, the tracer particles close to

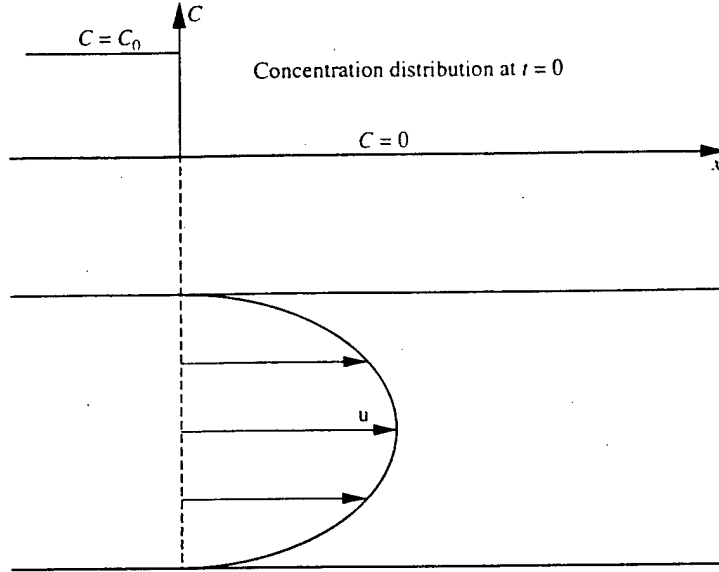


Figure 2.11: Taylor dispersion problem.

the wall move slower than those in the middle of the tube. The spreading of the concentration variation front is purely due to convection initially. However, as the front moves downward, the distribution of tracer becomes more uniform because of transverse molecular diffusion across the flow. The characteristic time for this transverse diffusion is,

$$t_c = \frac{R^2}{d_0}, \quad (2.84)$$

where \$R\$ is the radius of the tube. Using the general diffusion equation in cylindrical coordinates, Taylor showed that for \$t \gg t_c\$, the average cross section concentration \$C(x, t)\$ satisfies the following equation,

$$\frac{\partial C}{\partial t} + v_s \frac{\partial C}{\partial x} = (d_0 + \frac{R^2 v_s^2}{48 d_0}) \frac{\partial^2 C}{\partial x^2}. \quad (2.85)$$

Equation 2.85 indicates that longitudinal dispersion in a cylindrical straight tube obeys the same law as molecular diffusion with an effective dispersion coefficient \$D_{Taylor} = d_0 + \frac{R^2 v_s^2}{48 d_0}\$. The Taylor dispersion mechanism is one in which the transverse variation of longitudinal velocity and transverse mixing interact to produce an overall longitudinal mixing process that is Fickian. Aris (1956) generalized Taylor's approach

to irregularly shaped tubes, where local velocity distributions may not be parabolic and where d_0 varies with concentration. Using a moment-analysis technique, he obtained the coefficient of dispersion D_{Aris} as.

$$D_{Aris} = d_0 + \alpha \frac{R^2 v_s^2}{d_0}, \quad (2.86)$$

where R is a characteristic dimension of the cross section and α is a dimensionless number depending on the cross section.

In the Taylor-Aris theory of dispersion, the dispersion coefficient is proportional to v_s^2 . This theory cannot be applied to porous media in general because miscible flow in porous media is very different from the flow in a capillary. In porous media, most of dispersion comes from the meandering of streamtubes through the complex void structure, and not from the presence of a velocity profile within each pore.

Brenner (1980b, 1981, 1982) coined the name Taylor dispersion to honor Taylor's work. The geometric model postulates a geometry which hopefully bears some resemblance to real porous media, yet is sufficiently simple to allow analytical treatment.

2.3.4 Random Network Model

Some authors have developed porous media dispersion theory by representing the media as random networks of capillaries (De Josselin de Jong 1958; Saffman 1959; Saffman 1960). De Josselin de Jong (1958) was the first to suggest that transverse dispersion is smaller than longitudinal dispersion. However, his assumptions are very restrictive: he neglected molecular diffusion and assumed that fluid velocity is constant within each capillary. Saffman's model (Saffman 1959; Saffman 1960) was more general and represented a major step in the description of hydrodynamic dispersion. The model consists of a network of randomly oriented and distributed straight pores in each of which the flow is uniform (i.e., constant fluid velocity). The pores are connected with one another at the ends, and several pores may start or end at each of these junctions. The path of a fluid particle may be regarded as a random walk in which the length, direction, and duration of each step are random variables.

Using this approach, Saffman calculated a probability distribution function for the displacement of a particle in time and deduced values for the dispersion coefficients. By assuming the pores had equal circular cross sections of radius R , the pores were all of equal length L , and an average velocity v_s in the pores, he obtained the coefficient of longitudinal dispersion $D_{Saffman,L}$ and the coefficient of transverse dispersion $D_{Saffman,T}$ as.

$$D_{Saffman,L} = \frac{d_0}{3} + \frac{3}{80} \frac{R^2 v_s^2}{d_0} + \frac{L^2 v_s^2}{4} \int_0^1 (3x^2 - 1)^2 \frac{M \coth M - 1}{BM^2} dx. \quad (2.87)$$

and,

$$D_{Saffman,T} = \frac{d_0}{3} + \frac{1}{80} \frac{R^2 v_s^2}{d_0} + \frac{9L^2 v_s^2}{8} \int_0^1 x^2(1-x^2) \frac{M \coth M - 1}{BM^2} dx. \quad (2.88)$$

respectively, where $M = \frac{3}{2} \frac{Lv_s x}{B}$ and $B = d_0 + \frac{3R^2 v_s^2 x^2}{16d_0}$. Saffman's model was the first that showed the existence of several domains of dispersion with the change of the Peclet number Pe and the difference between transverse and longitudinal dispersion effects.

The models of De Josselin de Jong and Saffman were extended by Haring and Greenkorn (1970) to the case of non-uniform media by the use of beta distributions for the distributions of pore radius and pore length. Capillary pressure, permeability, and longitudinal and transverse dispersion coefficients were calculated in terms of the parameters of the beta distribution.

2.3.5 Statistically Geometric Model

The local volume averaging method produces a statistically geometric model. This approach is based on the concept of representative elementary volume (REV) (Bear 1972) and the Slattery-Whitaker averaging theorem (Slattery 1969; Whitaker 1969).

An REV in porous media is the smallest volume that yields the local average properties (e.g., porosity) such that addition of surrounding media to this volume does not change these average values (Figure 2.12). On the other hand, it must be sufficiently larger than the size of a single pore that it includes a sufficient number of

pores to permit the computation of meaningful statistical averages required for the continuum concept.

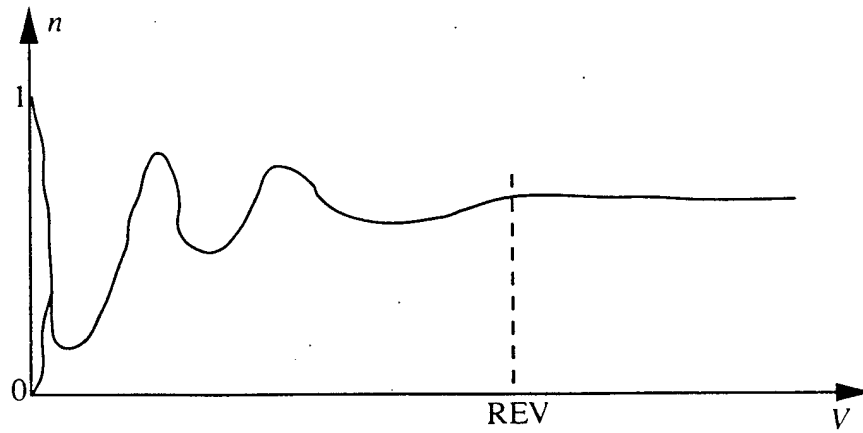


Figure 2.12: Porosity n versus its averaging volume V in a porous medium.

The Slattery-Whitaker averaging theorem relates a transport equation at the microscopic level to its macroscopic counterpart. The theorem states the relationship between gradients of averages and averages of gradients for functions defined in both solid and void phases which exhibit a discontinuity at the phase interface (Figure 2.13).

$$\langle \nabla \psi \rangle = \nabla \langle \psi \rangle + \frac{1}{V} \int_{A_{solid-fluid}} \psi \hat{n} dA, \quad (2.89)$$

where,

$$\langle \psi \rangle = \frac{1}{V} \int_V \psi dV = \frac{1}{V} \int_{V_{fluid}} \psi dV, \quad (2.90)$$

$\langle \cdot \rangle$ refers to an average quantity, ψ is a scalar, vector, or second-order tensor associated with the fluid, V denotes the averaging volume, V_{solid} and V_{fluid} are the solid and fluid volumes within V , respectively, A is the averaging area that encloses the volume V , $A_{solid-fluid}$ is the solid-fluid interfacial area within A , and \hat{n} is a unit vector normal to $A_{solid-fluid}$. Equations 2.89 and 2.90 make it possible to locally average the

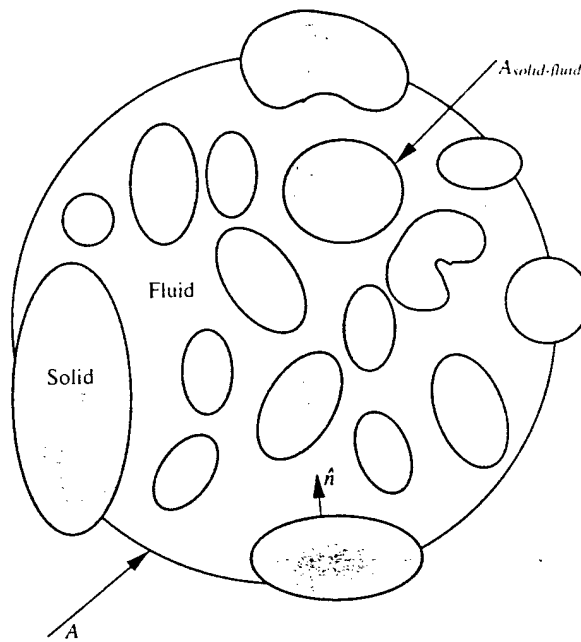


Figure 2.13: Representative elementary volume (REV).

Navier-Stokes equations and the convection-diffusion equation on an REV. A detailed derivation of this approach can be found in Whitaker (1969, 1973, 1986), Bear (1972), and Gray (1975).

By locally averaging quantities in the REV, a continuum model is established on the scale of the REV. This model is an assemblage of randomly interconnected channels of varying length, cross section, and orientation. However, due to the complexity of the flow paths and the interpore and pore-to-pore fluid dynamic interactions, a large number of empirical factors must be introduced in the derivations. Statistically geometric models ignore the microscopic nature of the dispersion process—dispersion occurs not in one continuous medium, but in a medium which exhibits abrupt changes in fundamental properties of its different constitutional phases. This approach is generally regarded as robust, but the principal weakness is that rigorous proof of the existence of satisfactory averaging volumes (obeying certain ergodic and invariance requirements) exists only for idealized porous media. In fact, porous media exhibiting

heterogeneity on a continuum of scales have no REV (Cushman 1990; Cushman et al. 1994).

2.3.6 Statistical Model

Probability theory and statistical mechanics have been long used to study mass transport in porous media. Bear (1972) argued that the path of a tracer particle can be visualized as the vector combination of two motions: one along the pathline of a liquid particle, and another between pathlines as a molecular diffusion process. The nature of both motions, the first determined by the intricate internal geometry of the medium, and the second by the random character of molecular diffusion, prevents any deterministic prediction of the paths of tracer particles. In a similar context, Greenkorn and Kessler (1969) stated that a deterministic description of dispersion is useless and hopeless in practice for at least two reasons: (1) determination of the precise fluid-solid boundary of a random porous medium is, and will remain, impossible; and (2) the tortuous boundary (even if known) will render the problem mathematically intractable.

The basic postulate of the statistical approach is that, although it is impossible to predict the exact path of an individual tracer particle, one may employ probability theory to predict the spatial distribution at any time of a cloud of tracer particles that are initially at a close proximity, and that move under same average condition (Bear 1972). If ergodic hypothesis applies, the problem of the spreading of a cloud of labeled particles is reduced in the statistical approach to the problem of random motion of a single tracer particle through an ensemble of random porous media. The simplest statistical model of dispersion is the one-dimensional random walk model. In this model, a particle moves along a straight line as a series of steps of equal length, and each step is taken either in the forward or backward direction with equal probability of $\frac{1}{2}$. It can be shown that if the particle undergoes n displacements per unit time, the probability that it will be between x and $x + \Delta x$ at time t is,

$$p(x, t)\Delta x = \left(\frac{1}{2\sqrt{\pi D t}} \exp\left(-\frac{x^2}{4Dt}\right) \right) \Delta x, \quad (2.91)$$

where $D = \frac{nL^2}{2}$ and L is the length of each step. Using the law of large numbers, Scheidegger (1954) showed that, for miscible tracers, concentration at a point in the displacing fluid is equal to the probability of finding a particle of displacing fluid at that point. He also extended the random walk theory to three dimensions. However, his analysis led to a scalar D resulting from his negligence of molecular diffusion and his assumption of isotropic spreading.

Unlike models which require non-physical restrictions on the allowable dynamics or media heterogeneity, or both, Cushman (1997) developed a general dispersion theory using classical statistical mechanics which is fully rigorous and obtained without any approximation within the conceptual framework of Hamiltonian dynamics. Theories in statistical mechanics provide the tools to go from the atomistic or molecular structure of matter to a continuum scale. Such theories allow detailed molecular data to be mapped into field and constitutive properties or material parameters (Cushman 1997). Cushman's nonequilibrium statistical mechanical theory of transport involves both diffusive and convective mixing (dispersion) at all scales. The results are based on a generalization of classical approaches used in molecular hydrodynamics and on time-correlation functions defined in terms of nonequilibrium expectations. The resulting constitutive laws are nonlocal and constitutive parameters are wave vector and frequency dependent.

2.3.7 Problem of Scale and Fickian Approximation

The convection-dispersion transport equation (Equation 2.70) forms the theoretical basis in almost every analysis of mass transport in groundwater systems. This approach has traditionally considered dispersivity as a characteristic single-valued property of the entire medium (Bear 1972). However, several studies suggest that dispersivity is not a constant but rather depends on the mean travel distance and

scale of the problem (Fried 1975; Lallemand-Barres and Peaudecerf 1978; Pickens and Grisak 1981; Gelhar et al. 1992). Field experiments have revealed that dispersivity increases with distance between the source and the point of observation as the tracer encounters progressively larger heterogeneities within the aquifer. Lallemand-Barres and Peaudecerf (1978) were the first to publish dispersivity values as a function of the distance traveled. A plot of a_L versus distance showed the following relationship.

$$a_L = \frac{x}{10}, \quad (2.92)$$

where x is the distance traveled by the contaminant. Equation 2.92 is known as the "one-tenth rule" and has been recommended by the EPA as a means to estimate dispersivity in preliminary studies where no data exists (U.S.EPA 1985). In a comprehensive review of data from 59 field studies, Gelhar et al. (1992) found that there was a systematic increase of a_L with observation scale. However, they stated that it is not appropriate to represent the relationship between a_L and x with a single universal line because of the differing degrees of aquifer heterogeneity at different sites. Most published values of aquifer dispersivities were obtained by calibrating a mass transport model to field data. This has usually resulted in relatively large values, typically on the order of tens of meters to over 100 meters. The magnitude of the dispersivity is a measure of uncertainty regarding heterogeneous flow phenomena in an aquifer. The larger the degree of heterogeneity, the larger will be the dispersivity if the system is treated as homogeneous with respect to velocity. If a non-homogeneous velocity distribution due to large-scale geologic heterogeneities is determined, dispersivities would depend on small pore-scale variations of velocity, resulting in values on the order of a few centimeters or less. Dispersivities in this range are typical of column experiments in which there are no large-scale heterogeneities (Gelhar et al. 1992).

As can be seen, the domain of research in the field of dispersion is part of the problem of change of scale, which is a very general problem in physics (Fried 1975). Recent theoretical developments have shown that multiple space-time scales appear naturally in the description of the transport of miscible, non-reactive solutes in saturated porous media (Cushman 1984; Cushman 1986; Koch and Brady 1987; Bhat-

tacharya and Gupta 1990; Cushman 1997). Dispersion phenomena manifest different behavior depending on different scales. Bhattacharya and Gupta (1983) showed that mechanical dispersion, pore diffusion, and molecular diffusion are manifested on three separate scales. Scales of interest often are labeled as microscopic, pore, macroscopic, full aquifer, and regional. Associated with each scale there is a separate transport equation which can be obtained by filtering of a lower scale equation (Cushman 1984; Cushman 1986).

The dispersion problem is also a measurement problem. The concept of scale is fundamentally connected with the measurement process (Cushman 1986). In practice, tracer concentrations are measured by some means. One should first decide on the scale of interest; and then, design an instrument to measure on that scale. The results from any solution of the transport equations are valid only with respect to the *a priori* scale and instrument (Cushman 1986). For example, laboratory analysis of a tracer sample leads to a concentration value averaged over a scale determined by the size of the sampling device. Baveye and Sposito (1984) attached an operational significance to the averaging associated with measurement devices and suggested defining a macroscopic variable by averaging microscopic values according to a weighting function associated with the sampling device. Moltyaner (1989) determined the weighting function associated with the so-called through-the-wall concentration measurement device by considering the interaction of gamma radiation with aquifer materials in a laboratory experiment. The function was found to follow an exponential attenuation law.

Some approaches have been proposed to model scale-dependent dispersion (Pickens and Grisak 1981; Tompson 1988). In the work of Pickens and Grisak (1981), dispersivity varies temporally as a function of mean travel distance and approaches a maximum or asymptotic value. Tompson (1988) described a second-order relationship for local dispersive transport which can be cast in the form of a standard Fickian relationship with apparent time-dependent dispersivity functions that grow to finite, asymptotic values. To model scale-dependent dispersion, the conventional

practice is to involve a simple scaling-up of the porous medium dispersivity value from very small values observed in column experiments to the much larger values calculated from field trials. However, some literature suggest that dispersivity may never approach a finite value asymptotically for some cases. As such, the Fickian approximation of dispersion and the traditional convection-dispersion equation are not valid for these cases. Matheron and Marsily (1980) showed for the special case of a stratified porous medium with flow parallel to the bedding, the transport of solute cannot, in general, be represented by the usual convection-dispersion equation, even for large time. Smith and Schwartz (1980) concluded that field-scale dispersion (macrodispersion), which is usually caused by mixing due to spatial heterogeneities in the permeability field, cannot be modeled by a large value diffusion process. Koch and Brady (1987) showed that when the length and time scales on which a transport process occurs are not much larger than the scales of variations in the velocity field experienced by a tracer particle, a description of the transport in terms of a local, average Fickian process is not applicable. In fact, in Cushman's nonequilibrium non-local theory of transport (Cushman 1997), the concept of classical Fickian dispersive flux is a special case.

2.4 Transport Through Spatially Periodic Porous Media

The analysis of transport processes in spatially periodic porous media is a relatively simple problem when numerical or analytical calculations are confined to a unit cell. However, if one were to analyze an irregular unit cell of arbitrary shape, the analysis would be no easier than that of other models. The simplest spatially periodic porous medium consists of a two-dimensional array of circular cylinders or three-dimensional array of spheres. Despite its simplicity, no rigorous solutions to the transport problem are available for irregular arrays. However, some are available for regular arrays of cylinders and spheres.

2.4.1 Single-Phase Flow

The flow problem is the steady state creeping flow of an incompressible viscous Newtonian fluid through a rigid spatially periodic porous medium. The equations to be solved are the Stokes equations.

$$0 = -\nabla P + \mu \nabla^2 \mathbf{u}, \quad (2.93)$$

$$\nabla \cdot \mathbf{u} = 0. \quad (2.94)$$

These equations should be supplemented by the no-slip boundary condition at the surface S_p of the solid particles.

$$\mathbf{u} = 0 \quad \text{on} \quad S_p. \quad (2.95)$$

In addition, another fundamental hypothesis is needed, i.e., the local fluid velocity \mathbf{u} is spatially periodic with the same periodicity as the porous medium.

$$\mathbf{u}(\mathbf{R}) = \mathbf{u}(\mathbf{R} + \mathbf{R}_n). \quad (2.96)$$

This hypothesis is based on: (1) as the pressure gradient is constant across the unit cell, it can be expected that the flux is also constant; and (2) locally, \mathbf{u} must satisfy the no-slip boundary conditions which is inherently spatially periodic.

Hasimoto (1959) was the first to calculate successfully periodic fundamental solutions of the Stokes equations for the flow past a periodic array of obstacles. His approach is based on Fourier series expansion and he applied the solution to dilute cubic arrays of spheres and square arrays of cylinders. Happel (1959) employed a free-surface model to study flows parallel and perpendicular to square arrays of cylinders. Snyder and Stewart (1966) calculated the velocity and pressure profiles for Newtonian creeping flow through dense cubic and simple cubic beds of spheres using Galerkin's method. Their solutions converged slowly and did not satisfy continuity exactly. Sorensen and Stewart (1974) improved their method by using a three-dimensional set of stream functions and a variational principle. Zick and Homsy (1982) started

from Hasimoto's fundamental solution and obtained a system of Fredholm integral equations of the first kind for the unknown stress vector at the surface of a sphere, and were able to lower the dimension of the problem as a result. Sangani and Acrivos (1982b) extended the analytical technique of Hasimoto and were able to deduce a scheme that was valid for the whole range of solid concentrations of cubic arrays of spheres. They also studied the cases of two-dimensional square and hexagonal arrays of cylinders. Drummond and Tahir (1984) adapted the method of singularities to biharmonic equations to study flows parallel and perpendicular to arrays of cylinders.

Due to computational limitations and/or the drawbacks of the approaches themselves, most numerical approaches are limited to study two-dimensional problems. Sangani and Acrivos (1982a) developed a numerical technique to study creeping flow through square and hexagonal arrays which is suitable for the whole range of porosity. Larson and Higdon (1986, 1987) employed the boundary-integral method to study microscopic axial and transverse flow near the surface of media composed of circular and elliptical inclusions. Sangani and Yao (1988a) developed a numerical method by extending Hasimoto's approach for evaluating macroscopic transport coefficients by computing the many-particle interactions in systems with an arbitrary size and spatial distribution of cylinders. They were able to provide creeping flow permeability even for some random spatially periodic structures. Using the finite element method, Mee-goda et al. (1989) studied the effect of specific surface area, void ratio, particle shape, material heterogeneity and arrangement of particles on the permeability of granular media. They proposed an equation, which is similar to the Kozeny-Carman equation, to predict permeability. Edwards et al. (1990) also employed the finite element technique to study flow fields within spatially periodic arrays of cylinders arranged in square and hexagonal lattices with microscale Reynolds numbers ranging between 0 and 200. Bruschke and Advani (1993) developed a closed-form solution numerically for flow across a periodic array of cylinders by matching the analytic solution using the lubrication approach for low porosities and the analytic cell model solution for high porosities. Ghaddar (1995) determined the statistical transverse permeability of

two-dimensional random arrays of cylinders by employing nip-elements and a parallel finite element procedure. Koch and Ladd (1997) employed the lattice-Boltzmann method to study the effects of fluid inertia on the pressure drop required to drive fluid flow through periodic and random arrays of cylinders.

Some of the calculations and major results of abovementioned work are briefly outlined below. To solve Equations 2.93 to 2.96 for an incompressible flow through a periodic array of obstacles with their centers at \mathbf{R}_n , a useful approach is to continue the interstitial fields analytically into the space occupied by the obstacles, replacing the obstacles with singular multipole force distribution (Hasimoto 1959). Equation 2.93 is replaced by,

$$0 = -\nabla P + \mu \nabla^2 \mathbf{u} - \mathbf{F}_n \sum_n \delta(\mathbf{R} - \mathbf{R}_n), \quad (2.97)$$

where \mathbf{F}_n is the force acting on one of the obstacles, and δ denotes Dirac delta function defined as,

$$\int_{\text{volume}} \delta(\mathbf{R} - \mathbf{R}_n) d^3 \mathbf{R} = \begin{cases} 1 & \text{when } \mathbf{R}_n \in \text{volume;} \\ 0 & \text{when } \mathbf{R}_n \notin \text{volume,} \end{cases} \quad (2.98)$$

and,

$$\delta(\mathbf{R} - \mathbf{R}_n) = 0 \quad \text{for } \mathbf{R} \neq \mathbf{R}_n. \quad (2.99)$$

Hasimoto (1959) then expanded \mathbf{u} and ∇P in Fourier series,

$$\mathbf{u} = \sum_{\hat{\mathbf{R}}_n} \mathbf{u}_{\hat{\mathbf{R}}_n} e^{-2\pi i (\hat{\mathbf{R}}_n \cdot \mathbf{R})}, \quad (2.100)$$

$$\nabla P = \sum_{\hat{\mathbf{R}}_n} \nabla P_{\hat{\mathbf{R}}_n} e^{-2\pi i (\hat{\mathbf{R}}_n \cdot \mathbf{R})}, \quad (2.101)$$

where,

$$\hat{\mathbf{R}}_n = n_1 \hat{\mathbf{I}}_1 + n_2 \hat{\mathbf{I}}_2 + n_3 \hat{\mathbf{I}}_3, \quad (2.102)$$

which are vectors in the reciprocal lattice determined by,

$$\hat{\mathbf{I}}_1 = \frac{\mathbf{I}_2 \times \mathbf{I}_3}{V_{\text{unit cell}}}, \quad (2.103)$$

$$\hat{\mathbf{I}}_2 = \frac{\mathbf{I}_3 \times \mathbf{I}_1}{V_{\text{unit cell}}}, \quad (2.104)$$

$$\hat{\mathbf{I}}_3 = \frac{\mathbf{I}_1 \times \mathbf{I}_2}{V_{\text{unit cell}}}. \quad (2.105)$$

By introducing the series into Equations 2.97 and 2.94, the periodic fundamental solution of the Stokes equations for the flow past a periodic array of obstacles is obtained. The analysis also leads to a relationship that the drag forces acting on the obstacles within the unit cell are balanced by the mean pressure gradient driving the fluid, i.e.,

$$\sum \mathbf{F}_n = -\nabla P V_{\text{unit cell}}. \quad (2.106)$$

Following the same procedure as Hasimoto (1959), for flow through simple cubic arrays of spheres with an average velocity of v_s in the direction of x_1 , Sangani and Acrivos (1982b) presented the formal solution in a x_1 - x_2 - x_3 Cartesian coordinate system as,

$$u_1 = v_s - \frac{1}{4\pi\mu} \left(G \left(S_1 - \frac{\partial^2 S_2}{\partial x_1^2} \right) + H \frac{\partial^2 S_1}{\partial x_1^2} - L \left(\frac{\partial^4}{\partial x_2^4} - 6 \frac{\partial^4}{\partial x_2^2 \partial x_3^2} + \frac{\partial^4}{\partial x_3^4} \right) S_1 \right), \quad (2.107)$$

$$u_2 = \frac{1}{4\pi\mu} \left(G \frac{\partial^2 S_2}{\partial x_1 \partial x_2} - H \frac{\partial^2 S_1}{\partial x_1 \partial x_2} - L \frac{\partial}{\partial x_1} \left(\frac{\partial^3}{\partial x_2^3} - 3 \frac{\partial^3}{\partial x_2^2 \partial x_3} \right) S_1 \right), \quad (2.108)$$

$$u_3 = \frac{1}{4\pi\mu} \left(G \frac{\partial^2 S_2}{\partial x_1 \partial x_3} - H \frac{\partial^2 S_1}{\partial x_1 \partial x_3} - L \frac{\partial}{\partial x_1} \left(\frac{\partial^3}{\partial x_3^3} - 3 \frac{\partial^3}{\partial x_2^2 \partial x_3} \right) S_1 \right), \quad (2.109)$$

$$\frac{\partial P}{\partial x_i} = -\frac{6\pi\mu v_s R \bar{F}_d}{V_{\text{unit cell}}} \delta_{i1} + \frac{1}{4\pi} G \frac{\partial^2 S_1}{\partial x_1 \partial x_i} \quad (i = 1, 2, 3), \quad (2.110)$$

where R is the radius of spheres, and \bar{F}_d is the dimensionless drag force of the sphere in the direction of x_1 defined as,

$$\bar{F}_d = \frac{F_d}{6\pi\mu v_s R}, \quad (2.111)$$

where F_d is the drag force acting on the sphere in the x_1 direction. G , H , and L are differential operators, such that,

$$\begin{pmatrix} G \\ H \\ L \end{pmatrix} = \sum_{M=0}^{\infty} \sum_{m=0}^{m \leq \frac{1}{2}M} \begin{pmatrix} A_{nm} \\ B_{nm} \\ C_{nm} \end{pmatrix} \left(\frac{\partial^{2n}}{\partial x_1^{2n}} \left[\left(\frac{\partial}{\partial \xi} \right)^{4m} + \left(\frac{\partial}{\partial \eta} \right)^{4m} \right] \right) \quad (M = n + 2m). \quad (2.112)$$

with,

$$\xi = x_2 + ix_3, \quad (2.113)$$

$$\eta = x_2 - ix_3, \quad (2.114)$$

and the unknown coefficients A_{nm} , B_{nm} , and C_{nm} are to be determined by applying the no-slip boundary condition at the surface of the spheres. S_1 and S_2 in the above equations are given by,

$$S_1 = \frac{1}{\pi V_{unit\ cell}} \sum_{\hat{\mathbf{R}}_n \neq 0} \frac{e^{-2\pi i(\hat{\mathbf{R}}_n \cdot \mathbf{R})}}{\hat{\mathbf{R}}_n^2}, \quad (2.115)$$

and,

$$S_2 = -\frac{1}{4\pi^3 V_{unit\ cell}} \sum_{\hat{\mathbf{R}}_n \neq 0} \frac{e^{-2\pi i(\hat{\mathbf{R}}_n \cdot \mathbf{R})}}{\hat{\mathbf{R}}_n^4}. \quad (2.116)$$

For two-dimensional flow perpendicular to an array of cylinders, if the mean flow has an average velocity of v_s in the x_1 direction, the velocity components are (Sangani and Acrivos 1982b),

$$u_1 = v_s - \frac{1}{4\pi\mu} \left(G \left(S_1 - \frac{\partial^2 S_2}{\partial x_1^2} \right) + H \frac{\partial^2 S_1}{\partial x_1^2} \right), \quad (2.117)$$

$$u_2 = \frac{1}{4\pi\mu} \left(G \frac{\partial^2 S_2}{\partial x_1 \partial x_2} - H \frac{\partial^2 S_1}{\partial x_1 \partial x_2} \right), \quad (2.118)$$

where,

$$\begin{pmatrix} G \\ H \end{pmatrix} = \sum_{n=0}^{\infty} \begin{pmatrix} A_n \\ B_n \end{pmatrix} \frac{\partial^{2n}}{\partial x_1^{2n}}. \quad (2.119)$$

The analysis leads to results about permeability or dimensionless drag force as functions of porosity of the media. For flow through a spatially periodic simple cubic array of spheres, the permeability k is related to the dimensionless drag force \bar{F}_d by,

$$k = \frac{V_{\text{unit cell}}}{6\pi R \bar{F}_d}. \quad (2.120)$$

Hasimoto (1959) found that,

$$\bar{F}_d^{-1} = 1 - 1.7601\phi^{\frac{1}{3}} + \phi - 1.5593\phi^2 + O(\phi^{\frac{8}{3}}). \quad (2.121)$$

where $\phi = 1 - n$ is the solid fraction of the media. Sangani and Acrivos (1982b) refined the above result as,

$$\bar{F}_d^{-1} = 1 - 1.7601\phi^{\frac{1}{3}} + \phi - 1.5593\phi^2 + 3.9799\phi^{\frac{8}{3}} - 3.0734\phi^{\frac{10}{3}} + O(\phi^{\frac{11}{3}}). \quad (2.122)$$

For two-dimensional flow perpendicular to the axes of circular cylinders, the dimensionless drag force is usually redefined as in the literature.

$$\bar{F}_d = \frac{F_d}{4\pi\mu v_s}, \quad (2.123)$$

which is the dimensionless drag force per unit length of the cylinder and the permeability k is related to \bar{F}_d by,

$$k = \frac{V_{\text{unit cell}}}{4\pi \bar{F}_d}. \quad (2.124)$$

Sangani and Acrivos (1982a) found that,

$$\bar{F}_d^{-1} = \ln \phi^{-0.5} - 0.738 + \phi - 0.887\phi^2 + 2.038\phi^3 + O(\phi^4), \quad (2.125)$$

for square arrays and,

$$\bar{F}_d^{-1} = \ln \phi^{-0.5} - 0.745 + \phi - 0.25\phi^2 + O(\phi^4), \quad (2.126)$$

for hexagonal arrays. Drummond and Tahir (1984) proposed that,

$$\bar{F}_d^{-1} = \ln \phi^{-1} - 1.476 + 2\phi - 0.5\phi^2 - 0.051\phi^4 - 0.0775\phi^8 + O(\phi^{12}), \quad (2.127)$$

for square arrays,

$$\bar{F}_d^{-1} = \ln \phi^{-1} - 1.498 + 2\phi - 0.5\phi^2 - 0.00251\phi^6 + O(\phi^{12}). \quad (2.128)$$

for staggered arrays, and,

$$\bar{F}_d^{-1} = \ln \phi^{-1} - 1.354 + 2\phi - 0.5\phi^2 - 0.358\phi^3 - 0.812\phi^6 + O(\phi^{12}). \quad (2.129)$$

for hexagonal arrays. Attention is needed that all the above functional forms between \bar{F}_d^{-1} and ϕ are usually only valid for small ϕ , i.e., high porosity media.

2.4.2 Hydrodynamic Dispersion

To describe tracer dispersion in spatially periodic porous media, in addition to solving Equations 2.93 to 2.96, the following convection-diffusion equation is needed.

$$\frac{\partial C}{\partial t} + \mathbf{u} \cdot \nabla C = d_0 \nabla^2 C. \quad (2.130)$$

Impenetrability of the solids to solute transport through their surfaces requires,

$$\hat{\mathbf{n}} \cdot (\mathbf{u}C - d_0 \nabla C) = 0 \quad \text{on } S_p, \quad (2.131)$$

where $\hat{\mathbf{n}}$ is the unit normal to the solid surfaces.

Brenner (1980a) and Brenner and Adler (1982) established a theory for dispersion in flow through spatially periodic porous media. The theory is based on the concept of Brownian motion of particles and makes use of the method-of-moments developed by Aris (1956) and later extended by Horn (1971). The theory leads to a general formula for the dispersion tensor. Brenner showed the tensor should be calculated by first solving a convection-diffusion problem in the periodic cell, i.e., the **B** field problem. Brenner's theory is rigorous in that no *ad hoc* assumptions are needed except for the assumption of periodicity of the media. The approach is now called the generalized Taylor dispersion theory (Brenner 1980b; Brenner 1981; Brenner 1982). By local volume averaging on the periodic cell, Carbonell and Whitaker (1983) were able to calculate the dispersion tensor through an **f** field problem. Koch et al. (1989)

studied the effect of grain periodicity on dispersion phenomena and the aspects of dispersion mechanisms which are artifacts of the periodicity constraint. They showed that for a square array of cylinders or a simple cubic array of spheres, and in the limit $Pe \rightarrow \infty$, D_L depends quadratically on Pe and D_T approaches a constant value. Mei (1992) used a homogenization method to study dispersion in porous media. Starting from the Navier-Stokes equations for the fluid and the convection-diffusion equation for the tracer, he arrived at Darcy's law and the convection-dispersion equation.

By solving the \mathbf{f} field problem of Carbonell and Whitaker (1983), Eidsath et al. (1983) carried out a numerical simulation of dispersion in the flow through a square array of cylinders. Using a finite element method, they first solved for the flow field, and then solved the convection-diffusion equation. Edwards et al. (1991) studied the Taylor dispersion of a passive solute within a fluid flowing through a two-dimensional spatially periodic porous media using finite element based on Brenner's \mathbf{B} field problem. The effects of microscale Peclet and Reynolds numbers on the longitudinal and transverse dispersivities were also investigated. Salles et al. (1993) examined theoretically dispersion in spatially periodic porous media and presented numerical results based on Brenner's \mathbf{B} method and random walk.

Brenner's theory (Brenner 1980a) and the method of homogenization (Mauri 1991; Mei 1992; Mei et al. 1996) for dispersion in spatially periodic porous media are briefly outlined below. Brenner's theory is based on Brownian motion theory for particles. Suppose that at time $t = 0$, a Brownian solute is introduced into a steady state flow at some arbitrary position \mathbf{R}' . The instantaneous position $\mathbf{R} \equiv \mathbf{R}(t|\mathbf{R}')$ of the particle is a stochastic variable. The probability density that the particle is located at \mathbf{R} at time t , knowing that it was released at \mathbf{R}' at time 0, is denoted by,

$$p(\mathbf{R}, t|\mathbf{R}'). \quad (2.132)$$

If the impenetrability of the solid phase applies, the solute must lie somewhere within the fluid volume for $t > 0$, i.e.,

$$\int_{V_{fluid}^{\infty}} pd^3\mathbf{R} = 1 \quad \text{for } t > 0, \quad (2.133)$$

where V_{fluid}^∞ denotes the fluid volumes in all unit cells. In addition, it will be assumed that,

$$p \rightarrow 0 \quad \text{as} \quad |\mathbf{R} - \mathbf{R}'| \rightarrow \infty, \quad (2.134)$$

at a sufficiently rapid rate with distance to ensure the convergence of the integral in Equation 2.133. Conservation and continuity of probability density requires that p satisfy the following equation,

$$\frac{\partial p}{\partial t} + \nabla \cdot \mathbf{J} = \delta(\mathbf{R} - \mathbf{R}') \cdot \delta(t), \quad (2.135)$$

where \mathbf{J} is the flux of the probability.

$$\mathbf{J} = \mathbf{u}p - d_0 \nabla p, \quad (2.136)$$

and satisfies,

$$\hat{\mathbf{n}} \cdot \mathbf{J} = 0 \quad \text{on} \quad S_p. \quad (2.137)$$

The probability density will evolve according to Equations 2.133 to 2.137. The moments of the probability density are written as,

$$\mathbf{M}_m = \int_{V_f^\infty} (\mathbf{R} - \mathbf{R}')^m p(\mathbf{R}, t | \mathbf{R}') d^3 \mathbf{R}. \quad (2.138)$$

The first three moments are physically the most interesting. Moreover, the transients that occur just after the introduction of the solute in the fluid phase are not of interest, but rather what occurs after a long enough time so that the tracer particle can sample all the interstitial space of the unit cells. This condition is expressed as,

$$\frac{d_0 t}{\mathcal{L}_D^2} \gg 1. \quad (2.139)$$

The spatial integration indicated by Equation 2.138 can be decomposed into two steps, integration over a unit cell and then over all unit cells. Brenner performed the calculation and found that,

$$M_0 = 1. \quad (2.140)$$

This zeroth-order moment represents the total probability. The first-order moment is,

$$\mathbf{M}_1 \cong \mathbf{v}_s t + \bar{\mathbf{B}} + Exp, \quad (2.141)$$

where *Exp* denotes terms that go exponentially to zero as $t \rightarrow \infty$ and,

$$\bar{\mathbf{B}} = \frac{1}{V_{unit\ cell}} \int_{V_{unit\ cell}} \mathbf{B}(\mathbf{r}) d^3\mathbf{r}. \quad (2.142)$$

in which $\mathbf{B}(\mathbf{r})$ is a field quantity which satisfies,

$$d_0 \nabla^2 \mathbf{B} - \nabla \cdot (\mathbf{u}\mathbf{B}) = \mathbf{v}_s, \quad (2.143)$$

and is subjected to the boundary condition,

$$\hat{\mathbf{n}} \cdot \nabla \mathbf{B} = 0 \quad \text{on } S_p. \quad (2.144)$$

Additionally, \mathbf{B} must satisfy the pair of jump conditions across opposite cell faces.

$$\langle \mathbf{B} \rangle = -\langle \mathbf{r} \rangle, \quad (2.145)$$

$$\langle \nabla \mathbf{B} \rangle = 0, \quad (2.146)$$

where the jump in value of the general field \mathbf{F} is defined as,

$$\langle \mathbf{F} \rangle = \mathbf{F}(\mathbf{R}_n, \mathbf{r} + \mathbf{I}_i) - \mathbf{F}(\mathbf{R}_n, \mathbf{r}), \quad (2.147)$$

and \mathbf{I}_i are the three basic lattice vectors (Figure 2.1). The first-order moment represents the average position of the solute after a long time. Brenner also showed that,

$$\frac{d\mathbf{M}_2}{dt} \cong 2\mathbf{v}_s \mathbf{v}_s t + \mathbf{v}_s \mathbf{B} + \mathbf{B} \mathbf{v}_s + 2 \frac{d_0}{V_{unit\ cell}} \int_{V_{unit\ cell}} \nabla \mathbf{B}^* \cdot \nabla \mathbf{B} d^3\mathbf{r} + Exp, \quad (2.148)$$

where the superscript * denotes a post-transposition operator (i.e., $A_{ijk}^* = A_{ikj}$ in Cartesian tensor notation). The physical meaning of the second-order moment lies in the calculation for the mean square displacement dyadic $\overline{(\mathbf{R} - \bar{\mathbf{R}})^2}$,

$$\overline{(\mathbf{R} - \bar{\mathbf{R}})^2} = \mathbf{M}_2 - \mathbf{M}_1 \mathbf{M}_1, \quad (2.149)$$

where $\bar{\mathbf{R}}$ is the mean displacement of the solute. Brenner then followed Einstein's generalized Brownian motion relation for continua and defined the dispersion tensor as.

$$\mathbf{D} \cong \frac{1}{2} \frac{d}{dt} \overline{(\mathbf{R} - \bar{\mathbf{R}})^2} = \frac{d_0}{V_{\text{unit cell}}} \int_{V_{\text{unit cell}}} \nabla \mathbf{B}^* \cdot \nabla \mathbf{B} d^3 \mathbf{r}. \quad (2.150)$$

Furthermore, Brenner (1980a) rigorously proved that the dispersion tensor defined in Equation 2.150 is the same quantity as in Equation 2.70 of the conventional continuum dispersion model as $t \rightarrow \infty$.

Mei (1992) rederived the key results of Brenner using the theory of homogenization, which is claimed to be a rigorous mathematical procedure particularly suited for periodic materials. It is based on two assumptions: (1) there are two vastly different length scales in the media, and (2) the media is periodic. The microscopic length scale \mathcal{L}_m and the macroscopic length scale \mathcal{L} of a spatially periodic porous medium are easily identified as the two different length scales for homogenization analysis. Using the ratio of the two length scales $\epsilon = \frac{\mathcal{L}_m}{\mathcal{L}} \ll 1$ as the small ordering parameter, the perturbation expansions are introduced,

$$u_i = u_i^{(0)} + \epsilon u_i^{(1)} + \epsilon^2 u_i^{(2)} + \dots, \quad (2.151)$$

$$P = P^{(0)} + \epsilon P^{(1)} + \epsilon^2 P^{(2)} + \dots, \quad (2.152)$$

$$C = C^{(0)} + \epsilon C^{(1)} + \epsilon^2 C^{(2)} + \dots, \quad (2.153)$$

where $u_i^{(j)}$ and $P^{(j)}$ are functions of x_i and $x'_i = \epsilon x_i$, and $C^{(j)}$ depends on $x_i, x'_i, t_1 = \epsilon t$, and $t_2 = \epsilon^2 t$. Substituting the expansions into the corresponding governing equations and boundary conditions, a set of perturbation equations are obtained at successive orders. The leading-order equation is homogeneous; either the solution itself or the coefficient of the homogeneous solution are indeterminate and independent of \mathcal{L}_m . The next-order solution enables the calculation of the leading-order equation and the constitutive coefficients, such as the permeability and dispersion tensors.

2.4.3 Spatially Periodic versus Real Porous Media

Spatially periodic porous media have been extensively studied for two reasons. one is the mathematical tractability and the other is the feasibility of numerical implementation. Although assuming spatial periodicity of porous media does not stand on solid physical evidence. the advantage of this deterministic approach (i.e.. by specifying geometry of solid inclusions in the unit cell) lies in the achievement of a complete and detailed understanding of the functional relations existing between the microscale and macroscale processes. To study phenomena occurring in spatially periodic porous media not only has academic importance. it also provides insights for real heterogeneous disordered porous media. Actually, the degree of geometric complexity that one is able to include in the attempt to simulate real porous media is limited only by the capacities of computers. With the continuing development of computer technology, the ability to model real porous media through the use of spatially periodic models is approaching.

The drawback of this approach is that, by assuming spatial periodicity, a discrete separation of scales has been required, i.e., periodicity of the “microstructure” with a “scale-of-observation” much larger than the period (Cushman 1997). Owing to the costs and poor technology associated with sampling natural porous media, a periodic unit cell is not known to exist *a priori*, and if it does exist, the scale-of-observation is not known such that the unit cell appears infinitely small. Then, local theories break down and nonlocal with infinite support on the scale-of-observation has to be assumed for the processes (Cushman 1997). Periodicity may also produce some artifacts in transport phenomena. Koch et al. (1989) studied the different mechanisms that contribute to dispersion. They stated that at high Peclet number, the mechanical dispersion that is induced by the stochastic fluid velocity field in disordered media and is independent of the molecular diffusion is absent in periodic media where the velocity field is deterministic.

In general, the potential applicability of some specific results gleaned from the spatially periodic analysis should not be overlooked (Brenner 1980a). However, conclusions drawn concerning transport in real disordered porous media from studies of ordered porous media should be viewed with caution (Koch et al. 1989).

2.5 Computational Fluid Dynamics Techniques

Once a porous media model for certain phenomena is developed, the necessary computations are carried out analytically or numerically. Using advanced computational fluid dynamics techniques, numerical simulations of porous media phenomena have made significant progresses. Conventional numerical methods include finite element, finite difference, and boundary integral methods. Their application in porous media transport can be found in many books (Thomasset 1981; Wang and Anderson 1982; Liggett and Liu 1983; Peyret and Taylor 1985). Lattice-gas and lattice-Boltzmann automata are two new methods which offer efficient simulations in complex geometries.

2.5.1 Lattice-gas Method

Broadwell (1964) was probably the first to develop an automata-type model for fluid flow. Velocity was a discrete variable in his model, but space and time were both continuous. Later, Hardy et al. (1976) developed a completely discrete model for fluid flow on a square lattice which could mimic several features of real flow problems.

Lattice-gas (LG) models, also called cellular-automata models, are large lattices in which each site can be in one of several discrete states. The lattice is populated by particles, and the Boolean variables describing the state of the system indicate the presence or absence of the particles at the intersections of the lattice. The evolution of the system is governed by a set of collision rules that determine how the particles move in the lattice, and how they are scattered once they collide with each other. Those rules are chosen to conserve mass and momentum for the system. Both time and space are discrete, and usually site connections are made between nearest neighbors only.

Frisch et al. (1986, 1987) and Wolfram (1986) showed that in order for the discrete equations to reduce to the Navier-Stokes equations, two-dimensional simulations have to be performed using a triangular lattice.

Rothman (1988) used lattice-gas automata to model flow through an artificial two-dimensional porous medium. He showed that flow rate through the medium was proportional to the average hydraulic gradient across the boundaries in accordance with Darcy's law. In addition, a lattice scale must be chosen such that the linear dimension of any void space is at least twice the mean free path, i.e., the average distance traveled before particle collision occurs. Brosa and Stauffer (1989, 1991) and Kohring (1991) also used two-dimensional lattice-gas models to simulate the flow through randomly generated porous structures. For systems with up to 22 million sites, Kohring (1991) found permeability varied with porosity according to $k \propto \frac{n - 0.6}{1 - n}$ for $n > 0.7$. He also noted that a detailed study of permeability as a function of particle size and size distribution is needed. Rothman (1990) and Gunstensen and Rothman (1991) used two-dimensional lattice-gas to model multiphase flow through simple pore structures. Baudet et al. (1989) used lattice-gas to simulate two-dimensional dispersion of tracer particles for flow between parallel plates. Simulation results agreed very closely with analytical solutions under laminar flow conditions.

Difficulties arise when lattice-gas is applied to three-dimensional problems. While a triangular lattice contains sufficient symmetry to yield a macroscopically isotropic two-dimensional fluid, no regular lattice exists that yields isotropy in three dimensions. d'Humieres et al. (1986) theorized that flow could be modeled in a four-dimensional face-centered hypercubic (FCHC) lattice. Three-dimensional results are obtained by projecting the four-dimensional data down to a three-dimensional space. Frisch et al. (1987) discussed the approach in detail. The FCHC model has been implemented by Rivet et al. (1988) for the simulation of three-dimensional vortex behind a circular plate in an uniform flow field.

2.5.2 Lattice-Boltzmann Method

Lattice-gas not only encounters difficulties in three-dimensional problem, it also suffers from statistical noise. The lattice-Boltzmann (LB) method has been developed to overcome some of the drawbacks of the lattice-gas method. In the spirit of the Boltzmann equation of kinetic theory, the lattice-Boltzmann technique models a fluid according to the average behavior of particles on a lattice rather than as the discrete particles themselves. The Boolean site populations of the lattice-gas automata become real numbers between 0 and 1 representing their average value through time as the simulation progresses. Thus, instead of following each particle in detail, the model follows the average behavior of particles at a given site. This also eliminates the statistical noise associated with the lattice-gas approach. Lattice-Boltzmann is particularly efficient for low Re simulations (McNamara and Zanetti 1988) and is unconditionally stable for the solution of the Navier-Stokes equations (Frisch 1991).

Using the lattice-Boltzmann FCHC method, Succi et al. (1989) simulated Darcy's law for fluid flow through a three-dimensional random medium with $32^3 = 32768$ sites. Pores were no smaller in cross section than 4×4 lattice units and no-slip boundary conditions were imposed at the walls. For three values of porosity, flow rate was found proportional to hydraulic gradient in accordance with Darcy's law when $Re < 5$. Furthermore, Succi et al. (1991) demonstrated that the Boltzmann technique is a viable tool to simulate the flow regime for a variety of hydraulics problems ranging from laminar to turbulent conditions. Cancelliere et al. (1990) simulated flow through a three-dimensional FCHC "penetrable sphere" model using lattice-Boltzmann method to calculate permeability as a function of the solid fraction of the media. The simulated data fit the Kozeny-Carman equation well. Gunstensen and Rothman (1992, 1993) used a lattice-Boltzmann model for the simulation of immiscible flow of two fluids through a three-dimensional porous medium consisting of randomly overlapping spheres. Ladd (1994a, 1994b) simulated the hydrodynamic interaction of particles in a fluid suspension using the lattice-Boltzmann method.

2.5.3 Smoothed Particle Hydrodynamics (SPH)

Smoothed Particle Hydrodynamics (SPH) can also be used to investigate pore-scale transport phenomenon in porous media. First developed for astrophysical applications (Lucy 1977; Gingold and Monaghan 1977), SPH has been applied successfully to a wide range of problems. SPH is a fully Lagrangian computational fluid dynamics technique in which the numerical solution is achieved without a grid. Using this approach, fluid velocity, pressure and tracer distributions, discharge velocity, and fluid particle pathlines can be computed, as well as other information that would be difficult or impossible to observe experimentally or with other numerical approaches. SPH has a number of advantages over competing numerical techniques. Mobile solid boundaries are difficult to incorporate into more conventional methods, which require either continual remeshing of the domain or complicated algorithmic modifications. The meshless nature of SPH simplifies the simulation of mobile (Monaghan 1994) or even deformable boundaries (Liberky and Petschek 1990; Benz and Asphaug 1995; Randles and Libersky 1996). The Lagrangian nature of SPH simplifies the inclusion of extra physical effects at a fluid-fluid boundary. For example, it is possible to simulate immiscible fluids with SPH (Morris 1999), which is of crucial importance to modeling the mobility of non-aqueous phase liquids within a solid matrix. Most methods suffer from an increase in complexity when extended to three-dimensional problems. The SPH algorithm remains essentially unchanged when considering one, two, or three dimensions. In addition, most formulations of SPH guarantee local conservation of mass, momentum, and energy. This is not typically the case with competing methods, such as the finite element method. While SPH is versatile, errors can sometimes be larger than those obtained using grid-based methods tailored for specific problems. Moreover, SPH can be computationally expensive for certain applications, although at comparable resolutions, the computational expense of SPH is comparable with conventional methods. SPH has been extended to model solid dynamics problems as well (Liberky and Petschek 1990; Benz and Asphaug 1995; Randles and Libersky

1996) and it has only recently been applied to low Reynolds number incompressible flows (Morris et al. 1997; Zhu et al. 1997; Zhu et al. 1999).

2.6 Summary

A systematic study of pore-scale transport through spatially periodic porous media using a true Lagrangian method has not been reported in the literature. Although the flow problem has been studied extensively using both circular and elliptical inclusions (Hasimoto 1959; Happel 1959; Snyder and Stewart 1966; Sørensen and Stewart 1974; Zick and Homsy 1982; Sangani and Acrivos 1982b; Sangani and Acrivos 1982a; Larson and Higdon 1986; Larson and Higdon 1987; Sangani and Yao 1988a; Sangani and Yao 1988b; Drummond and Tahir 1984; Meegoda et al. 1989; Edwards et al. 1990; Bruschke and Advani 1993; Ghaddar 1995; Ranganathan et al. 1996; Koch and Ladd 1997), only a few papers have discussed the problem of diffusion and hydrodynamic dispersion for circular inclusions (Eidsath et al. 1983; Koch et al. 1989; Edwards et al. 1991; Salles et al. 1993). However, most of the solutions were achieved by either solving Brenner (1980a) \mathbf{B} field problem or Carbonell and Whitaker (1983) \mathbf{f} field problem without obtaining the evolution and distribution of concentration. The following chapters present a study of pore-scale transport through spatially periodic porous media using Smoothed Particle Hydrodynamics. Starting from basic fluid flow and diffusion equations, the flow and concentration fields are solved to yield values of permeability and coefficient of diffusion and hydrodynamic dispersion. Using this Lagrangian approach, all relevant information regarding flow, diffusion, tracer convection and hydrodynamic dispersion can be obtained.

CHAPTER 3 DEVELOPMENT AND VERIFICATION OF A PORE-SCALE FLOW MODEL USING SMOOTHED PARTICLE HYDRODYNAMICS

Smoothed Particle Hydrodynamics (SPH) was originally developed for astrophysical applications to model compressible fluids at high Reynolds number (Lucy 1977; Gingold and Monaghan 1977). SPH is well suited to model compressible flows because, in SPH, the fluid is driven by local density fluctuations at the particles. Monaghan (1994) extended SPH to inviscid incompressible flow problems involving free surfaces for high Reynolds numbers and free-slip boundary conditions. Efforts have also been made to simulate compressible gases with Reynolds numbers as low as 5 (Takeda et al. 1994). The extension of SPH to model low Reynolds number ($Re \leq 1$) incompressible flows calls for modifications of the standard SPH formalism which are discussed by Morris et al. (1997), Zhu et al. (1997), and Zhu et al. (1999). In this chapter, an overview of SPH is first provided, the SPH numerical approach to model porous media flow is discussed in detail and verification of the model is presented.

3.1 Overview of SPH

The standard approach to SPH is reviewed by Benz (1990) and Monaghan (1992). In SPH, a compressible fluid is represented by a field of disordered particles (Figure 3.1), typically of fixed mass, which follow the local fluid motion, convect contact discontinuities, preserve Galilean invariance, and reduce computational diffusion of various fluid properties including momentum. The equations governing the evolution of the fluid become expressions for interparticle forces and fluxes when written in SPH forms. In standard SPH, each particle carries mass m , density ρ , velocity \mathbf{u} , and other fluid quantities specific to a given problem. The particle is mathematically treated

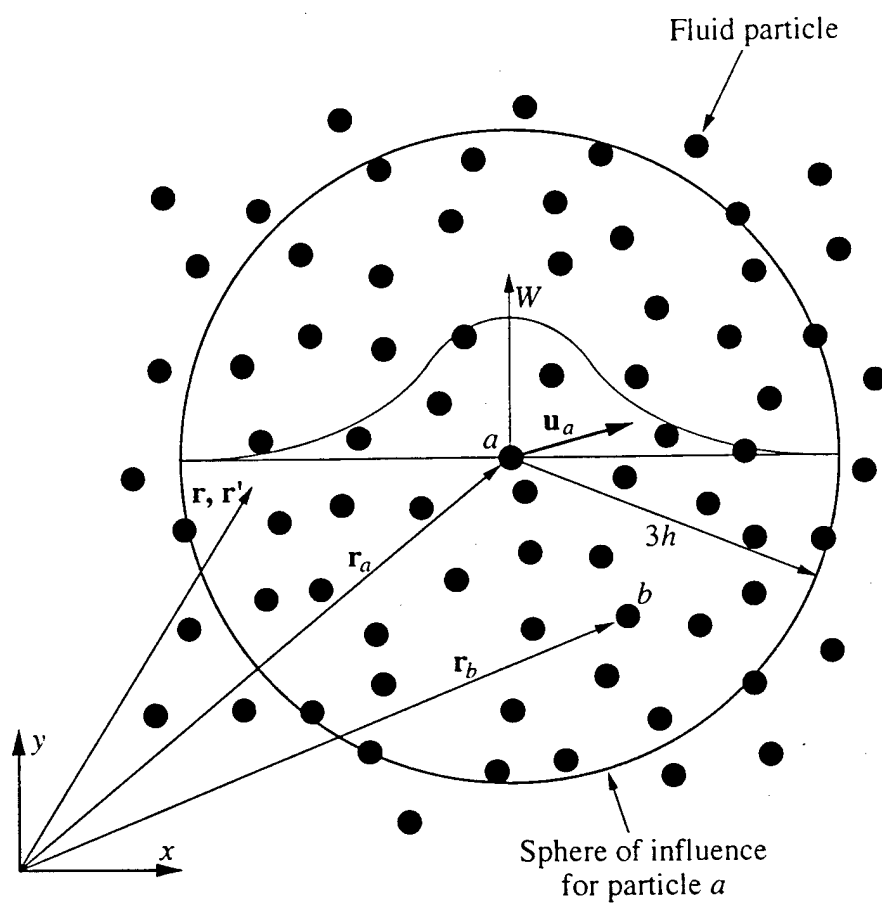


Figure 3.1: Sphere of influence for SPH particle a .

as an interpolation point at which fluid properties are computed as the weighted sum of values from neighboring particles. To illustrate, consider a field quantity $A(\mathbf{r})$ expressed by,

$$A(\mathbf{r}) = \int A(\mathbf{r}') \delta(\mathbf{r} - \mathbf{r}') d\mathbf{r}', \quad (3.1)$$

where \mathbf{r} and \mathbf{r}' are position vectors and δ is the Dirac delta function. If δ is replaced with an interpolation kernel $W(\mathbf{r}, h)$, an integral interpolant $A_i(\mathbf{r})$ of the function is obtained.

$$A_i(\mathbf{r}) = \int A(\mathbf{r}') W(\mathbf{r} - \mathbf{r}', h) d\mathbf{r}'. \quad (3.2)$$

The kernel typically takes the form,

$$W(\mathbf{r}, h) = \frac{1}{h^\sigma} f\left(\frac{|\mathbf{r}|}{h}\right), \quad (3.3)$$

where σ is the number of dimensions for the problem and h is the smoothing length, a natural length scale associated with the method of SPH. The kernel has the following properties,

$$\int W(\mathbf{r} - \mathbf{r}', h) d\mathbf{r}' = 1, \quad (3.4)$$

and,

$$\lim_{h \rightarrow 0} W(\mathbf{r} - \mathbf{r}', h) = \delta(\mathbf{r} - \mathbf{r}'). \quad (3.5)$$

For numerical work, $A_i(\mathbf{r})$ is approximated by a summation interpolant $A_s(\mathbf{r})$ over the particle field,

$$A_s(\mathbf{r}) = \sum_b \frac{m_b}{\rho_b} A_b W(|\mathbf{r} - \mathbf{r}_b|, h), \quad (3.6)$$

where field quantities at particle b are denoted by subscript b . The quantity $\frac{m_b}{\rho_b}$ is the inverse of the number density at particle b and can be considered as the volume of fluid associated with that particle.

Using the above concepts, SPH equations governing fluid motion can be obtained. For example, the fluid density ρ_a at particle a , may be evaluated by direct particle mass summation as,

$$\rho_a = \sum_b m_b W_{ab}. \quad (3.7)$$

where,

$$W_{ab} = W(\mathbf{r}_{ab}, h). \quad (3.8)$$

and,

$$\mathbf{r}_{ab} = \mathbf{r}_a - \mathbf{r}_b. \quad (3.9)$$

Other expressions for derived field quantities at the particles are obtained by summations involving the kernel and/or its derivatives. As derivatives can be obtained by ordinary differentiations provided that $W(\mathbf{r}, h)$ is differentiable, there is no need for a grid. For example, the gradient and divergence of $A(\mathbf{r})$ can be obtained by,

$$\nabla A_s(\mathbf{r}) = \sum_b \frac{m_b}{\rho_b} A_b \nabla W(|\mathbf{r} - \mathbf{r}_b|, h), \quad (3.10)$$

and,

$$\nabla \cdot A_s(\mathbf{r}) = \sum_b \frac{m_b}{\rho_b} A_b \cdot \nabla W(|\mathbf{r} - \mathbf{r}_b|, h), \quad (3.11)$$

respectively. However, in practice, it is usually more accurate to use,

$$\nabla A = \frac{1}{\rho} (\nabla(\rho A) - A \nabla \rho) = \frac{1}{\rho_a} \sum_b m_b (A_b - A_a) \nabla W(|\mathbf{r} - \mathbf{r}_b|, h), \quad (3.12)$$

and,

$$\nabla \cdot A = \frac{1}{\rho} (\nabla \cdot (\rho A) - A \cdot \nabla \rho) = \frac{1}{\rho_a} \sum_b m_b (A_b - A_a) \cdot \nabla W(|\mathbf{r} - \mathbf{r}_b|, h). \quad (3.13)$$

3.2 Model Establishment for Pore-Scale Flow Problem

Groundwater flow is generally regarded as incompressible since the bulk fluid velocity is much smaller than the corresponding speed of sound. The solution to an incompressible flow problem is achieved by solving the following mass and momentum conservation equations throughout the flow domain subjected to proper boundary conditions.

$$\nabla \cdot \mathbf{u} = 0, \quad (3.14)$$

$$\frac{d\mathbf{u}}{dt} = -\frac{1}{\rho} \nabla p + \nu \nabla^2 \mathbf{u} + \mathbf{g}, \quad (3.15)$$

where ν is the fluid kinematic viscosity.

While SPH is well suited to model compressible fluids, the required modifications and extensions on the method of SPH for modeling porous media incompressible flow include treatment of real viscosity, introduction of dynamic pressure concept, choice of the equation of state and kernel interpolation, and implementation of no-slip flow boundary conditions.

3.2.1 Equation of State

SPH cannot model a truly incompressible fluid as in SPH, fluid pressure is an explicit function of local fluid density and particle motions are driven by local density gradients. In SPH, an incompressible flow must be approximated by solving for the flow of a nearly incompressible, or quasi-incompressible, fluid. As a result, to close the group of equations used for describing compressible fluids, an equation of state is required in the form of,

$$p = f(\rho). \quad (3.16)$$

Theoretically the actual state equation for the fluid modeled could be used but this usually results in a prohibitively small time step for numerical stability due to CFL condition (Courant et al. 1928). Therefore, in SPH, the incompressible fluid flow

has to be modeled as a quasi-incompressible flow through a quasi-incompressible equation of state. But the choice of the numerical speed of sound should control the density variation within a reasonable range. In this work, the chosen sound speed is low enough to be practical, and yet high enough to limit fluid density fluctuations to about 1%. A similar approach has been used in grid-based techniques to model steady incompressible flows (Chorin 1967; Turkel 1987; Tamamidis et al. 1996).

Most grid-based techniques model the flow of water as incompressible since the speed of sound in water is usually very large compared with the bulk fluid motions (i.e., a very low Mach number). Previous applications of SPH to incompressible flows of water (Monaghan 1994; Monaghan 1995b) have modified a state equation suggested by Batchelor (1967) which describes sound waves accurately,

$$p = p_0 \left(\left(\frac{\rho}{\rho_0} \right)^\gamma - 1 \right), \quad (3.17)$$

where $\gamma = 7$ and a zero subscript denotes reference quantities. The choice of $\gamma = 7$ in Equation 3.17 causes pressure to respond strongly to variations in density. Thus, perturbations to the density field remain small, even at high Reynolds numbers. However, as the density fluctuations increase, small errors in density correspond to increasing larger errors in pressure. For lower Reynolds number porous media flows, more accurate pressure estimates are obtained using SPH if γ is taken to be unity as in grid-based approaches (Chorin 1967; Turkel 1987; Tamamidis et al. 1996), since errors in density and pressure remain proportional.

In previous work involving incompressible fluids, the subtraction of 1 in Equation 3.17 was introduced to remove spurious boundary effects at a free surface. It is well established that SPH is unstable when attractive forces act between particles (Morris 1994; Swegle et al. 1995; Balsara 1995; Morris 1996b). Consequently, for flow simulations in this work, this subtraction was found to lead to numerical instabilities in regions of sustained low pressure. Since the simulations (and many other applications) have particles filling all space (section 3.3.1), the following artificial equation of state is used.

$$p = c^2 \rho, \quad (3.18)$$

where c is the speed of sound.

The sound speed must be chosen carefully to ensure both an efficient and accurate solution of a given problem. The value of c must be large enough that the behavior of the corresponding quasi-incompressible fluid is sufficiently close to that of the real fluid, yet it should not be so large as to make the time step prohibitively small. Monaghan (1994) argued that, for density to vary by at most 1%, the Mach number of the flow which is defined as,

$$Ma = \frac{\mathcal{U}}{c}, \quad (3.19)$$

should be 0.1 or less, where \mathcal{U} is the typical fluid velocity scale of the problem. In fact, for typical smoothing lengths used with SPH, the kernel interpolation is only accurate to within approximately 1%. The principal cause of this variation is small fluctuations in density which inevitably occur as particles move past one another. Thus, local pressure gradients obtained using a high sound speed are potentially noisy. Nevertheless, the velocities obtained are accurate if smoothed either by XSPH (Monaghan 1989) or viscosity. It was found that the computed pressure field is in close agreement with other techniques when c is chosen such that the density varies about 1%.

Considering the balance of forces in Equation 3.15, c^2 should be comparable with the largest of,

$$\frac{\mathcal{U}^2}{\lambda}, \frac{\nu \mathcal{U}}{\mathcal{L} \lambda}, \frac{F \mathcal{L}}{\lambda}, \quad (3.20)$$

where \mathcal{L} is the typical length scale of the problem, F is the magnitude of the driving body force of the flow, and λ is defined as,

$$\lambda = \frac{\Delta \rho}{\rho_0}, \quad (3.21)$$

where $\Delta\rho$ is the maximum density difference in the flow and ρ_0 is the initial fluid density. A value of $\lambda = 1\%$ was chosen for this study because SPH kernel interpolation is only accurate to within approximately 1%. The first term in Equation 3.20 corresponds to that derived by Monaghan (1994). The second and third terms ensure that pressure forces are comparable with viscous and body forces, respectively. Equation 3.20 provides a first estimate of the sound speed to use for a given problem. To obtain a better estimate of c^2 , an initial simulation is run at low resolution to find the distance ΔL in the direction of the applied body force between the locations of minimum and maximum fluid density. The third term of Equation 3.20 then becomes,

$$\frac{\rho_0 F \Delta L}{\Delta\rho}. \quad (3.22)$$

3.2.2 Evolution of Density

If Equation 3.7 is used to evolve density when modeling incompressible free surface flows, particle density is smoothed out at the edge of the fluid and spurious pressure gradients are induced at the surface. To avoid this problem, Monaghan (1994) initially set the density to a reference value, applied a more accurate estimate of the divergence of the velocity field, and evolved particle densities according to the following SPH equation for continuity,

$$\frac{d\rho_a}{dt} = \sum_b m_b \mathbf{u}_{ab} \cdot \nabla_a W_{ab}, \quad (3.23)$$

where ∇_a denotes the gradient with respect to the coordinates of particle a and,

$$\mathbf{u}_{ab} = \mathbf{u}_a - \mathbf{u}_b. \quad (3.24)$$

Equation 3.23 is derived from the mass conservation equation for a compressible fluid,

$$\frac{d\rho}{dt} = -\rho \nabla \cdot \mathbf{u}. \quad (3.25)$$

The simulations of interest here do not involve free surfaces and Equation 3.7 may be used to evolve particle densities. One disadvantage of this approach is that density must be evaluated by summing over the particles before other quantities may

be interpolated. However, Equation 3.23 allows density to be evolved concurrently with particle velocities and other field quantities, thus significantly reducing the computational effort. Although Equation 3.23 does not conserve mass exactly (Equation 3.7 does, provided that the total number and masses of particles are constant), this is usually only important for faster flows involving shocks. Direct particle summation can be used intermittently during a simulation to prevent significant “drift” in particle densities regarding to the fluid masses around.

3.2.3 Evaluation of Acceleration

The evaluation of particle accelerations comes from the SPH form for the momentum equation which is dependent on how to evaluate the pressure gradient acceleration and implement the fluid viscosity. Benz (1990) had detailed derivation for this equation for inviscid fluids.

3.2.3.1 Pressure Gradient Acceleration

In SPH, the pressure gradient acceleration term in Equation 3.15 is usually symmetrized by writing,

$$\frac{\nabla p}{\rho} = \nabla \left(\frac{p}{\rho} \right) + \frac{p}{\rho^2} \nabla \rho. \quad (3.26)$$

This results in the most common SPH expression for the term,

$$-\left(\frac{1}{\rho} \nabla p \right)_a = - \sum_b m_b \left(\frac{p_a}{\rho_a^2} + \frac{p_b}{\rho_b^2} \right) \nabla_a W_{ab}. \quad (3.27)$$

Provided that the kernel is an even function of \mathbf{r} , Equation 3.27 conserves linear and angular momenta exactly since the forces acting between individual particles are antisymmetric. It is natural because of the law of action and reaction. Momentum conservation can be satisfied by an infinite number of symmetric forms of the pressure gradient acceleration term given by Monaghan (1992),

$$-\left(\frac{1}{\rho} \nabla p \right)_a = - \sum_b m_b \left(\frac{p_a}{\rho_a^\varepsilon \rho_b^{2-\varepsilon}} + \frac{p_b}{\rho_b^\varepsilon \rho_a^{2-\varepsilon}} \right) \nabla_a W_{ab}, \quad (3.28)$$

where ε may take any value. The following form (i.e., $\varepsilon = 1$) provides certain advantages for problems involving contact discontinuities, and was used for the research described herein.

$$-\left(\frac{1}{\rho}\nabla p\right)_a = -\sum_b m_b \left(\frac{p_a + p_b}{\rho_a \rho_b}\right) \nabla_a W_{ab}. \quad (3.29)$$

3.2.3.2 Viscosity

Many forms of artificial viscosity have been proposed for modeling viscous fluid in SPH (Benz 1990; Monaghan 1992). The most commonly used form is incorporated into the momentum equation as,

$$\frac{d\mathbf{u}_a}{dt} = -\sum_b m_b \left(\frac{p_a + p_b}{\rho_a \rho_b} + \Pi_{ab}\right) \nabla_a W_{ab} + \mathbf{g}, \quad (3.30)$$

where,

$$\Pi_{ab} = \begin{cases} \frac{-0.5\alpha(c_a + c_b)\tilde{\mu}_{ab} + \beta\tilde{\mu}_{ab}^2}{0.5(\rho_a + \rho_b)} & \text{if } \mathbf{u}_{ab} \cdot \mathbf{r}_{ab} < 0; \\ 0 & \text{otherwise,} \end{cases} \quad (3.31)$$

$$\tilde{\mu}_{ab} = \frac{h\mathbf{u}_{ab} \cdot \mathbf{r}_{ab}}{\mathbf{r}_{ab}^2 + 0.01h^2}. \quad (3.32)$$

This viscosity is Galilean invariant and conserves total linear and angular momenta. The Π_{ab} term produces a shear and bulk viscosity which permit the modeling of strong shocks. α and β are chosen to be 1 and 2, respectively, for best results. The $0.01h^2$ term is included to keep the denominator nonzero. In this form, viscosity is intended only to provide the needed dissipation at a shock front to convert kinetic energy into internal energy, so it is only active for approaching particles.

Although this formulation has been used to model real viscosity (Artymowicz and Lubow 1994), it produced inaccurate velocity profiles for simulations in this work. Equation 3.30 guarantees conservation of angular momentum, which is important for applications involving relatively large fluid velocities or an unbounded fluid edge. Since the applications in porous media flow involve low velocities and SPH particles

fill all space, a more realistic form of viscosity has been adopted. Other expressions have been proposed to model real viscous forces: however, their implementation requires nested summations over the particles and hence twice the computational effort (Flebbe et al. 1994; Watkins et al. 1996), or second derivatives of the kernel which introduce sizable errors at low resolution interpolations (Takeda et al. 1994). This method employed an SPH estimation of viscous diffusion as,

$$(\nu \nabla^2 \mathbf{u})_a = \left(\frac{\mu}{\rho} \nabla^2 \mathbf{u} \right)_a = \sum_b \frac{m_b (\mu_a + \mu_b) \mathbf{r}_{ab} \cdot \nabla_a W_{ab}}{\rho_a \rho_b (\mathbf{r}_{ab}^2 + 0.01 h^2)} \mathbf{u}_{ab}. \quad (3.33)$$

Equation 3.33 is based on a similar SPH expression used by Monaghan (1995a) to model heat conduction. This hybrid expression combines a standard SPH first derivative with a finite difference approximation of a first derivative. By taking a Taylor expansion about particle a , it can be shown that this expression is approximate (Monaghan 1995a). This formulation conserves linear momentum exactly, while angular momentum is only approximately conserved. If the kernel takes the form of Equation 3.3, Equation 3.33 simplifies to,

$$(\nu \nabla^2 \mathbf{u})_a = \sum_b \frac{m_b (\mu_a + \mu_b) \mathbf{u}_{ab}}{\rho_a \rho_b} \frac{1}{|\mathbf{r}_{ab}|} \frac{\partial W_{ab}}{\partial r_{ab}}. \quad (3.34)$$

Substituting Equations 3.29 and 3.34 into Equation 3.15, the SPH form of the momentum equation is,

$$\frac{d\mathbf{u}_a}{dt} = - \sum_b m_b \left(\frac{p_a + p_b}{\rho_a \rho_b} \right) \nabla_a W_{ab} + \sum_b \frac{m_b (\mu_a + \mu_b) \mathbf{u}_{ab}}{\rho_a \rho_b} \left(\frac{1}{|\mathbf{r}_{ab}|} \frac{\partial W_{ab}}{\partial r_{ab}} \right) + \mathbf{g}, \quad (3.35)$$

which is used to evaluate particle accelerations.

3.2.4 Dynamic Pressure

For low Reynolds number flows, local variations in pressure gradient which force fluid motion can be very small in comparison to the hydrostatic pressure gradient. This is of special significance to SPH since pressure is obtained using an explicit function of density and is only accurate to about 1%. Consequently, for many problems, it is simpler to model the dynamic pressure p_d defined as,

$$p_d = p_t - p_h, \quad (3.36)$$

where p_t and p_h are the total and hydrostatic pressures, respectively. Thus, it is the dynamic pressure which is modeled by Equation 3.18 and used in Equation 3.35. Since pressure appears in the Navier-Stokes equations only as a gradient, the effect of p_h is that of a body force.

$$-\frac{1}{\rho} \nabla p_t = -\frac{1}{\rho} \nabla p_d - \frac{1}{\rho} \nabla p_h. \quad (3.37)$$

Substituting Equation 3.37 into Equation 3.15 gives,

$$\frac{d\mathbf{u}}{dt} = -\frac{1}{\rho} \nabla p_d + \nu \nabla^2 \mathbf{u} + \mathbf{g} - \frac{1}{\rho} \nabla p_h = -\frac{1}{\rho} \nabla p_d + \nu \nabla^2 \mathbf{u} + \mathbf{F}, \quad (3.38)$$

where \mathbf{F} is the net body force driving the flow defined as,

$$\mathbf{F} = \mathbf{g} - \frac{1}{\rho} \nabla p_h, \quad (3.39)$$

i.e., fluid particles move in response to an imbalance of forces due to gravity and a large-scale static pressure field. Using this approach, pressure gradient driven flow through a periodic lattice can be easily simulated. For simplicity, p is used in the followings to denote the dynamic pressure p_d .

3.2.5 Boundary Conditions

Initial applications of quasi-incompressible SPH involved high Reynolds number simulations of free surface flows interacting with free-slip boundaries (Monaghan 1994; Monaghan 1995b; Monaghan 1995c). Such work employed boundary particles which exerted strong repulsive forces to prevent SPH particles from penetrating solid surfaces. The force has the form of Lennard-Jones form for forces between molecules. To realistically model porous media flow, no-slip fluid-solid boundary conditions are needed. In addition, for the free surface flows considered by Monaghan (1994), boundary particles do not contribute to the density of the free SPH particles, thus permitting the fluid to freely leave a solid boundary with no pressure-driven restoring force. In this work, boundary particles contribute to the density of fluid particles such that pressure decreases when fluid and boundary particles diverge. It is possible to implement such a boundary condition using image particles (Liberky and Petschek 1990;

Liberky et al. 1993; Randles and Libersky 1996). The images are created by reflecting fluid particles across the boundary with opposite velocities. This procedure works well for straight channels, but introduces density errors for curved surfaces. Takeda et al. (1994) achieved a no-slip boundary condition using special boundary terms which mimic a half-space filled with SPH image particles. While the approach has proved useful for compressible and moderate to high Reynolds number flows, it did not yield sufficiently stable results for quasi-incompressible low Reynolds number simulations.

In this work, real SPH particles are used to create no-slip boundaries. These particles contribute to the usual SPH expressions for density and momentum, and their own densities are also evolved. Evolving the densities of boundary particles was found to better capture peak pressures than if the densities of boundary particles were kept constant. Obstacles are created by initially placing SPH particles on a regular lattice and deleting those particles which fall within the solid matrixes. Then boundary particles are placed in layers parallel to the solid surfaces. Figure 3.2 illustrates the concept for a curved boundary.

For each fluid particle a , the normal distance d_a to the boundary is calculated. This normal defines a tangent plane (a line in two dimensions) from which the normal distance d_B to each boundary particle B is calculated. The velocity of particle a is extrapolated across the tangent plane, assuming zero velocity on the plane itself, giving each boundary particle the velocity,

$$\mathbf{u}_B = -\frac{d_B}{d_a} \mathbf{u}_a. \quad (3.40)$$

By doing so, boundary particles are assigned artificial velocities such that antisymmetry in the velocity field is created across the boundary surface. Ideally, local estimates of the velocity gradients at the surface of the boundary would be used to assign these artificial velocities to interior points, however, such estimates would require a second summation over the particles and, hence, a substantial increase in the computation efforts. The approach presented here is simple, stable, accurate, and requires little extra computation.

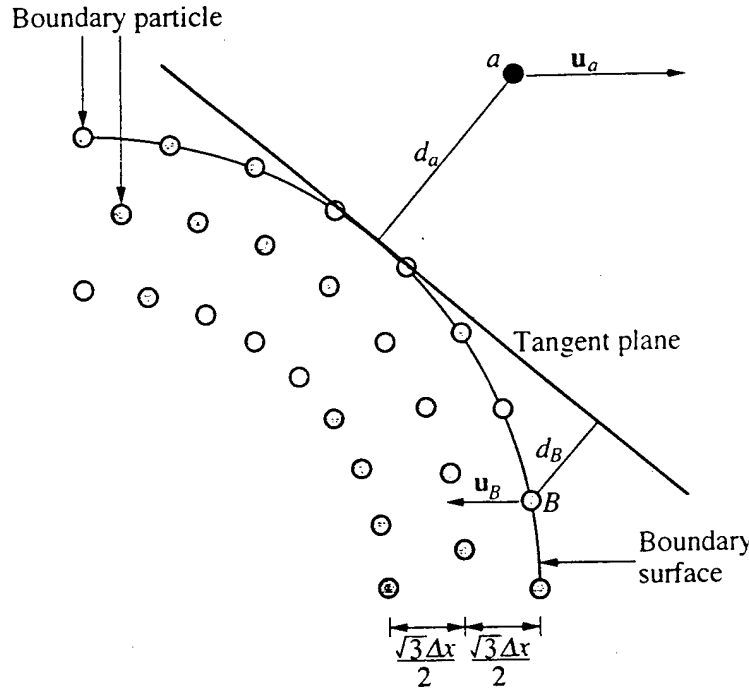


Figure 3.2: Construction of no-slip fluid-solid boundary for a curved surface.

If the boundary is in motion, \mathbf{u}_a should be replaced by the fluid velocity relative to the boundary. The artificial velocity \mathbf{u}_B is used to calculate viscous forces, whereas the actual boundary velocity is used to evolve boundary particle positions and densities. In practice, the discrete arrangement of boundary particles may permit a fluid particle to closely approach the nominal curve describing the boundary. In such circumstances, potentially large artificial velocities for boundary particles may result. To prevent this problem, d_a is bounded according to,

$$d_a = \max(d_a, \frac{\sqrt{3}}{4} \Delta x), \quad (3.41)$$

where Δx is the initial nearest neighbor distance between fluid particles (Figure 3.3). Every SPH particle has its mass associated with. As the first layer of boundary particles is placed on the solid surface, the porous medium simulated actually has a lesser porosity than intended. This effect diminishes as Δx decreases.

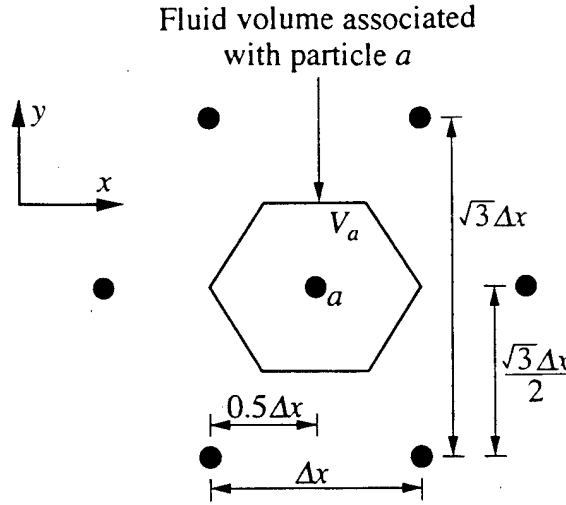


Figure 3.3: Initial hexagonal configuration of SPH fluid particles.

3.2.6 Interpolation Kernel

The interpolation kernel is used to calculate a weighted sum of fluid properties at a point. The use of different kernels for SPH is analogous to the use of different finite difference operators for the finite difference method. Most SPH applications employ a cubic spline kernel (Schoenberg 1946; Monaghan and Lattanzio 1985) since it resembles a Gaussian while having compact support,

$$W(\mathbf{r}, h) = \frac{10}{7\pi h^2} \begin{cases} 1 - \frac{3}{2}s^2 + \frac{3}{4}s^3 & \text{if } 0 \leq s < 1; \\ \frac{(2-s)^3}{4} & \text{if } 1 \leq s < 2; \\ 0 & \text{if } s \geq 2, \end{cases} \quad (3.42)$$

where,

$$s = \frac{|\mathbf{r}|}{h}, \quad (3.43)$$

and the above equation is normalized for two dimensions. However, it has been shown that SPH can be unstable to transverse modes when kernels with compact support are used (Morris 1994; Morris 1996b). As higher-order splines more closely approximating a Gaussian are employed, these instabilities are reduced. One reason

for the poor performance of lower-order splines is that the stability properties of SPH depend strongly upon the second derivative of the kernel. The second derivative of the cubic spline is a piecewise-linear function, and, accordingly, the stability properties are inferior to those of smoother kernels. For low Reynolds number quasi-incompressible flow simulations, cubic spline kernel rapidly produced significant noise in pressure and velocity fields. The following quintic spline kernel (Schoenberg 1946) has been chosen in this work, here normalized for two dimensions, which results in much less noise in the pressure and velocity fields.

$$W(\mathbf{r}, h) = \frac{7}{478\pi h^2} \begin{cases} (3-s)^5 - 6(2-s)^5 + 15(1-s)^5 & \text{if } 0 \leq s < 1; \\ (3-s)^5 - 6(2-s)^5 & \text{if } 1 \leq s < 2; \\ (3-s)^5 & \text{if } 2 \leq s < 3; \\ 0 & \text{if } s \geq 3. \end{cases} \quad (3.44)$$

Figure 3.4 shows Wh^2 as a function of s for the quintic spline kernel given by Equation

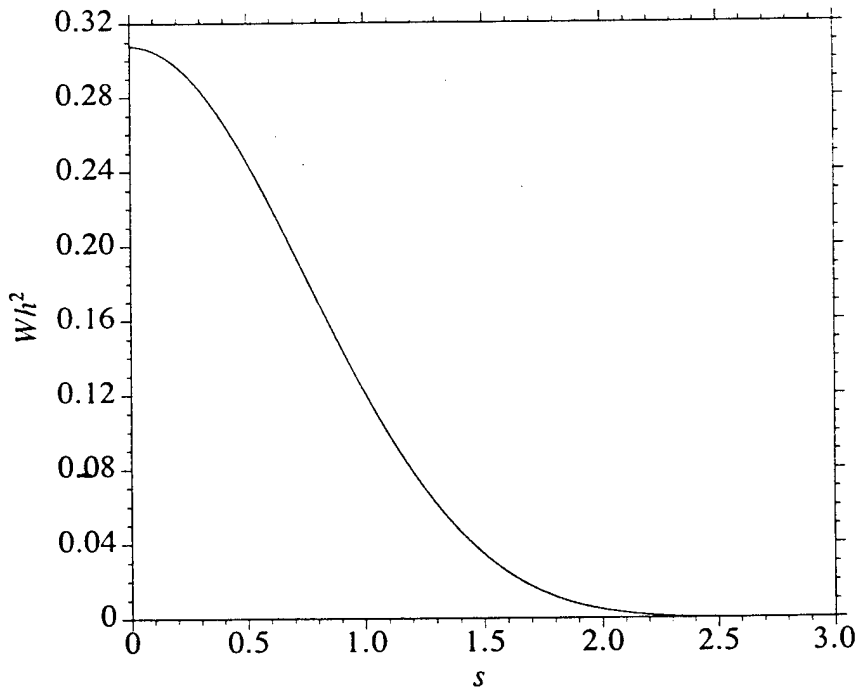


Figure 3.4: Wh^2 versus s for quintic spline kernel.

3.44. By using a quintic spline, particles interact within a distance of $3h$ (Figure 3.1). This produces property estimates that are smoother than those obtained using a cubic spline. The numerical solution also has better stability properties as a result (Morris 1996b). The quintic spline is, however, more computationally expensive than the cubic spline by approximately a factor of two.

3.2.7 Locating the Nearest Neighboring Particles

As defined by a kernel with compact support, each particle has a finite number of “neighboring” particles with which it interacts. For the quintic kernel, particles interact within a distance of $3h$ (Figure 3.1). The problem still remains, however, to efficiently identify these interacting pairs of particles. In this work, an algorithm employing a linked list data structure is used to locate neighboring particles (Monaghan and Lattanzio 1985; Morris 1996a).

The computational domain is divided into square cells, each with a side length of $3h$. A list of particles belonging to each cell is created. A particle located within a given cell then must only consider interactions with particles in neighboring cells. The lists of particles within each cell are implemented as linked lists. That is, there is a pointer to the first particle in a cell, and that particle then points to the second particle and so on. In one dimension, the algorithm reads as:

```

for  $i = 1$  to all particles do
     $j = \text{int}((x_i - x_{\min})/(3h))$ 
     $\text{next}_i = \text{head}_j$ 
     $\text{head}_j = i$ 

```

head_j is a pointer to the first particle in cell j , and is initially set to 0, while next_i is a pointer from particle i to the next particle in the linked list. head_j will point to 0 if cell j is empty and next_i will point to 0 if particle i is the last particle in the list. Finding the nearest neighbors of particle i in cell j is now performed as:

```

for  $cell = j - 1$  to  $j + 1$  do
     $k = \text{head}_{cell}$ 

```

```

while ( $k \neq 0$ ) do
    consider particle  $k$ 
     $k = next_k$ 

```

However, in practice, it is much more efficient to create a temporary list of particles in a given cell and interacting neighboring cells and evaluate the interactions between them. Also, it is enough to only consider the neighboring cell to one side of the home cell because the cell on the other side will consider this home cell as its neighboring cell and include it. For example, considering the SPH interactions for cell j , a list of particles from cell j (home cell) and cell $j + 1$ (the neighboring cell to the right) is created:

```

 $i = 0$ 
 $k = head_j$ 
while ( $k \neq 0$ ) do
     $i = i + 1$ 
     $list_i = k$ 
     $k = next_k$ 
     $n_{home} = i$ 
     $k = head_{j+1}$ 
    while ( $k \neq 0$ ) do
         $i = i + 1$ 
         $list_i = k$ 
         $k = next_k$ 
     $n_{total} = i$ 

```

Then the SPH contributions can be readily obtained by considering pairs of particles as:

```

for  $i_1 = 1$  to  $n_{home}$  do
     $a = list_{i_1}$ 
    for  $i_2 = i_1$  to  $n_{total}$  do
         $b = list_{i_2}$ 
        consider particles  $a$  and  $b$ 

```

These loops consider all the interactions between particles in the home cell j with each other and with those particles in the neighboring cell $j+1$. The first loop is over n_{home} particles while the second is over n_{total} particles since the interactions between particles in the neighboring cell with themselves are not intended.

3.2.8 Time Integration

The time integration of SPH equations can be performed using the same basic approaches which are employed for other explicit hydrodynamic methods. The chosen method should provide high order accuracy with a minimum number of sweeps over the particles. In this model, explicit time integration is performed using the modified Euler method in which the time step τ is limited by stability constraints. The CFL condition (Courant et al. 1928) essentially states that the maximum numerical rate of propagation of information must exceed the physical rate. In SPH, this translates to,

$$\tau \leq 0.25 \frac{h}{c}. \quad (3.45)$$

Additional constraints arise from the magnitude of particle accelerations f_a (Monaghan 1992),

$$\tau \leq 0.25 \min_a \sqrt{\frac{h}{f_a}}, \quad (3.46)$$

and viscous diffusions,

$$\tau \leq 0.125 \frac{h^2}{\nu}. \quad (3.47)$$

Equation 3.47 is based upon the usual condition for an explicit finite difference method simulating diffusion. For simulations having high resolution (small h) or large viscosity, Equation 3.47 is typically the dominant time constraint. The choice of kernel and the initial arrangement of particles influence the coefficients in Equations 3.45 to 3.47. In particular, different splines can have different “effective” resolution lengths for the same value of h . For example, use of a cubic spline (which is “narrower” than

a quintic for the same smoothing length) may require slightly smaller coefficients in the above expressions.

The time stepping is carried out using a predictor-corrector scheme (Al-Khafaji and Tooley 1986). The following equations are used to obtain the field quantities at the next time step,

$$\tilde{u}^{\frac{1}{2}} = u^0 + \frac{\tau}{2} f_a^0, \quad (3.48)$$

$$\tilde{x}^{\frac{1}{2}} = x^0 + \frac{\tau}{2} u^0, \quad (3.49)$$

$$\tilde{\rho}^{\frac{1}{2}} = \rho^0 + \frac{\tau}{2} f_\rho^0, \quad (3.50)$$

$$f_a^{\frac{1}{2}} = f(m, \tilde{x}^{\frac{1}{2}}, \tilde{u}^{\frac{1}{2}}, \tilde{\rho}^{\frac{1}{2}}, \dots), \quad (3.51)$$

$$f_\rho^{\frac{1}{2}} = f(m, \tilde{x}^{\frac{1}{2}}, \tilde{u}^{\frac{1}{2}}, \dots), \quad (3.52)$$

$$u^{\frac{1}{2}} = u^0 + \frac{\tau}{2} f_a^{\frac{1}{2}}, \quad (3.53)$$

$$x^{\frac{1}{2}} = x^0 + \frac{\tau}{2} u^{\frac{1}{2}}, \quad (3.54)$$

$$\rho^{\frac{1}{2}} = \rho^0 + \frac{\tau}{2} f_\rho^{\frac{1}{2}}, \quad (3.55)$$

$$u^1 = 2u^{\frac{1}{2}} - u^0, \quad (3.56)$$

$$x^1 = 2x^{\frac{1}{2}} - x^0, \quad (3.57)$$

$$\rho^1 = 2\rho^{\frac{1}{2}} - \rho^0, \quad (3.58)$$

where the superscripts are the time step index, and f_a and f_ρ are the acceleration and rate of change of density, respectively. In practice, the predictor step uses values of f_a and f_ρ at the previous midpoint, e.g., $f_a^0 = f_a^{-\frac{1}{2}}$, since this reduces the computation work without changing the order of the scheme.

3.3 Model Initialization and Execution

3.3.1 Initialization

For each simulation, fluid particles are initially placed throughout the computational domain, i.e., the unit cell of the periodic porous medium, in a hexagonal arrangement (Figure 3.3). Each particle is assigned an initial density ρ_0 , an initial velocity of zero, and a mass $m_a = \rho_0 V_a$, where V_a is the volume associated with particle a (Figure 3.3). Fluid particles that fall within the solid matrixes are deleted. The choice for the number of fluid particles is governed by the desired resolution and the computational expense. Larger numbers of particles produce more accurate results but also increase computation time. For porous media simulations, it is recommended that each pore throat should be spanned by at least 15 particles. As a result, the computation time for problems having small porosity (i.e., narrow pore throats) dramatically increases due to the larger number of particles and the reduced numerical time step (Equations 3.45 to 3.47).

Boundary particles are placed on the solid inclusions using a pseudo-hexagonal arrangement (Figure 3.2). The first layer of boundary particles are positioned on the perimeter with an equal spacing of approximately Δx (depending on the size of the solid obstacles). A second layer of an equal number of particles is then placed at a distance of $\frac{\sqrt{3}}{2}\Delta x$ from the boundary. A third layer of particles is positioned similarly and the process is continued until boundary particles fill an annular zone having a thickness of at least $6h$ from the solid surface. Particles farther than $6h$ are not needed because they would not contribute to the calculations due to the use of quintic spline kernel. Once the boundary particles are positioned, each is assigned a mass consistent with its contributing volume and an initial density of ρ_0 . The solid inclusion is usually large enough to accommodate the annular zone of boundary particles. However, when it is small, Δx may be reduced to enforce the boundary particle condition (i.e., an annular zone having a thickness of at least $6h$ from the solid surface). In this work, the number of total SPH particles N_{part} (including boundary

particles) chosen for a simulation is either determined by having about 20 particles spanning the narrowest pore throat or having enough boundary particles for the solid inclusions.

The positioning of boundary particles disrupts the initial hexagonal arrangement of fluid particles in the problem domain. To account for changes in particle density near the boundaries, the initial density field (fluid particles and boundary particles) is recalculated using direct summation (Equation 3.7). Once particle densities are corrected, a body force \mathbf{F} is applied to initiate fluid motion. \mathbf{F} is related to the hydraulic gradient \mathbf{i} by,

$$\mathbf{i} = \frac{\mathbf{F}}{g}. \quad (3.59)$$

In this model, \mathbf{F} can be applied in any direction. Periodic unit cell boundary conditions are applied to all fluid quantities and the flow is driven by the effective body force.

3.3.2 Execution

Once the body force is applied to the system, particle densities are evolved according to Equation 3.23 and particle accelerations are computed using Equation 3.35. The smoothing length h is chosen equal to $2\Delta x$ for the quintic kernel. To ensure stability of the integration scheme, the time step is limited according to the conditions set forth in section 3.2.8. Particle velocities, positions, and densities are updated using a predictor-corrector method (section 3.2.8). No-slip fluid-solid boundary conditions are simulated by assigning artificial velocities to the boundary particles using Equation 3.40. Although computationally less expensive, Equation 3.23 does not conserve mass exactly and may introduce errors over the course of a simulation. To correct for this, particle densities are updated every 50 time steps by direct summation (Equation 3.7). Using this procedure, computational speed is maintained and fluid mass is conserved as well. Locating neighboring particles is achieved by creating the linked lists for SPH particles (section 3.2.7).

Periodic unit cell boundaries are created through the use of solid inclusion and fluid particle images (Figure 3.5), and by wrapping fluid particles around the flow domain when they leave one boundary (Figure 3.6). Image fluid particles and solid inclusions are created within a distance of $3h$ (i.e., one quintic kernel radius) from the unit cell to provide the necessary “neighbors” for particles within the cell.

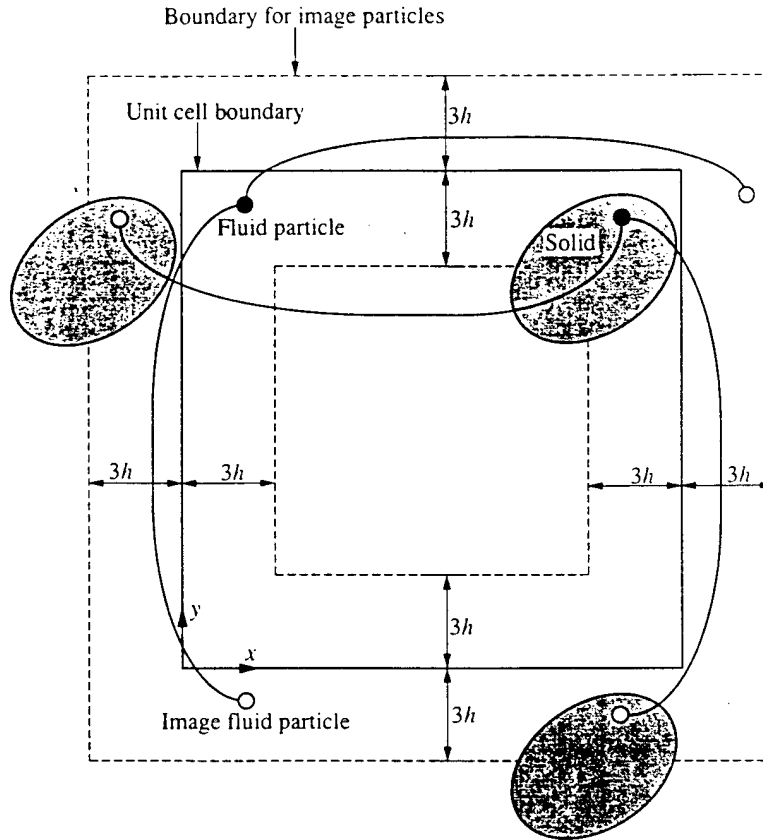


Figure 3.5: Construction of image particles to simulate a periodic porous medium.

The Darcy velocities v_x and v_y in x and y directions are defined as,

$$v_x = \frac{1}{V_{\text{unit cell}}} \int_{V_{\text{fluid}}} u_x dV, \quad (3.60)$$

and,

$$v_y = \frac{1}{V_{\text{unit cell}}} \int_{V_{\text{fluid}}} u_y dV, \quad (3.61)$$

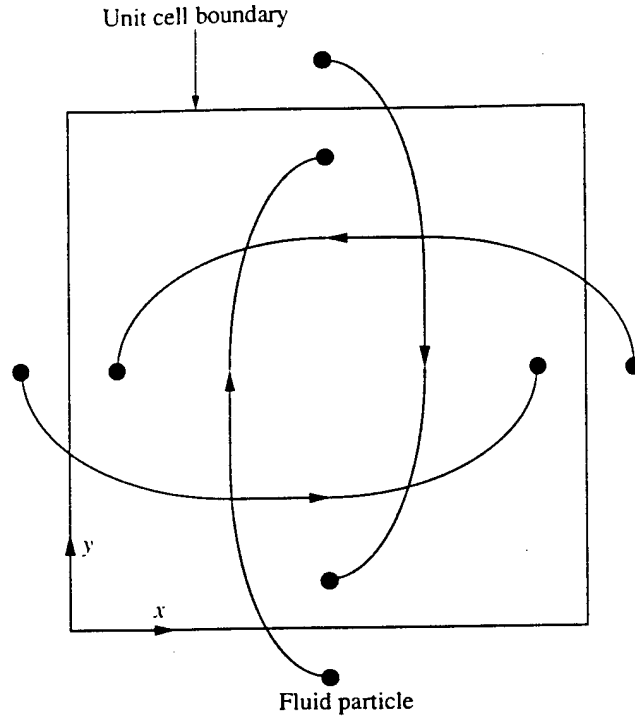


Figure 3.6: Wrapping fluid particles around unit cell.

respectively. In SPH, they are evaluated as,

$$v_x = \frac{1}{V_{\text{unit cell}}} \sum_b \frac{m_b}{\rho_b} u_{b,x}, \quad (3.62)$$

and,

$$v_y = \frac{1}{V_{\text{unit cell}}} \sum_b \frac{m_b}{\rho_b} u_{b,y}, \quad (3.63)$$

where $u_{b,x}$ and $u_{b,y}$ are x and y components of the velocity of particle b , respectively. During the course of a simulation, v_x , v_y , and the maximum particle velocity u_{\max} are recorded. Changes in these values with time are used to determine whether or not the flow has reached steady state.

3.4 Flow Model Verification

The SPH numerical flow model has been tested in many cases. Simulations using the method show close agreement with series solutions for Couette and Poiseuille flows and with other solutions for flow past regular lattices of obstacles.

3.4.1 Simulations of Couette and Poiseuille Flows

3.4.1.1 Couette Flow

Couette flow is simulated between infinite plates located at $y = 0$ and $y = L$ (Figure 3.7). The system is initially at rest. At time $t = 0$, the upper plate moves at

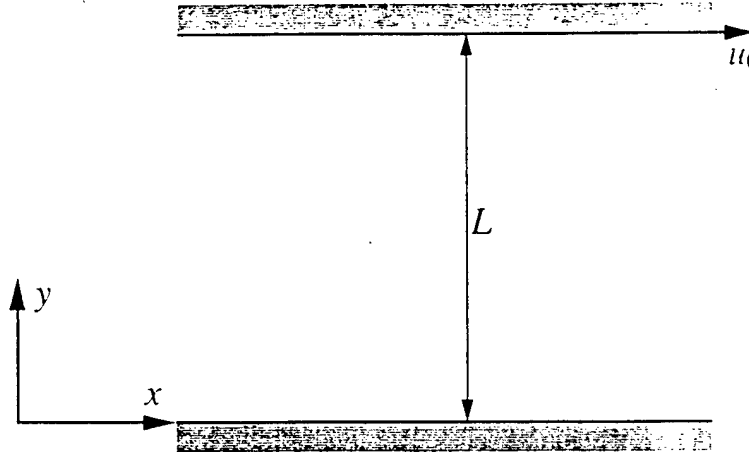


Figure 3.7: Couette flow.

constant velocity u_0 parallel to the x axis. The series solution for the time-dependent behavior of this flow is,

$$u_x(y, t) = \frac{u_0}{L} y + \sum_{n=1}^{\infty} \frac{2u_0}{n\pi} (-1)^n \sin\left(\frac{n\pi}{L} y\right) \exp\left(-\nu \frac{n^2 \pi^2}{L^2} t\right), \quad (3.64)$$

where u_x is the fluid velocity in the x direction. The flow was simulated using SPH for $\nu = 10^{-6} \frac{m^2}{s}$, $L = 10^{-3} m$, $\rho = 10^3 \frac{kg}{m^3}$, $u_0 = 1.25 \times 10^{-5} \frac{m}{s}$, and with 50 particles spanning the channel. This corresponds to a Reynolds number of 0.0125 if using,

$$Re = \frac{u_0 L}{\nu}. \quad (3.65)$$

Figure 3.8 shows a comparison between velocity profiles obtained using Equation 3.64 and SPH at several times including the steady state solution ($t = \infty$). The results are in close agreement within 0.5%, confirming the accuracy of the approach used to evaluate viscous and boundary forces with SPH. Lower resolution simulation completed with 20 particles spanning the channel was found to agree to within approximately 2% of the series solution values.

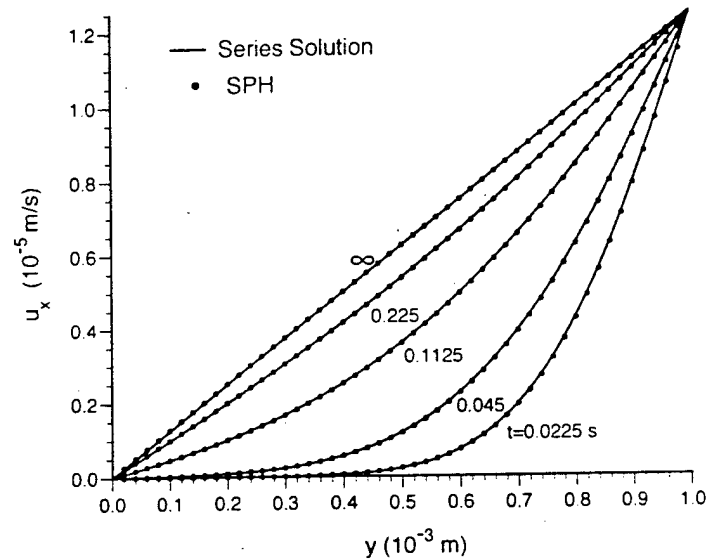


Figure 3.8: Comparison of SPH and series solutions for Couette flow ($Re = 0.0125$).

3.4.1.2 Poiseuille Flow

Poiseuille flow between stationary infinite plates at $y = 0$ and $y = L$ is simulated (Figure 3.9). The fluid is initially at rest and driven by an applied body force F

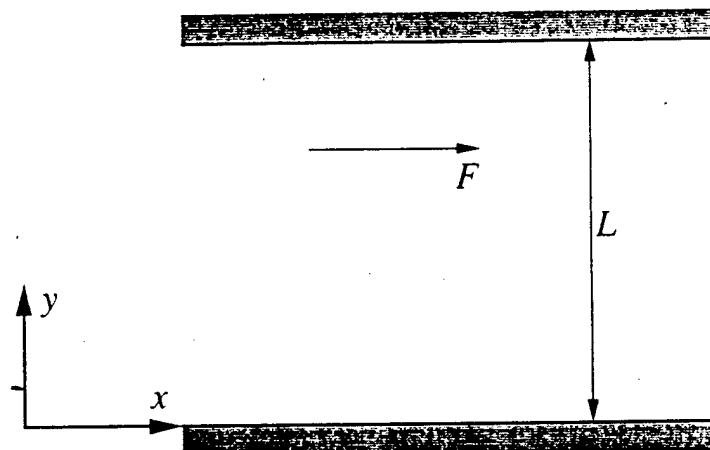


Figure 3.9: Poiseuille flow.

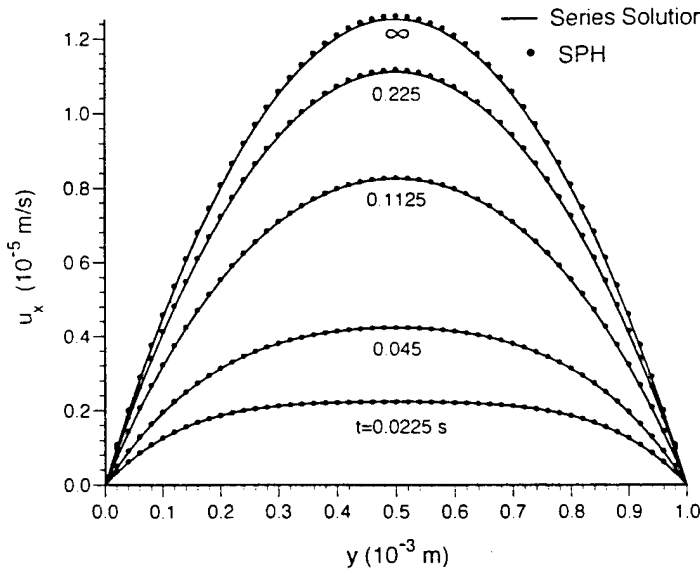


Figure 3.10: Comparison of SPH and series solutions for Poiseuille flow ($Re = 0.0125$).

parallel to the x axis for $t \geq 0$. The series solution for the transient behavior is,

$$u_x(y, t) = \frac{F}{2\nu}y(L - y) + \sum_{n=0}^{\infty} \frac{4FL^2}{\nu\pi^3(2n+1)^3} \sin\left(\frac{\pi y}{L}(2n+1)\right) \exp\left(-\frac{(2n+1)^2\pi^2\nu}{L^2}t\right). \quad (3.66)$$

SPH was used to simulate Poiseuille flow for $\nu = 10^{-6} \frac{\text{m}^2}{\text{s}}$, $L = 10^{-3} \text{ m}$, $\rho = 10^3 \frac{\text{kg}}{\text{m}^3}$, $F = 10^{-4} \frac{\text{m}}{\text{s}^2}$, and with 50 particles spanning the channel. This corresponds to a peak fluid velocity $u_0 = 1.25 \times 10^{-5} \frac{\text{m}}{\text{s}}$ and a Reynolds number of 0.0125 if using Equation 3.65. A comparison between velocity profile obtained using Equation 3.66 and SPH appears in Figure 3.10. The results are again in close agreement with the largest discrepancy being about 0.7% for the steady state solution. Lower resolution simulation completed with 20 particles spanning the channel was found to agree to within approximately 2% of the series solution values.

3.4.2 Simulations of Flow Through Periodic Lattices of Obstacles

The Couette and Poiseuille flow simulations tested the interaction between viscous and body forces and the effectiveness of the no-slip boundary conditions in the model.

However, these flows are essentially one-dimensional and do not produce variations in dynamic pressure. A more challenging test of the method involves flow through lattices of obstacles. In this SPH model, circular and elliptical obstacles have been implemented. Before presenting the simulations, three kinds of regular arrays of obstacles for spatially periodic porous media considered throughout this report are introduced. These are square, staggered, and hexagonal arrays of obstacles.

3.4.2.1 Square, Staggered, and Hexagonal Arrays of Obstacles

According to Perrins et al. (1979), there are five possible ways of packing obstacles in regular two-dimensional arrays (International tables for X-ray crystallography 1962). Three of these arrays—square, staggered, and hexagonal—are used in this work. Figures 3.11 to 3.13 depict the unit cell geometry for the three arrays with circular and elliptical inclusions. The unit cell for the square or staggered array

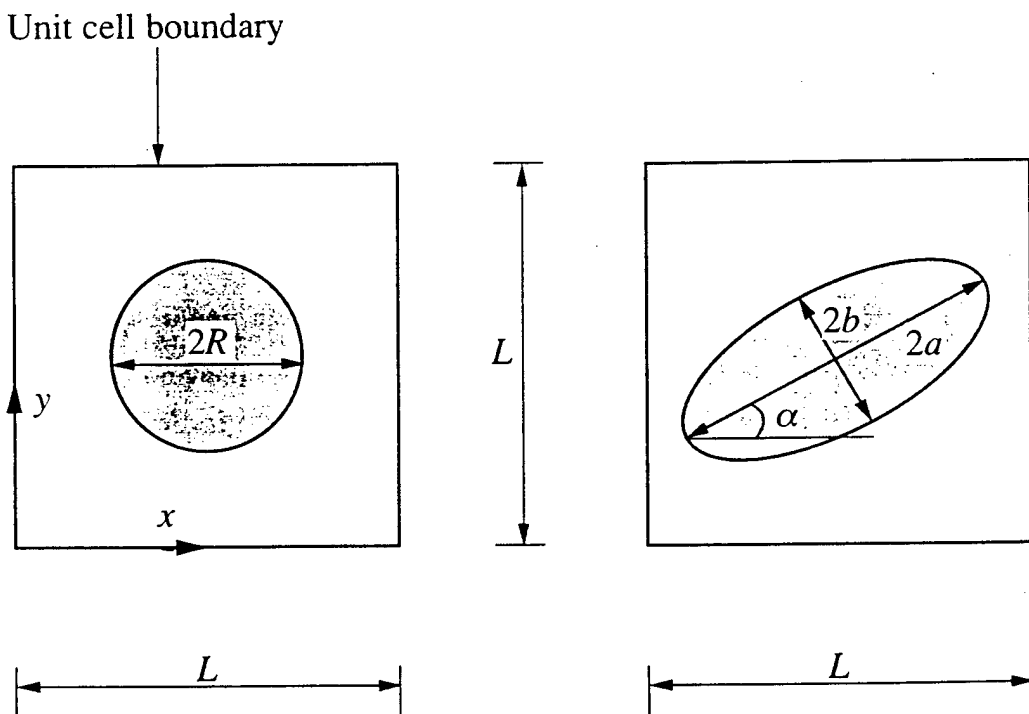


Figure 3.11: Two-dimensional cross sectional representations of unit cell geometry for square array with circular and elliptical inclusions.

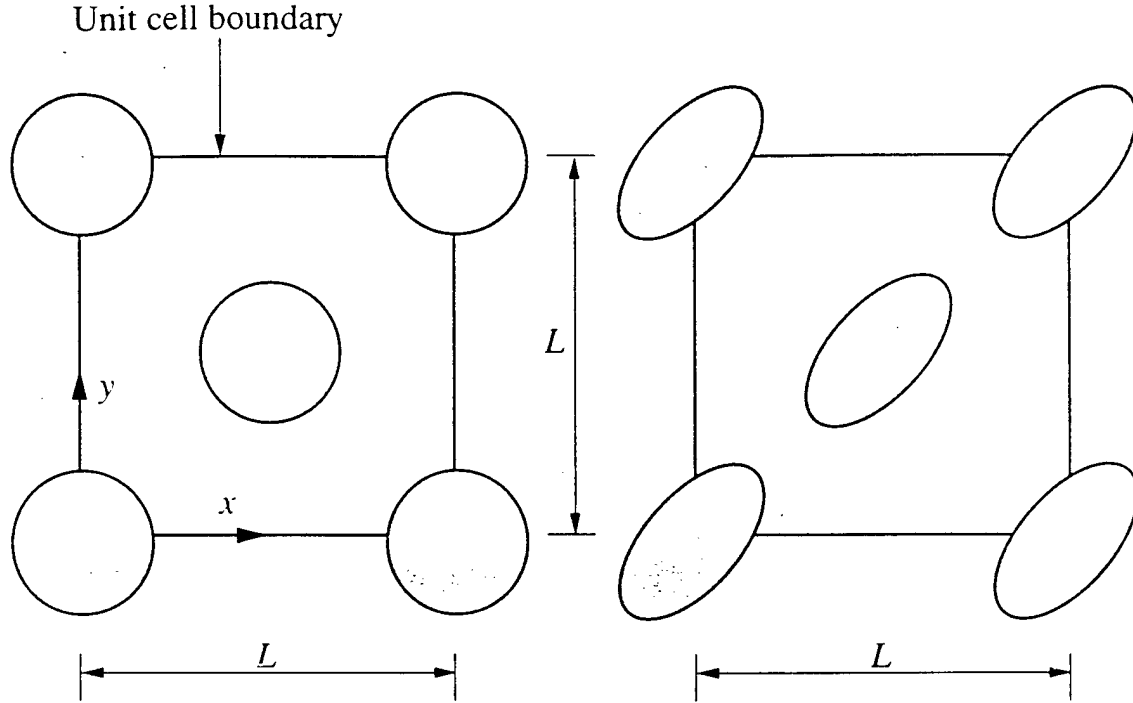


Figure 3.12: Two-dimensional cross sectional representations of unit cell geometry for staggered array with circular and elliptical inclusions.

has side length L , and the unit cell for the hexagonal array has side lengths L_1 and $L_2 = \sqrt{3}L_1$. The staggered array may be regarded as a superposition of two square arrays. The circular inclusion is simply characterized by the radius R , while the elliptical inclusion is characterized by the major axis $2a$, minor axis $2b$, and the angle α ($0^\circ \leq \alpha \leq 180^\circ$) between the direction of the major axis and the positive x direction. For circular inclusions, the three lattices are isotropic for fields applied in the plane, while for elliptical inclusions, intrinsic anisotropy exists.

3.4.2.2 Flow Through a Periodic Square Lattice of Circular Cylinders

The flow through a periodic square lattice of circular cylinders was first simulated. This particular configuration has been studied extensively as a simple model of flow through fibrous porous media. The periodic flow was simulated using SPH for $L = 0.1\text{ m}$, $\nu = 10^{-6}\frac{\text{m}^2}{\text{s}}$, $R = 0.02\text{ m}$, $F = 1.5 \times 10^{-7}\frac{\text{m}}{\text{s}^2}$, and $c = 5.77 \times 10^{-4}\frac{\text{m}}{\text{s}}$. Replacing

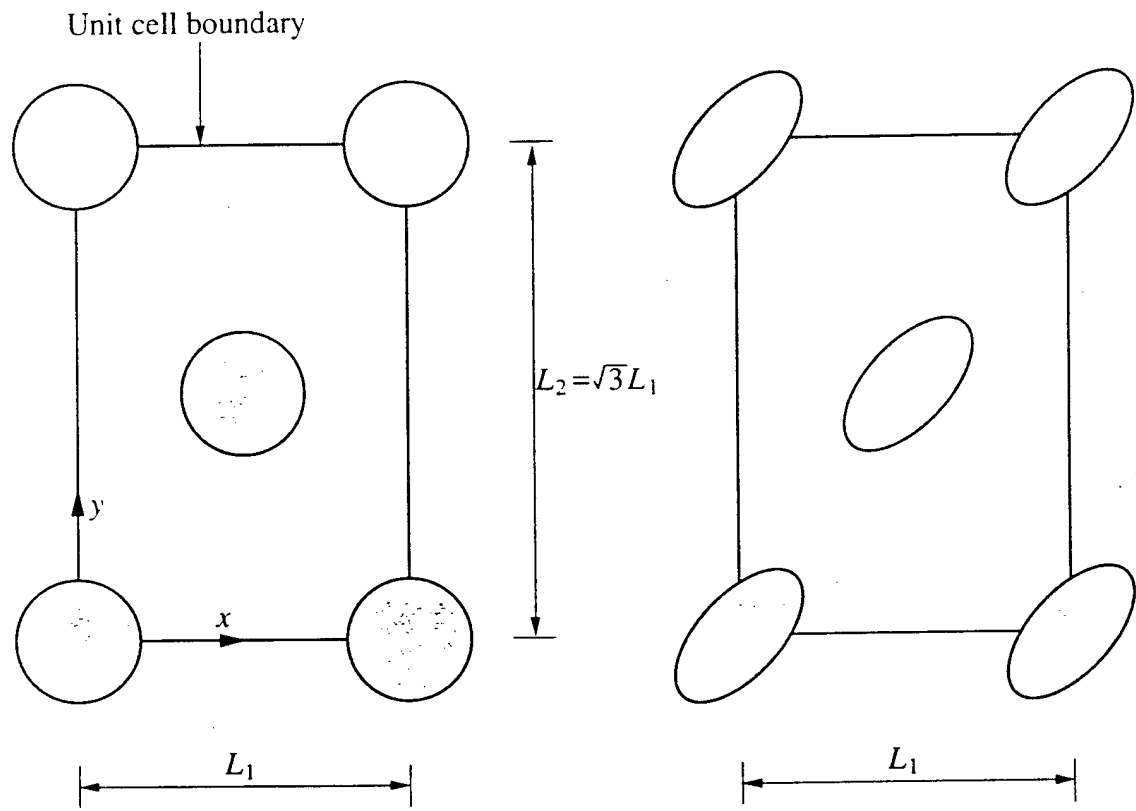


Figure 3.13: Two-dimensional cross sectional representations of unit cell geometry for hexagonal array with circular and elliptical inclusions.

L with R in Equation 3.65 and taking the velocity scale to be $u_0 = 5 \times 10^{-5} \frac{m}{s}$ gives $Re = 1$. The SPH simulation was run using approximately 3000 particles with a nearest neighbor distance Δx of 0.002 m. Steady state was reached after approximately 1500 time steps. To investigate long-term behavior, the simulation was continued for another 6000 time steps such that particle arrangements became disordered. The problem was also modeled using a finite element method (FEM) program for steady incompressible viscous flow. Velocity and pressure distributions from the two solutions were compared by plotting values within one nearest neighbor distance of the four paths described in Figure 3.14. The results were also compared

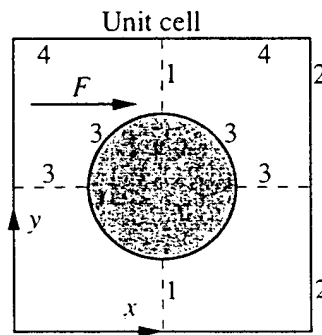


Figure 3.14: Paths for comparison of SPH and FEM solutions for flow through a periodic square lattice of circular cylinders.

using contour plots. As the FEM employs a mesh to obtain a solution, it is relatively easy to obtain contour plots. The corresponding plots for SPH were obtained by interpolating the particle quantities to a 50 by 50 array of grid points using the quintic kernel. Smoothing lengths of 1 and 3 grid spacings were used for the velocity and pressure, respectively. A greater amount of smoothing was needed to remove small fluctuations from the pressure field. Contours generated using this method are inaccurate in the immediate vicinity of the cylinder.

Figure 3.15 shows a comparison of velocity profiles obtained using SPH and FEM for paths 1 and 2 defined in Figure 3.14. The results obtained using SPH are in close agreement with those from FEM throughout the flow domain. Corresponding contour

plots of velocity magnitude are shown in Figure 3.16. Good agreement is obtained for the bulk of the flow, although the contour smoothing method inaccurately represents SPH velocities near the cylinder.

Figure 3.17 shows the dynamic pressure along paths 3 and 4 in Figure 3.14. The arc of path 3 was taken as 0.002 m (one SPH nearest neighbor distance) beyond the cylinder boundary. The SPH dynamic pressure profile shows small local fluctuations in the vicinity of the cylinder. Elsewhere, the SPH and FEM solutions are in close agreement. The peaks in the pressure obtained using SPH on the boundary itself fell short of the FEM results by approximately 8%. The FEM better captures pressure extrema since grid-stretching increases resolution in the vicinity of the cylinder. Corresponding contour plots of pressure given in Figure 3.18 show that good agreement is again obtained for the bulk of the flow. This simulation was repeated with twice the particle resolution (approximately 11000 particles) and peak pressures were reproduced to within 5%. Pressure values in the immediate vicinity of the boundary, however, still exhibited small fluctuations.

Flow through a periodic square lattice of circular cylinders was also solved for $L = 0.1\text{ m}$, $\nu = 10^{-4}\frac{\text{m}^2}{\text{s}}$, $R = 0.02\text{ m}$, $F = 5 \times 10^{-5}\frac{\text{m}}{\text{s}^2}$, and $c = 1 \times 10^{-2}\frac{\text{m}}{\text{s}}$. $u_0 = 1.5 \times 10^{-4}\frac{\text{m}}{\text{s}}$ gives $Re = 0.03$. The steady state of this flow was reached after approximately 1500 time steps. However, the initial lattice was relatively unchanged at this point. To demonstrate the long-term behavior of the method, the simulation was run for another 300000 time steps. A comparison of velocities along paths 1 and 2 appears in Figure 3.19 and velocity contour plots are shown in Figure 3.20. The results obtained using SPH are in close agreement with those obtained by FEM. A comparison of pressure fields presented in Figures 3.21 and 3.22 also shows close agreement for the bulk of the flow, with similar fluctuations as observed for $Re = 1$. Although pressure extrema on the boundary were not fully captured by SPH, the discrepancies were somewhat smaller (about 5%). The simulation was repeated for fewer time steps with twice the resolution (approximately 11000 particles) and peak pressures were obtained with less than 4% discrepancy. Once again, however, small pressure fluctuations were observed near the boundary.

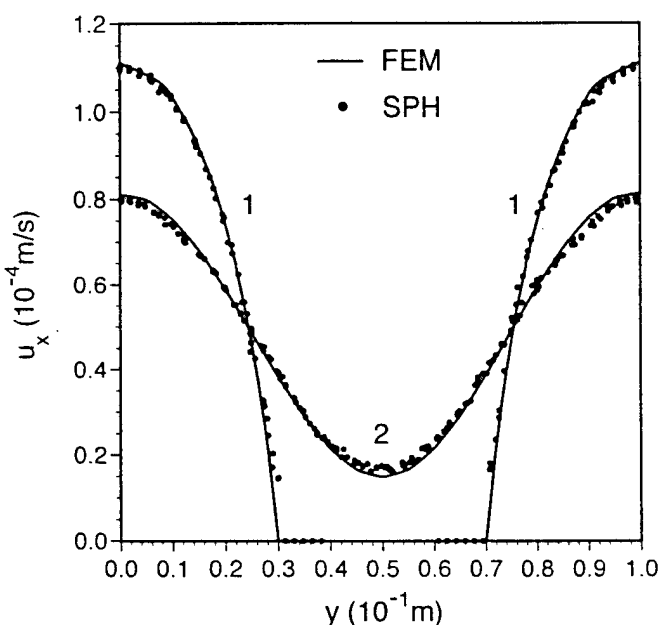
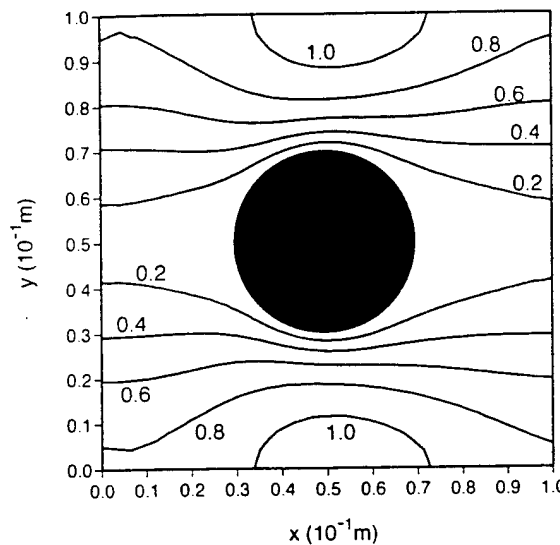
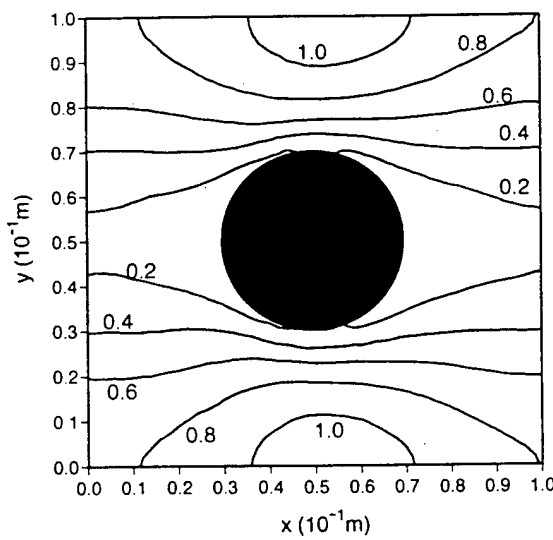


Figure 3.15: Comparison of SPH and FEM velocity profiles along paths 1 and 2 in Figure 3.14 for $Re = 1$.



(a)



(b)

Figure 3.16: Contour plots of velocity magnitude using (a) FEM, and (b) SPH for $Re = 1$ (contour lines are labeled in unit of $10^{-4} \frac{\text{m}}{\text{s}}$).

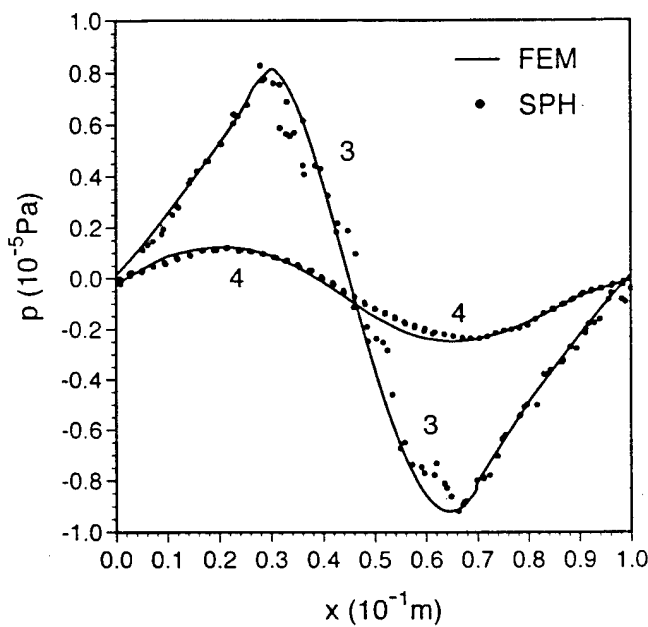
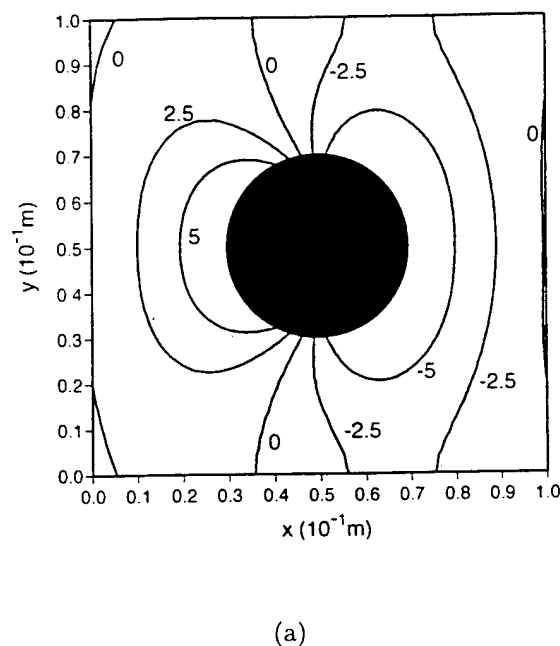
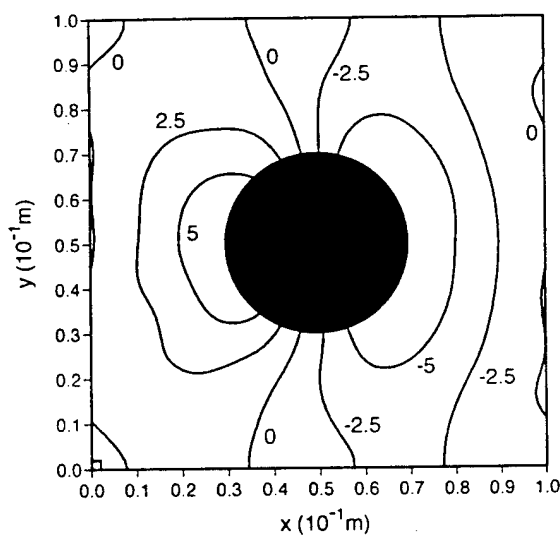


Figure 3.17: Comparison of SPH and FEM pressure profiles along paths 3 and 4 in Figure 3.14 for $Re = 1$.



(a)



(b)

Figure 3.18: Contour plots of pressure using (a) FEM, and (b) SPH for $Re = 1$ (contour lines are labeled in unit of $10^{-6} Pa$).

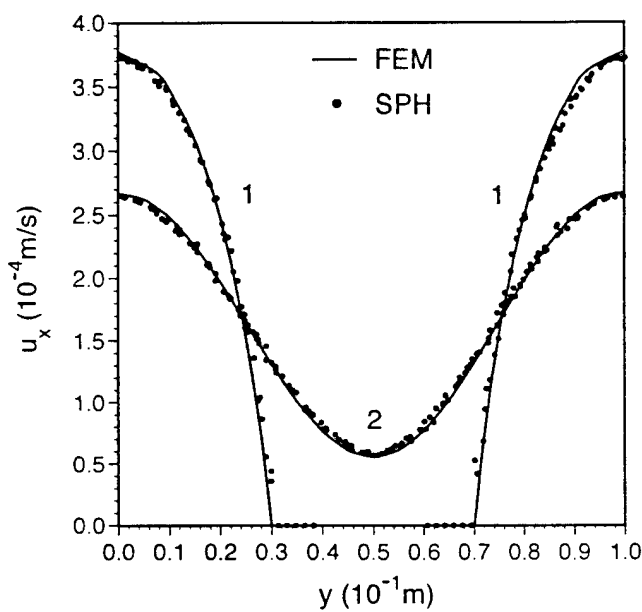
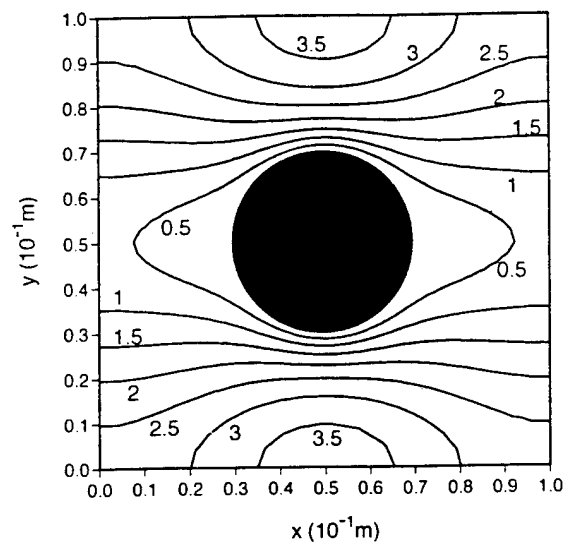
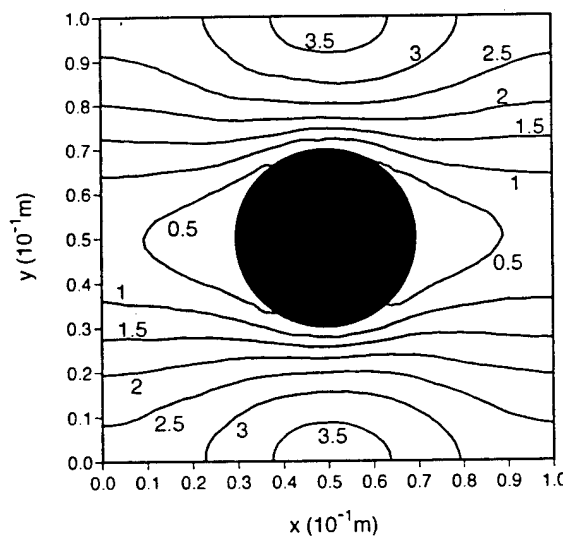


Figure 3.19: Comparison of SPH and FEM velocity profiles along paths 1 and 2 in Figure 3.14 for $Re = 0.03$.



(a)



(b)

Figure 3.20: Contour plots of velocity magnitude using (a) FEM, and (b) SPH for $Re = 0.03$ (contour lines are labeled in unit of $10^{-4} \frac{\text{m}}{\text{s}}$).

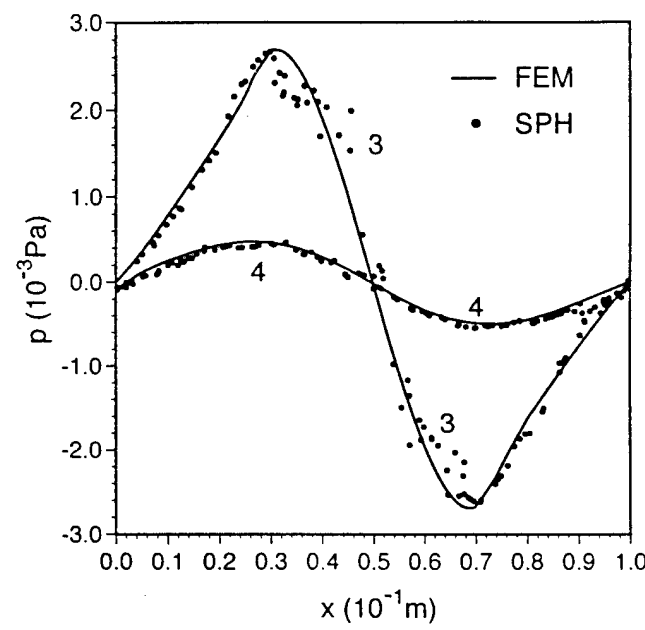
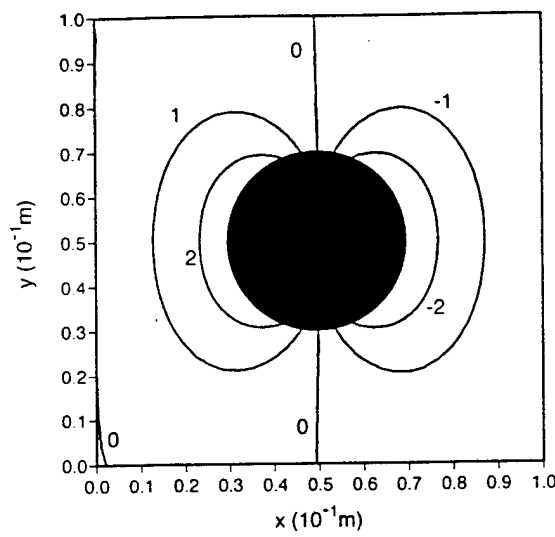
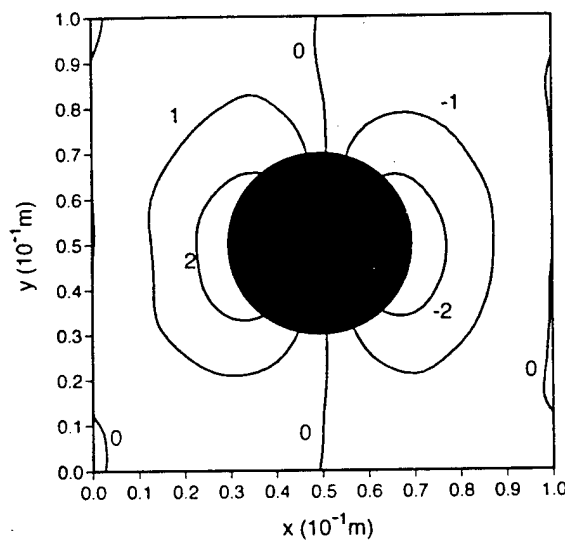


Figure 3.21: Comparison of SPH and FEM pressure profiles along paths 3 and 4 in Figure 3.14 for $Re = 0.03$.



(a)



(b)

Figure 3.22: Contour plots of pressure using (a) FEM, and (b) SPH for $Re = 0.03$ (contour lines are labeled in unit of 10^{-3} Pa).

3.4.2.3 Flow Through a Periodic Square Lattice of Elliptical Cylinders

The flow through a periodic square lattice of elliptical cylinders was also simulated using both SPH and FEM for comparative study. Velocity and pressure distributions from the two solutions were compared by plotting values within one nearest neighbor distance of the four paths described in Figure 3.23. The problem was solved for

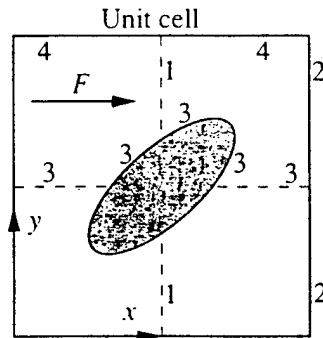


Figure 3.23: Paths for comparison of SPH and FEM solutions for flow through a periodic square lattice of elliptical cylinders.

$L = 2.16 \text{ mm}$, $\nu = 10^{-6} \frac{\text{m}^2}{\text{s}}$, $a = 0.771 \text{ mm}$, $\frac{a}{b} = 2$, $\alpha = 45^\circ$, $F = 0.001 \frac{\text{m}}{\text{s}^2}$, and $c = 0.012 \frac{\text{m}}{\text{s}}$. The steady state Darcy velocity v_x was found to be $8.10 \times 10^{-5} \frac{\text{m}}{\text{s}}$ using SPH and $8.29 \times 10^{-5} \frac{\text{m}}{\text{s}}$ using FEM. The two values agree within a 2.3% difference. The average value of v_x gives $Re = 0.06$ if a is used as the length scale. The SPH simulation was run for 50200 time steps using 41412 particles with a nearest neighbor distance Δx of 0.0108 mm.

Figure 3.24 shows a comparison of velocity profiles obtained using SPH and FEM for paths 1 and 2. The results obtained using SPH are in close agreement with those from FEM throughout the flow domain. Figure 3.25 shows a comparison of dynamic pressure along paths 3 and 4. The two solutions are in close agreement except at the peaks in the pressure in the vicinity of the cylinder. The fluctuations are similar to those observed for circular inclusions (Figures 3.17 and 3.21). Figures 3.24 and 3.25 confirm that SPH is capable of modeling flow past elliptical inclusions in general.

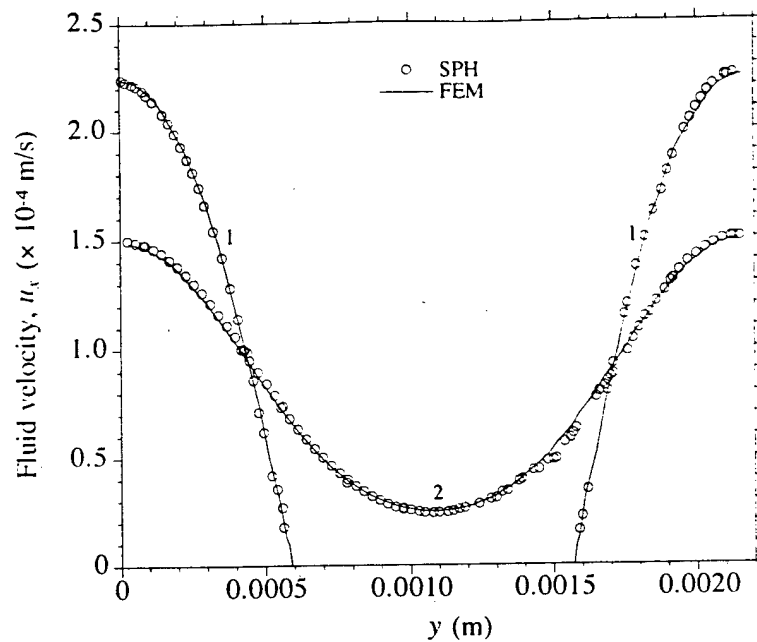


Figure 3.24: Comparison of SPH and FEM velocity profiles along paths 1 and 2 in Figure 3.23.

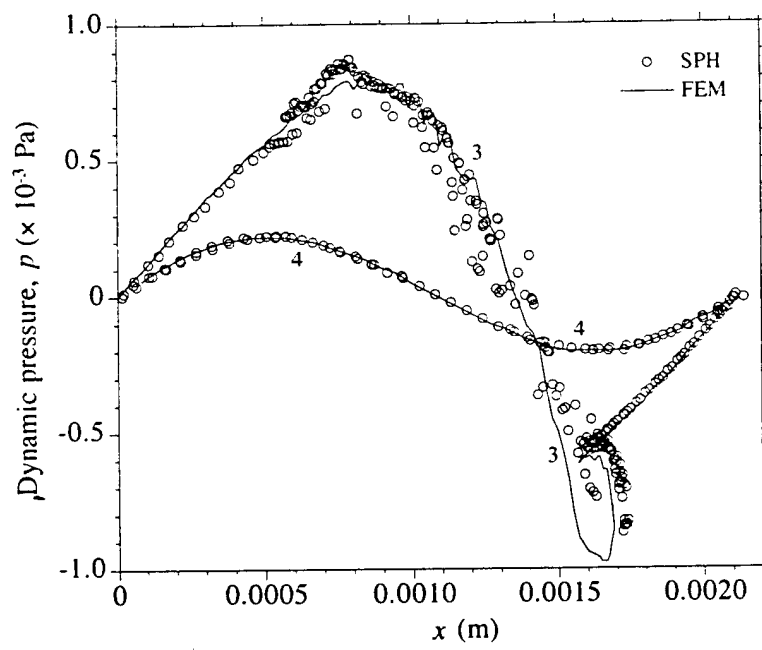


Figure 3.25: Comparison of SPH and FEM pressure profiles along paths 3 and 4 in Figure 3.23.

3.4.2.4 Flow Through Periodic Square and Hexagonal Lattices of Circular Cylinders

The SPH model was further used to simulate two-dimensional creeping flows of water ($\rho = 10^3 \frac{kg}{m^3}$, $\nu = 10^{-6} \frac{m^2}{s}$) through two spatially periodic porous media. The primary objective of the simulations was to verify the results of the model through a comparison with other available solutions in the literature. The media are composed of circular cylinders having radius R that are arranged in regular square and hexagonal lattices (Figures 3.11 and 3.13). For the square lattice, simulations were performed for $L = 1.2 mm$ and porosity $n = 0.3, 0.4, 0.5$, and 0.6 . The corresponding values of cylinder radius are $R = 0.566, 0.524, 0.479$, and $0.428 mm$, respectively. Simulations for the hexagonal lattice were performed for $L_1 = 1.2 mm$ and $n = 0.3, 0.4, 0.5$, and 0.6 . The corresponding values of cylinder radius for these simulations are $R = 0.527, 0.488, 0.446$, and $0.399 mm$, respectively. The cylinder diameters used in this study fall in the size range of medium sand. In particular, to have a better view about the SPH fluid particles, the unit cell chosen here for the square lattice is different from the one in Figure 3.11. The unit cells used in this section and the paths for comparison are shown in Figure 3.26.

During the course of a simulation, the cylinder drag force in the x direction, i.e., the direction of the applied body force, was also recorded in addition to v_x and $u_{x,max}$ every 100 time steps. The cylinder drag force in the x direction F_d is the sum of boundary particle forces upon the cylinder in that direction. A dimensionless drag force \bar{F}_d is defined as,

$$\bar{F}_d = \frac{F_d}{\mu v_x}. \quad (3.67)$$

The Reynolds number and Mach number of a flow are,

$$Re = \frac{2Rv_x}{\nu}, \quad (3.68)$$

and,

$$Ma = \frac{v_x}{c}, \quad (3.69)$$

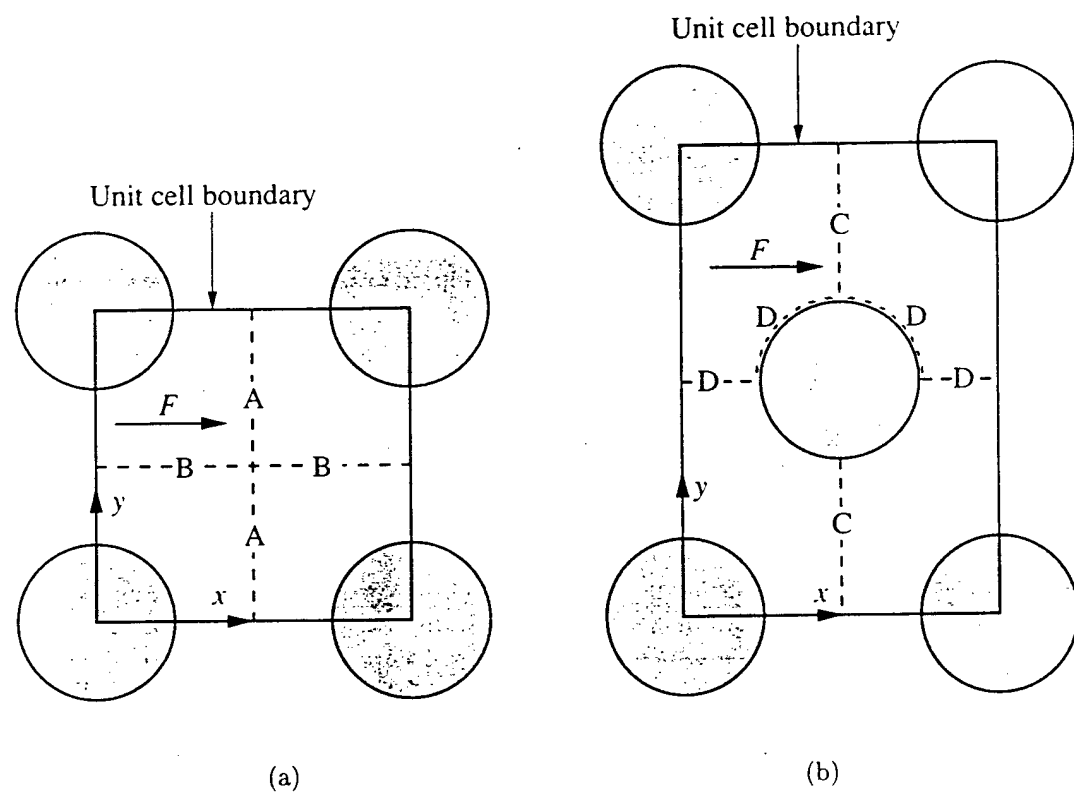


Figure 3.26: Paths for comparison of SPH and FEM solutions for flow through a periodic (a) square lattice, and (b) hexagonal lattice of circular cylinders.

respectively. Tables 3.1 and 3.2 present a summary of the results obtained for the steady state flows. The small values of Re correspond to creeping flow conditions and the small values of Ma indicate that each flow is quasi-incompressible.

For any SPH simulation, the fluid particles will eventually become disordered as they move through the flow domain. Due to the low Reynolds numbers, however, steady state conditions were achieved in a considerably shorter time for the numerical simulations in this study. The long-term performance of the model was investigated for each cylinder lattice for $n = 0.5$ and $F = 0.049 \frac{m}{s^2}$. The initial and final particle positions are shown in Figures 3.27 and 3.28 for the square and hexagonal lattices, respectively. The model was run for 39000 time steps for the square lattice and 27506

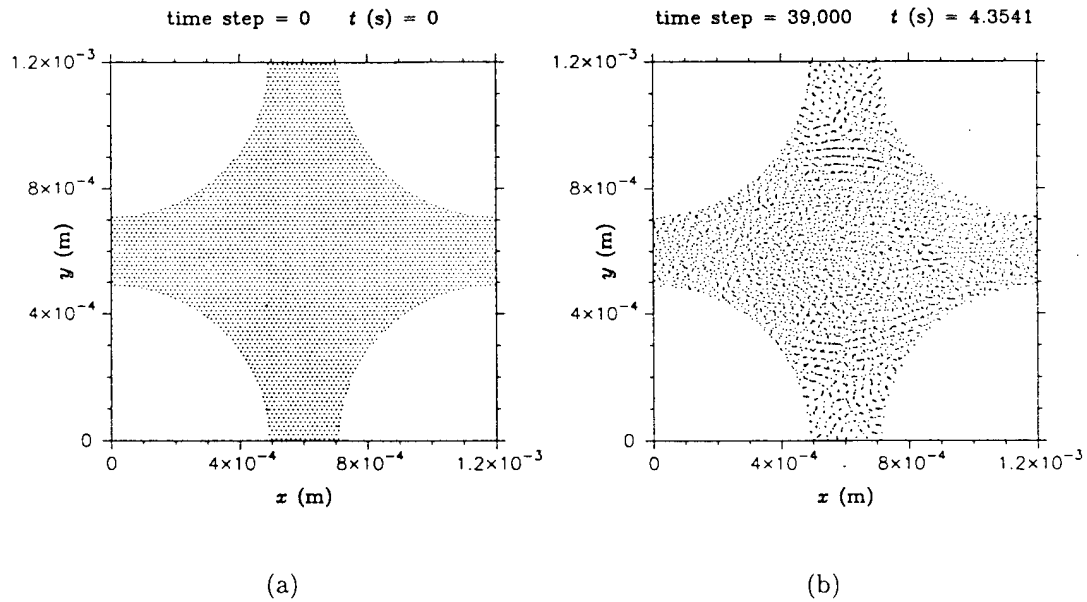


Figure 3.27: Particle positions for square lattice with $n = 0.5$ and $F = 0.049 \frac{m}{s^2}$ (a) initial positions, and (b) final positions. Fluid and boundary particles are shown in black and grey, respectively.

steps for the hexagonal lattice. In each case, the fluid particles were fully disordered at the end of the simulation. Figure 3.29 shows $u_{x,max}$ and \bar{F}_d as a function of time for each simulation. The values quickly reached steady state, and thereafter exhibited only minor fluctuations. The corresponding plot of Darcy velocity is shown in Figure

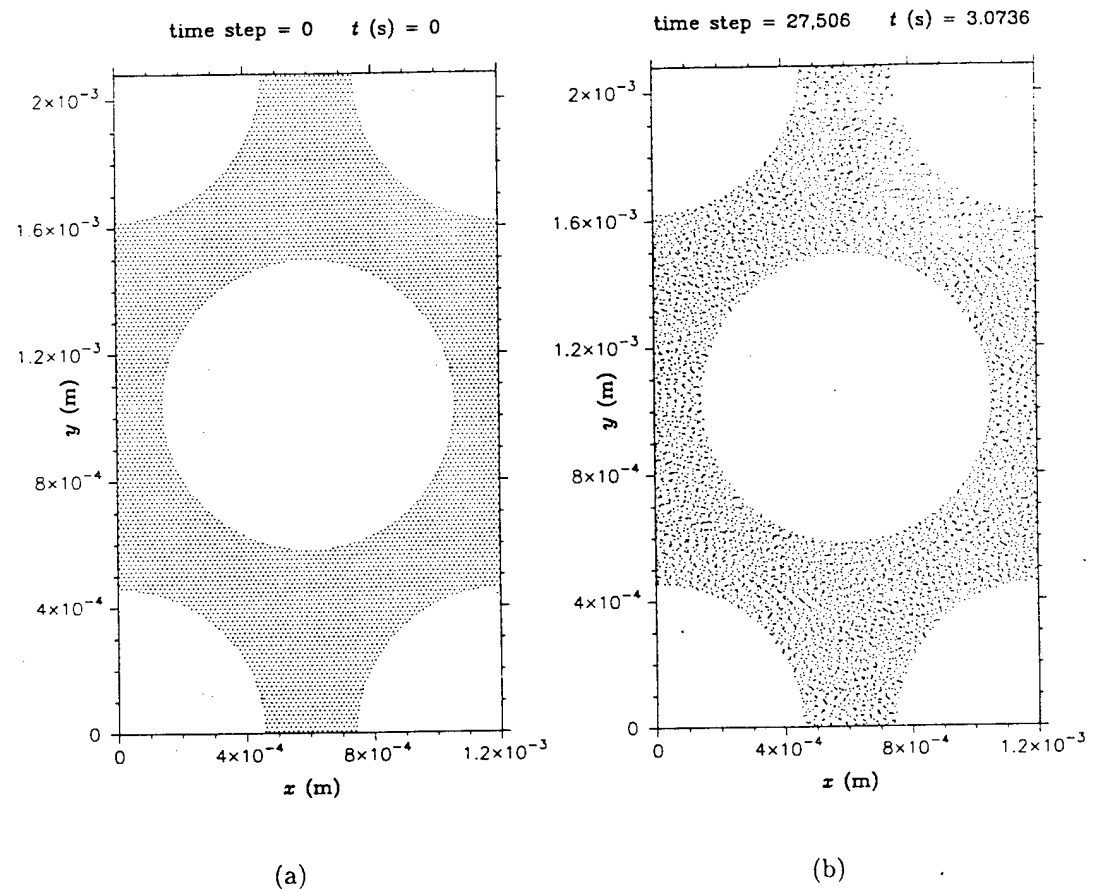


Figure 3.28: Particle positions for hexagonal lattice with $n = 0.5$ and $F = 0.049 \frac{m}{s^2}$
 (a) initial positions, and (b) final positions. Fluid and boundary particles are shown
 in black and grey, respectively.

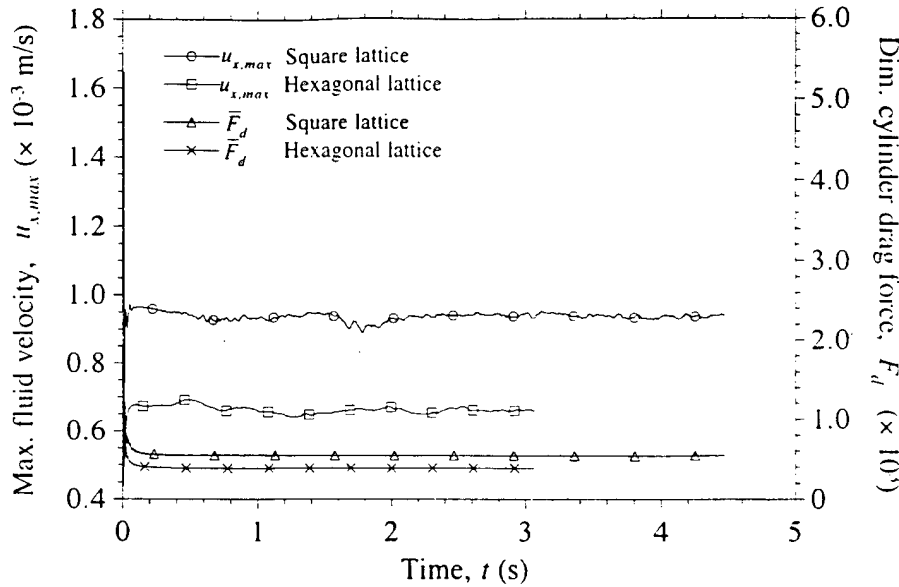


Figure 3.29: Maximum fluid velocity and dimensionless cylinder drag force versus time for square and hexagonal lattices ($n = 0.5$, $F = 0.049 \frac{m}{s^2}$).

3.30. Steady state Darcy velocity was also achieved quickly. Figures 3.29 and 3.30 illustrate that the model is numerically stable well after steady state conditions are reached. Each problem was also solved using FEM for steady incompressible viscous flow. In terms of computation time, SPH reached steady state faster than FEM for a similar number of particles and nodes. However, a much longer time was required for the SPH fluid particles to become fully disordered. Velocity and dynamic pressure distributions from the two methods are compared by plotting values within one nearest neighbor distance (Δx) of the four paths (A,B,C,D) shown in Figure 3.26. Figure 3.31 shows profiles of fluid velocity in the x direction and dynamic pressure for paths A and B, respectively, through the square lattice unit cell for $n = 0.5$ and $F = 0.049 \frac{m}{s^2}$. Corresponding plots for paths C and D through the hexagonal lattice unit cell are shown in Figure 3.32. For both lattices, the values are in close agreement with typical errors of about 5%. The plots show that the SPH results are less smooth than those obtained using the FEM. This “noise” is due to particles moving past each other, which is then amplified by the relatively stiff equation of state. In

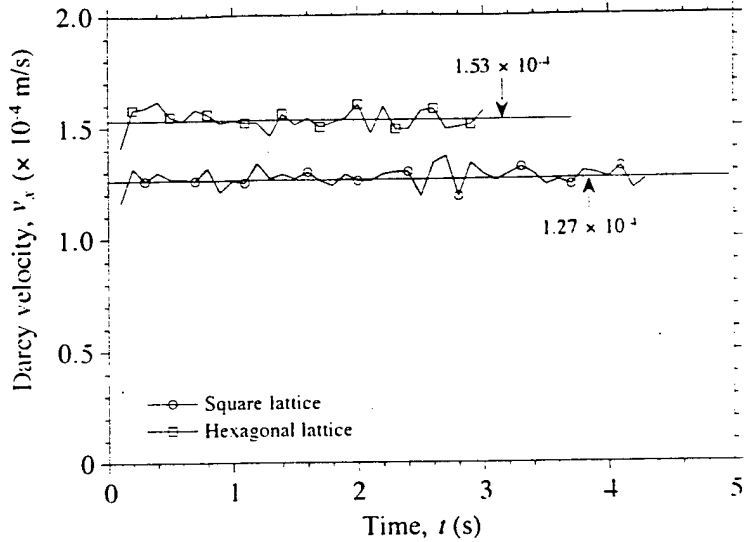
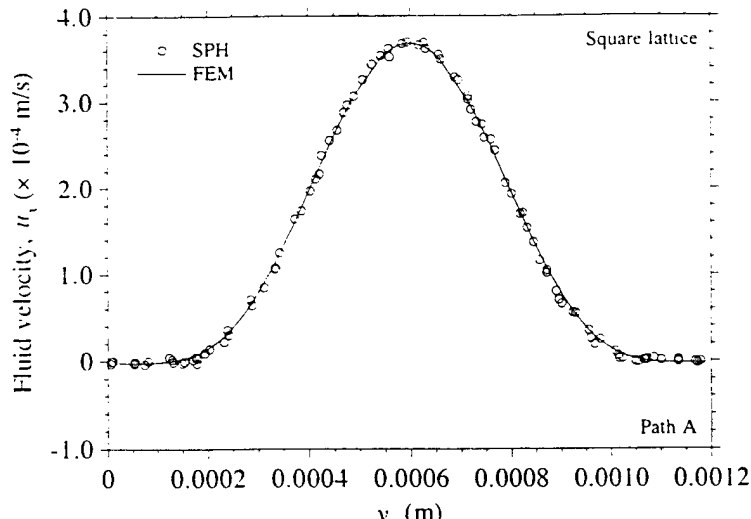


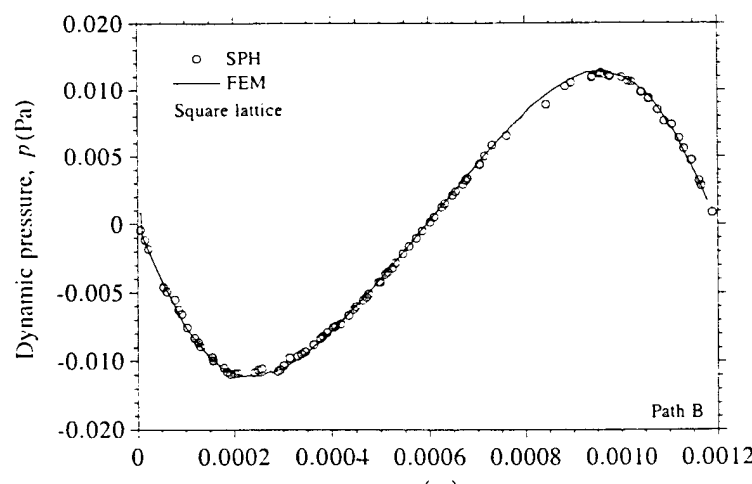
Figure 3.30: Darcy velocity versus time for square and hexagonal lattices ($n = 0.5$, $F = 0.049 \frac{m}{s^2}$).

general, values obtained using SPH show more variability as the compressibility of the fluid decreases. The plots also indicate that computed pressures for the hexagonal lattice are not fully realized near the stagnation points of the cylinders. This is consistent with the findings in the last few sections which showed that, at comparable resolutions, SPH does not fully capture pressure extrema on solid boundaries. The FEM better captures the extrema since grid-stretching increases resolution in the vicinity of a cylinder. The SPH and FEM solutions are, however, in close agreement for the bulk of the flow.

Four additional simulations were performed for each cylinder lattice for $n = 0.5$ and $F = 0.0392, 0.0245, 0.0098$, and $0.0049 \frac{m}{s^2}$. Figure 3.33 shows steady state Darcy velocity varies linearly with hydraulic gradient for each lattice, which is in agreement with Darcy's law. The computed values of hydraulic conductivity are $k_{Hx} = 0.0255 \frac{m}{s}$ for the square lattice and $k_{Hx} = 0.0307 \frac{m}{s}$ for the hexagonal lattice. At $n = 0.5$, the hexagonal lattice has a higher hydraulic conductivity than the square lattice because of the larger flow channels in the hexagonal lattice unit cell. Values of k_{Hx} are plotted



(a)



(b)

Figure 3.31: Comparison of SPH and FEM results for square lattice (a) velocity profile for path A, and (b) dynamic pressure profile for path B ($n = 0.5, F = 0.049 \frac{\text{m}}{\text{s}^2}$).

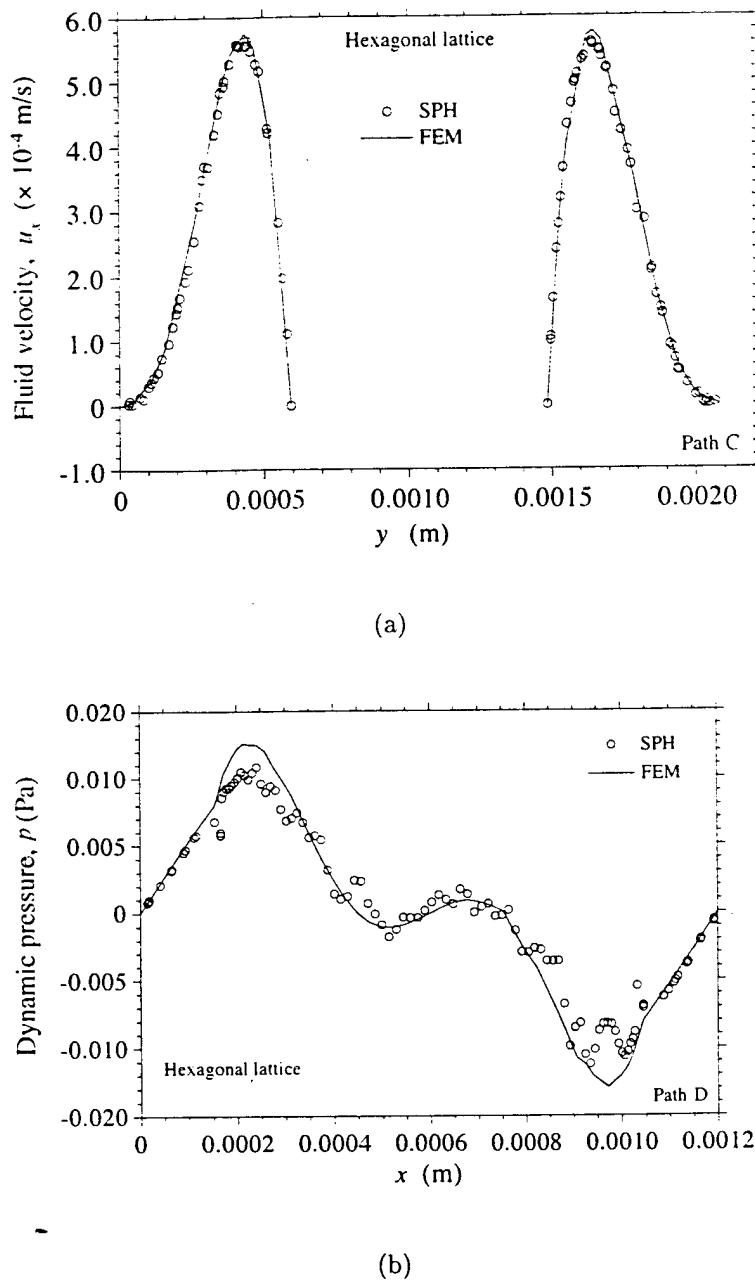


Figure 3.32: Comparison of SPH and FEM results for hexagonal lattice (a) velocity profile for path C, and (b) dynamic pressure profile for path D ($n = 0.5, F = 0.049 \frac{m}{s^2}$).

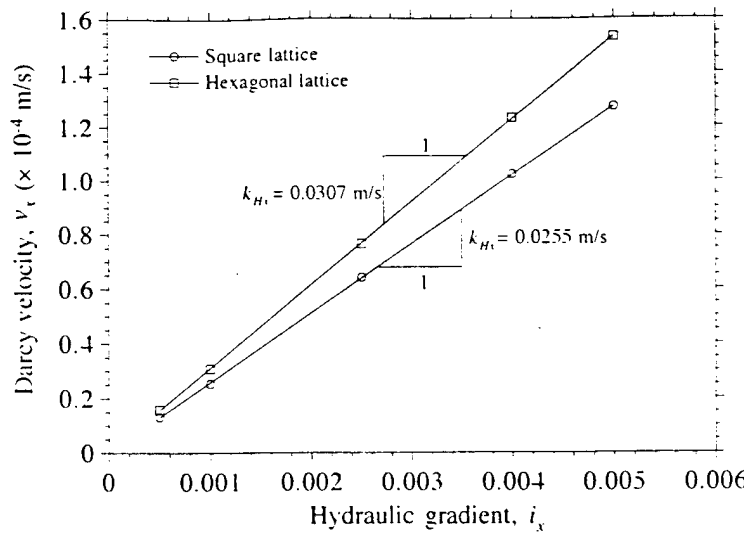


Figure 3.33: Darcy velocity versus hydraulic gradient for square and hexagonal lattices ($n = 0.5$).

as a function of n for both lattices in Figure 3.34. Noting the linearity of plots in Figure 3.33, values of k_{Hx} for media having porosities other than 0.5 were calculated using $F = 0.049 \frac{m}{s^2}$. As n increases, k_{Hx} increases for both lattices and the difference in k_{Hx} for the lattices decreases.

Values of $\frac{k_x}{R^2}$ and \bar{F}_d for each numerical simulation are shown as functions of porosity in Figure 3.35. Solutions obtained using FEM as well as published results from previous studies (Sangani and Acrivos 1982b; Sangani and Yao 1988b; Meegoda et al. 1989; Edwards et al. 1990; Ghaddar 1995), which were obtained for various values of R , are also shown for comparison. One additional solution has been included in Figure 3.35(a) for the square lattice at $n = 0.558$ for comparison with the data of Meegoda et al. (1989). Values are in good agreement with a maximum difference of 5%, indicating that SPH is capable of producing results that are comparable with those obtained using other methods. Figure 3.35 also indicates that $\frac{k_x}{R^2}$ is a unique function of n for each periodic lattice.

Recalling the definition of \bar{F}_d in Equation 3.67, Equation 2.106 leads to the following relation for the media considered in this work,

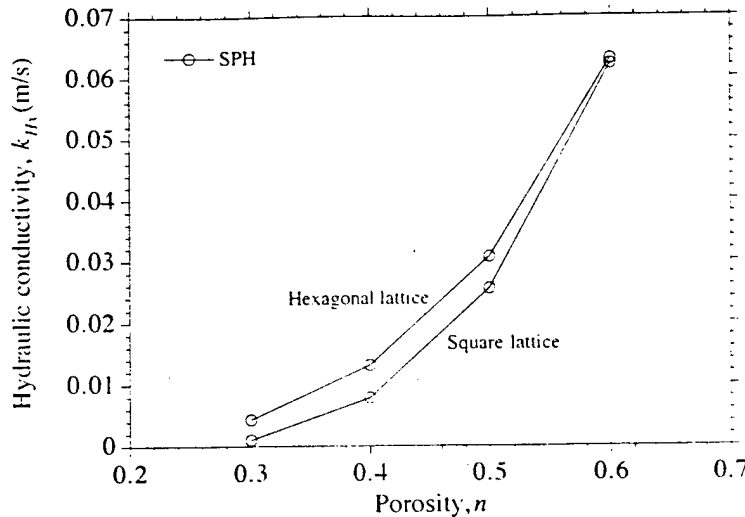


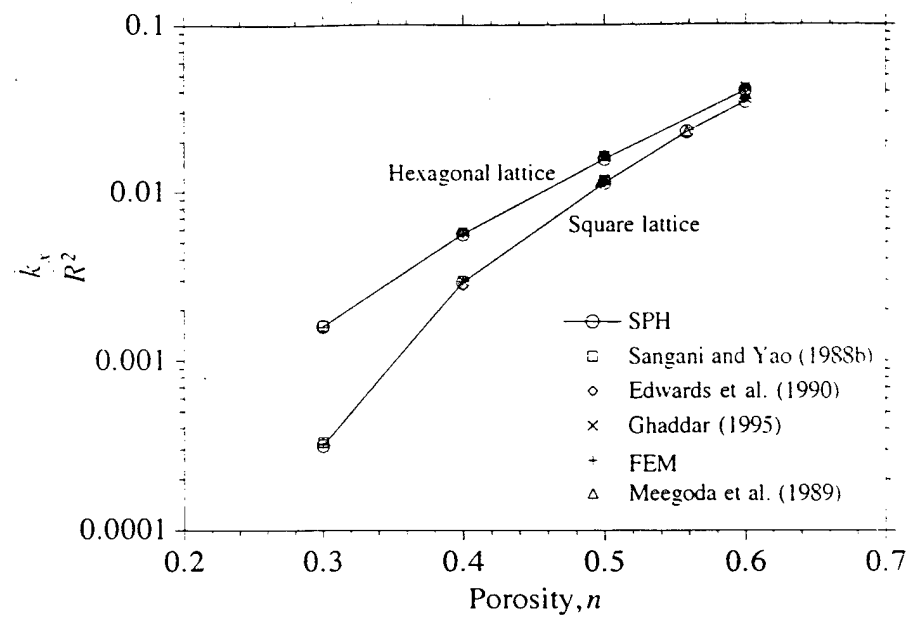
Figure 3.34: Hydraulic conductivity versus porosity for square and hexagonal lattices.

$$A_{\text{unit cell}} = n_s k_x \bar{F}_d, \quad (3.70)$$

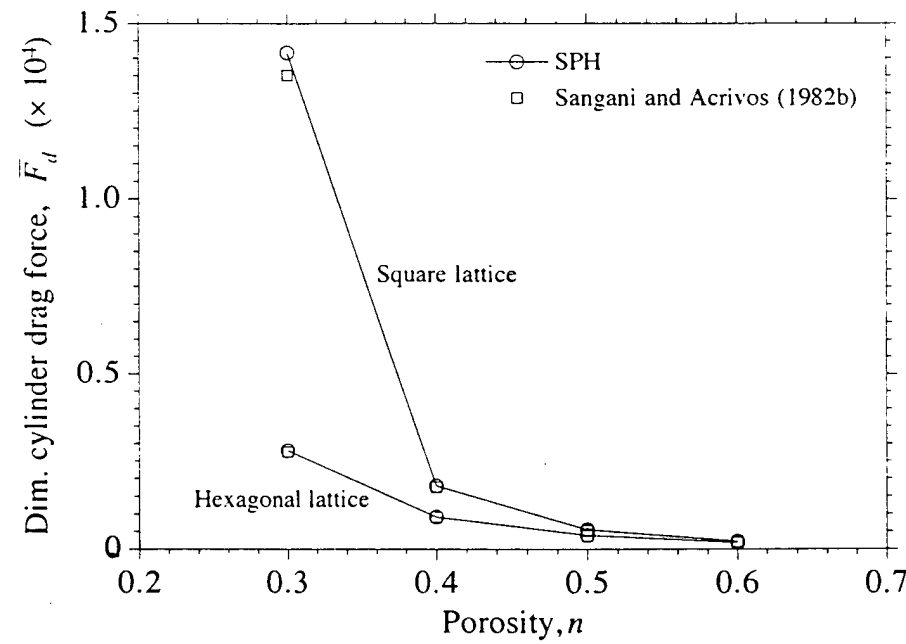
where n_s is the number of solid obstacles in the unit cell and $A_{\text{unit cell}}$ is the area of the unit cell. This relationship provides another independent check of SPH simulation results, which appears in Tables 3.3 and 3.4. It is evident that the maximum error of the SPH numerical results is about 6%.

3.5 Summary

Necessary extensions have been implemented and tested which allow SPH to model incompressible flow through porous media. Test results confirm that the proposed modifications to the equation of state, viscosity formulation, boundary conditions, and interpolation kernel result in a method which is stable and accurate. Simulations of flow through spatially periodic porous media show Darcy velocity proportional to hydraulic gradient, as required by Darcy's law. In addition, the solutions are in close agreement with values obtained using the finite element method and published solutions in the literature.



(a)



(b)

Figure 3.35: $\frac{k_x}{R^2}$ and dimensionless cylinder drag force versus porosity for square and hexagonal lattices (a) $\frac{k_x}{R^2}$, and (b) dimensionless cylinder drag force.

Table 3.1: Summary of results for flow simulations through square lattice.

Simulation	n	R (mm)	N_{part}	F ($\frac{m}{s^2}$)	i	c ($\frac{m}{s}$)	v_x ($\frac{m}{s}$)	k_{Hx} ($\frac{m}{s}$)	k_x (m^2)	\bar{F}_d	Re	Ma
1	0.6	0.428	4344	0.049	0.005	0.045	3.11×10^{-4}	0.0621	6.31×10^{-9}	214	0.2662	0.0069
2	0.5	0.479	6394	0.049	0.005	0.045	1.27×10^{-4}	0.0255	2.60×10^{-9}	547	0.1217	0.0028 ϵ
3	0.5	0.479	6394	0.0392	0.004	0.04	1.02×10^{-4}	0.0256	2.61×10^{-9}	541	0.0977	0.00255
4	0.5	0.479	6394	0.0245	0.0025	0.032	6.40×10^{-5}	0.0256	2.61×10^{-9}	543	0.0613	0.002
5	0.5	0.479	6394	0.0098	0.001	0.02	2.53×10^{-5}	0.0253	2.58×10^{-9}	548	0.0242	0.00127
6	0.5	0.479	6394	0.0049	0.0005	0.014	1.32×10^{-5}	0.0264	2.69×10^{-9}	535	0.0126	0.00094
7	0.4	0.524	16006	0.049	0.005	0.045	3.91×10^{-5}	0.00782	7.98×10^{-10}	1790	0.041	0.00087
8	0.3	0.566	43156	0.049	0.005	0.045	4.96×10^{-6}	0.000992	1.01×10^{-10}	14165	0.0056	0.00011

Table 3.2: Summary of results for flow simulations through hexagonal lattice.

Simulation	n	R (μm)	N_{part}	F ($\frac{m}{s^2}$)	i	c ($\frac{m}{s}$)	v_x ($\frac{m}{s}$)	k_{Hx} ($\frac{m}{s^2}$)	k_x (m^2)	\bar{F}_d	Re	Ma
1	0.6	0.399	7700	0.049	0.005	0.045	3.15×10^{-4}	0.063	6.43×10^{-9}	185	0.2514	0.007
2	0.5	0.446	11440	0.049	0.005	0.045	1.53×10^{-4}	0.0307	3.13×10^{-9}	393	0.1365	0.00341
3	0.5	0.446	11440	0.0392	0.004	0.04	1.23×10^{-4}	0.0308	3.14×10^{-9}	387	0.1097	0.00308
4	0.5	0.446	11440	0.0245	0.0025	0.032	7.65×10^{-5}	0.0306	3.12×10^{-9}	391	0.0682	0.00239
5	0.5	0.446	11440	0.0098	0.001	0.02	3.08×10^{-5}	0.0308	3.14×10^{-9}	390	0.0275	0.00154
6	0.5	0.446	11440	0.0049	0.0005	0.014	1.58×10^{-5}	0.0315	3.21×10^{-9}	379	0.0141	0.00113
7	0.4	0.488	19824	0.049	0.005	0.045	6.56×10^{-5}	0.0131	1.34×10^{-9}	904	0.064	0.00146
8	0.3	0.527	24656	0.049	0.005	0.045	2.18×10^{-5}	0.00435	4.44×10^{-10}	2795	0.023	0.00048

Table 3.3: Check of results for flow simulations through square lattice using Equation 3.70.

Simulation	n_s	$k_x (m^2)$	\bar{F}_d	$A_{unit\ cell}$ from Equation 3.70 (m^2)	Actual $A_{unit\ cell} (m^2)$	error
1	1	6.34×10^{-9}	214	1.3568	1.44	-5.78%
2	1	2.60×10^{-9}	547	1.4222	1.44	-1.24%
3	1	2.61×10^{-9}	541	1.4120	1.44	-1.94%
4	1	2.61×10^{-9}	543	1.4172	1.44	-1.58%
5	1	2.58×10^{-9}	548	1.4138	1.44	-1.82%
6	1	2.69×10^{-9}	535	1.4392	1.44	-0.06%
7	1	7.98×10^{-10}	1790	1.4284	1.44	-0.80%
8	1	1.01×10^{-10}	14165	1.4307	1.44	-0.65%

Table 3.4: Check of results for flow simulations through hexagonal lattice using Equation 3.70.

Simulation	n_s	$k_x (m^2)$	\bar{F}_d	$A_{unit\ cell}$ from Equation 3.70 (m^2)	Actual $A_{unit\ cell} (m^2)$	error
1	2	6.43×10^{-9}	185	2.3791	2.4942	-4.61%
2	2	3.13×10^{-9}	393	2.4602	2.4942	-1.36%
3	2	3.14×10^{-9}	387	2.4304	2.4942	-2.56%
4	2	3.12×10^{-9}	391	2.4398	2.4942	-2.18%
5	2	3.14×10^{-9}	390	2.4492	2.4942	-1.80%
6	2	3.21×10^{-9}	379	2.4332	2.4942	-2.44%
7	2	1.34×10^{-9}	904	2.4227	2.4942	-2.86%
8	2	4.44×10^{-10}	2795	2.4820	2.4942	-0.49%

CHAPTER 4 DEVELOPMENT, VERIFICATION, AND APPLICATION OF A PORE-SCALE DIFFUSION MODEL USING SMOOTHED PARTICLE HYDRODYNAMICS

In this chapter, the method of SPH is formulated to solve the convection-diffusion equation to model tracer diffusion through porous media. Solutions obtained using SPH are compared with other solutions and the model is used to calculate diffusion coefficients of spatially periodic porous media for the steady state diffusion problem. Diffusion coefficients are then used to calculate nondimensional diffusivities of the media. The effects of media properties on the values of nondimensional diffusivity are also studied.

4.1 Model Establishment for Pore-Scale Diffusion Problem

For the tracer diffusion problem, concentration C becomes a property associated with SPH particles in addition to mass m and density ρ . If the convection-diffusion equation (Equation 2.57) is rewritten as,

$$\frac{dC}{dt} = d_0 \nabla^2 C = \frac{d_0 \rho}{\rho} \nabla^2 C, \quad (4.1)$$

it becomes evident that the method used to treat viscosity (Equation 3.33) can be adopted to evolve tracer concentration,

$$\frac{dC_a}{dt} = \left(\frac{d_0 \rho}{\rho} \nabla^2 C \right)_a = \sum_b \frac{m_b (d_{0,a} \rho_a + d_{0,b} \rho_b) \mathbf{r}_{ab} \cdot \nabla_a W_{ab}}{\rho_a \rho_b (\mathbf{r}_{ab}^2 + 0.01 h^2)} C_{ab}, \quad (4.2)$$

where,

$$C_{ab} = C_a - C_b. \quad (4.3)$$

Accordingly, the time step for the integration scheme is limited by,

$$\tau \leq 0.125 \frac{h^2}{d_0}. \quad (4.4)$$

The following predictor-corrector equations are used to obtain particle concentrations at the next time step,

$$\tilde{C}^{\frac{1}{2}} = C^0 + \frac{\tau}{2} f_C^0, \quad (4.5)$$

$$f_C^{\frac{1}{2}} = f(m, \tilde{x}^{\frac{1}{2}}, \tilde{\rho}^{\frac{1}{2}}, \tilde{C}^{\frac{1}{2}}, \dots), \quad (4.6)$$

$$C^{\frac{1}{2}} = C^0 + \frac{\tau}{2} f_C^{\frac{1}{2}}, \quad (4.7)$$

$$C^1 = 2C^{\frac{1}{2}} - C^0, \quad (4.8)$$

where f_C is the rate of change of concentration in time. As in the flow problem, the predictor step uses the value of f_C at the previous midpoint (i.e., $f_C^0 = f_C^{-\frac{1}{2}}$).

The impenetrable solid boundary condition (Equation 2.131) locally requires $\frac{\partial C}{\partial \mathbf{n}} = 0$, which could be achieved by assigning an appropriate artificial concentration for each boundary particle. However, this approach may not prevent solute mass from diffusing into the solid phase in a global sense. In this model, the impenetrable solid boundary condition is easily implemented by allowing the exchange of solute mass only between fluid particles.

4.2 Calculation of Diffusion Coefficients of Porous Media Using SPH

A steady state diffusion problem is solved using SPH to illustrate the calculation of diffusion coefficients for spatially periodic porous media (Figure 4.1). Faces $x = x_1$ and $x = x_2$ of the medium are maintained at constant concentrations C_1 and C_2 , respectively, with $C_1 > C_2$. As a consequence of the concentration difference $C_1 - C_2$, a steady state flow of solute mass necessarily occurs across the medium. If the molecular diffusion coefficient d_0 is assumed to be constant, that is, independent of local concentration C and position \mathbf{R} , it is expected on a physical basis that the concentration, averaged at a length scale greater than the size of the unit cell, will decrease linearly across the medium. This linear behavior would be obtained for a

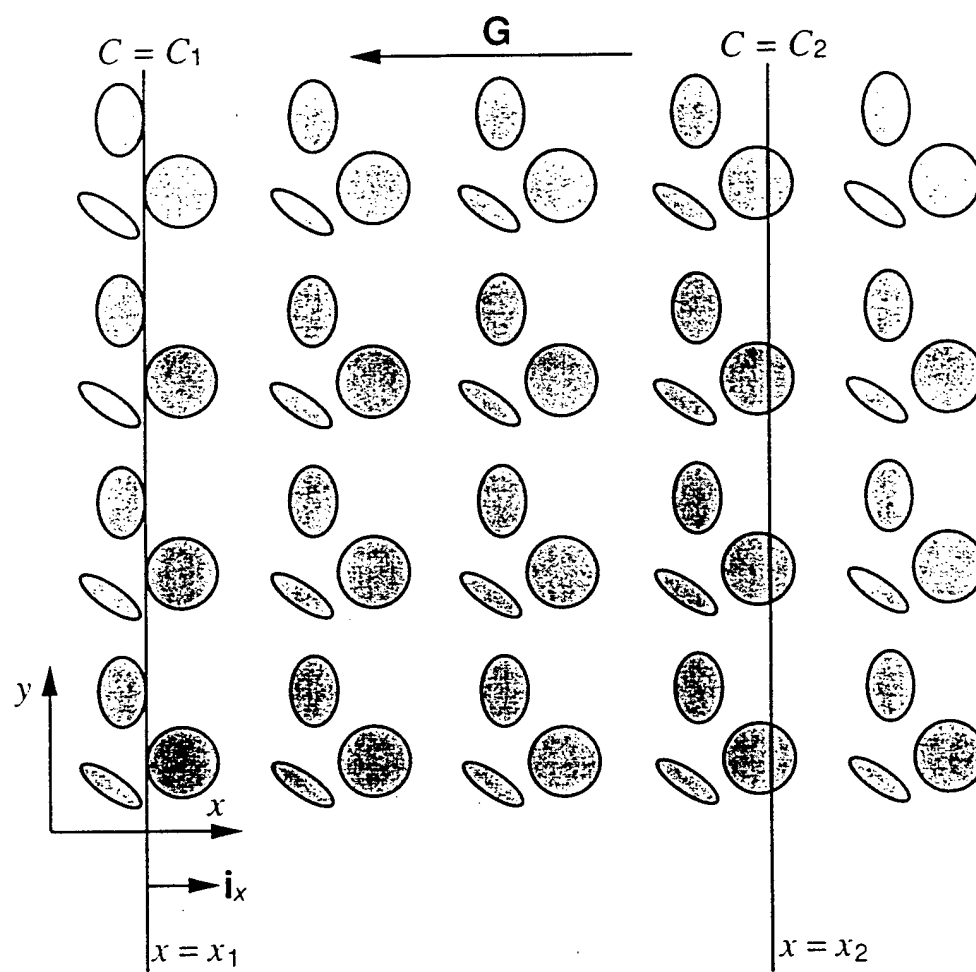


Figure 4.1: Steady state diffusion through a spatially periodic porous medium.

homogeneous medium under the same conditions. Hence, a constant macroscopic concentration gradient \mathbf{G} is introduced as,

$$\mathbf{G} = \frac{C_2 - C_1}{x_2 - x_1} \mathbf{i}_x, \quad (4.9)$$

where \mathbf{i}_x is a unit vector pointing in the positive x direction. The constant macroscopic concentration gradient and the periodicity of the medium inevitably lead to a fundamental hypothesis that the local concentration gradient ∇C is also spatially periodic with the same periodicity as the porous medium (Adler 1992), i.e.,

$$\nabla C(\mathbf{R}) = \nabla C(\mathbf{R} + \mathbf{R}_n), \quad (4.10)$$

which results in,

$$C(\mathbf{R}) = \check{C}(\mathbf{R}) + \mathbf{G} \cdot \mathbf{R}, \quad (4.11)$$

where \check{C} is the spatially periodic component of the concentration field.

Based on above concepts, a steady state diffusion problem can be solved within a unit cell of a spatially periodic porous medium. Thus, the SPH concentration field can be used to determine the diffusion coefficients of the medium. For a two-dimensional anisotropic porous medium (Figure 4.2), Equations 2.59 and 2.60 lead to,

$$j_x = -d_{xx} \frac{\partial C}{\partial x} - d_{xy} \frac{\partial C}{\partial y}, \quad (4.12)$$

and,

$$j_y = -d_{yx} \frac{\partial C}{\partial x} - d_{yy} \frac{\partial C}{\partial y}, \quad (4.13)$$

where j_x and j_y are mass fluxes in x and y directions, respectively. If a concentration gradient $\frac{dC}{dx}$ is imposed in the x direction only (Figure 4.2(a)), these equations become,

$$j_x = -d_{xx} \frac{dC}{dx}, \quad (4.14)$$

and,

$$j_y = -d_{yx} \frac{dC}{dx}. \quad (4.15)$$

In this case, j_x and j_y are evaluated from the discrete SPH fluid particles as,

$$j_x = -d_0 \frac{\sum_a \frac{\partial C_a}{\partial x} \frac{m_a}{\rho_a}}{\sum_a \frac{m_a}{\rho_a}}, \quad (4.16)$$

and,

$$j_y = -d_0 \frac{\sum_a \frac{\partial C_a}{\partial y} \frac{m_a}{\rho_a}}{\sum_a \frac{m_a}{\rho_a}}, \quad (4.17)$$

where $\frac{\partial C_a}{\partial x}$ and $\frac{\partial C_a}{\partial y}$ are the local concentration gradients in x and y directions, respectively, at particle a . Values of d_{xx} and d_{yy} are obtained from Equations 4.14 to 4.17. If another concentration gradient $\frac{dC}{dy}$ is imposed in the y direction only (Figure 4.2(b)), the same procedure leads to values of d_{xy} and d_{yy} .

In SPH, the local concentration gradient ∇C_a is evaluated as,

$$\nabla C_a = \sum_b \frac{m_b}{\rho_b} C_{ba} \nabla_a W_{ab}. \quad (4.18)$$

If particle a is close to a solid inclusion, the absence of particle concentrations within the inclusion has to be taken into account. To do this, Equation 4.18 is used to obtain an intermediate estimate $(\nabla C_a)^*$,

$$(\nabla C_a)^* = \sum_b \frac{m_b}{\rho_b} C_{ba} \nabla_a W_{ab}, \quad (4.19)$$

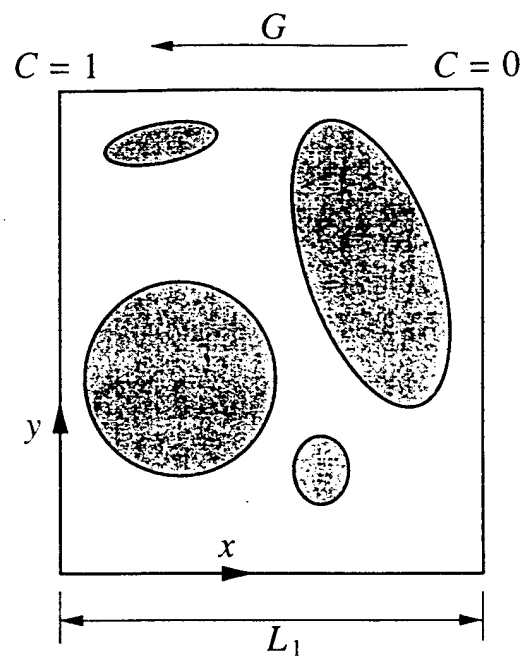
which is then corrected by a factor C_a ,

$$\nabla C_a = (\nabla C_a)^*/C_a, \quad (4.20)$$

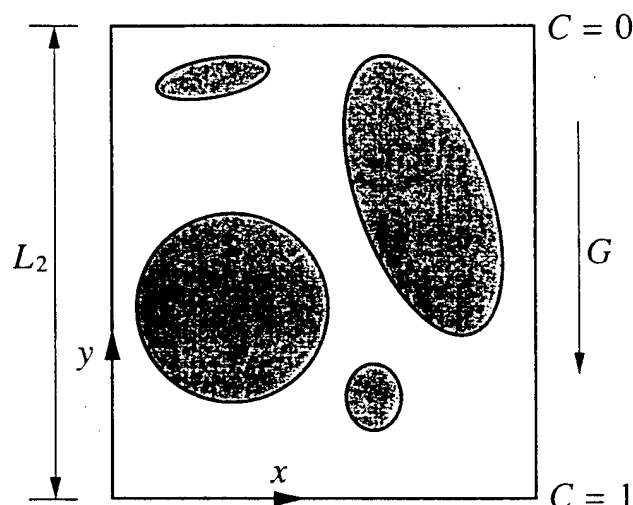
where,

$$C_a = \sum_b \frac{m_b}{\rho_b} W_{ab}. \quad (4.21)$$

C_a reflects the local number density of fluid particles contributing to the concentration at particle a . Similar approaches have been used to improve the accuracy of first



(a)



(b)

Figure 4.2: Problem geometries to determine diffusion coefficients of an anisotropic porous medium (a) a concentration gradient is imposed in the x direction, and (b) a concentration gradient is imposed in the y direction.

derivatives (Randles and Libersky 1996) and calculation of surface tension force (Morris 1999) and can be derived within the formalism of element free Galerkin methods (Belytschko et al. 1996).

The diffusion coefficients of a porous medium depend on both medium properties and the molecular diffusion coefficient of the interstitial fluid d_0 . The influence of d_0 is separated out by defining the nondimensional diffusivity d^* (Equation 2.58) and \mathbf{d}^* (Equation 2.61) for isotropic and anisotropic porous media, respectively. These values are functions of the media only.

4.3 Model Initialization and Execution

4.3.1 Initialization

For each simulation, fluid and boundary particles are initialized in the same way as for the flow problems described in Chapter 3. Since SPH fluid particles do not move for a pure diffusion simulation, particle velocities are not computed. This also results in a constant density field and the same neighboring particles for every SPH particle throughout a simulation.

After positioning fluid and boundary particles, linked lists are created for the particles and the density field is recalculated. The linked lists and density field remain unchanged thereafter (i.e., $\tilde{x}^{\frac{1}{2}} = x^0$ and $\tilde{\rho}^{\frac{1}{2}} = \rho^0$ in Equation 4.6). For the problem in Figure 4.2(a), concentrations on the left and right edges of the unit cell are assigned to be 1 and 0, respectively, resulting in a concentration gradient of $\frac{1}{L_1}$. For the problem in Figure 4.2(b), concentrations on the bottom and top edges of the unit cell are assigned to be 1 and 0, respectively, resulting in a concentration gradient of $\frac{1}{L_2}$. To expedite the solution, the concentration field in the computational domain is initialized according to the imposed macroscopic concentration gradient.

4.3.2 Execution

Once the concentration field is initialized, rates of change of particle concentrations are computed using Equation 4.2. The quintic spline kernel is employed and the smoothing length h is chosen equal to $2\Delta x$. The time step is limited according to Equation 4.4. Concentrations are updated using the predictor-corrector method described by Equations 4.5 to 4.8. The impenetrable solid boundary condition is implemented by allowing the exchange of solute mass only between fluid particles.

Image particles and solid inclusions are created within a distance of $3h$ (i.e., one quintic kernel radius) from the unit cell to provide the necessary “neighbors” for particles within the cell (Figure 3.5). Concentrations of the image fluid particles are updated according to Equation 4.11 to maintain the imposed concentration gradient.

Values of particle concentrations are recorded periodically during the course of a simulation to determine the diffusion coefficients of the porous medium. Changes in these values with time are used to determine whether or not the diffusion process has reached steady state.

4.4 Diffusion Model Verification

The SPH diffusion model has been tested for many cases. Simulations using the method show excellent agreement with analytical solutions for diffusion in aqueous solution and close agreement with other solutions for diffusion through a regular lattice of obstacles.

4.4.1 Simulations of Diffusion in Aqueous Solution

Two cases of diffusion in a pure aqueous solution with a molecular diffusion coefficient of $d_0 = 10^{-10} \frac{m^2}{s}$ were simulated using SPH. Figure 4.3 shows the geometry for one-dimensional diffusion of a substance initially confined to the region $-h \leq x \leq +h$. The analytical solution for the values of concentration as a function of time and position is (Crank 1975),

$$C = \frac{1}{2} C_0 \left(\operatorname{erf} \left(\frac{h-x}{2\sqrt{d_0 t}} \right) + \operatorname{erf} \left(\frac{h+x}{2\sqrt{d_0 t}} \right) \right), \quad (4.22)$$

where erf is the error function defined as.

$$\operatorname{erf}(z) = \frac{2}{\pi^{\frac{1}{2}}} \int_0^z \exp(-\eta^2) d\eta. \quad (4.23)$$

Figure 4.4 shows a comparison between the normalized concentration ($\frac{C}{C_0}$) profiles obtained using Equation 4.22 and SPH for $h = 0.0004 \text{ m}$ at several times. The SPH solution was obtained with 20 particles spanning the distance h . The maximum error of SPH is about 0.5%, confirming the accuracy of the approach.

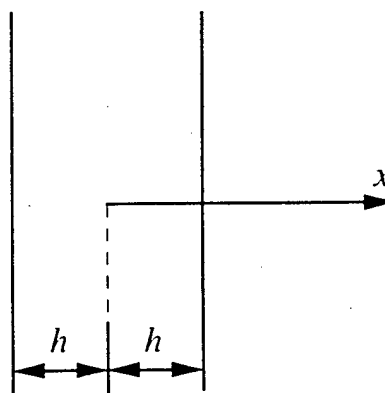


Figure 4.3: Geometry for one-dimensional diffusion in an aqueous solution.

Figure 4.5 shows the geometry for the diffusion of a substance initially confined in a circular area of radius R (i.e., diffusion due to an instantaneous cylindrical source). The analytical solution for the values of concentration as a function of time and position is (Crank 1975),

$$C = \frac{C_0}{2d_0 t} \exp \left(-\frac{r^2}{4d_0 t} \right) \int_0^R \exp \left(-\frac{x^2}{4d_0 t} \right) I_0 \left(\frac{rx}{2d_0 t} \right) x dx, \quad (4.24)$$

where I_0 is the modified Bessel function of the first kind of order zero. Figure 4.6 shows a comparison between the normalized concentration ($\frac{C}{C_0}$) profiles obtained using Equation 4.24 and SPH for $R = 0.0005 \text{ m}$ at several times. The SPH solution was obtained with 25 particles spanning the distance R . Again, the results are in excellent agreement with a maximum error of about 0.5%.

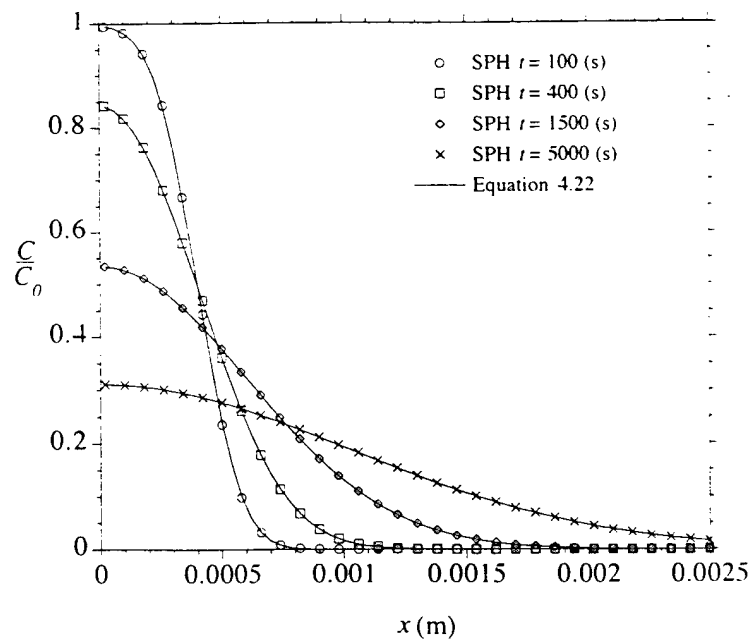


Figure 4.4: Normalized concentration versus distance for one-dimensional diffusion in an aqueous solution.

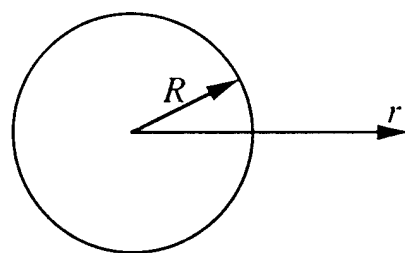


Figure 4.5: Geometry for two-dimensional diffusion in an aqueous solution.

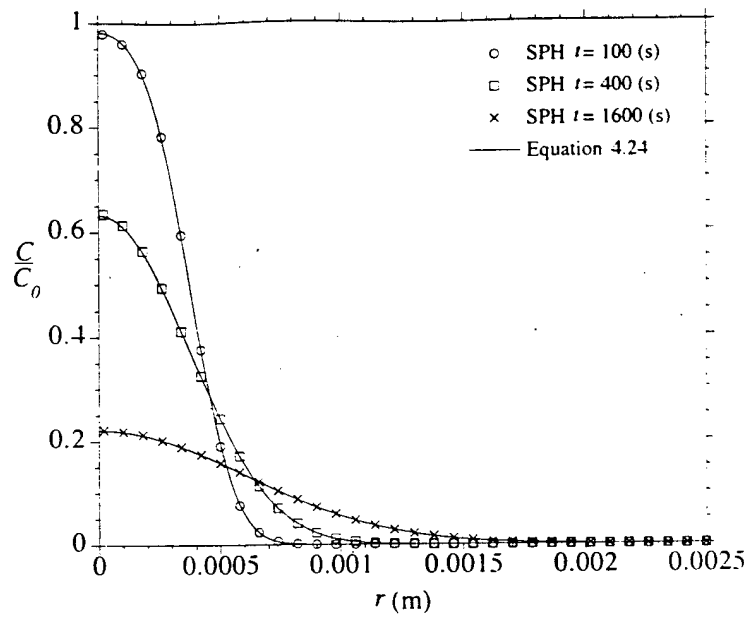
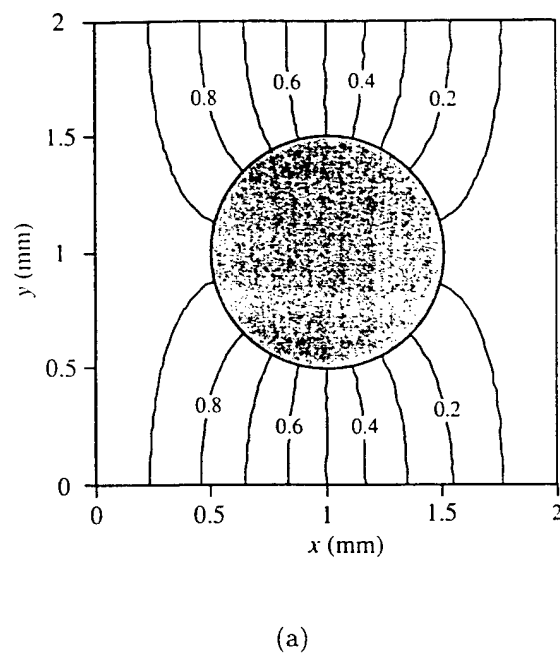


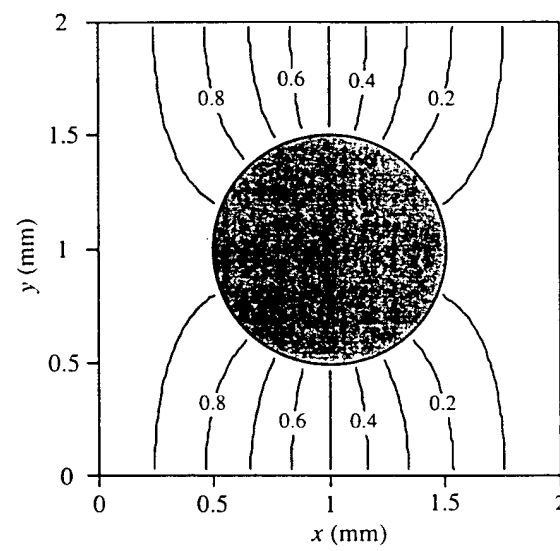
Figure 4.6: Normalized concentration versus distance for an instantaneous cylindrical diffusion source.

4.4.2 Simulations of Diffusion Through Periodic Lattices of Obstacles

A more challenging test of the method involves diffusion through obstacles arranged in a periodic lattice. Steady state diffusion through a square lattice of circular cylinders was simulated using SPH for $d_0 = 10^{-10} \frac{m^2}{s}$, $L = 2 \text{ mm}$, and $R = 0.5 \text{ mm}$. A solution for the same problem was also obtained using a FEM program. The results from both solutions are compared in Figure 4.7. Another comparison appears in Figure 4.8 to confirm the ability of the model to treat elliptical inclusions. The latter problem was solved for $d_0 = 10^{-10} \frac{m^2}{s}$, $L = 2 \text{ mm}$, $a = 0.8 \text{ mm}$, $\frac{a}{b} = 2$, and $\alpha = 45^\circ$. Good agreement is obtained for the bulk of the void space in both cases.

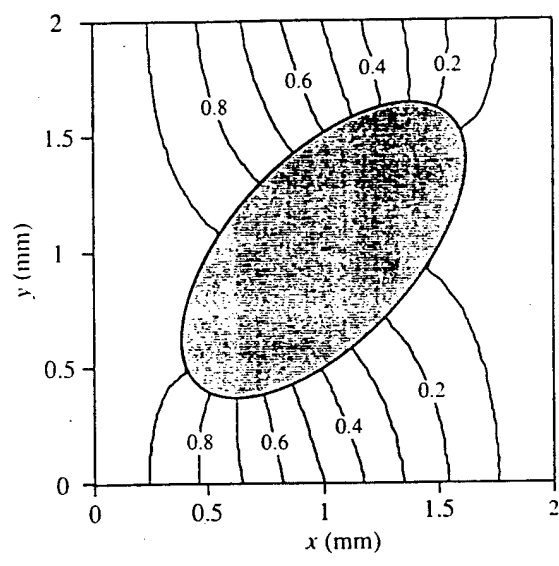


(a)

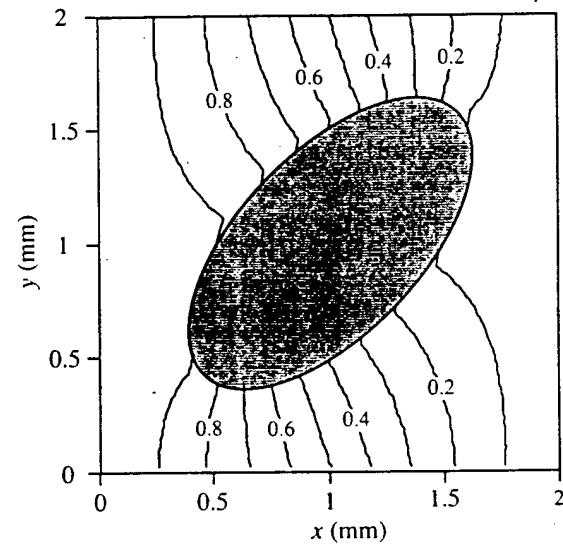


(b)

Figure 4.7: Contour plots of concentration using (a) FEM, and (b) SPH for a square array of circular cylinders.



(a)



(b)

Figure 4.8: Contour plots of concentration using (a) FEM, and (b) SPH for a square array of elliptical cylinders.

4.4.3 Simulations of Diffusion Through Composite Media

If the solid phase is assigned a non-zero molecular diffusion coefficient (i.e., the solid inclusion is penetrable in terms of tracer diffusion), effective diffusion coefficients for diffusion through the resulting composite medium can be calculated. To do this, SPH boundary particles are treated as fluid particles having a different diffusion coefficient. In this case, boundary particles must span the entirety of solid inclusion, not only an annular region from the solid surface. The problem of calculating composite-media diffusion coefficients dates back to the classical studies of Maxwell (1873) and Rayleigh (1892). Perrins et al. (1979) furnished a complete theoretical solution of the effective conductivity problem for circular cylinders in square and hexagonal arrays by extending the method of Rayleigh (1892). Table 4.1 shows the comparison between the values of nondimensional diffusivity d^* obtained using SPH and published by Perrins et al. (1979) for square arrays of circular cylinders (Figure 4.9). The solutions are in close agreement with a maximum difference of about 5.5%. The SPH solutions approach the values of Perrins et al. (1979) as the resolution (i.e., number of particles N_{part}) increases.

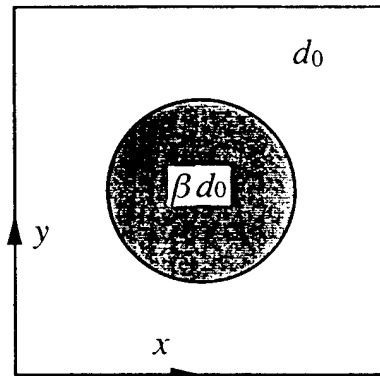


Figure 4.9: Unit cell of a square array of circular cylinders. The interstitial phase has a diffusion coefficient of d_0 and the cylinder has a diffusion coefficient of βd_0 .

Table 4.1: Values of d^* for composite media.

porosity	β	N_{part}	SPH solution	Perrins et al. (1979)	difference
0.6	2	11600	1.3136	1.3080	+0.43%
0.6	2	46000	1.3120	1.3080	+0.31%
0.6	5	11600	1.7785	1.7307	+2.76%
0.6	5	46000	1.7568	1.7307	+1.51%
0.6	10	11600	2.0900	1.9806	+5.52%
0.6	10	46000	2.0370	1.9806	+2.85%
0.4	2	46000	1.5076	1.5028	+0.32%
0.4	5	46000	2.4251	2.3744	+2.14%
0.4	10	46000	3.1796	3.0372	+4.69%

4.5 Diffusion Model Application

The steady state diffusion problem was solved using SPH for spatially periodic porous media with circular and elliptical cylinders arranged in square, staggered, and hexagonal arrays. Diffusion coefficients were obtained from the steady state concentration fields, and then used to calculate values of nondimensional diffusivity d^* . The effects of specific surface area S_0 , porosity n , anisotropy, and cylinder arrangement on the values of d^* are presented. A total of 154 simulations were completed with a molecular diffusion coefficient of the interstitial fluid $d_0 = 10^{-10} \frac{m^2}{s}$. Impenetrable solid boundary condition applies for all simulations in this section (i.e., $\beta = 0$). The SPH simulation results are summarized in Tables 4.2 and 4.3.

Table 4.2: Summary of results for diffusion simulations with circular cylinders.

simulation	$S_0 (\frac{1}{m})$	n	$R (mm)$	N_{part}	d^*
square array:					
sq1	2000	0.9	1.0	6938	0.8978
sq2	4000	0.9	0.5	6938	0.8978
sq3	20000	0.9	0.1	6938	0.8978
sq4	4000	0.8	0.5	3384	0.8144
sq5	4000	0.7	0.5	6484	0.7536
sq6	2000	0.6	1.0	9984	0.6968
sq7	4000	0.6	0.5	9984	0.6968
sq8	20000	0.6	0.1	9984	0.6968
sq9	4000	0.5	0.5	9182	0.6339
sq10	2000	0.4	1.0	25806	0.5648
sq11	4000	0.4	0.5	25806	0.5648
sq12	20000	0.4	0.1	25806	0.5648
sq13	4000	0.3	0.5	71458	0.4363
staggered array:					
st1	2000	0.9	1.0	12572	0.8976
st2	4000	0.9	0.5	12572	0.8976
st3	20000	0.9	0.1	12572	0.8976
st4	4000	0.8	0.5	8320	0.8155
st5	4000	0.7	0.5	11812	0.7527
st6	2000	0.6	1.0	11240	0.6916
st7	4000	0.6	0.5	11240	0.6916
st8	20000	0.6	0.1	11240	0.6916
st9	4000	0.5	0.5	20228	0.6355
<i>continued on next page</i>					

Table 4.2: Continue.

simulation	$S_0 (\frac{1}{m})$	n	$R (mm)$	N_{part}	d^*
st10	2000	0.4	1.0	41920	0.5633
st11	4000	0.4	0.5	41920	0.5633
st12	20000	0.4	0.1	41920	0.5634
st13	4000	0.3	0.5	115044	0.4350
hexagonal array:					
he1	2000	0.9	1.0	13760	0.8975
he2	4000	0.9	0.5	13760	0.8975
he3	20000	0.9	0.1	13760	0.8976
he4	4000	0.8	0.5	8160	0.8156
he5	4000	0.7	0.5	18892	0.7579
he6	2000	0.6	1.0	17632	0.7023
he7	4000	0.6	0.5	17632	0.7023
he8	20000	0.6	0.1	17632	0.7024
he9	4000	0.5	0.5	16292	0.6543
he10	4000	0.4	0.5	19824	0.6110
he11	2000	0.3	1.0	38884	0.5659
he12	4000	0.3	0.5	38884	0.5659
he13	20000	0.3	0.1	38884	0.5660
he14	4000	0.2	0.5	95884	0.4942

Table 4.3: Summary of results for diffusion simulations with elliptical cylinders.

simulation	$\frac{a}{b}$	$a \text{ (mm)}$	α	N_{part}	d_{xx}^*	d_{yy}^*	d_{xy}^*	d_{yx}^*	d_1^*	d_2^*	θ
square array with $S_0 = 4000 \frac{1}{m}$ and $n = 0.8$:											
sq1	1.5	0.6313	0^0	7644	0.8893	0.7190	0.0000	0.0000	0.8893	0.7190	0.00 ⁰
sq2	1.5	0.6313	15^0	7646	0.8786	0.7327	0.0354	0.0354	0.8867	0.7246	12.94 ⁰
sq3	1.5	0.6313	30^0	7644	0.8506	0.7657	0.0595	0.0592	0.8811	0.7352	27.21 ⁰
sq4	1.5	0.6313	45^0	7636	0.8086	0.8086	0.0697	0.0697	0.8783	0.7389	45.00 ⁰
sq5	2.0	0.7710	0^0	7722	0.9249	0.6175	0.0000	0.0000	0.9249	0.6175	0.00 ⁰
sq6	2.0	0.7710	15^0	7734	0.9073	0.6486	0.0604	0.0601	0.9206	0.6353	12.49 ⁰
sq7	2.0	0.7710	30^0	7730	0.8591	0.7114	0.1048	0.1043	0.9133	0.6572	27.38 ⁰
sq8	2.0	0.7710	45^0	7726	0.7885	0.7885	0.1208	0.1208	0.9093	0.6677	45.00 ⁰
sq9	2.5	0.9157	0^0	11726	0.9490	0.5214	0.0000	0.0000	0.9490	0.5214	0.00 ⁰
sq10	2.5	0.9157	15^0	11728	0.9256	0.5721	0.0800	0.0796	0.9428	0.5549	12.15 ⁰
sq11	2.5	0.9157	30^0	11732	0.8614	0.6684	0.1386	0.1383	0.9337	0.5961	27.56 ⁰
sq12	2.5	0.9157	45^0	11742	0.7701	0.7701	0.1606	0.1606	0.9307	0.6095	45.00 ⁰
staggered array with $S_0 = 4000 \frac{1}{m}$ and $n = 0.8$:											
st1	1.5	0.6313	0^0	12396	0.8783	0.7369	0.0000	0.0000	0.8783	0.7369	0.00 ⁰
st2	1.5	0.6313	7.5^0	12376	0.8744	0.7385	0.0215	0.0216	0.8777	0.7352	8.80 ⁰

continued on next page

Table 4.3: Continue.

simulation	$\frac{a}{b}$	a (mm)	α	N_{part}	d_{xx}^*	d_{yy}^*	d_{xy}^*	d_{yx}^*	d_1^*	d_2^*	θ
st3	1.5	0.6313	15 ⁰	12388	0.8667	0.7461	0.0419	0.0421	0.8799	0.7329	17.43 ⁰
st4	1.5	0.6313	30 ⁰	12392	0.8390	0.7691	0.0740	0.0741	0.8859	0.7222	32.37 ⁰
st5	1.5	0.6313	45 ⁰	12392	0.8026	0.8026	0.0854	0.0854	0.8880	0.7172	45.00 ⁰
st6	2.0	0.7710	0 ⁰	12532	0.9083	0.6654	0.0000	0.0000	0.9083	0.6654	0.00 ⁰
st7	2.0	0.7710	7.5 ⁰	12540	0.9034	0.6691	0.0375	0.0376	0.9093	0.6632	8.89 ⁰
st8	2.0	0.7710	15 ⁰	12528	0.8879	0.6788	0.0738	0.0742	0.9114	0.6553	17.65 ⁰
st9	2.0	0.7710	30 ⁰	12536	0.8350	0.7144	0.1323	0.1330	0.9204	0.6290	32.78 ⁰
st10	2.0	0.7710	45 ⁰	12536	0.7700	0.7700	0.1546	0.1546	0.9246	0.6154	45.00 ⁰
st11	2.5	0.9157	0 ⁰	26068	0.9304	0.6100	0.0000	0.0000	0.9304	0.6100	0.00 ⁰
st12	2.5	0.9157	7.5 ⁰	26068	0.9235	0.6147	0.0491	0.0493	0.9311	0.6071	8.84 ⁰
st13	2.5	0.9157	15 ⁰	26082	0.9038	0.6267	0.0962	0.0965	0.9340	0.5965	17.41 ⁰
st14	2.5	0.9157	30 ⁰	26070	0.8285	0.6705	0.1761	0.1768	0.9428	0.5562	32.94 ⁰
st15	2.5	0.9157	45 ⁰	26068	0.7364	0.7364	0.2127	0.2127	0.9491	0.5237	45.00 ⁰
staggered array with $S_0 = 4000 \frac{1}{m}$ and $n = 0.5$:											
st16	1.5	0.6313	0 ⁰	10700	0.7298	0.5263	0.0000	0.0000	0.7298	0.5263	0.00 ⁰
st17	1.5	0.6313	7.5 ⁰	18206	0.7261	0.5333	0.0695	0.0699	0.7487	0.5107	17.93 ⁰
st18	1.5	0.6313	15 ⁰	18210	0.6985	0.5370	0.1382	0.1389	0.7781	0.4574	29.88 ⁰

continued on next page

Table 4.3: Continue.

simulation	$\frac{a}{b}$	$a \text{ (mm)}$	α	N_{part}	d_{xx}^*	d_{yy}^*	d_{xy}^*	d_{yx}^*	d_1^*	d_2^*	θ
st19	2.0	0.7710	0^0	14476	0.8141	0.4307	0.0000	0.0000	0.8141	0.4307	0.00^0
st20	2.0	0.7710	7.5^0	20782	0.7960	0.4428	0.0975	0.0982	0.8213	0.4175	14.49^0
st21	2.0	0.7710	15^0	20788	0.7329	0.4640	0.2022	0.2038	0.8419	0.3550	28.24^0
st22	2.5	0.9157	0^0	33940	0.8823	0.3206	0.0000	0.0000	0.8823	0.3206	0.00^0
st23	2.5	0.9157	7.5^0	33968	0.8544	0.3474	0.1023	0.1026	0.8743	0.3275	11.00^0
st24	2.5	0.9157	15^0	33966	0.7699	0.4020	0.2196	0.2207	0.8728	0.2991	25.06^0
hexagonal array with $S_0 = 4000 \frac{1}{m}$ and $n = 0.8$:											
he1	1.5	0.6313	0^0	13512	0.8838	0.7285	0.0000	0.0000	0.8838	0.7285	0.00^0
he2	1.5	0.6313	15^0	13496	0.8726	0.7390	0.0377	0.0377	0.8825	0.7291	14.72^0
he3	1.5	0.6313	30^0	13516	0.8445	0.7694	0.0656	0.0656	0.8825	0.7314	30.11^0
he4	1.5	0.6313	45^0	13512	0.8051	0.8074	0.0774	0.0774	0.8837	0.7288	45.43^0
he5	1.5	0.6313	60^0	13508	0.7673	0.8448	0.0671	0.0671	0.8835	0.7286	60.00^0
he6	1.5	0.6313	75^0	13512	0.7398	0.8727	0.0397	0.0397	0.8837	0.7288	74.57^0
he7	1.5	0.6313	90^0	13516	0.7313	0.8825	0.0000	0.0000	0.8825	0.7313	90.00^0
he8	2.0	0.7710	0^0	13676	0.9184	0.6381	0.0000	0.0000	0.9184	0.6381	0.00^0
he9	2.0	0.7710	15^0	13693	0.9004	0.6623	0.0648	0.0648	0.9169	0.6458	14.28^0
he10	2.0	0.7710	30^0	13692	0.8481	0.7179	0.1148	0.1152	0.9151	0.6509	30.24^0

continued on next page

Table 4.3: Continue.

simulation	$\frac{a}{b}$	$a\,(mm)$	α	N_{part}	d_{rx}^*	d_{yy}^*	d_{xy}^*	d_{yx}^*	d_1^*	d_2^*	θ
he11	2.0	0.7710	45 ⁰	136668	0.7761	0.7840	0.1364	0.1366	0.9166	0.6435	45.83 ⁰
he12	2.0	0.7710	60 ⁰	13696	0.7089	0.8491	0.1214	0.1214	0.9192	0.6388	60.00 ⁰
he13	2.0	0.7710	75 ⁰	136668	0.6638	0.8963	0.0718	0.0716	0.9166	0.6435	74.17 ⁰
he14	2.0	0.7710	90 ⁰	13692	0.6509	0.9151	0.0000	0.0000	0.9151	0.6509	90.00 ⁰
he15	2.5	0.9157	0 ⁰	20551	0.9419	0.5574	0.0000	0.0000	0.9419	0.5474	0.00 ⁰
he16	2.5	0.9157	15 ⁰	20552	0.9176	0.5937	0.0852	0.0849	0.9386	0.5727	13.85 ⁰
he17	2.5	0.9157	30 ⁰	20556	0.8481	0.6749	0.1506	0.1508	0.9353	0.5877	30.06 ⁰
he18	2.5	0.9157	45 ⁰	20544	0.7489	0.7627	0.1824	0.1826	0.9384	0.5732	46.08 ⁰
he19	2.5	0.9157	60 ⁰	20560	0.6537	0.8460	0.1666	0.1666	0.9422	0.5575	60.00 ⁰
he20	2.5	0.9157	75 ⁰	20544	0.5961	0.9104	0.0973	0.0970	0.9380	0.5685	74.14 ⁰
he21	2.5	0.9157	90 ⁰	20563	0.5877	0.9353	0.0000	0.0000	0.9353	0.5877	90.00 ⁰

4.5.1 Effect of Specific Surface Area

The specific surface area S_0 is based on the solid volume of the porous media.

$$S_0 = \frac{\text{surface area of solid inclusions}}{\text{volume of solid inclusions}}. \quad (4.25)$$

In two dimensions, it becomes,

$$S_0 = \frac{\text{perimeter of solid inclusions}}{\text{area of solid inclusions}}. \quad (4.26)$$

In this work, because only uniform solid obstacles are considered,

$$S_0 = \frac{2}{R}, \quad (4.27)$$

for circular inclusions and,

$$S_0 = \frac{4 \int_0^{\frac{\pi}{2}} \sqrt{a^2 \cos^2 x + b^2 \sin^2 x} dx}{\pi ab}, \quad (4.28)$$

for elliptical inclusions, respectively.

The effect of S_0 on d^* was studied by calculating values of d^* for the three circular cylinder arrays having $S_0 = 2000 \frac{1}{m}$, $4000 \frac{1}{m}$, and $20000 \frac{1}{m}$. Three porosities of 0.4, 0.6, and 0.9 were chosen for the square and staggered arrays, while three porosities of 0.3, 0.6, and 0.9 were chosen for the hexagonal array. The results are presented in rows sq1-sq3, sq6-sq8, sq10-sq12, st1-st3, st6-st8, st10-st12, he1-he3, he6-he8, and he11-he13 of Table 4.2. It is evident that d^* is not a function of S_0 for any case. This is not surprising since d^* is dimensionless and is thus not a function of any length scale.

4.5.2 Effect of Porosity

The functional relationship between d^* and porosity n was generated using the data in Table 4.2 and is shown in Figure 4.10. Values of d^* decrease with decreasing n for each array. d^* is essentially independent of array type for $n \geq 0.6$. For $n < 0.6$, the hexagonal array yields larger values of d^* while values for the other arrays are nearly

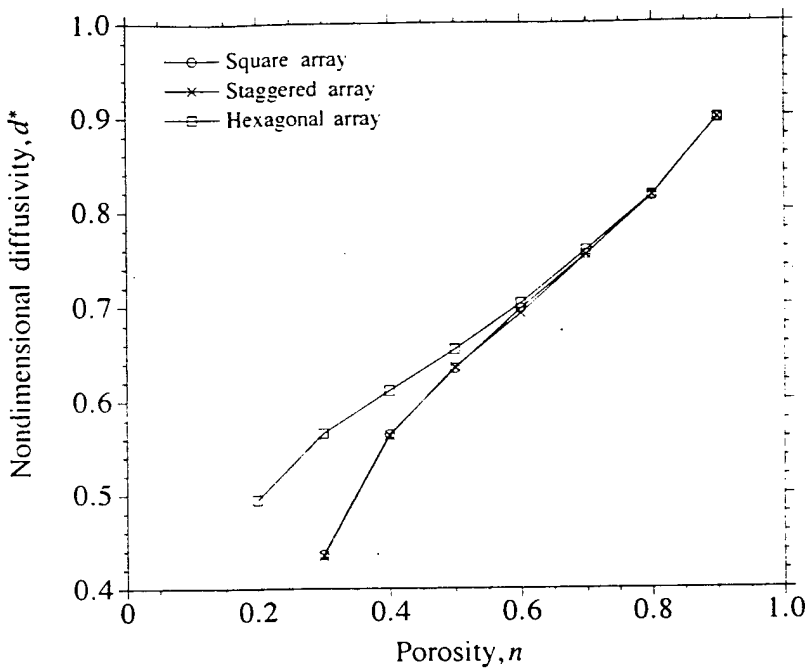


Figure 4.10: Nondimensional diffusivity versus porosity for square, staggered, and hexagonal circular cylinder arrays.

indistinguishable. Due to the absence of diffusion within the solids, the diffusion process is controlled by the distribution of voids within the media. The hexagonal array has larger diffusion channels with the same porosity than square and staggered arrays, and this effect becomes significant when porosity is low, resulting in a larger diffusivity for hexagonal array.

Perkins and Johnston (1963) suggested a single value of 0.7 for d^* of consolidated granular media. This value corresponds to a medium of a porosity of about 0.6 according to Figure 4.10. Fried and Combarous (1971) reported values of 0.4 to 0.8 for d^* , which is consistent with Figure 4.10. Apparently, a value of $\frac{1}{3}$ for d^* predicted by Saffman's model (Equations 2.87 and 2.88) only applies to very low porosity media.

4.5.3 Effect of Anisotropy

The effect of anisotropy was studied using elliptical inclusions (Figures 3.11 to 3.13). In Table 4.3, the values of d_{xx}^* , d_{yy}^* , d_{xy}^* , d_{yx}^* , as well as the principal nondimen-

sional diffusivities d_1^* and d_2^* , and the angle θ (Figure 2.8) are reported. Equations 2.49 and 2.50 were employed to obtain d_1^* , d_2^* , and θ . The values confirm that $d_{xy}^* = d_{yx}^*$ in all cases.

Figure 4.11 shows $\frac{d_1^*}{d^*}$ and $\frac{d_2^*}{d^*}$ versus the aspect ratio $\frac{a}{b}$, respectively, for elliptical cylinder arrays having different α . d^* is the corresponding nondimensional diffusivity of the anisotropic medium's isotropic counterpart, i.e., the value for a corresponding circular cylinder array with the same porosity n and specific surface area S_0 . Figure 4.11 shows that the anisotropy of the media increases with increasing $\frac{a}{b}$ and that the values of $\frac{d_1^*}{d^*}$ and $\frac{d_2^*}{d^*}$ are less dependent on α and array type. Figure 4.12 presents $\frac{d_1^*}{d^*}$ and $\frac{d_2^*}{d^*}$ versus α , respectively, for elliptical cylinder arrays having different $\frac{a}{b}$. In Figure 4.12, values of $\frac{d_1^*}{d^*}$ and $\frac{d_2^*}{d^*}$ are grouped in distinguishable bands according to $\frac{a}{b}$. Figure 4.12 also shows that the effect of α increases with increasing $\frac{a}{b}$. It is concluded that α influences the directional properties of the anisotropy; while the magnitude of the anisotropy of the media, which can be defined as the value of $\frac{d_1^*}{d_2^*}$, is mainly determined by the aspect ratio of the solid obstacles.

Figures 4.11 and 4.12 were generated for $n = 0.8$. For the staggered array, some simulations were completed for $n = 0.5$. Figure 4.13 shows $\frac{d_1^*}{d^*}$ and $\frac{d_2^*}{d^*}$ versus $\frac{a}{b}$, respectively, for the two sets of simulations for staggered array with porosities of 0.5 and 0.8. As can be seen, a lower value of porosity not only enhances the magnitude of anisotropy of the media, it also increases the effect of α .

The relationship between θ and α is shown in Figure 4.14 for $n = 0.8$. θ is almost identical with α for hexagonal arrays, while is slightly greater than α for staggered arrays and slightly less than α for square arrays when α is less than 45° . In practice, a linear relationship between θ and α could be assumed, i.e., the first principal diffusion axis is aligned with the preferred orientation of the elongated solid obstacles. Unfortunately, this is not true when Figure 4.15 is plotted, which also shows θ versus α for the simulations for $n = 0.5$. A lower value of porosity shifts the first principal diffusion axis away from the direction of particle orientation; however, the degree of shifting decreases with increasing aspect ratio $\frac{a}{b}$.

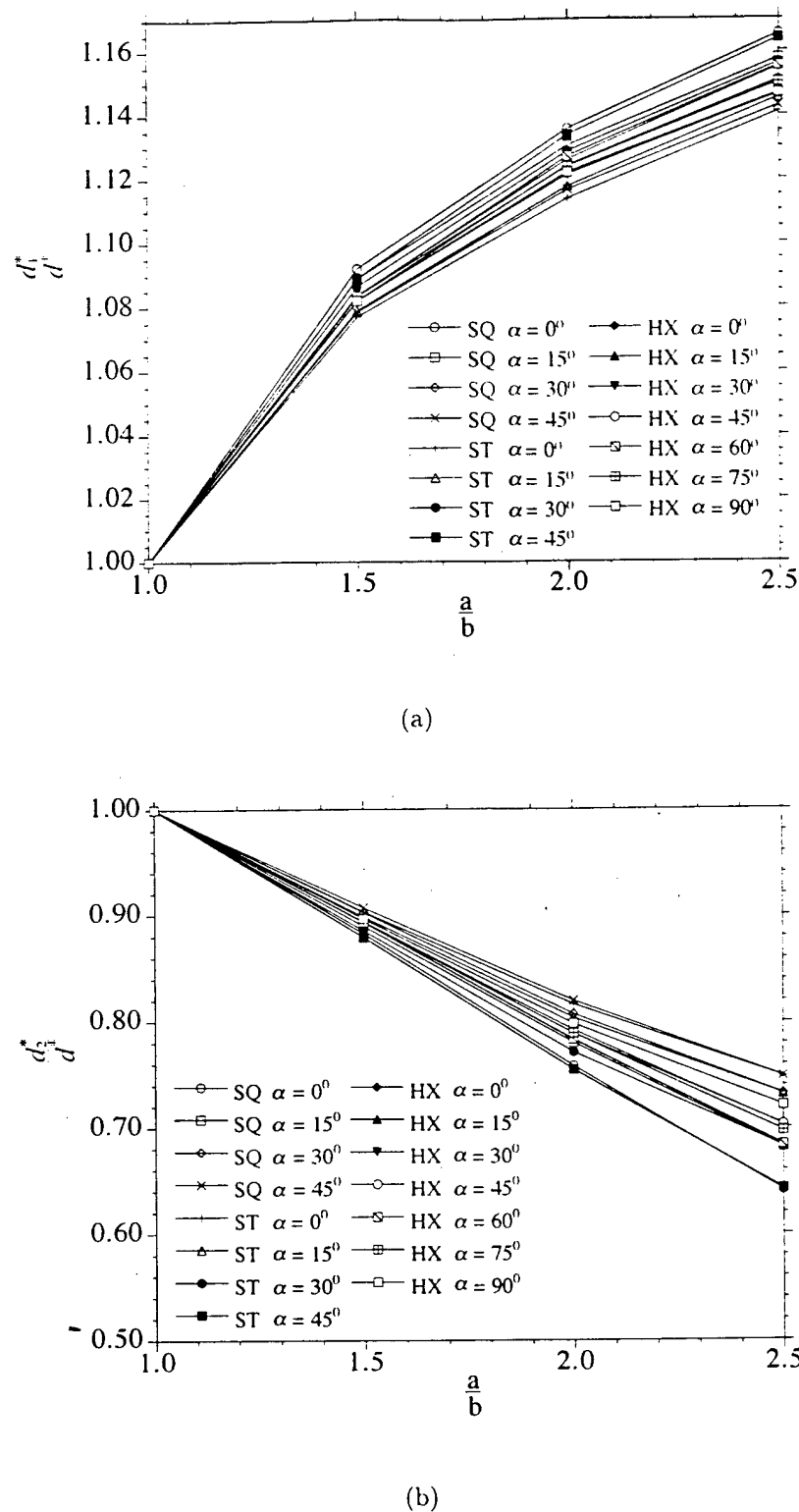


Figure 4.11: Normalized principal nondimensional diffusivity (a) $\frac{d_1^*}{d^*}$, and (b) $\frac{d_2^*}{d^*}$ versus aspect ratio $\frac{a}{b}$ for elliptical cylinder arrays having $n = 0.8$ (SQ = square array, ST = staggered array, HX = hexagonal array).

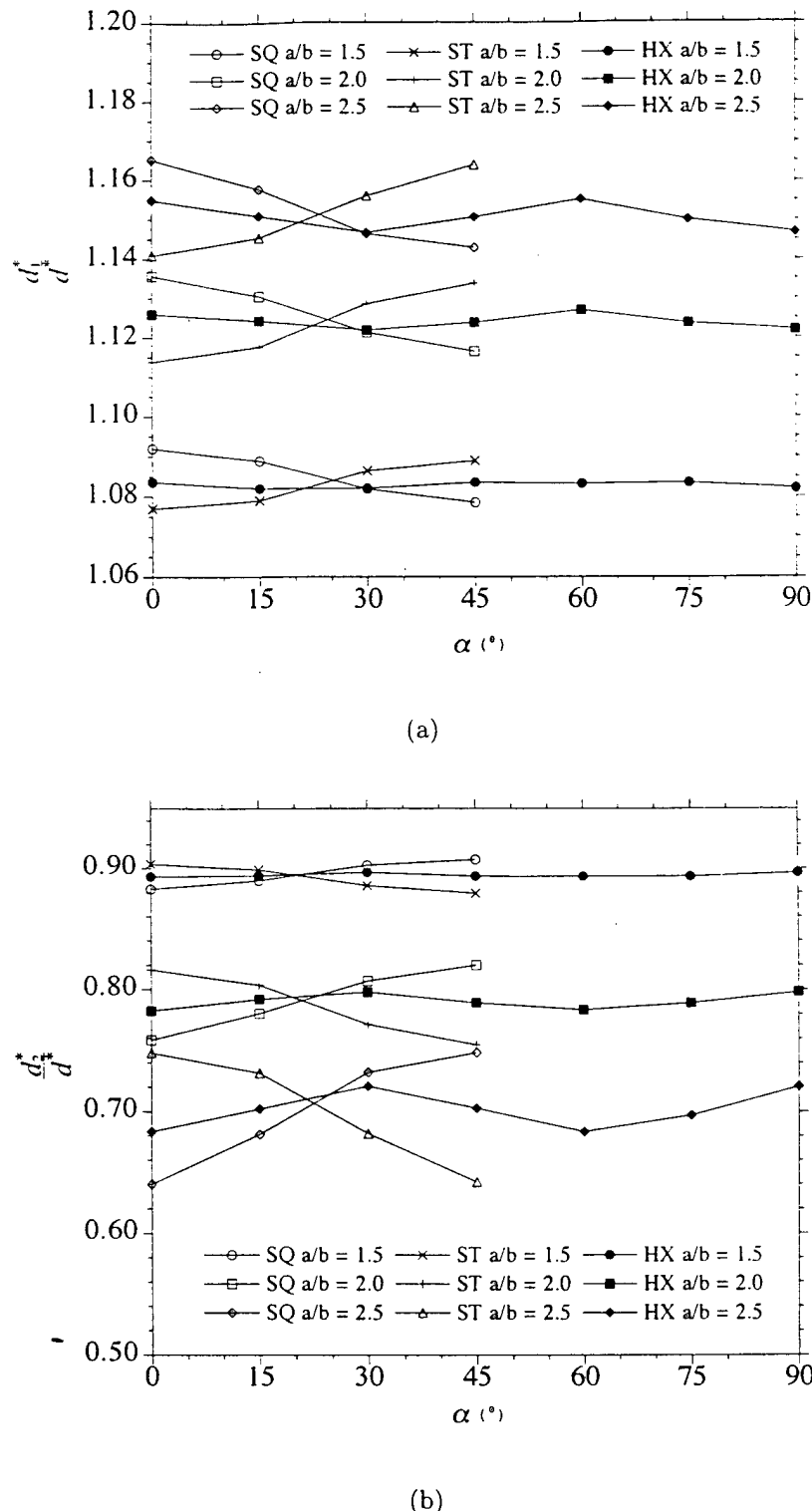


Figure 4.12: Normalized principal nondimensional diffusivity (a) $\frac{d_1^*}{d^*}$, and (b) $\frac{d_2^*}{d^*}$ versus α for elliptical cylinder arrays having $n = 0.8$.

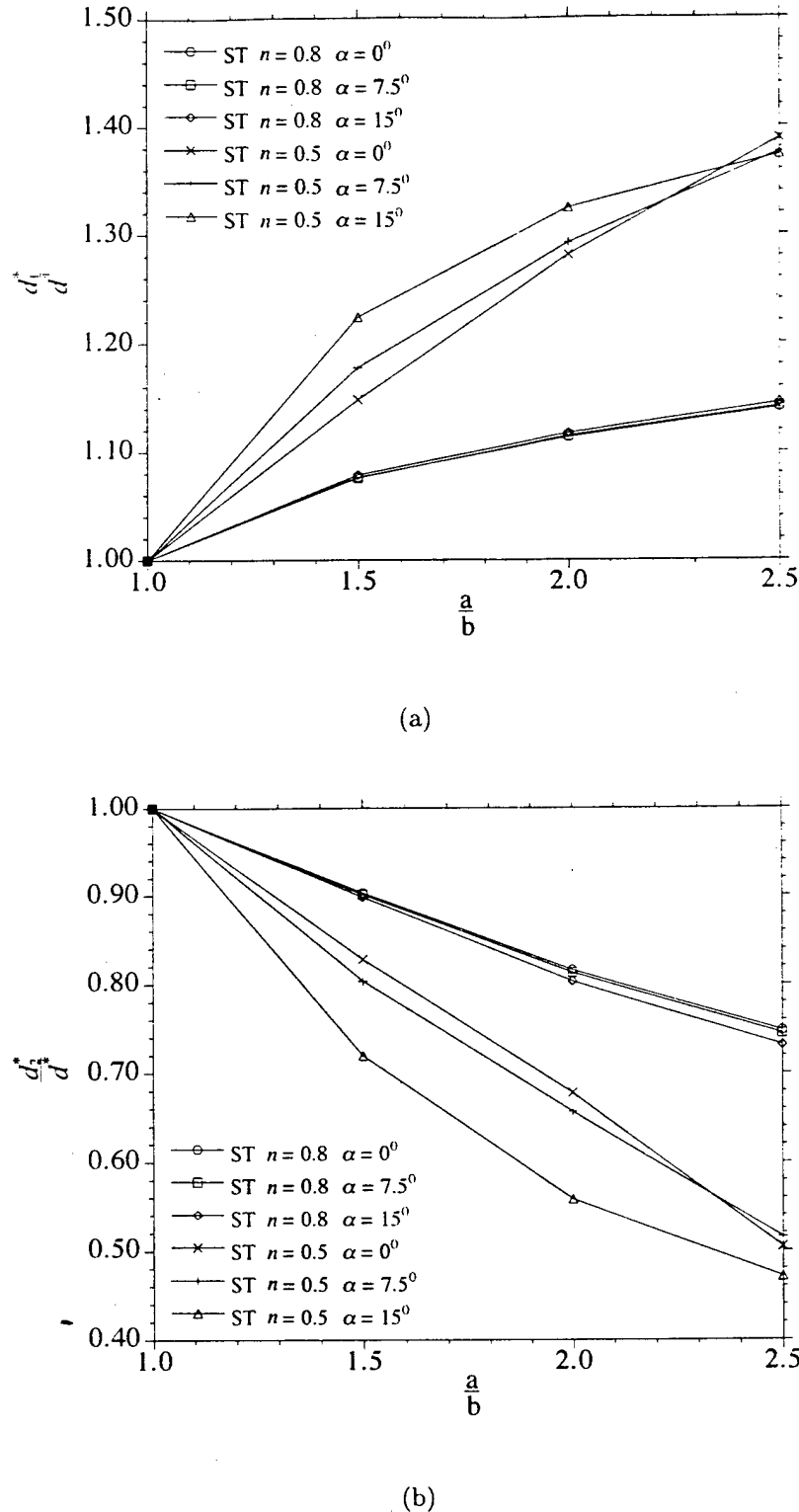


Figure 4.13: Normalized principal nondimensional diffusivity (a) $\frac{d_1^*}{d^*}$, and (b) $\frac{d_2^*}{d^*}$ versus aspect ratio $\frac{a}{b}$ for staggered elliptical cylinder arrays having $n = 0.5$ and 0.8 .

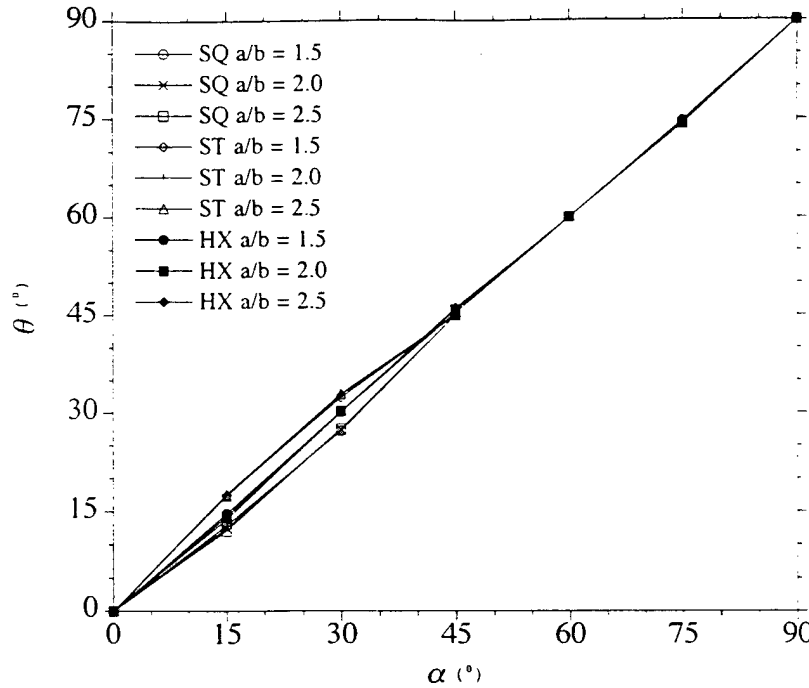


Figure 4.14: θ versus α for elliptical cylinder arrays having $n = 0.8$.

4.5.4 Effect of Cylinder Arrangement

The effect of cylinder arrangement is manifested in the above figures. Figure 4.10 shows that a hexagonal array will likely result in a higher d^* value than square and staggered arrays for the same porosity. The effect of cylinder arrangement on anisotropy is minor as seen in Figure 4.12. The values for different arrangements are grouped in a narrow band for different aspect ratios. It is interesting to see that, hexagonal array always has a value of anisotropy in between those for the square and staggered arrays; and square array shows the most anisotropy and the staggered array the least when α is less than about 27° .

4.6 Summary

Smoothed Particle Hydrodynamics (SPH) has been implemented to model tracer diffusion through porous media. Comparative studies confirm the approach is accurate. Nondimensional diffusivities \mathbf{d}^* were calculated using the model for spatially

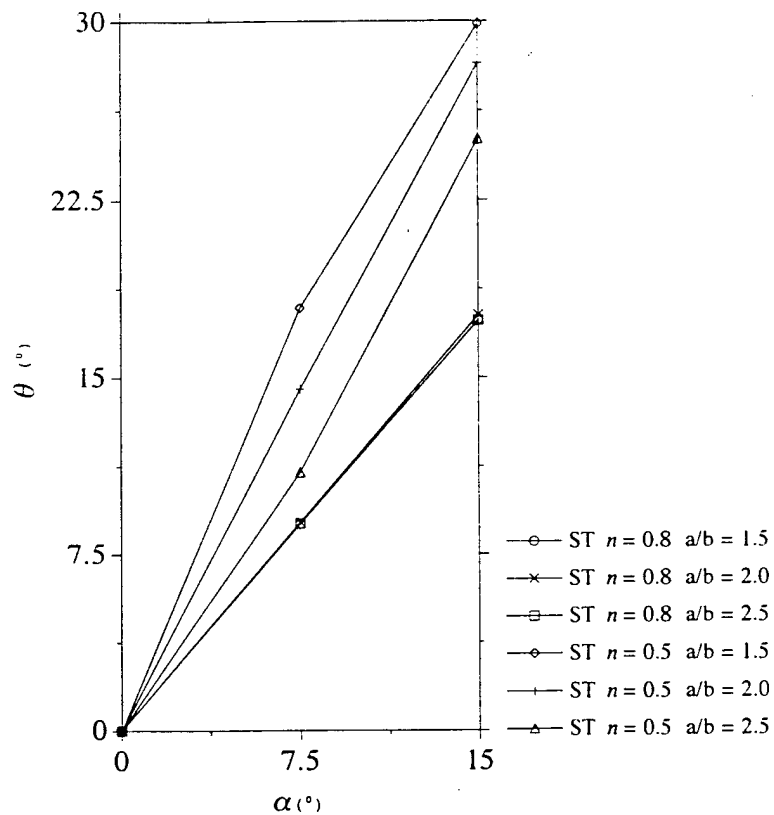


Figure 4.15: θ versus α for staggered elliptical cylinder arrays having $n = 0.5$ and 0.8.

periodic porous media with circular and elliptical cylinders arranged in square, staggered, and hexagonal arrays. The results provide guidance for determining the values of d^* of real porous media. While specific surface area S_0 does not affect d^* , porosity n and array type were found to be the most and least important parameters, respectively, which influence the values of d^* . Anisotropy of a medium is mainly determined by aspect ratio $\frac{a}{b}$ of its solid inclusions.

CHAPTER 5 PORE-SCALE TRACER CONVECTION AND HYDRODYNAMIC DISPERSION SIMULATIONS

This chapter extends the SPH numerical models described in Chapters 3 and 4 to study tracer convection and hydrodynamic dispersion in spatially periodic porous media. SPH is used to solve the Taylor dispersion problem and explore the characterization of dispersion as an asymptotic Fickian process. Discrete SPH particle data are analyzed using the method of moments and the advantages and limitations of the numerical model are discussed.

5.1 Pore-Scale Tracer Convection Model

In the problem of tracer convection (i.e., without diffusion), some fluid particles are tagged as tracers and their movement through void system of the porous medium is monitored. Being a Lagrangian technique, SPH tracks the trajectories of fluid particles naturally and the SPH flow model (Chapter 3) was easily extended to study tracer convection. Implementation of the convection-diffusion equation (Chapter 4) was not needed for the tracer convection model because there is no mass exchange between tracer and tracer or tracer and carrier fluid. Thus, the solute mass associated with each SPH tracer particle is constant during the course of a simulation. Tracer and fluid particles are simply distinguished as “black” and “white” SPH fluid particles, respectively, in this model.

Due to the periodicity of flow, the tracer convection problem is solved within a single unit cell. The flow is first evolved to steady state; then a chosen number of fluid (white) particles within the unit cell are tagged as tracer (black) particles. If tracers are assumed to have a concentration C , each tracer particle z carries a constant solute mass \mathcal{M}_z of,

$$\mathcal{M}_z = C \frac{m_z}{\rho_z}. \quad (5.1)$$

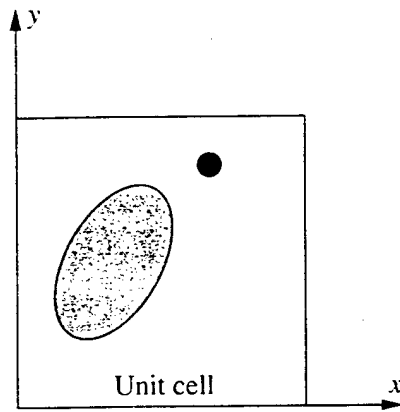
As the flow continues, tracer and fluid particles are wrapped around the unit cell in the same manner as described in Chapter 3 (Figure 3.6). However, information regarding the wrapping of tracer particles around the unit cell is recorded and used to construct the real tracer field in the corresponding spatially periodic porous medium. For example, in Figure 5.1(a), if the tracer particle is known to have crossed the upper unit cell boundary once and the right unit cell boundary twice, its real position in the spatially periodic porous medium is shown in Figure 5.1(b). Calculations are needed for only one unit cell to simulate tracer convection using this method.

5.2 Pore-Scale Hydrodynamic Dispersion Model

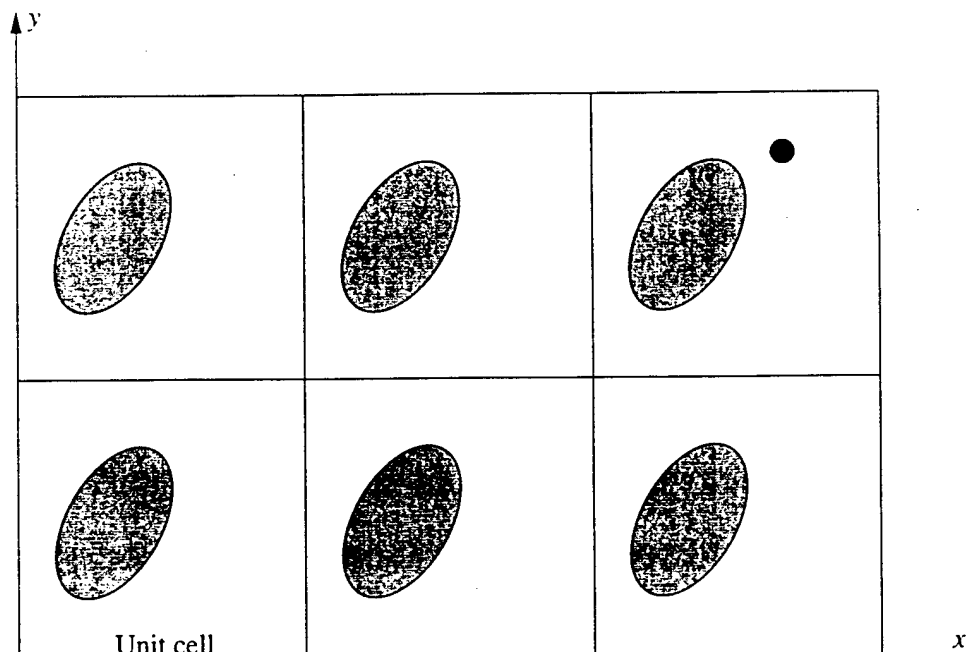
With implementations of both flow (Chapter 3) and convection-diffusion (Chapter 4) equations, a pore-scale tracer hydrodynamic dispersion model was developed using SPH. The SPH model easily simulates the process of tracer hydrodynamic dispersion in principle, however, in practice, simulations are limited by computation time.

In spatially periodic porous media, while the flow field is also periodic in nature, this is not true for the concentration field. As a result, in the problem of simulating tracer hydrodynamic dispersion, a computing domain consisting of multiple unit cells is needed for evolving the concentration field. For example, although the initial tracer plume is confined within one unit cell in Figure 5.2(a), the tracer plume at a later time spans to six unit cells in Figure 5.2(b). An efficient algorithm to model the evolution of concentration which takes advantage of the periodic nature of flow field is described below.

Figure 5.3 shows the initial concentration field for a problem of tracer dispersion. The concentration computing domain consists of six unit cells which are identified by the (i, j) coordinates. For this tracer hydrodynamic dispersion model, the flow field is calculated in a single unit cell corresponding to $i = 1$ and $j = 1$. Every SPH



(a)



(b)

Figure 5.1: Tracer particle positions (a) within the unit cell, and (b) within the corresponding spatially periodic porous medium.

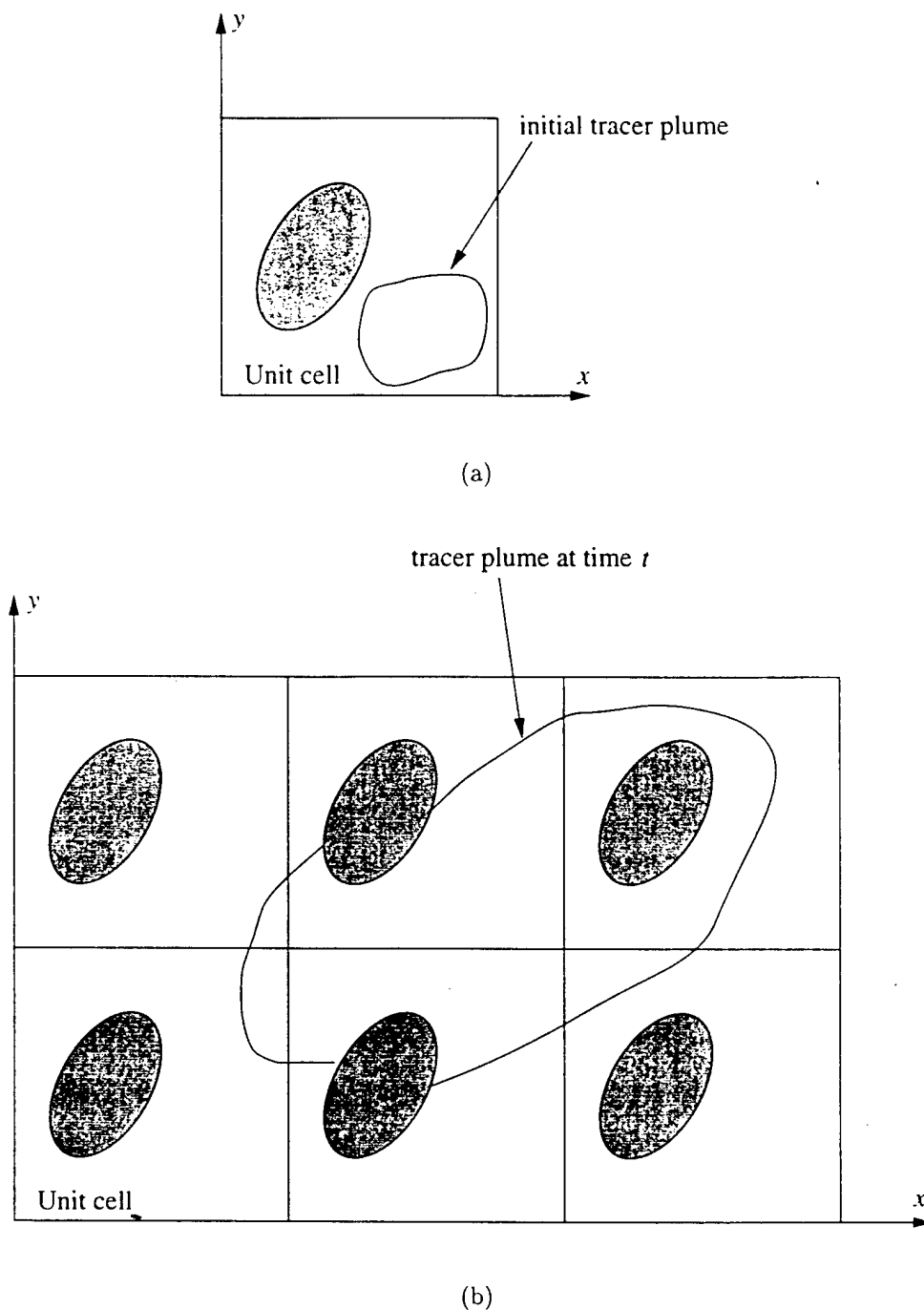


Figure 5.2: Tracer plumes for the problem of tracer hydrodynamic dispersion: (a) initial tracer plume, and (b) tracer plume at time t .

fluid particle only has one set of flow related quantities (e.g., velocity and density) and carries as many concentration values as the number of unit cells which constitute the concentration computing domain. In this case, every fluid particle has six values of concentration, one for each unit cell in the concentration computing domain. The concentration field is determined by the particle concentration values for each unit cell. However, particle positions in unit cell (i, j) other than unit cell $(1, 1)$ are not needed during the course of a simulation. According to Equation 4.2, the evolution of concentration field is driven by local concentration gradients and only the relative positions between particles are needed to calculate the rates of change for concentration. The relative positions between particles are calculated from the position values in unit cell $(1, 1)$ and they are the same for every unit cell. For the purpose of analyzing and visualizing the concentration field, SPH particles (both fluid and boundary particles) are mapped to other unit cells from unit cell $(1, 1)$ in the concentration computing domain.

To perform the simulation in Figure 5.3, the flow field is evolved to steady state with all particle concentrations equal to zero. In order to initialize the dispersion process, particles in area A (Figure 5.4) are assigned $C_0 = 1$ for unit cell $(1, 1)$. Likewise, particles in area B, C, D (Figure 5.4) are assigned $C_0 = 1$ for unit cells $(1, 2), (2, 2)$, and $(2, 1)$, respectively.

Once the concentration field is initialized, the flow continues according to the methods described in Chapter 3 and the concentration field is evolved according to the methods described in Chapter 4. As fluid particles are wrapped around the unit cell $(1, 1)$ and recalling that all SPH particles physically reside in unit cell $(1, 1)$, concentration values of the wrapped particles are reassigned accordingly. For example, as fluid particle a (Figure 5.5) is wrapped back into unit cell $(1, 1)$, its value of concentration for unit cell (i, j) after wrapping equals to the value of concentration for unit cell $(i - 1, j)$ before wrapping.

Values of concentration must also be correctly assigned for image fluid particles. For example, if particle c is the image particle of particle b in unit cell $(1, 1)$ (Figure

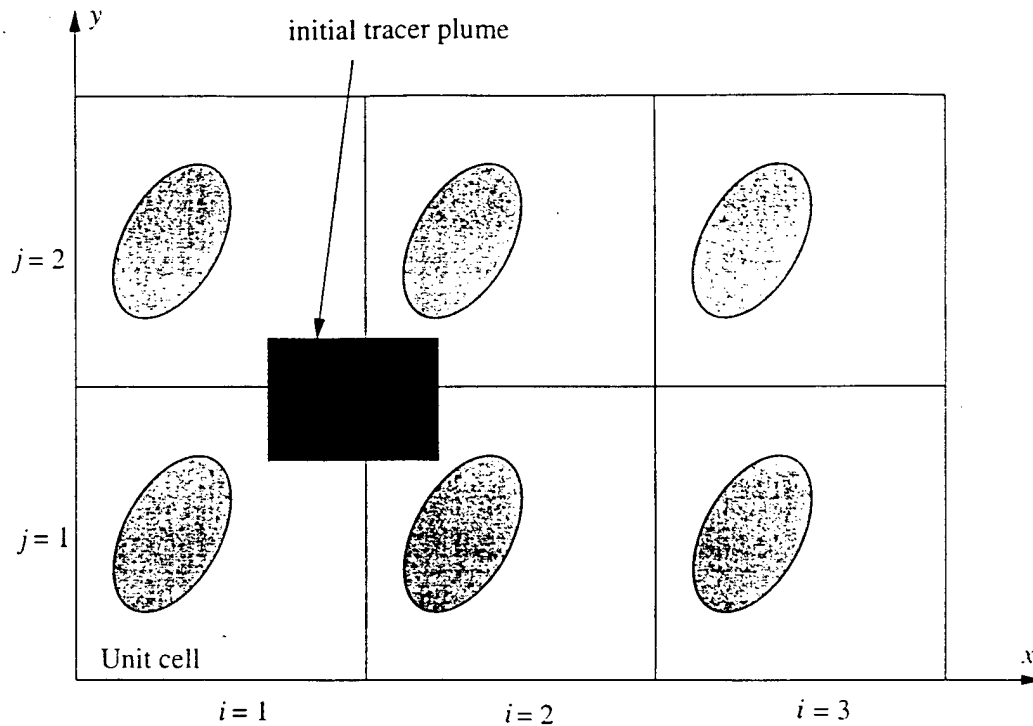


Figure 5.3: Initial concentration field for a problem of tracer hydrodynamic dispersion in a spatially periodic porous medium.

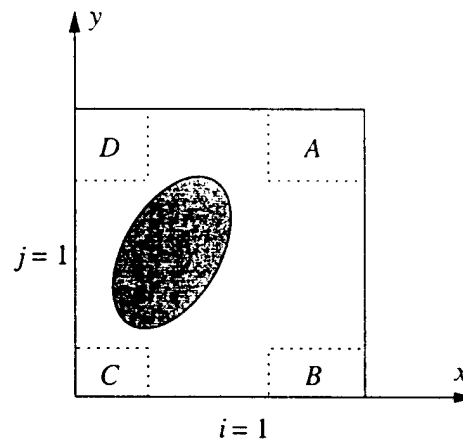


Figure 5.4: Unit cell $(1, 1)$ for the problem in Figure 5.3.

5.5), the value of concentration for particle c corresponding to unit cell (i, j) is equal to the value of concentration for particle b corresponding to unit cell $(i + 1, j)$.

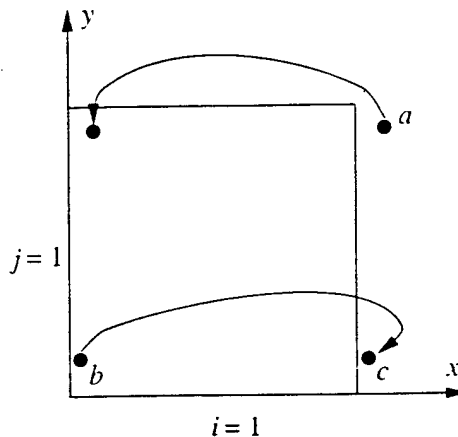


Figure 5.5: Wrapping fluid particles and creating image particles to simulate tracer dispersion in a spatially periodic porous medium.

The concentration computing domain used in this work consists of a constant number of unit cells. A large concentration computing domain is unnecessary during the initial stage of a simulation. For example, the unit cells corresponding to column $i = 3$ in Figure 5.3 are not needed when the dispersion simulation begins. It is possible to dynamically change the size of concentration computing domain to accommodate the evolution of concentration. However, this requires dynamically determining the tracer plume front. The advantages of a dynamically changing concentration computing domain during the course of a simulation are not explored in this work. For a constant concentration computing domain, a simulation terminates when the plume front crosses the boundary of the domain. A meaningful simulation of hydrodynamic dispersion usually requires several tens of unit cells for modeling the evolution of concentration. This significantly lengthens the computation time for each simulation.

Since SPH uses an explicit time integration scheme, the time step is limited by stability constraints. For a low Reynolds number flow simulation, the time step is usually limited by fluid viscosity according to Equation 3.47,

$$\tau \leq 0.125 \frac{h^2}{\nu}.$$

The time step for properly integrating particle-to-particle diffusion is (Equation 4.4),

$$\tau \leq 0.125 \frac{h^2}{d_0}.$$

As liquids have a Schmidt number $Sc = \frac{\nu}{d_0}$ on the order of 10^3 to 10^4 , the maximum time step is limited by Equation 3.47 for a simulation of liquid-type tracer dispersion. As a result, the chosen time step is relatively small for evolving concentrations and lengthy computer simulations are needed to simulate dispersion phenomena, due to the large concentration computing domain.

5.3 Method of Moments

Spatial moments of tracer distribution provide an estimation of the permeability and dispersivity of porous media (Aris 1956; Horn 1971; Brenner 1980a). In the SPH tracer convection model, the tracer field is characterized by individual tracer particle position \mathbf{R} and its associated solute mass \mathcal{M}_z . The zeroth moment of tracer distribution is,

$$M_0 = \frac{\int d\mathcal{M}}{\int d\mathcal{M}_0} \cong \frac{\sum_z \mathcal{M}_z}{\sum_z \mathcal{M}_{z,0}}. \quad (5.2)$$

M_0 will have a constant value of unity since $\mathcal{M}_z = \mathcal{M}_{z,0}$ in this model. The first moment of tracer distribution is,

$$\mathbf{M}_1 = \frac{\int \mathbf{R} d\mathcal{M}}{\int d\mathcal{M}_0} \cong \frac{\sum_z \mathbf{R}_z \mathcal{M}_z}{\sum_z \mathcal{M}_{z,0}}. \quad (5.3)$$

\mathbf{M}_1 represents the position of the center of tracer mass and is used to calculate the seepage velocity \mathbf{v}_s as,

$$\mathbf{v}_s = \frac{\Delta \mathbf{M}_1}{\Delta t}. \quad (5.4)$$

The centered second moment is,

$$\mathbf{M}_2 = \frac{\int (\mathbf{R} - \mathbf{M}_1)^2 d\mathcal{M}}{\int d\mathcal{M}_0} \cong \frac{\sum_z (\mathbf{R}_z - \mathbf{M}_1)^2 \mathcal{M}_z}{\sum_z \mathcal{M}_{z,0}}. \quad (5.5)$$

\mathbf{M}_2 represents the spreading of a tracer field about its center and is used to calculate the dispersion coefficient as,

$$\mathbf{D} = \frac{\Delta \mathbf{M}_2}{2 \Delta t}. \quad (5.6)$$

Equation 5.6 is consistent with Equation 2.150.

For the SPH tracer hydrodynamic dispersion model, the solute mass of a given particle is not constant and Equations 5.2, 5.3, and 5.5 become,

$$M_0 = \frac{\int d\mathcal{M}}{\int d\mathcal{M}_0} = \frac{\int C dV}{\int C_0 dV} \cong \frac{\sum_b C_b \frac{m_b}{\rho_b}}{\sum_b C_{b,0} \frac{m_b}{\rho_{b,0}}}. \quad (5.7)$$

$$\mathbf{M}_1 = \frac{\int \mathbf{R} d\mathcal{M}}{\int d\mathcal{M}_0} = \frac{\int \mathbf{R} C dV}{\int C_0 dV} \cong \frac{\sum_b \mathbf{R}_b C_b \frac{m_b}{\rho_b}}{\sum_b C_{b,0} \frac{m_b}{\rho_{b,0}}}. \quad (5.8)$$

and,

$$\mathbf{M}_2 = \frac{\int (\mathbf{R} - \mathbf{M}_1)^2 d\mathcal{M}}{\int d\mathcal{M}_0} = \frac{\int (\mathbf{R} - \mathbf{M}_1)^2 C dV}{\int C_0 dV} \cong \frac{\sum_b (\mathbf{R}_b - \mathbf{M}_1)^2 C_b \frac{m_b}{\rho_b}}{\sum_b C_{b,0} \frac{m_b}{\rho_{b,0}}}. \quad (5.9)$$

where summations are performed over all fluid particles. Due to molecular diffusion, every SPH fluid particle could potentially carry some solute mass in the tracer hydrodynamic dispersion model. The zeroth moment (Equation 5.7) will have a constant value of unity if tracer mass is conserved during a simulation and this provides a first check of the model.

If tracer dispersion is a Fickian process, the dispersive flux is proportional to the concentration gradient (Equation 2.67). It is usually believed that tracer dispersion

is an asymptotic Fickian process. Under such conditions, the dispersive flux can be characterized by a constant dispersion coefficient after a characteristic time t_c , which is the time required for the tracer to sample interstitial space of the unit cells (Brenner 1980a). However, there are some studies in literature where dispersivity may never approach an asymptotic value (section 2.3.7).

5.4 Interpretation of Tracer Diffusion Using Method of Moments

Figure 5.6 shows the geometry for one-dimensional diffusion of a substance initially confined to a finite region. The solid configuration is a periodic square array of circular cylinders. The problem was solved for $d_0 = 10^{-10} \frac{m^2}{s}$, $R = 0.5 \text{ mm}$, $n = 0.8$, and $h = 0.6 \text{ mm}$. The method of moments was used to calculate the diffusion

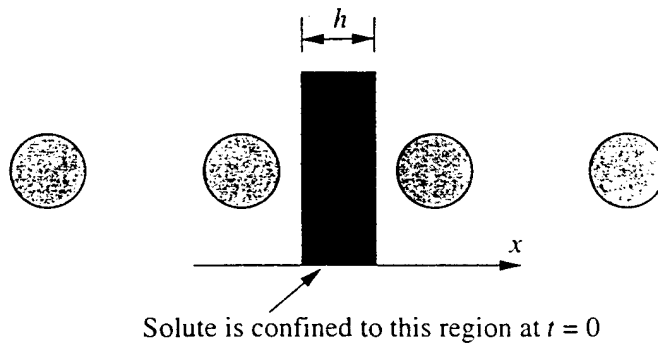


Figure 5.6: Initial condition for a tracer diffusion through a square array of circular cylinders.

coefficient in the x direction d_x using Equation 5.6 with $\Delta t = 1570 \text{ s}$. d_x was then used to calculate the nondimensional diffusivity in the x direction d_x^* (Equation 2.58). Figure 5.7 shows d_x^* as a function of t . Values of d_x^* approach an asymptotic value of 0.8138 with time. For the same media configuration, d_x^* was found to be 0.8144 using the steady state diffusion approach presented in Chapter 4 (Table 4.2). The method of moments produced a result which is consistent with that obtained using the steady state diffusion approach. However, the method of moments simulation used a concentration computing domain consisting of 30 unit cells and therefore required a

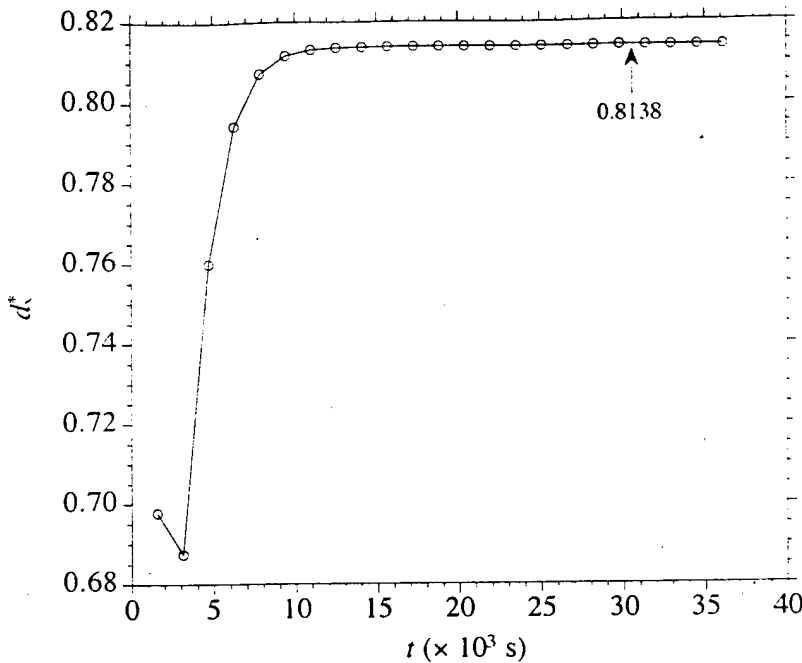


Figure 5.7: Nondimensional diffusivity versus time for diffusion through a square array of circular cylinders.

much longer time to run.

5.5 Simulations of Taylor Dispersion

Taylor dispersion between stationary infinite plates at $y = 0$ and $y = L$ (Figure 3.9) was simulated using the tracer hydrodynamic dispersion model. The method of moments was employed to yield Taylor dispersion coefficients which were compared with values from Taylor's analytical solution.

Taylor (1953) derived Equation 2.85 to describe the average cross section concentration in a cylindrical straight tube. Equation 2.85 indicates that such dispersion may be characterized as an asymptotic diffusional process with an effective dispersion coefficient $D_{Taylor} = d_0 + \frac{R^2 v_s^2}{48d_0}$. For the system shown in Figure 3.9; the Taylor dispersion coefficient becomes (Horne and Rodriguez 1983; Hull et al. 1987),

$$D_{Taylor} = d_0 + \frac{L^2 v_s^2}{210d_0}, \quad (5.10)$$

where v_s is the average channel velocity determined by,

$$v_s = \frac{1}{12\nu} FL^2. \quad (5.11)$$

The Reynolds number and Peclet number are,

$$Re = \frac{Lv_s}{\nu}, \quad (5.12)$$

and,

$$Pe = \frac{Lv_s}{d_0}, \quad (5.13)$$

respectively. The relationship between D_{Taylor} and Pe is,

$$\frac{D_{Taylor}}{d_0} = 1 + \frac{1}{210} Pe^2. \quad (5.14)$$

SPH was used to simulate Taylor dispersion between stationary infinite plates with $L = 0.001 \text{ m}$, $\rho = 10^3 \frac{\text{kg}}{\text{m}^3}$, $\nu = 10^{-6} \frac{\text{m}^2}{\text{s}}$, $d_0 = 10^{-6} \frac{\text{m}^2}{\text{s}}$, $F = 0.05, 0.10$, and $0.15 \frac{\text{m}}{\text{s}^2}$, and 50 fluid particles spanning the distance L . Poiseuille flow was evolved in a square unit cell of the size $L \times L$ and the size of the dispersion computing domain was $40L \times L$ (Figure 5.8).

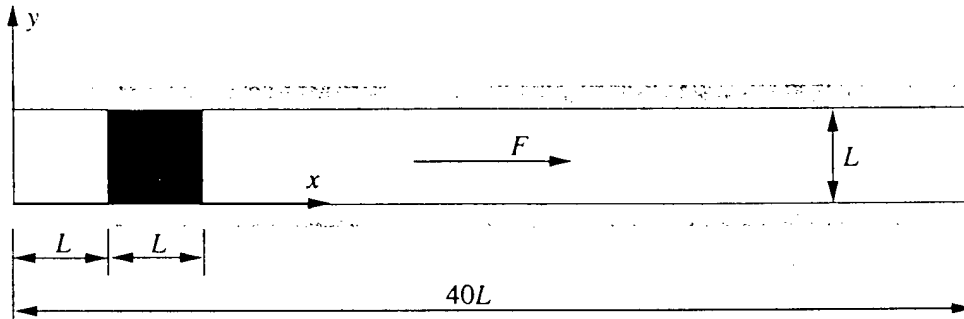


Figure 5.8: Initial condition ($t = 0$) for Taylor dispersion between two infinite plates.

A Schmidt number of 1 (i.e., $\nu = d_0 = 10^{-6} \frac{\text{m}^2}{\text{s}}$) was assumed for the fluid so that the time step due to viscosity would be comparable with that due to molecular diffusion. While the chosen value of ν is reasonable for a liquid, the value of d_0 is more appropriate for a gas. For the simulations considered here, the maximum time

step is $\Delta t = 0.0002 \text{ s}$ as determined by Equation 3.47. To observe the asymptotic Taylor dispersion behavior, time t must evolve to a value greater than t_c , which is defined appropriately for this problem geometry as.

$$t_c = \frac{L^2}{4d_0}, \quad (5.15)$$

according to Equation 2.84. Equation 5.15 yields $t_c = 0.25 \text{ s}$ for $d_0 = 10^{-6} \frac{\text{m}^2}{\text{s}}$. A simulation with a value of d_0 appropriate for a liquid, such as $d_0 = 10^{-10} \frac{\text{m}^2}{\text{s}}$, could be conducted; however, the value of t_c would then be 2500 s and at least 12,500,000 time steps ($\Delta t = 0.0002 \text{ s}$) would be required for $t > t_c$. Furthermore, as the tracer plume would be transported much further with increasing time, a much larger dispersion computing domain would be needed to contain the tracer body. Within practical limits, such a simulation could not be completed using currently available computers.

After the Poiseuille flow was evolved to steady state, the Taylor dispersion simulation started with the initial condition shown in Figure 5.8. Figure 5.9 shows plots of the tracer concentration field at four times for a simulation with $F = 0.10 \frac{\text{m}}{\text{s}^2}$. The plots were generated directly using discrete SPH data with the grey-scale representing the value of concentration.

Tracer dispersion was analyzed using the method of moments. Figure 5.10 is a plot of the zeroth moment M_0 as a function of time. The plot shows that tracer mass was conserved in the simulations. Figure 5.11 is a plot of the first moment in the x direction M_{1x} as a function of time. Values of M_{1x} were computed by subtracting the first moment at time $t = 0$ from that at time t . Figure 5.11 shows that the center of tracer mass moved at a constant velocity in each case. The average channel velocity v_s was calculated using Equation 5.4 with $\Delta t = 0.023, 0.019$ and 0.020 s for $F = 0.05, 0.10$, and $0.15 \frac{\text{m}}{\text{s}^2}$, respectively, and is shown in Figure 5.12. Figure 5.12 indicates that the flow fields were numerically stable after steady state conditions were reached. SPH solutions for v_s differ from the analytical solutions by a maximum of 1.2%.

Figure 5.13 is a plot of centered second moment in the x direction M_{2x} as a function of time. Values of M_{2x} were computed by subtracting centered second moment at time $t = t_c$ from that at time t . Figure 5.13 shows that, in each case, tracer spreading about its center grows linearly with time for $t > t_c$. The dispersion coefficient in the x direction D_x was calculated using Equation 5.6 with $\Delta t = 0.023$, 0.019 and 0.020 s for $F = 0.05$, 0.10 , and $0.15 \frac{m}{s^2}$, respectively, and is shown in Figure 5.14. It is seen that for $t > t_c = 0.25$ s, D_x fluctuates about an average value. Asymptotic values of D_x were taken as Taylor dispersion coefficients D_{Taylor} and were found to be 1.0605×10^{-6} , 1.3034×10^{-6} , and $1.6848 \times 10^{-6} \frac{m^2}{s}$ for $F = 0.05$, 0.10 , and $0.15 \frac{m}{s^2}$, respectively. SPH solutions for D_{Taylor} were less than the analytical solutions by a maximum of 3.4%. Taylor dispersion is essentially a one-dimensional phenomenon. The changes in the first moment and centered second moment in the y direction were found to have a maximum magnitude of $10^{-8} m$ and $10^{-9} m^2$, respectively, for SPH simulations. These values likely result from numerical errors. A summary of results for Taylor dispersion simulations is shown in Table 5.1.

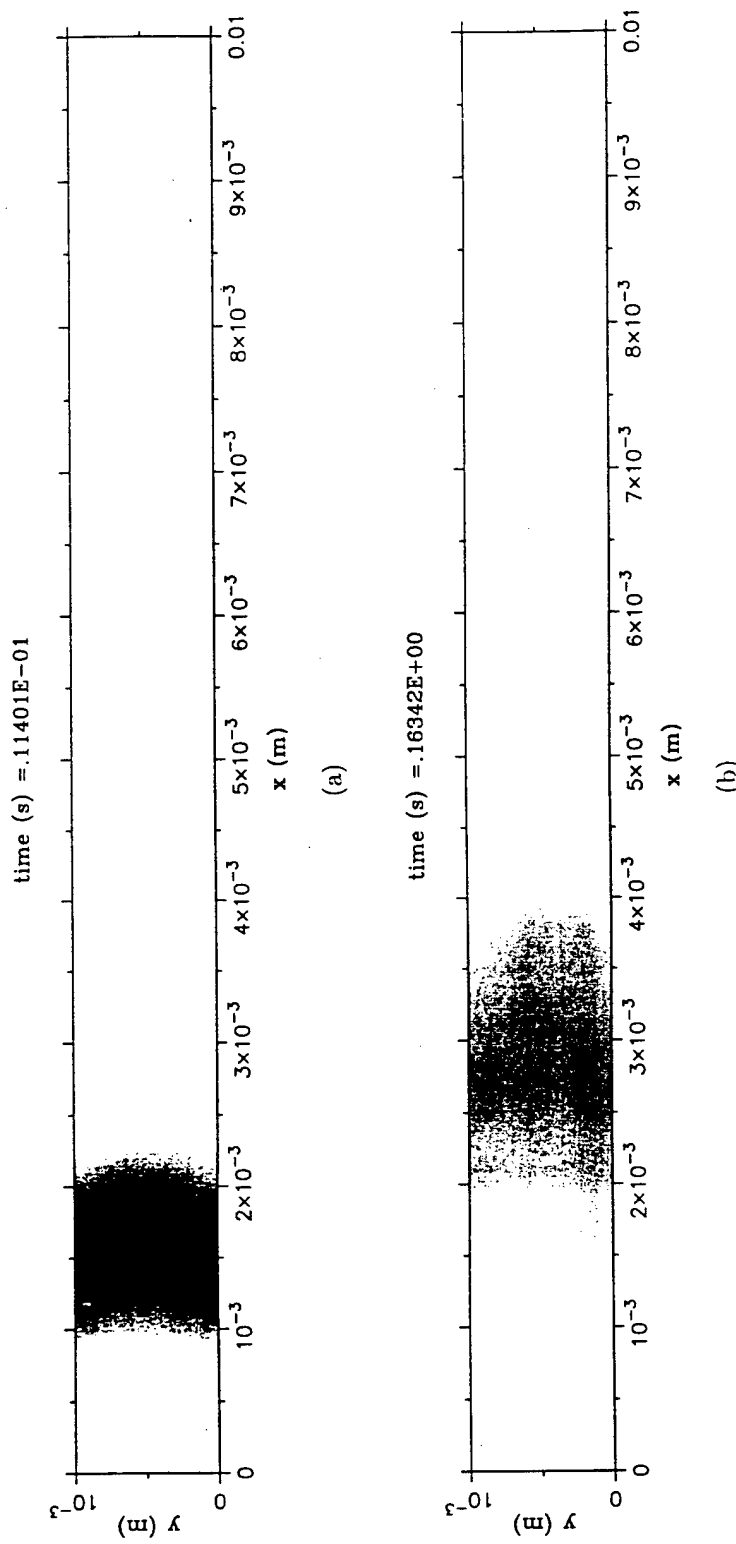


Figure 5.9: Tracer concentration fields for Taylor dispersion between two infinite plates at elapsed times of (a) 0.01140 s , (b) 0.16342 s , (c) 0.35344 s , and (d) 0.52448 s .

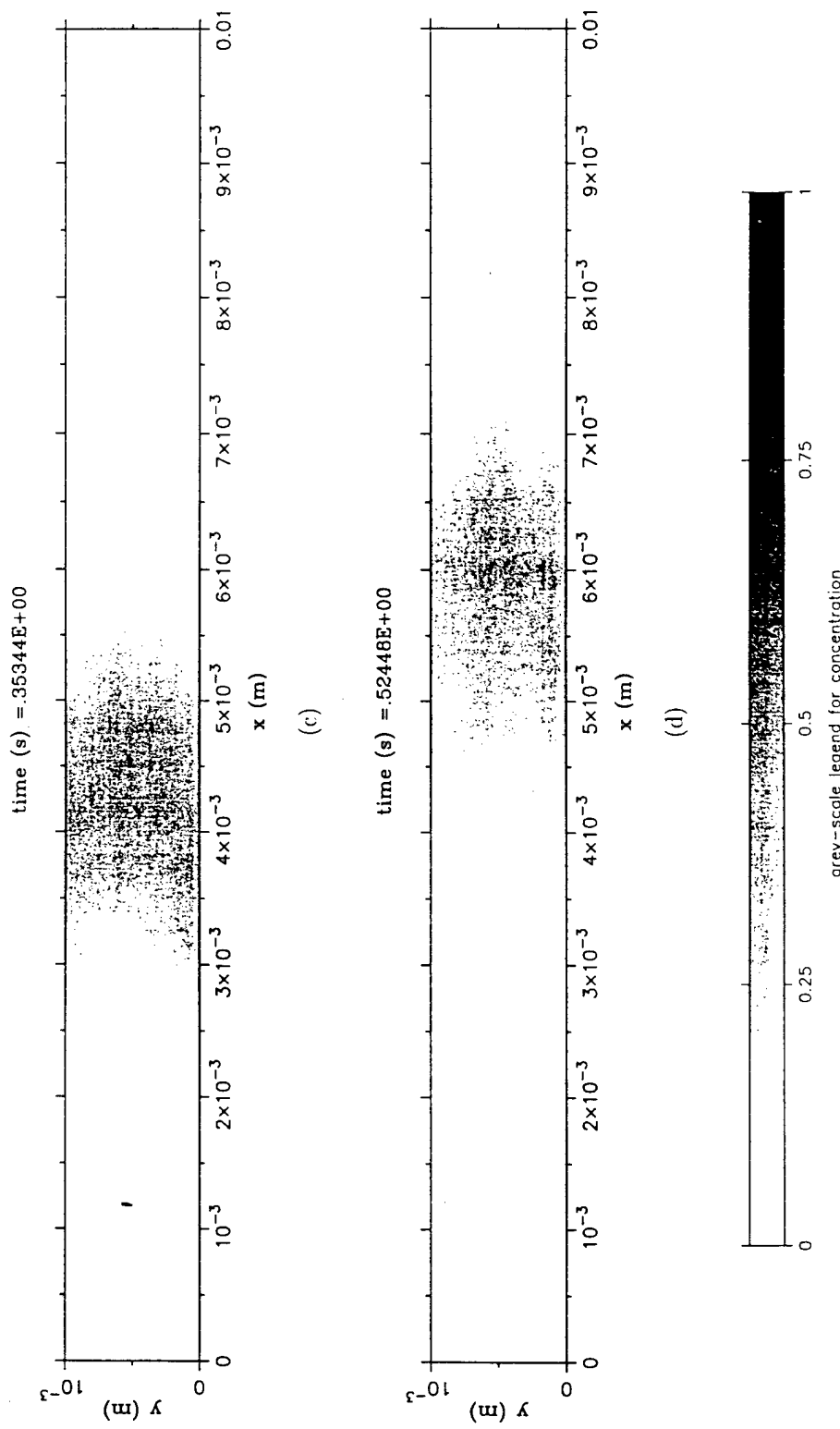


Figure 5.9: Continue.

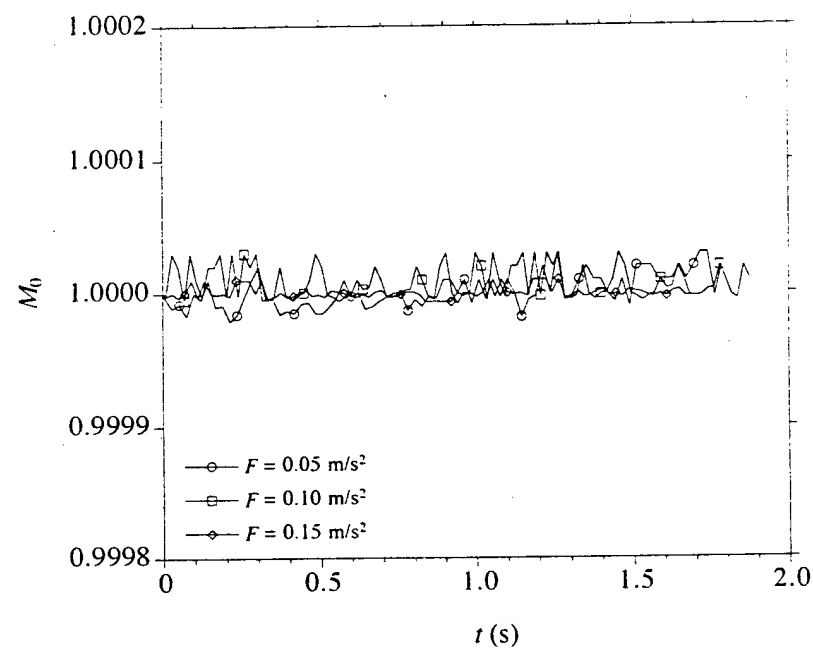


Figure 5.10: The zeroth moment of tracer distribution versus time for Taylor dispersion between two infinite plates.

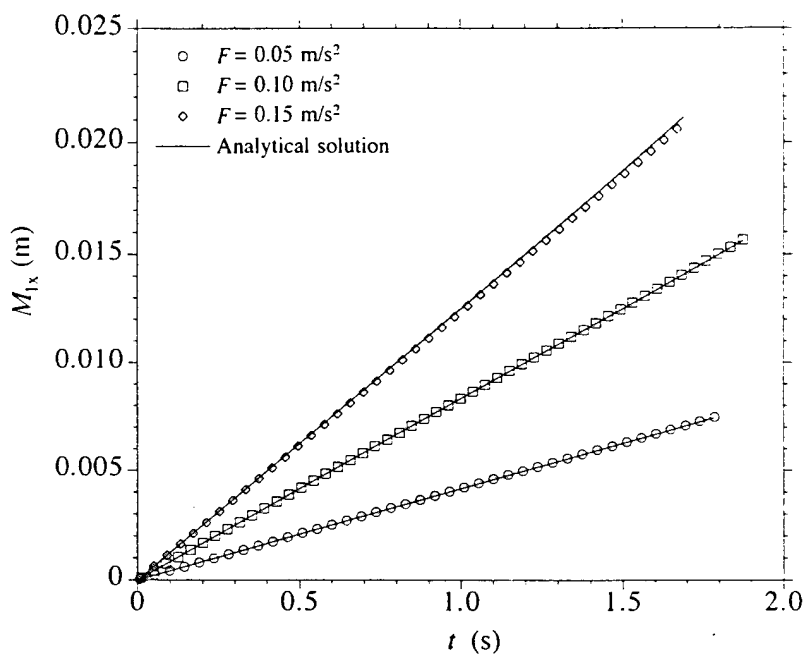


Figure 5.11: The first moment in the x direction of tracer distribution versus time for Taylor dispersion between two infinite plates.

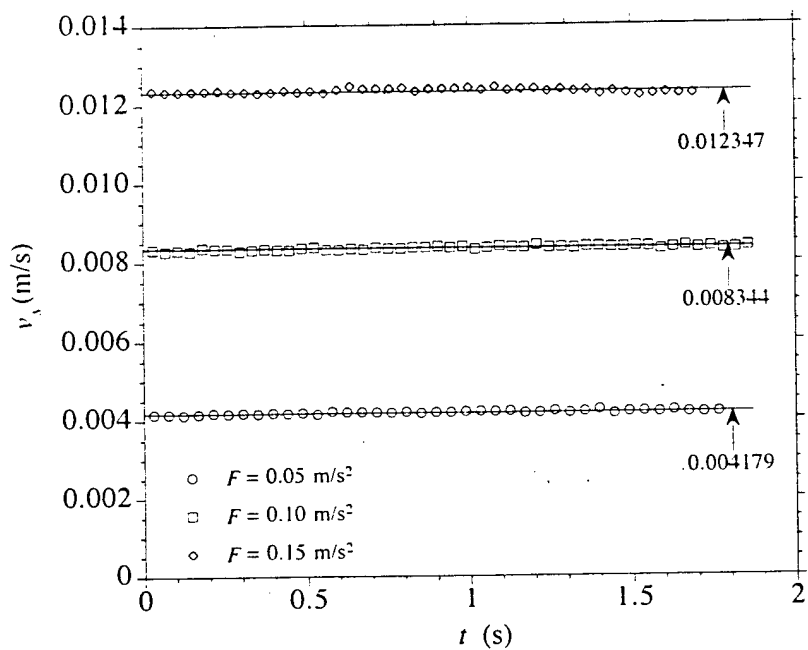


Figure 5.12: Average channel velocity versus time for Taylor dispersion between two infinite plates.

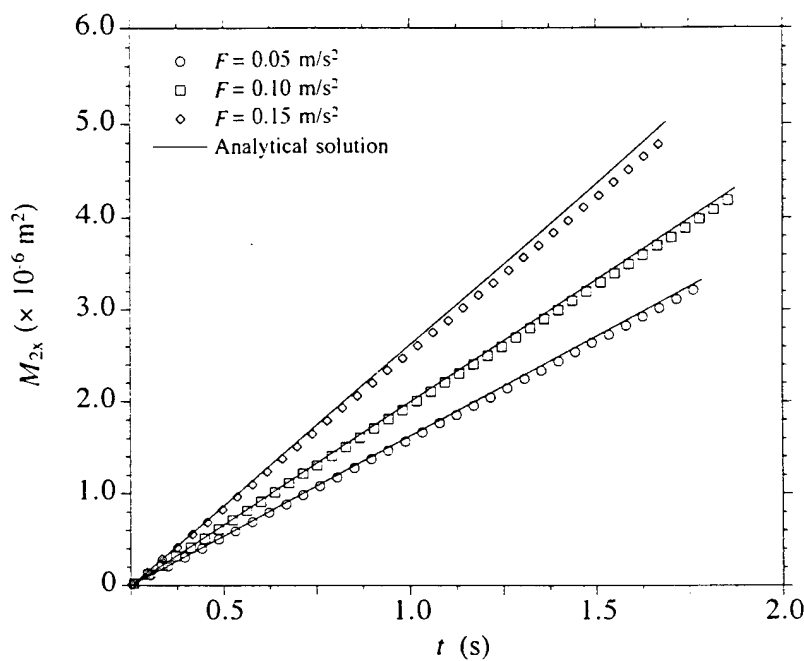


Figure 5.13: Centered second moment in the x direction of tracer distribution versus time for Taylor dispersion between two infinite plates.

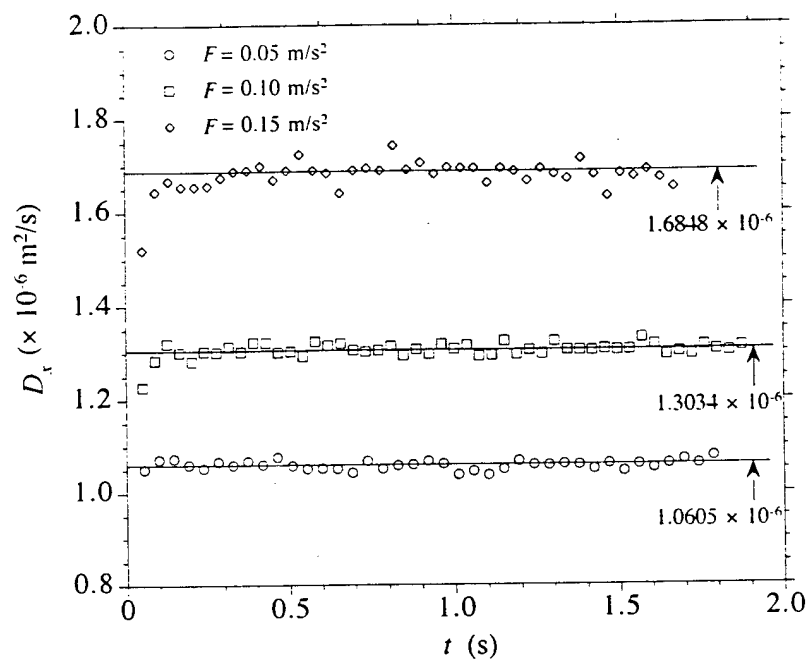


Figure 5.14: Hydrodynamic dispersion coefficient in the x direction versus time for Taylor dispersion between two infinite plates.

Table 5.1: Summary of results for Taylor dispersion simulations.

$L = 0.001 \text{ m}$, $\nu = 10^{-6} \frac{\text{m}^2}{\text{s}}$, $d_0 = 10^{-6} \frac{\text{m}^2}{\text{s}}$, $\rho = 10^3 \frac{\text{kg}}{\text{m}^3}$, $Re = Pe$							
$F \left(\frac{m}{s} \right)$	Re, Pe	$v_s \left(\frac{m}{s} \right)$ (SPH)	$v_s \left(\frac{m}{s} \right)$ (Eq. 5.11)	error (v_s)	$\frac{D_{Taylor}}{d_0}$ (SPH)	$\frac{D_{Taylor}}{d_0}$ (Eq. 5.14)	error ($\frac{D_{Taylor}}{d_0}$)
0.05	4.1667	0.004179	0.004167	+0.29%	1.0605	1.0827	-2.04%
0.10	8.3333	0.008344	0.008333	+0.13%	1.3034	1.3307	-2.05%
0.15	12.5000	0.012347	0.012500	-1.22%	1.6848	1.7440	-3.40%

5.6 Simulations of Tracer Convection

In this section, the process of tracer convection (i.e., without diffusion) in two-dimensional spatially periodic porous media is studied. Five simulations were completed for tracer convection through spatially periodic porous media with circular cylinders arranged in square, staggered, and hexagonal arrays. The fluid was modeled as water, i.e., $\rho = 10^3 \frac{kg}{m^3}$ and $\nu = 10^{-6} \frac{m^2}{s}$ and tracer convection was driven by body force F . As shown in Figure 5.15, γ is the angle between the direction of F and the positive x direction. The direction of F is denoted by L , while the direction perpendicular to L is denoted by T . Table 5.2 presents a summary of information for the tracer convection simulations. Figures 5.16 to 5.20 show the tracer fields at four times for each simulation. The tracer fields were analyzed using the method of moments for seepage velocity v_s , effective porosity n_{eff} , and mechanical dispersion coefficients D_{mL} and D_{mT} . Tortuosity \mathcal{T} of the media was also calculated. A summary of results for the tracer convection simulation analysis is presented in Table 5.3.

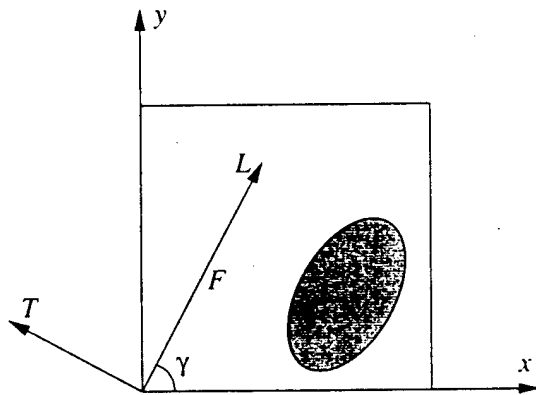


Figure 5.15: Body force F direction L and perpendicular direction T .

Table 5.2: Summary of information for tracer convection simulations.

Simulation	array type	R (mm)	n	N_{part}	F ($\frac{m}{s^2}$)	γ
1	square array	0.5	0.8	3384	0.001	0°
2	staggered array	0.5	0.8	8320	0.001	0°
3	staggered array	0.5	0.8	8320	0.001	30°
4	hexagonal array	0.5	0.8	8160	0.0007	0°
5	hexagonal array	0.5	0.8	8160	0.0007	45°

Table 5.3: Summary of results for tracer convection simulation analysis.

Simulation	\mathcal{T}	v_s ($\frac{m}{s}$)	Re	v ($\frac{m}{s}$)	n_{eff}	n
1	1.051	9.30×10^{-5}	0.047	7.35×10^{-5}	0.790	0.8
2	1.139	9.06×10^{-5}	0.045	7.17×10^{-5}	0.791	0.8
3	1.067	9.08×10^{-5}	0.045	7.18×10^{-5}	0.791	0.8
4	1.094	6.57×10^{-5}	0.033	5.19×10^{-5}	0.790	0.8
5	1.082	6.56×10^{-5}	0.033	5.18×10^{-5}	0.790	0.8

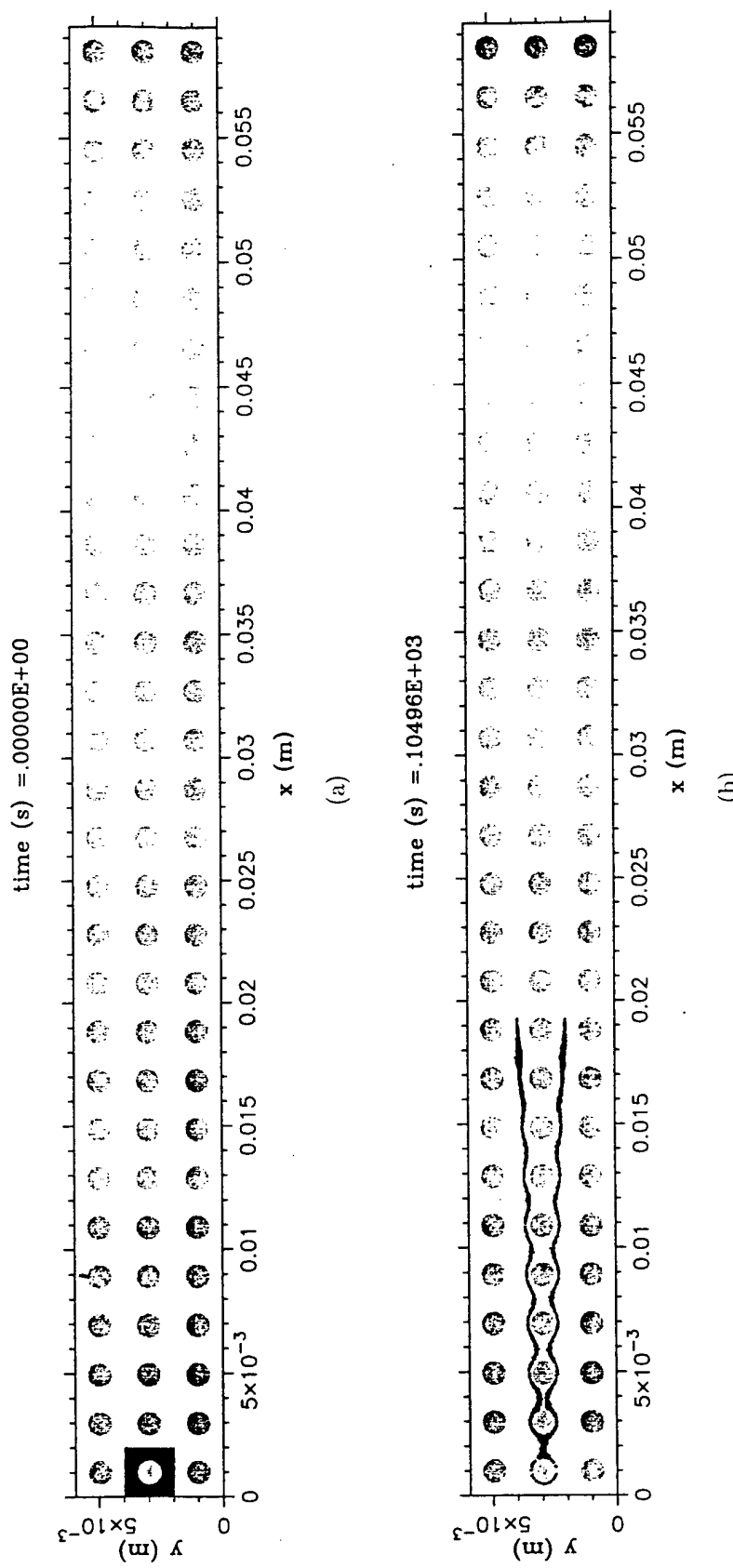


Figure 5.16: Tracer convection through a square array of circular cylinders ($\gamma = 0^0$). Tracer particles are shown in black.

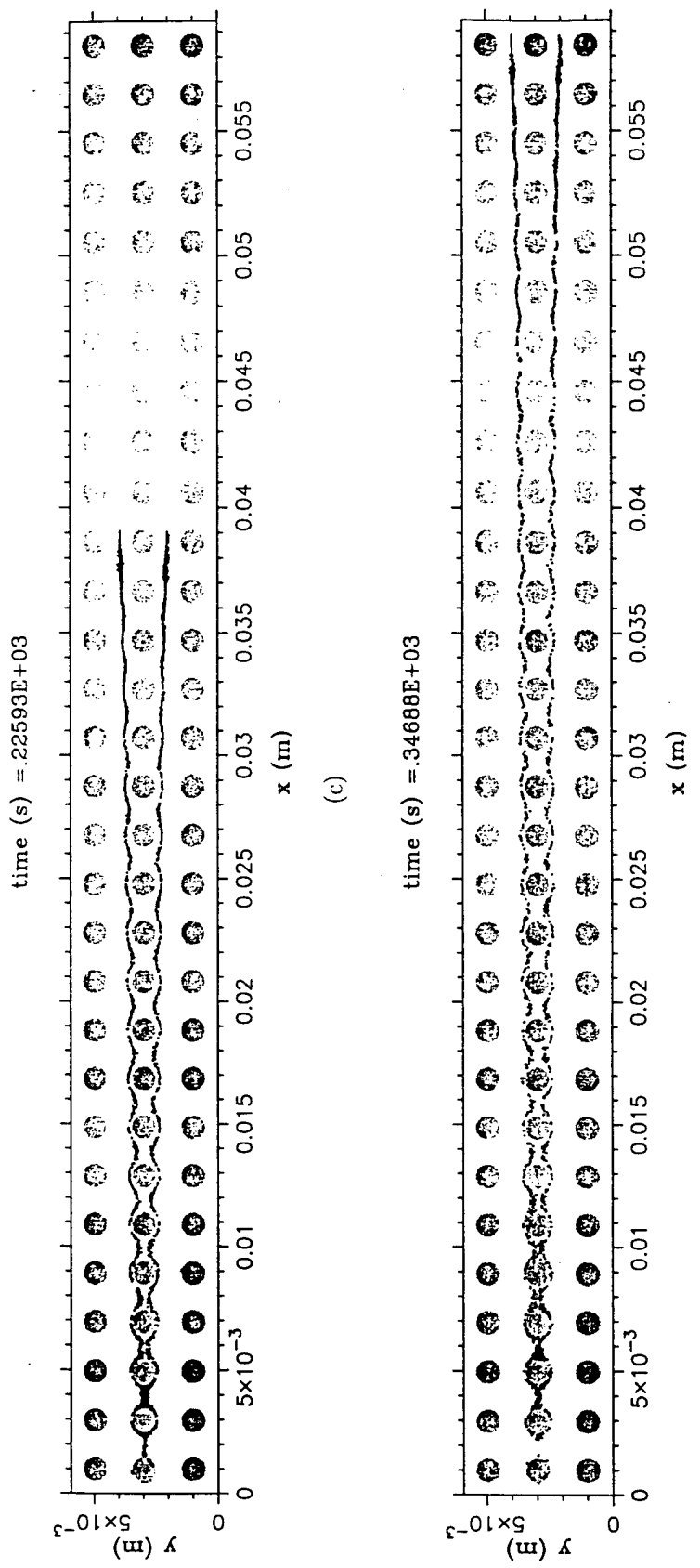


Figure 5.16: Continue.

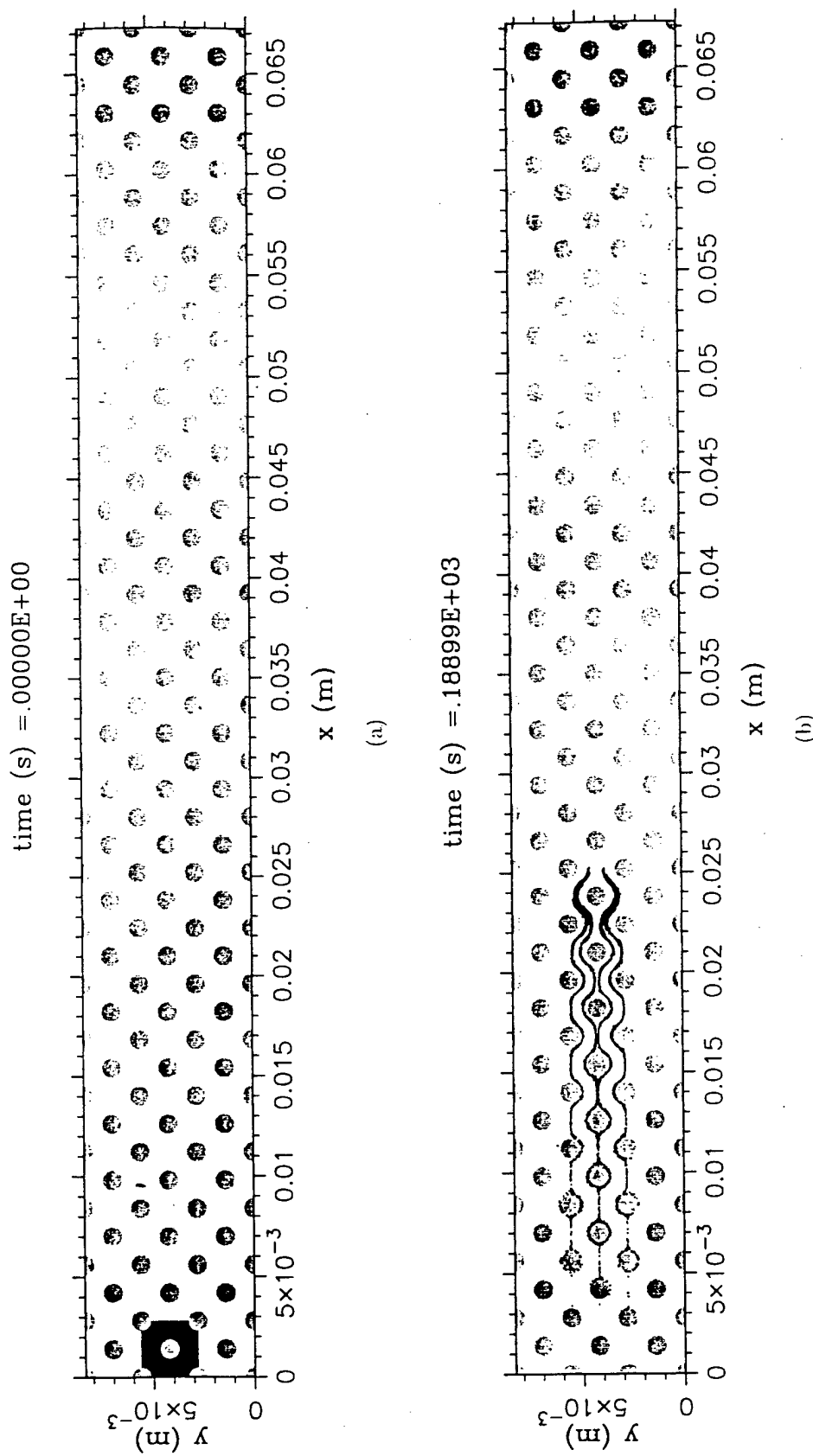


Figure 5.17: Tracer convection through a staggered array of circular cylinders ($\gamma = 0^0$). Tracer particles are shown in black.

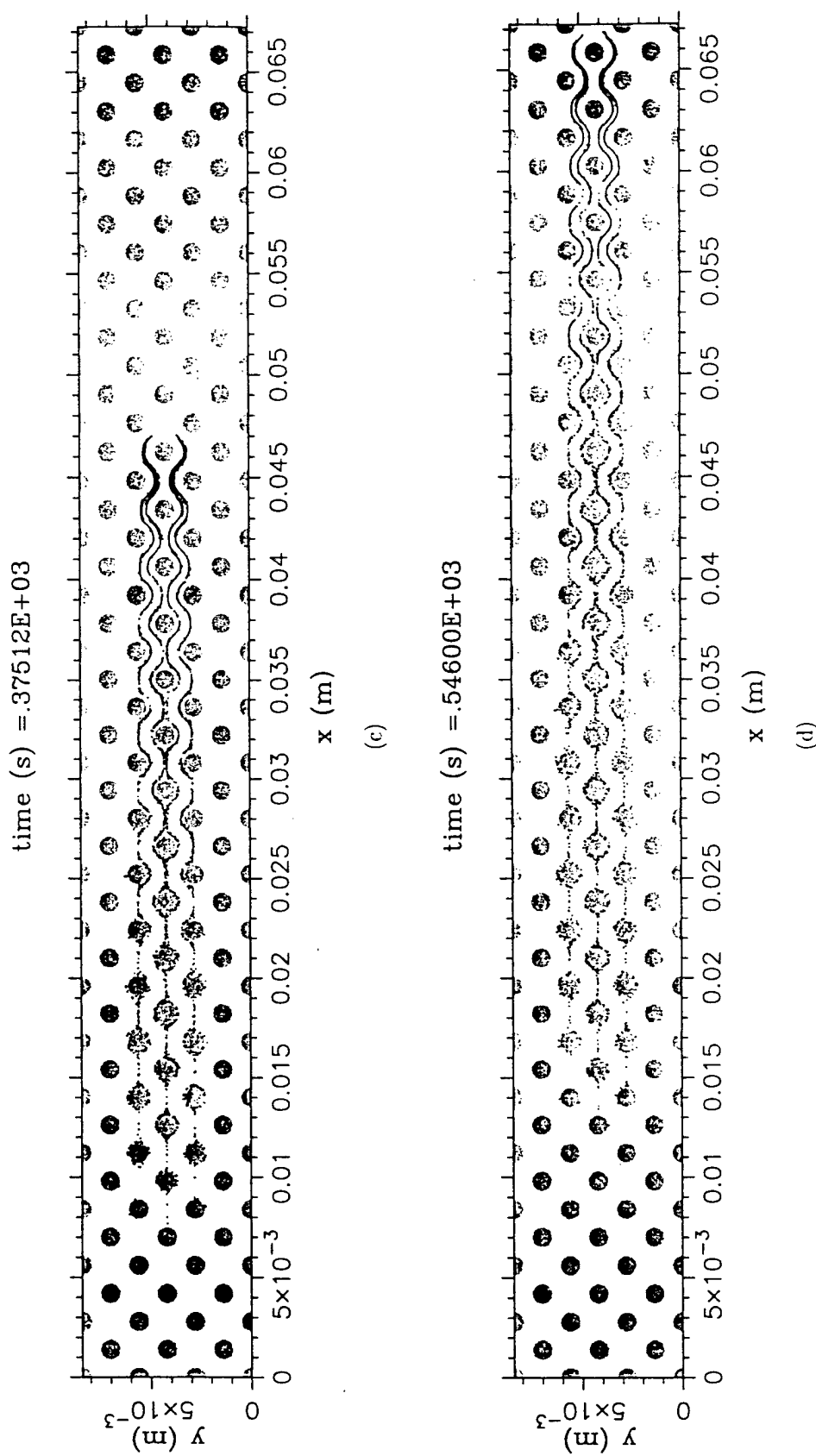


Figure 5.17: Continue.

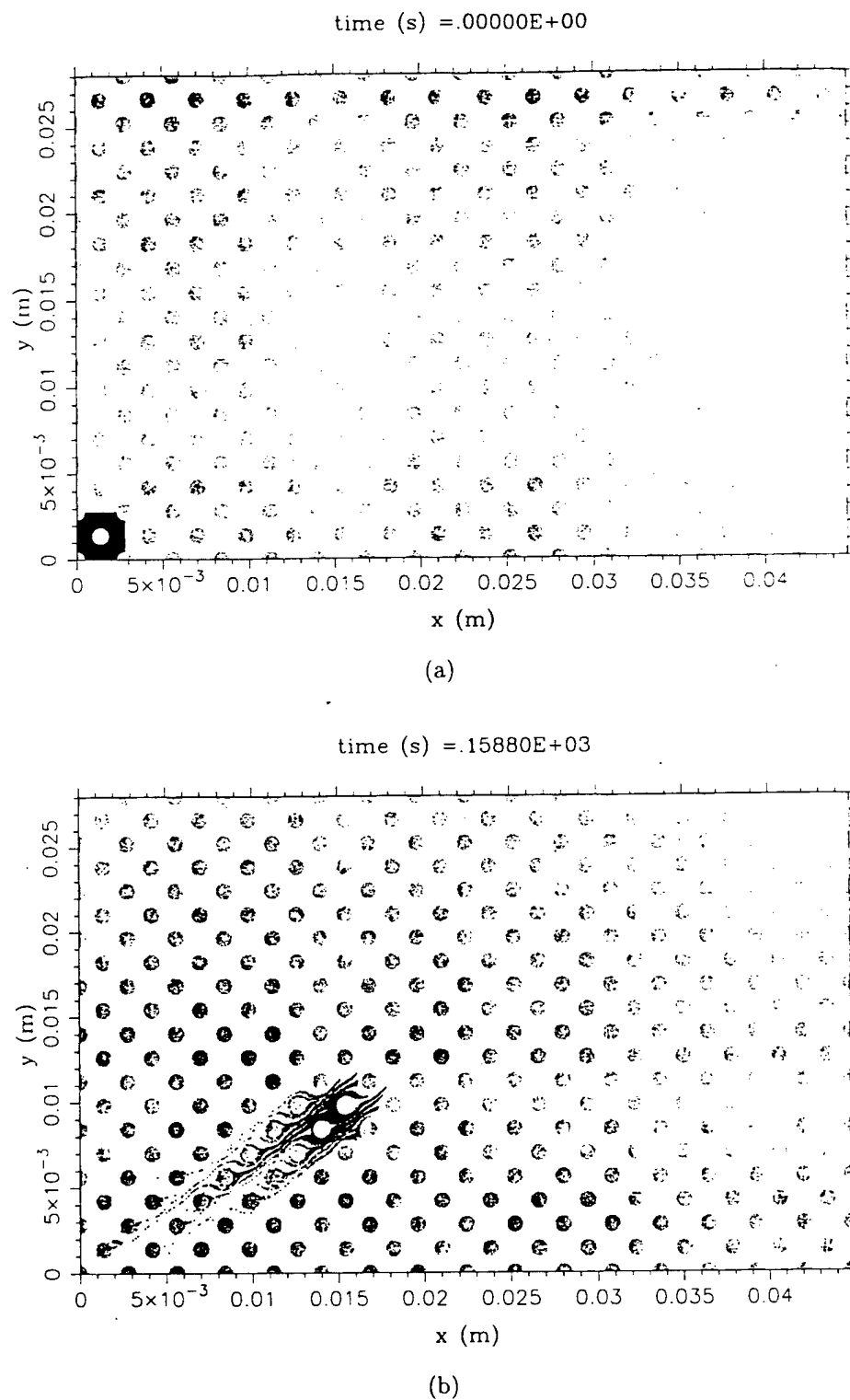


Figure 5.18: Tracer convection through a staggered array of circular cylinders ($\gamma = 30^\circ$). Tracer particles are shown in black.

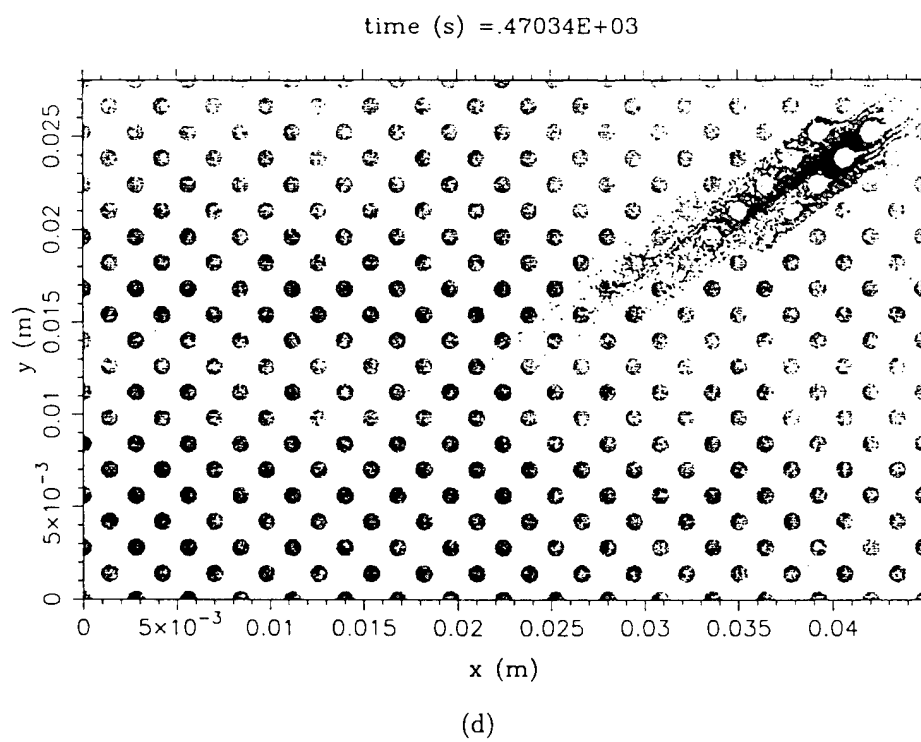
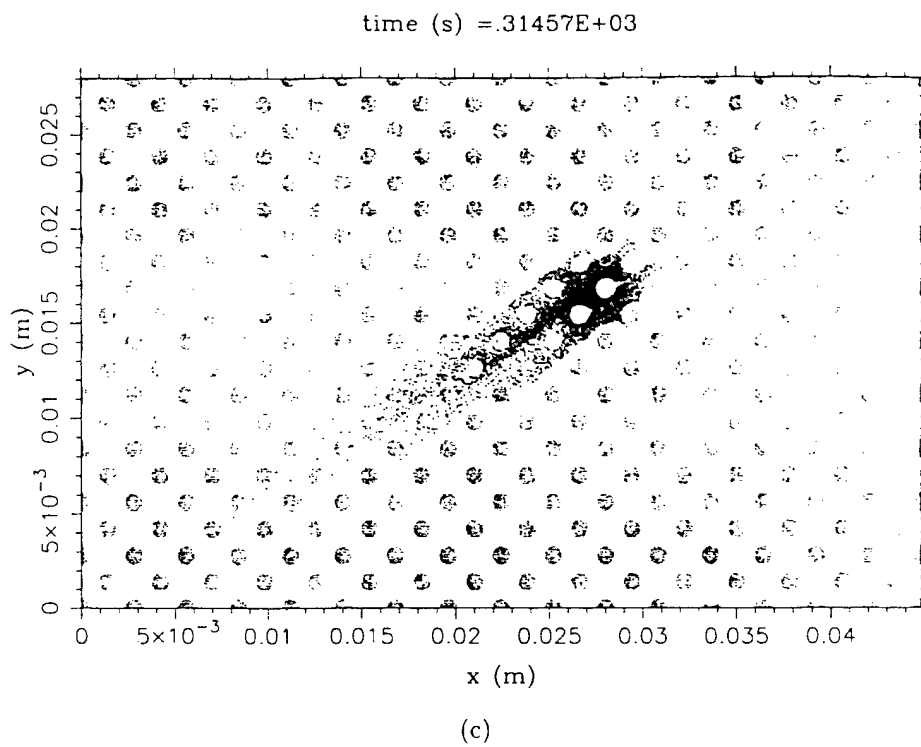
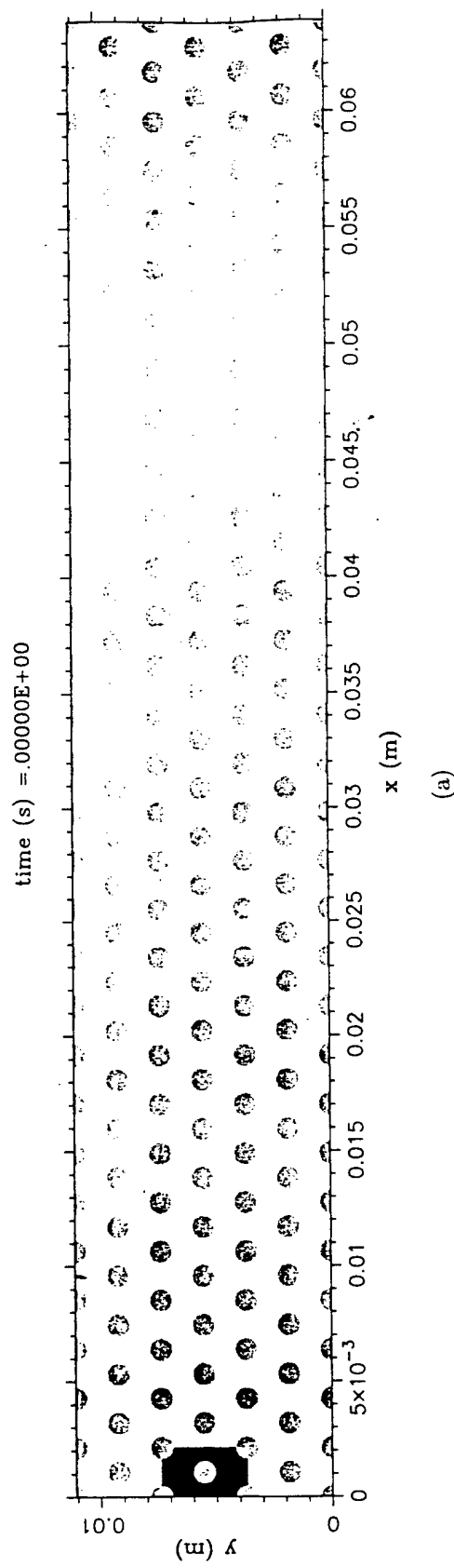
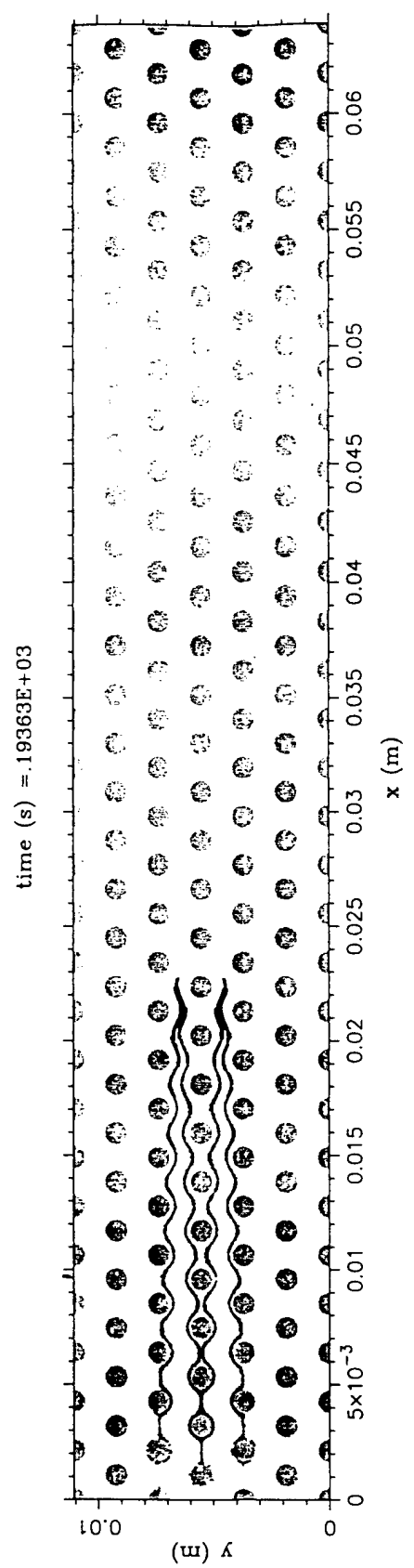


Figure 5.18: Continue.



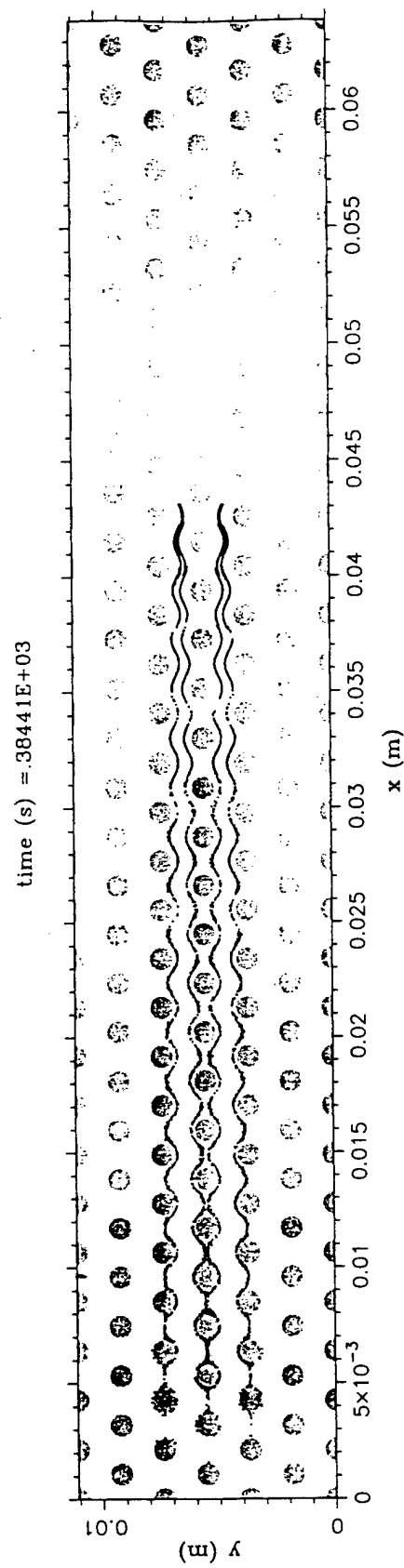
(a)

Figure 5.19: Tracer convection through a hexagonal array of circular cylinders ($\gamma = 0^0$). Tracer particles are shown in black.



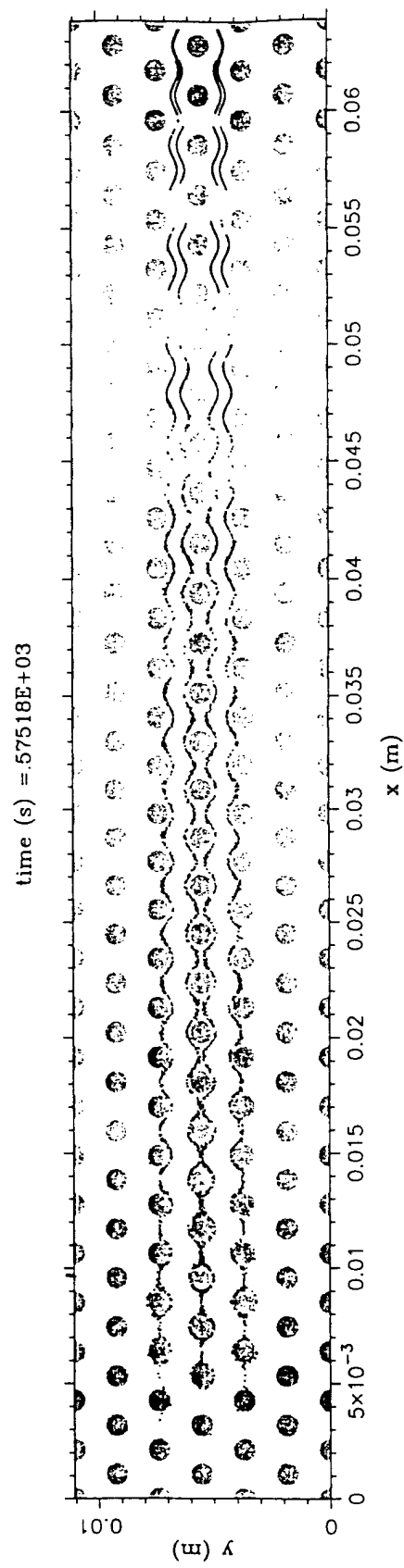
(b)

Figure 5.19: Continue.



(c)

Figure 5.19: Continue.



(d)

Figure 5.19: Continue.

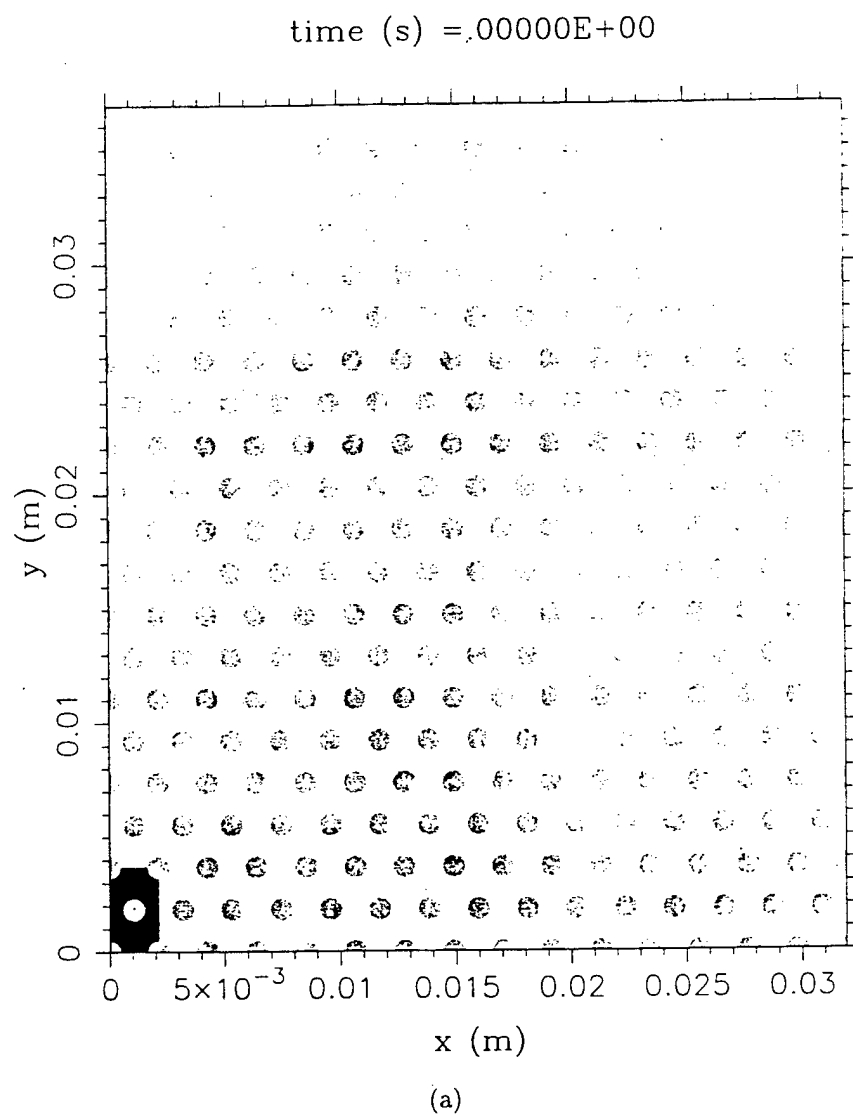


Figure 5.20: Tracer convection through a hexagonal array of circular cylinders ($\gamma = 45^0$). Tracer particles are shown in black.

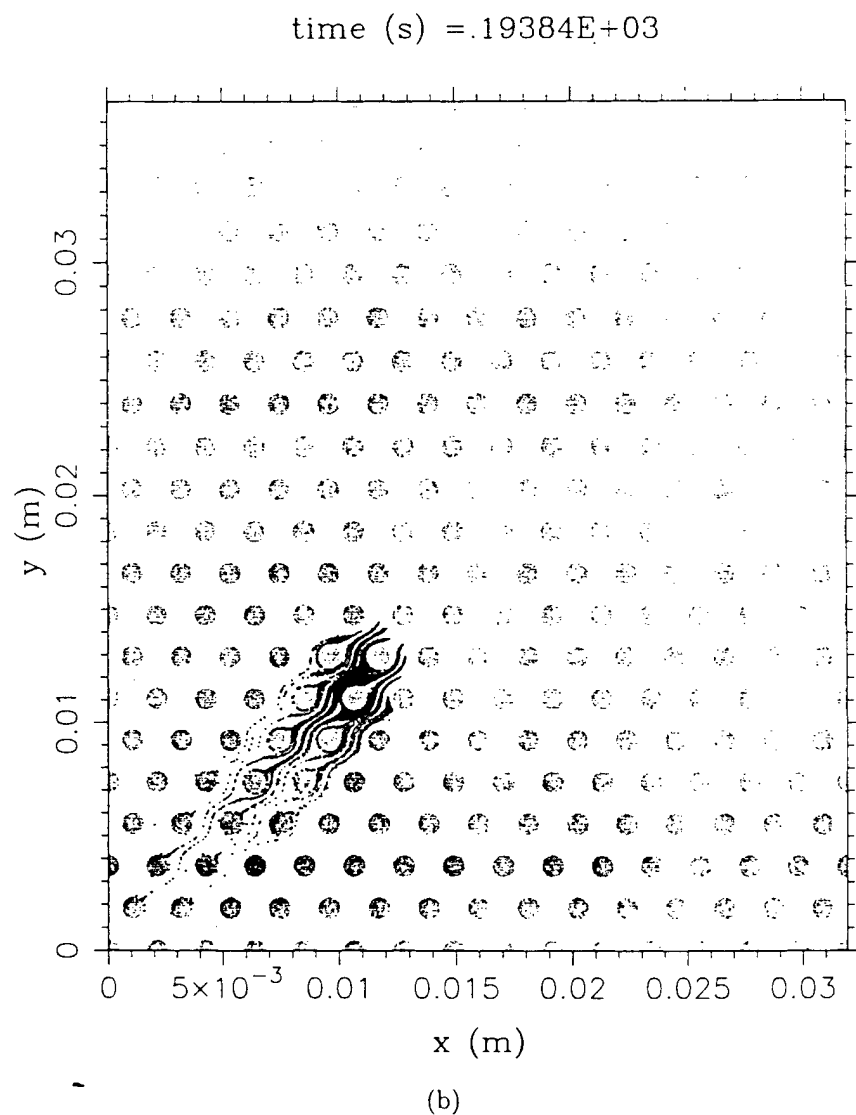


Figure 5.20: Continue.

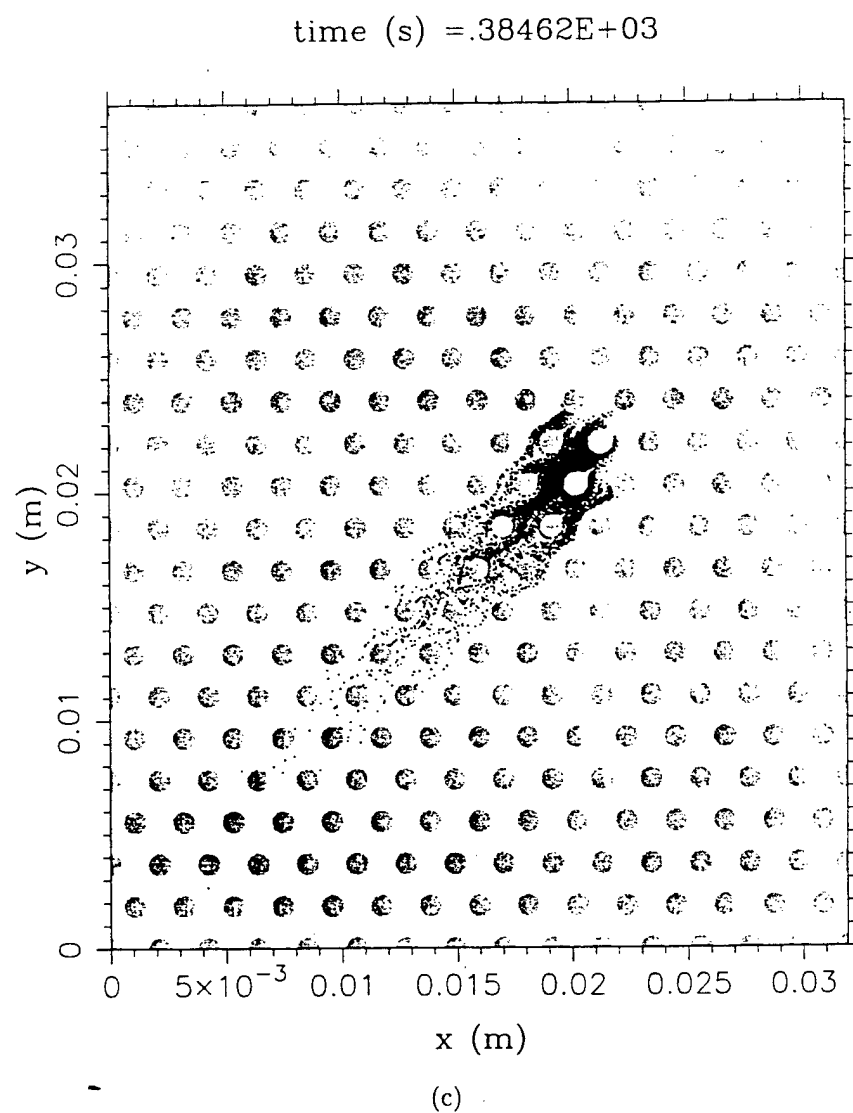


Figure 5.20: Continue.

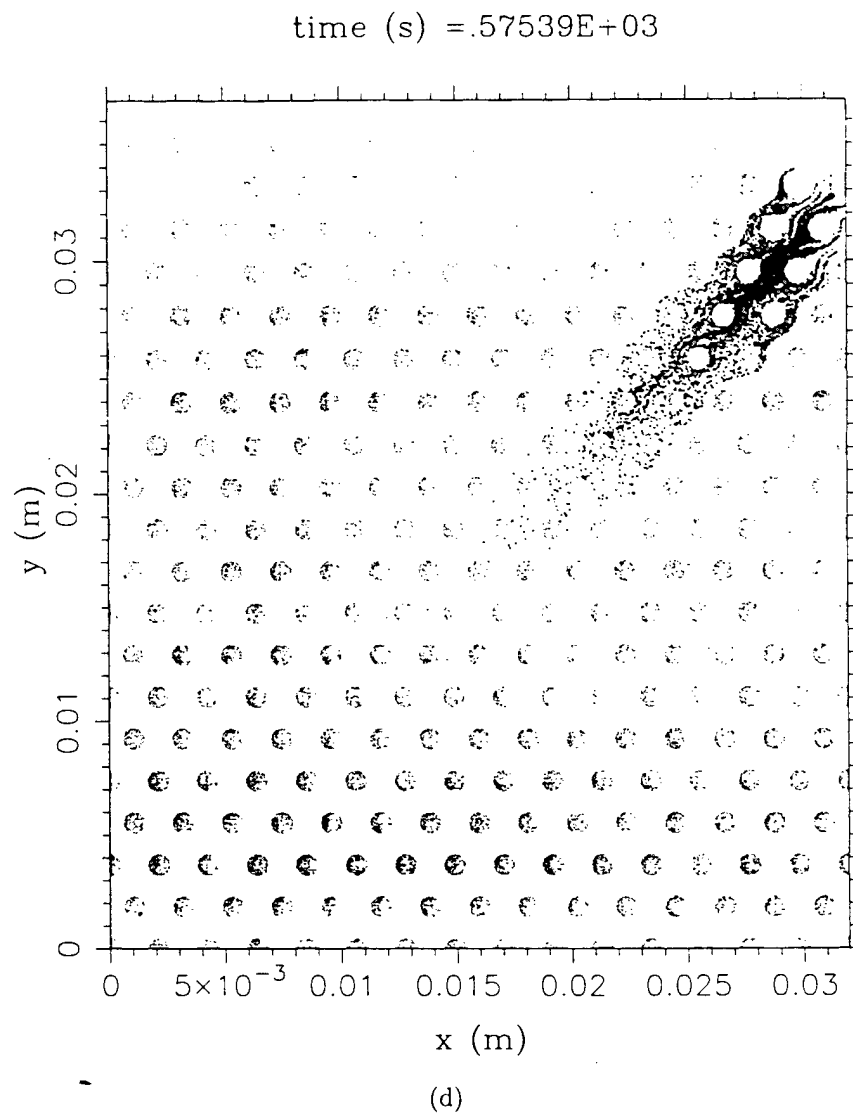


Figure 5.20: Continue.

5.6.1 Tortuosity of Porous Media

In SPH, trajectories of individual fluid masses (SPH tracer particles) can be recorded as they travel through the void system of the medium. Figures 5.22 to 5.26 show the trajectories of four tracer particles for each simulation in Table 5.2. Tortuosity of the porous medium \mathcal{T} was calculated as.

$$\mathcal{T} = \frac{\sum_z \frac{L_{e,z}}{L_z}}{N_{tracer}}, \quad (5.16)$$

where $L_{e,z}$ and L_z are the length of trajectory and the straight-line distance traveled by tracer particle z , respectively (Figure 5.21), and N_{tracer} is the total number of tracer particles in the flow field.

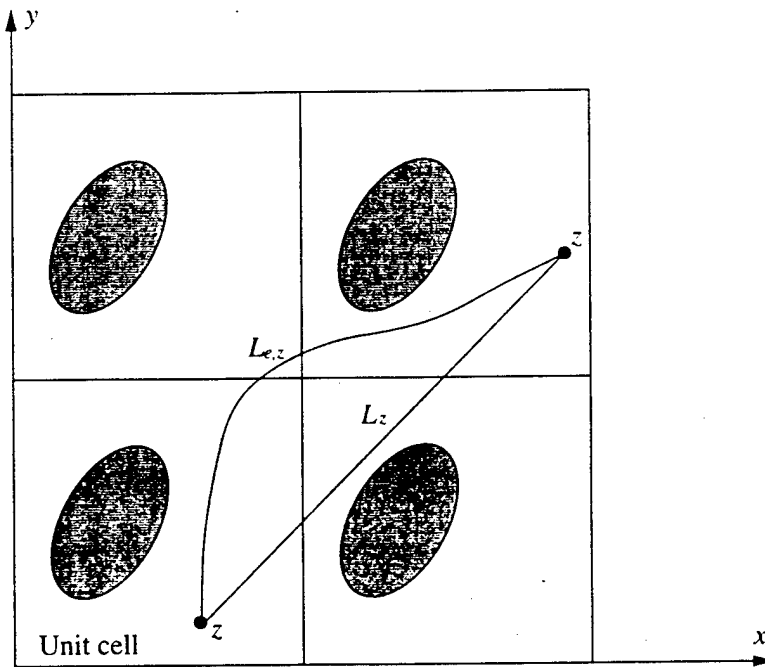


Figure 5.21: Trajectory $L_{e,z}$ and straight-line distance L_z traveled by tracer particle z .

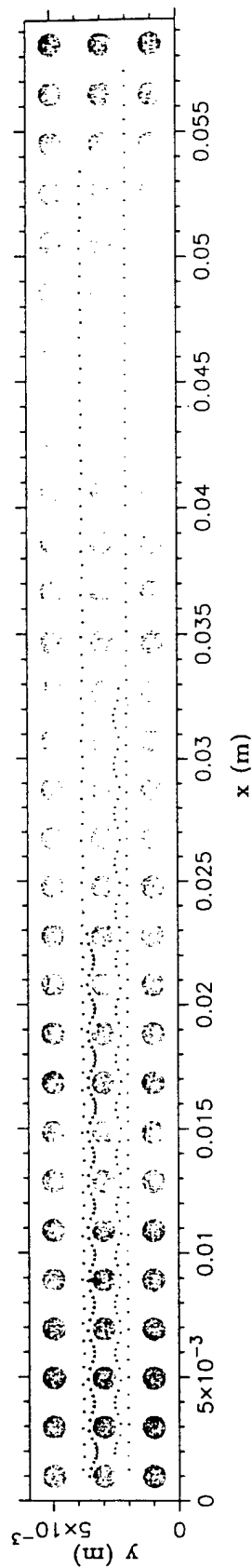


Figure 5.22: Trajectories of tracer particles in a square array of circular cylinders ($\gamma = 0^0$).

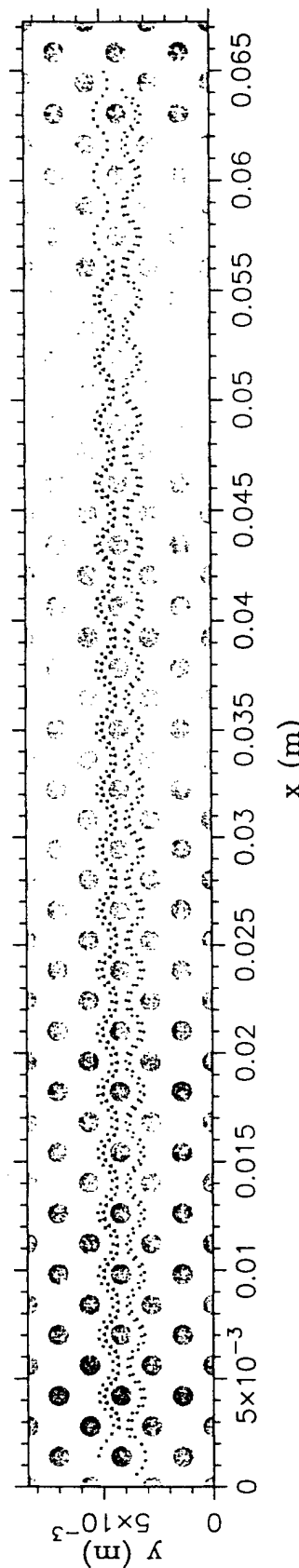


Figure 5.23: Trajectories of tracer particles in a staggered array of circular cylinders ($\gamma = 0^0$).

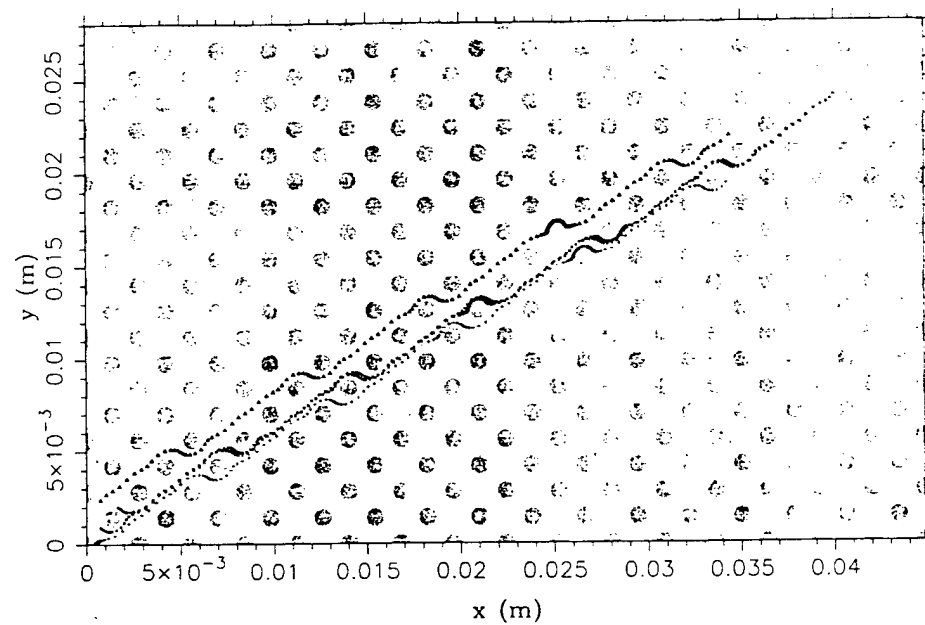


Figure 5.24: Trajectories of tracer particles in a staggered array of circular cylinders ($\gamma = 30^\circ$).

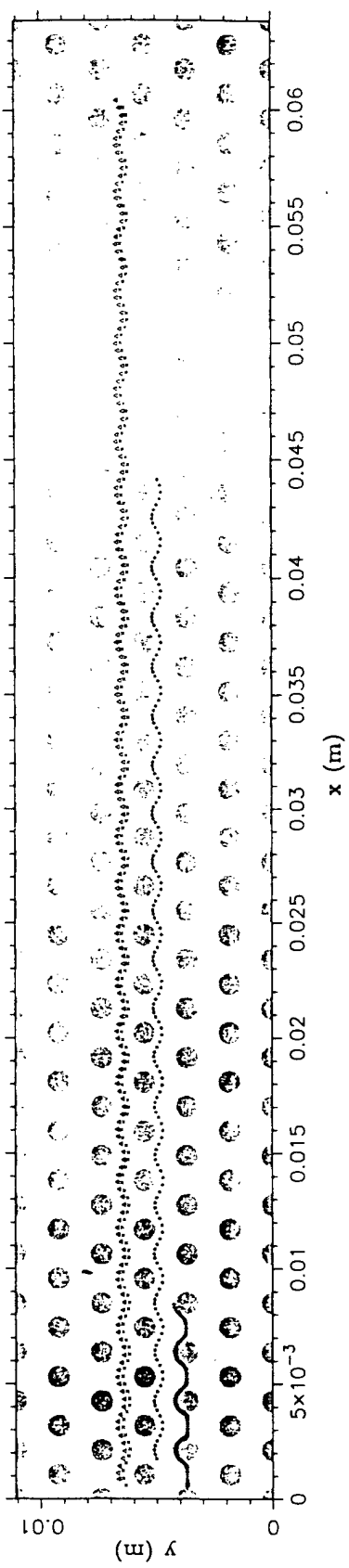


Figure 5.25: Trajectories of tracer particles in a hexagonal array of circular cylinders ($\gamma = 0^\circ$).

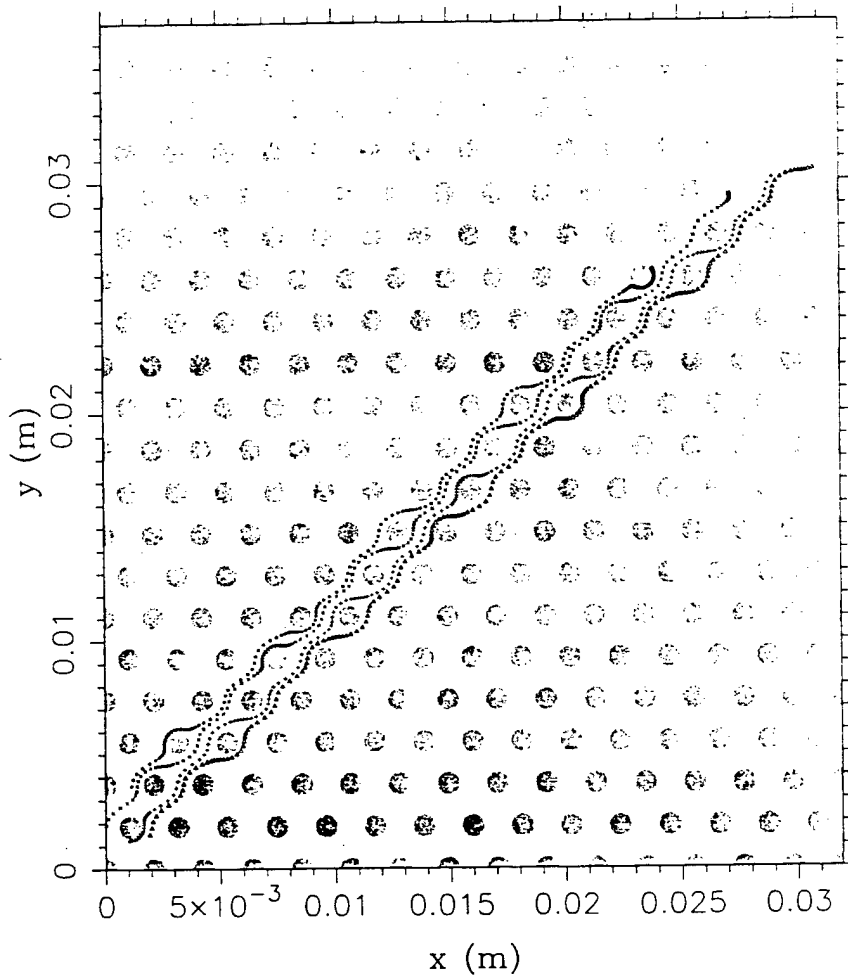


Figure 5.26: Trajectories of tracer particles in a hexagonal array of circular cylinders ($\gamma = 45^\circ$).

Figure 5.27 shows the tortuosity of the media as a function of time for each tracer convection simulation in Table 5.2. A constant tortuosity value exists for each case, which is presented in Table 5.3. A few interesting observations can be made from Figure 5.27. Tortuosity values are considerably less than the commonly-

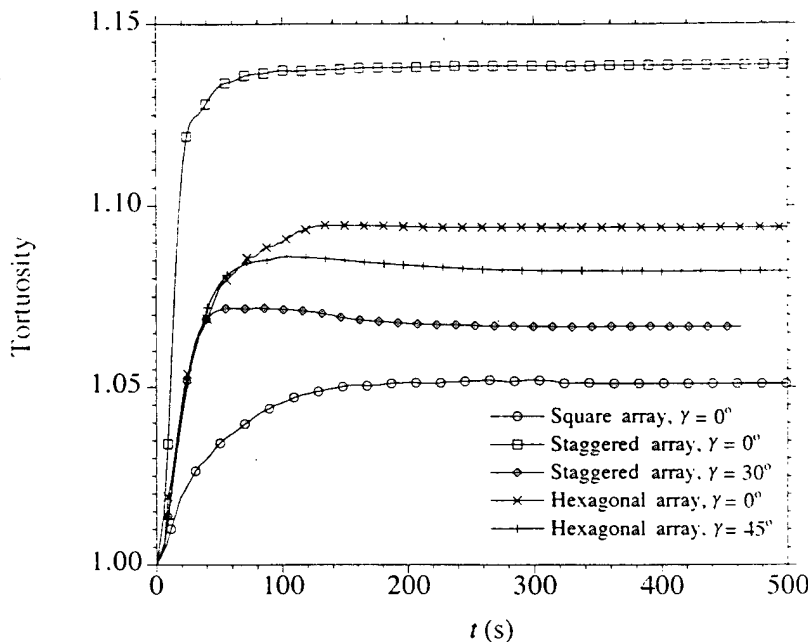


Figure 5.27: Tortuosity versus time for simulations in Table 5.2.

used value of $\sqrt{2} = 1.414$, which was originally proposed by Carman (1937) for unconsolidated porous aggregates. It is also apparent that tortuosity is a function of media geometry. For the three simulations with $\gamma = 0$, the square and staggered arrays have the smallest and largest tortuosity, respectively. For the square array with $\gamma = 0$, most of the tracer particles will have an unobstructed travel path (Figure 5.22), which produces a tortuosity value close to unity. The staggered array introduces more obstacles into the flow field and tortuosity increases as a result. Although the hexagonal array has the same solid surface area in the unit cell as the staggered array, it has larger flow channels which results in a tortuosity larger than the square array, but less than the staggered array.

Not only a function of media geometry, tortuosity is also a function of the direction of the applied body force. The effect of body force direction on tortuosity is apparent

for the staggered array (simulations 2 and 3 in Table 5.2). For $\gamma = 30^0$, fewer tracer particles must travel around the center solid in the staggered array than that if $\gamma = 0$. This results in a lower tortuosity value for $\gamma = 30^0$. Similar observations can be made regarding the effect of γ for the hexagonal array.

5.6.2 Seepage Velocity and Effective Porosity of Porous Media

Seepage velocity for each tracer convection simulation was calculated using Equation 5.4. Figure 5.28 shows seepage velocity in the L direction v_{sL} and in the T direction v_{sT} as a function of time for simulation 1 in Table 5.2. v_{sL} fluctuates about an average value of $v_s = 9.30 \times 10^{-5} \frac{m}{s}$ within a 5% range, which indicates that the tracer flow field is numerically stable. v_{sT} is essentially zero as expected. The fluctuations of v_{sT} about zero likely result from numerical errors. Other values of v_{sL} and v_{sT} for other simulations in Table 5.2 show similar patterns when plotted as a function of time. Values of v_s are presented in Table 5.3, which were also used to calculate $Re = \frac{v_s R}{\nu}$ for the simulations. The small values of Re indicate creeping flow conditions.

Effective porosity n_{eff} of the medium was calculated as,

$$n_{eff} = \frac{v}{v_s}, \quad (5.17)$$

where v is the Darcy velocity in body force direction calculated using Equations 3.62 and 3.63 for the steady state flow field. Values of n_{eff} are presented in Table 5.3. The effective porosity excludes “dead end” pores and thus represents the fraction of pore space that is available to transmit fluids. For the media type considered in this work, n_{eff} should be equal to n . The small difference between n_{eff} and n in Table 5.3 is due to the placement of SPH boundary particles. As the first layer of boundary particles is placed on the solid surface, the porous medium simulated actually has a porosity slightly smaller than the nominal value. Although n_{eff} is nearly equal to n for uniform granular materials, it is significantly less than n for clays due to their more complex microfabric of clay particle clusters and intercluster voids.

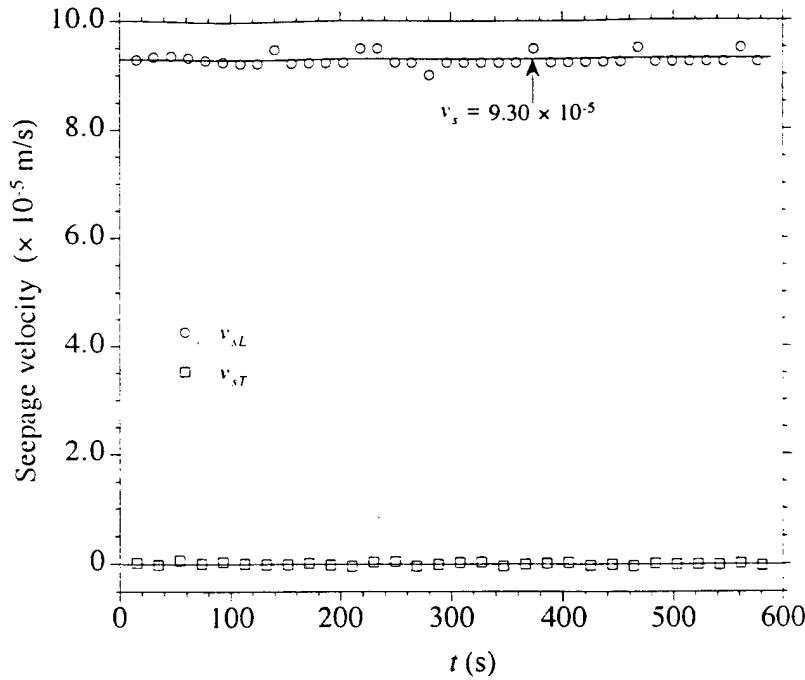
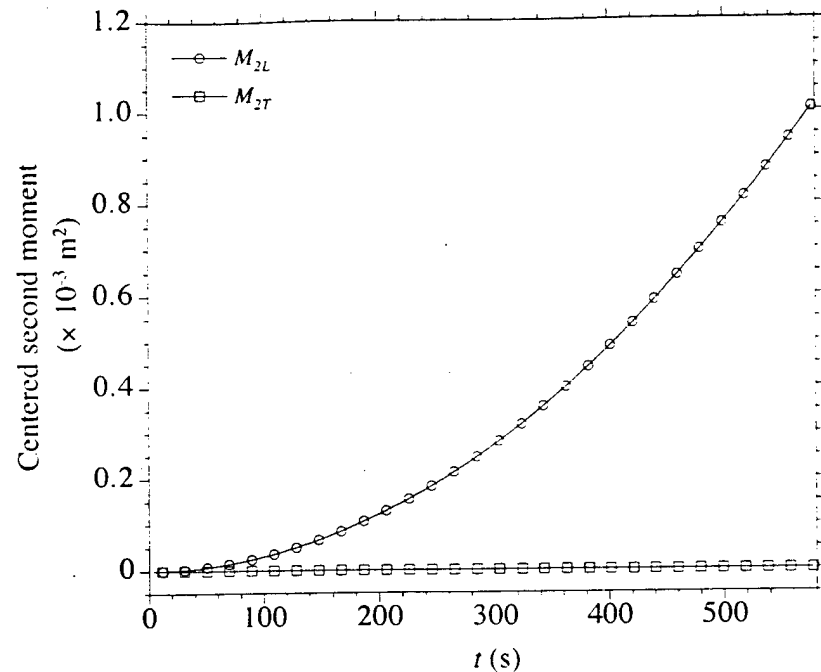


Figure 5.28: Seepage velocity versus time for simulation 1 in Table 5.2.

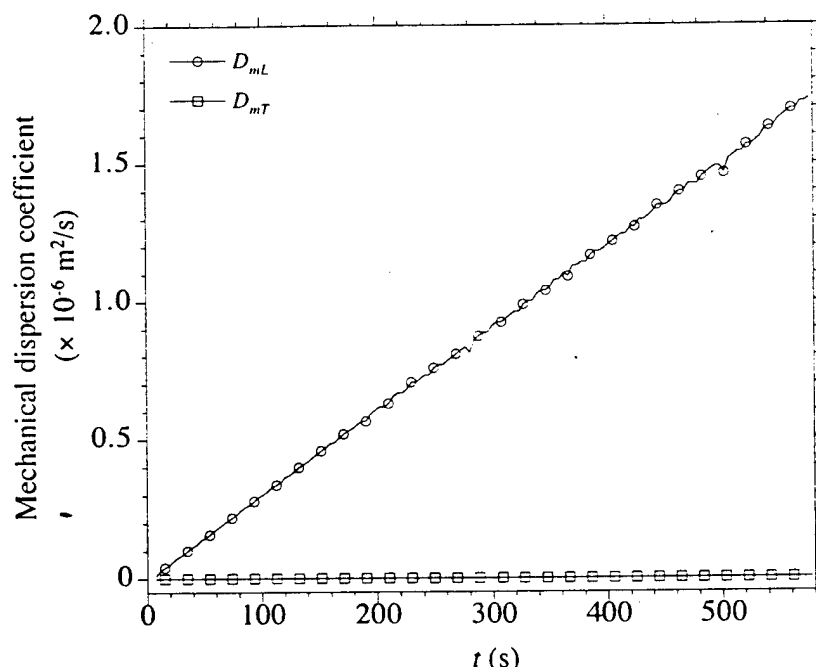
5.6.3 Mechanical Dispersion Coefficient of Porous Media

Mechanical dispersion coefficients for tracer convection were calculated using Equation 5.6. Figures 5.29 to 5.33 show M_{2L} , M_{2T} , D_{mL} , and D_{mT} as a function of time for each tracer convection simulation. M_{2L} , M_{2T} , D_{mL} , and D_{mT} denote centered second moments and mechanical dispersion coefficients in the L and T directions, respectively. Values of M_{2L} and M_{2T} were computed by subtracting centered second moments at time $t = 0$ from those at time t .

M_{2L} and D_{mL} show different types of behavior depending on the body force direction. When F is aligned with a line of symmetry for the solid inclusions, periodic streamlines exist and the increase of M_{2L} with t is nearly quadratic. As a result, D_{mL} increases nearly linearly with t (Figures 5.29, 5.30, and 5.32). However, when F is not aligned with a line of symmetry for the solid inclusions, irregular streamlines exist and M_{2L} shows a more complicated behavior with t (Figures 5.31 and 5.33). Although M_{2L} generally increases with t in this case, it may decrease with t for short



(a)



(b)

Figure 5.29: (a) Centered second moment, and (b) mechanical dispersion coefficient versus time for tracer convection through a square array of circular cylinders ($\gamma = 0^\circ$).

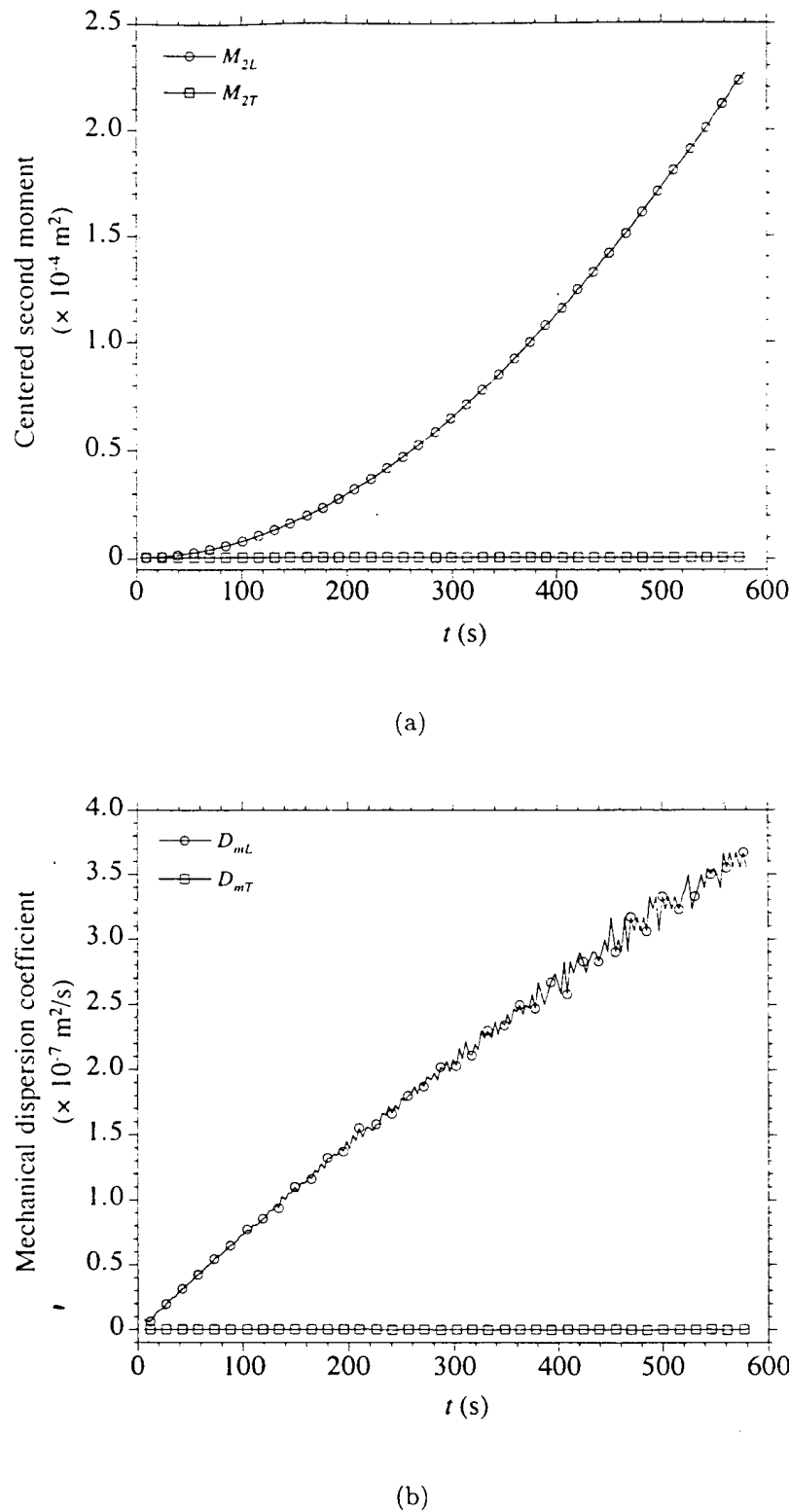


Figure 5.30: (a) Centered second moment, and (b) mechanical dispersion coefficient versus time for tracer convection through a staggered array of circular cylinders ($\gamma = 0^\circ$).

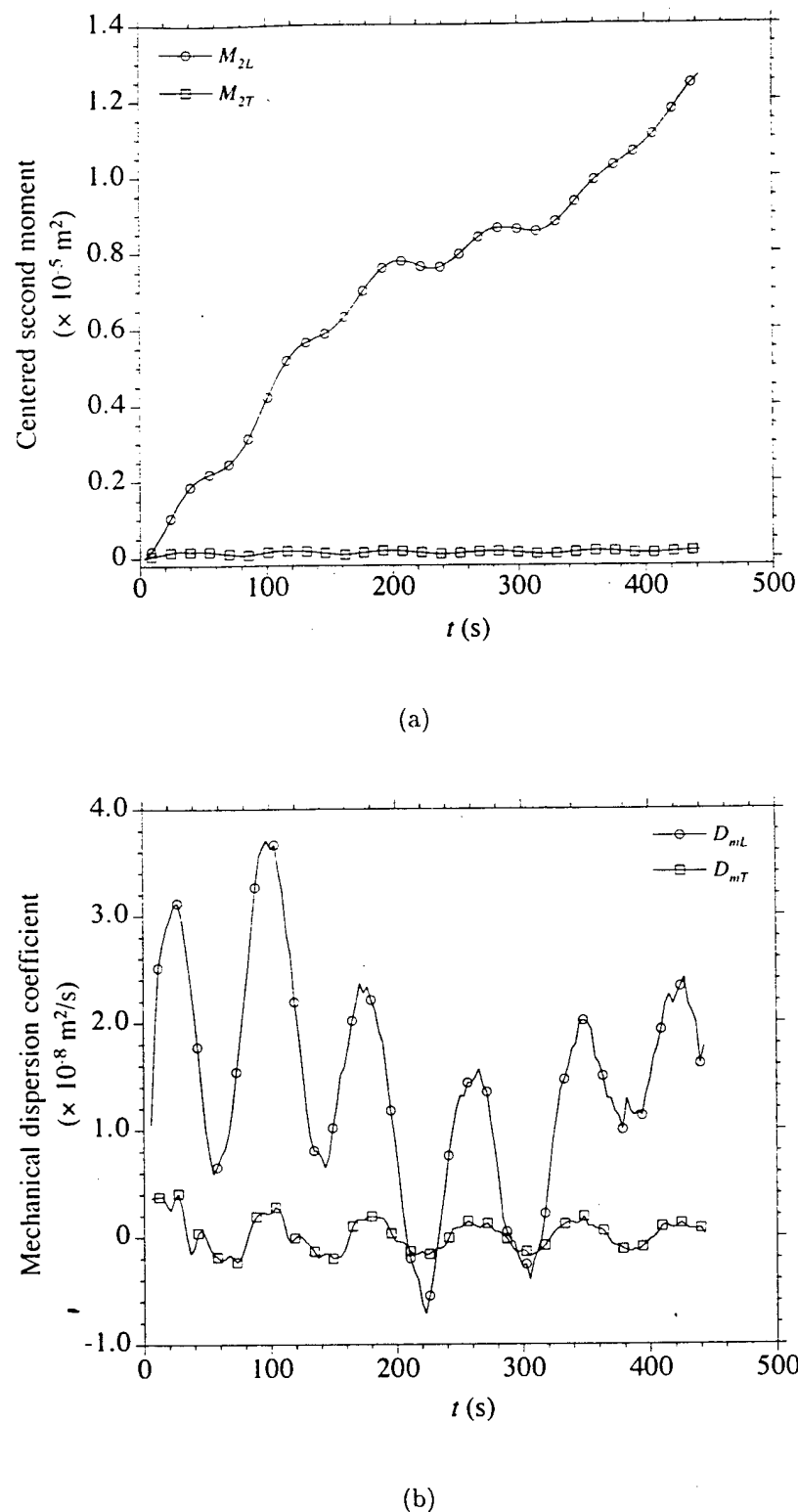


Figure 5.31: (a) Centered second moment, and (b) mechanical dispersion coefficient versus time for tracer convection through a staggered array of circular cylinders ($\gamma = 30^\circ$).

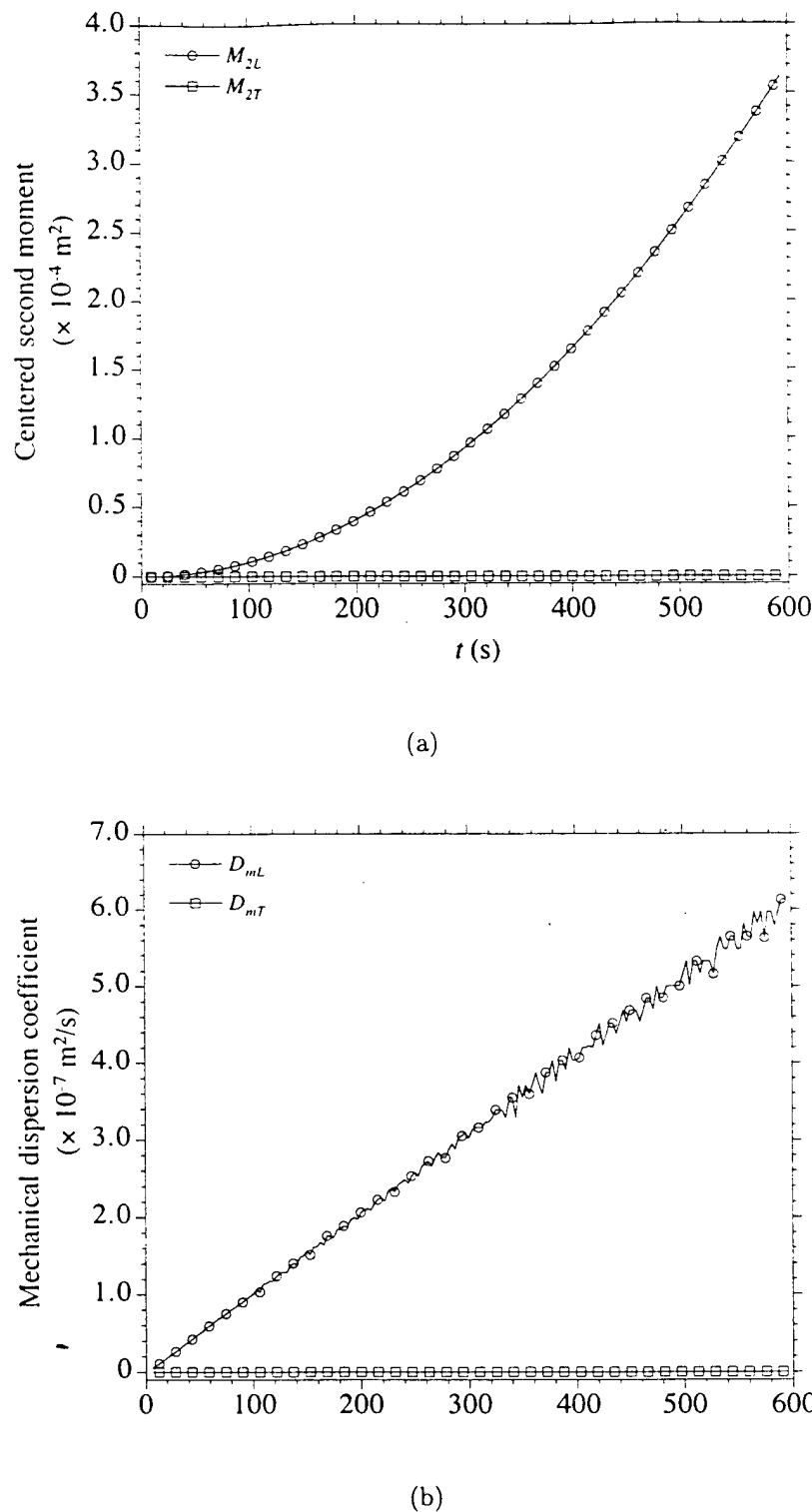


Figure 5.32: (a) Centered second moment, and (b) mechanical dispersion coefficient versus time for tracer convection through a hexagonal array of circular cylinders ($\gamma = 0^\circ$).

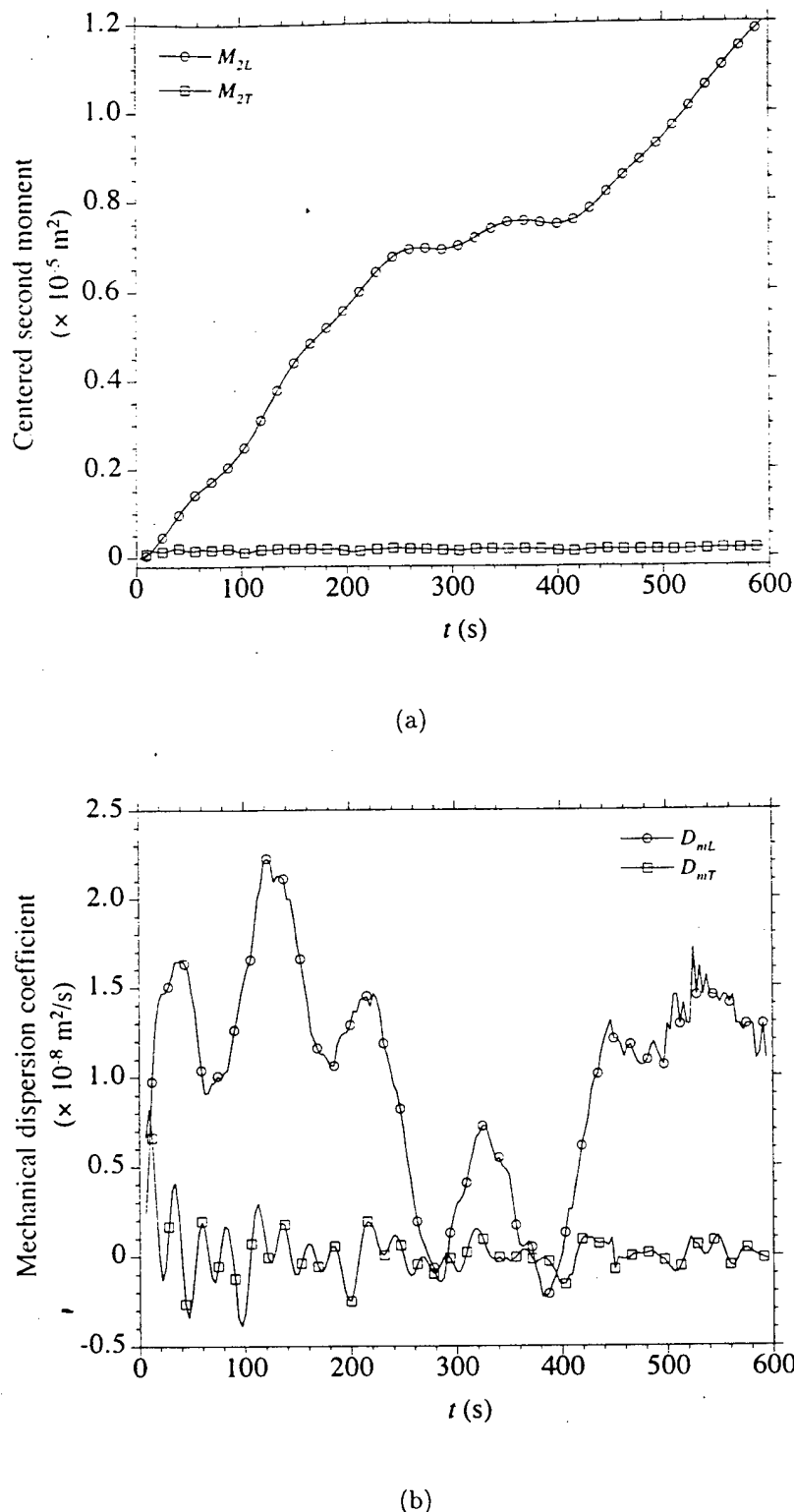


Figure 5.33: (a) Centered second moment, and (b) mechanical dispersion coefficient versus time for tracer convection through a hexagonal array of circular cylinders ($\gamma = 45^\circ$).

periods, which results in a negative value of D_{mL} . Figures 5.31(b) and 5.33(b) show that D_{mL} does not grow with time and instead fluctuates about an average value. When F is aligned with a line of media symmetry, M_{2T} and D_{mT} are practically zero (Figures 5.29, 5.30, and 5.32). When F is not aligned with a line of media symmetry, M_{2T} shows small fluctuations about zero which are amplified when D_{mT} is calculated (Figures 5.31 and 5.33). However, the magnitude of D_{mT} is consistently smaller than that of D_{mL} .

The relationship between centered second moment M_2 and time can also be studied using a *log-log* scale. It is usually believed that $\log(M_2)$ and $\log(t)$ have a linear relationship as,

$$\log(M_2) = s \log(t), \quad (5.18)$$

where s provides an indication of dispersion behavior (Cushman 1997). A value of $s = 1$ corresponds to Fickian behavior. Figures 5.34 to 5.38 show *log-log* plots for each tracer convection simulation with a line fitted using least squares. The slope of the fitted line s and the regression coefficient R are denoted on the plots. An approximately linear relationship exists for $\log(M_{2L})$ with $\log(t)$ ($R > 0.92$), however, it is not appropriate to fit a line for the variation of $\log(M_{2T})$ versus $\log(t)$ ($R \leq 0.1$). The linear fits for M_{2L} are quite good if F is aligned with a line of media symmetry (Figures 5.34 and 5.37). *log-log* plots cannot be made for M_{2T} since these values are practically zero. When F is not aligned with a line of media symmetry, s has a value close to unity for the $\log(M_{2L})$ - $\log(t)$ relationship, which suggests an approximate Fickian dispersion behavior for this case.

From the tracer convection simulations under laminar flow conditions, an asymptotic mechanical dispersion coefficient was not found for two-dimensional spatially periodic porous media when F is aligned with a line of media symmetry, even for large times. It is necessary to reexamine the fundamentals of the theory of Fickian approximation to understand why the phenomenon does not exist for this case. The Fickian approximation assumes that the travel time for an individual tracer particle

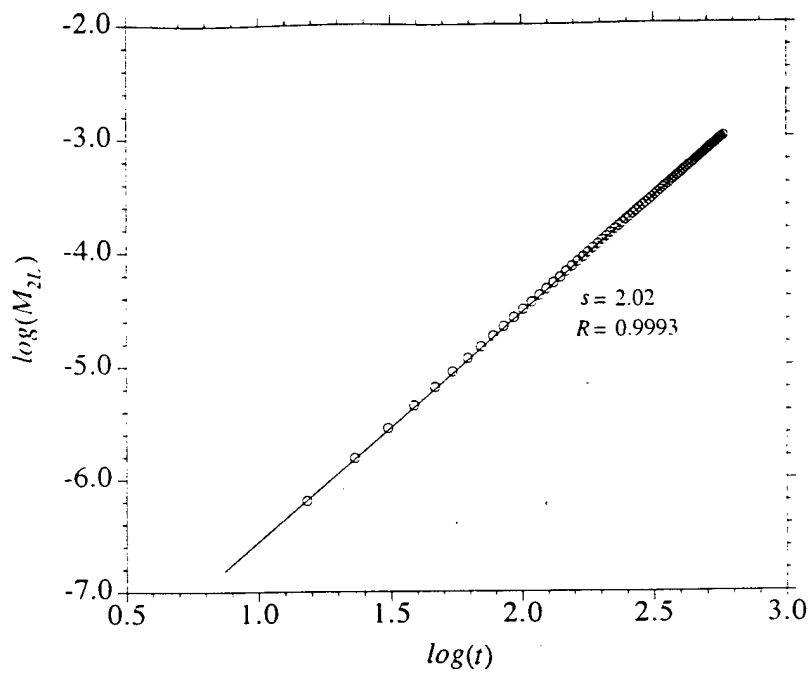


Figure 5.34: $\log(M_{2L})$ versus $\log(t)$ for tracer convection through a square array of circular cylinders ($\gamma = 0^0$).

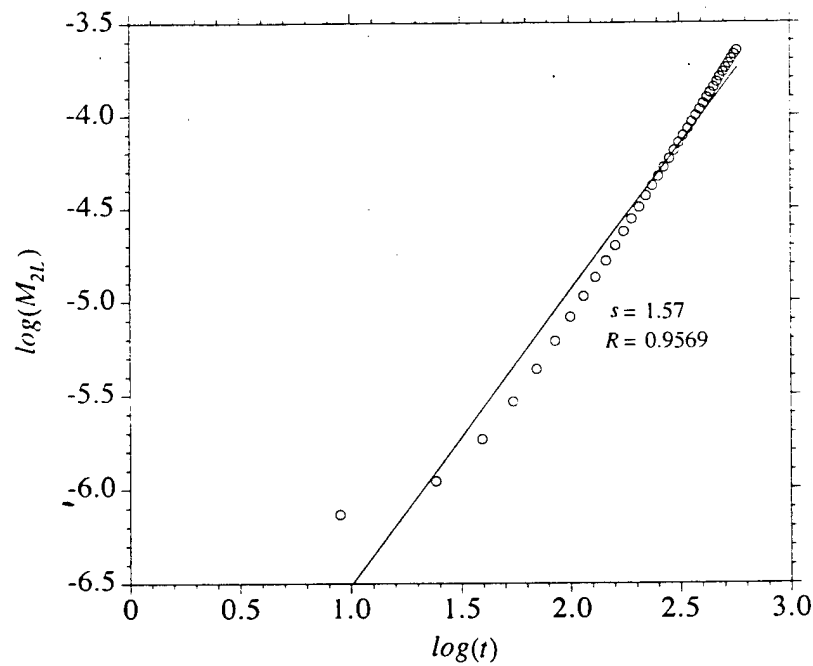


Figure 5.35: $\log(M_{2L})$ versus $\log(t)$ for tracer convection through a staggered array of circular cylinders ($\gamma = 0^0$).

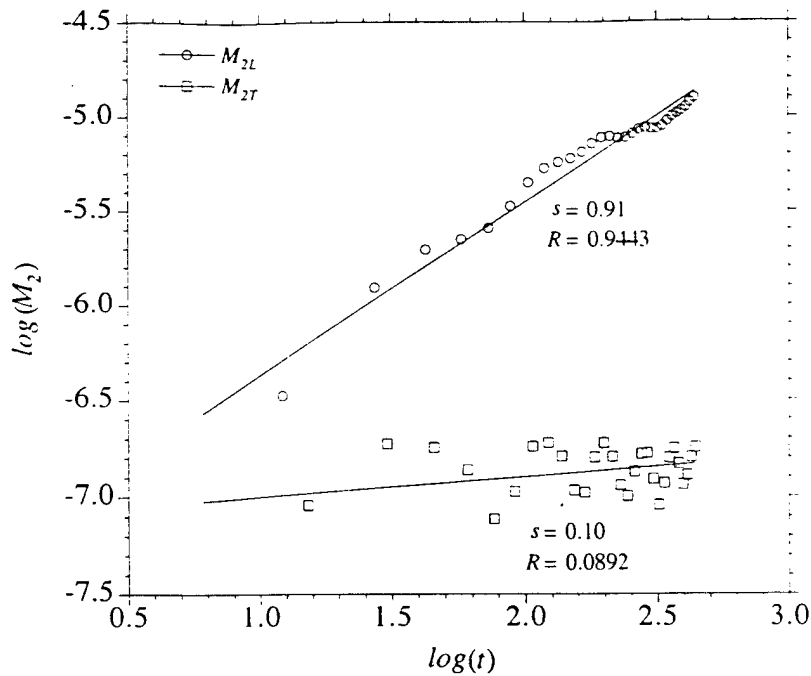


Figure 5.36: $\log(M_2)$ versus $\log(t)$ for tracer convection through a staggered array of circular cylinders ($\gamma = 30^\circ$).

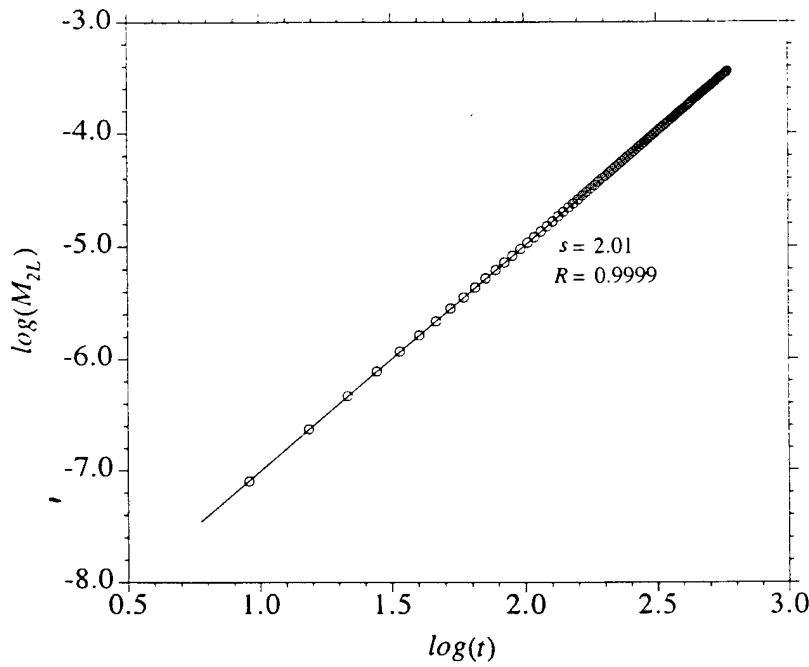


Figure 5.37: $\log(M_{2L})$ versus $\log(t)$ for tracer convection through a hexagonal array of circular cylinders ($\gamma = 0^\circ$).

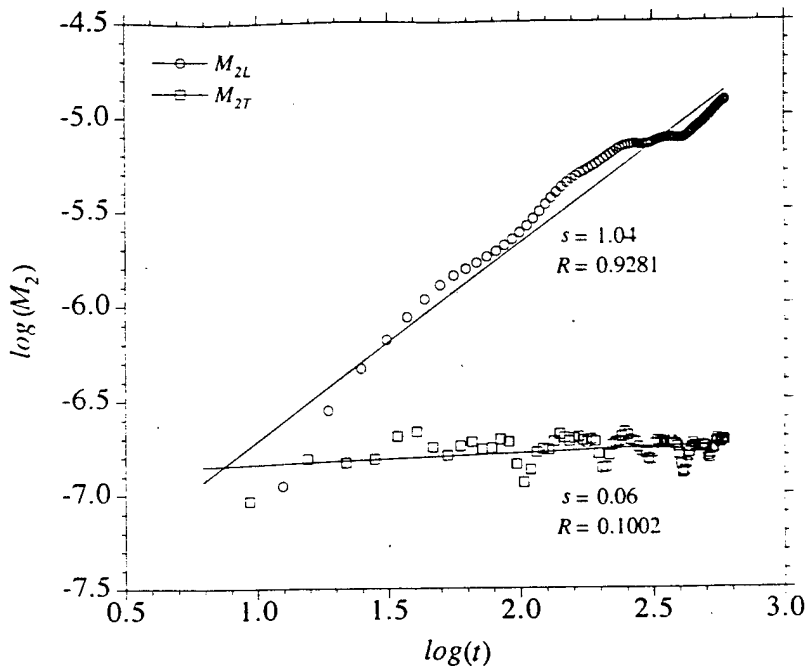


Figure 5.38: $\log(M_2)$ versus $\log(t)$ for tracer convection through a hexagonal array of circular cylinders ($\gamma = 45^\circ$).

is much larger than the time interval during which its successive velocities are correlated. Total displacement is considered as the sum of a large number of elementary displacements which are statistically independent of one another. Each particle in the tracer cloud is assumed to transverse all possible variations in the velocity field. These assumptions lead to a normal distribution of a cloud of initially close particles according to the central limit theorem for an ergodic system, which is characterized by a constant dispersivity (Bear 1972). In a random porous medium, these assumptions are reasonable to some extent.

Constant dispersivity implies that a single velocity path is statistically representative of all velocity paths. This means that a tracer particle released anywhere in the unit cell of a spatially periodic porous medium eventually samples the entire unit cell by convection alone. When F is aligned with a line of media symmetry, Figures 5.22, 5.23, and 5.25 show that different subsets of tracer particles may experience entirely different velocity paths in periodic porous media. Preferred flow paths and spatially

periodic flow patterns are apparent in those figures. In this case, the structure of the periodic porous medium and, therefore, the velocity experienced by a tracer particle traversing a streamline, remain correlated throughout all space. The distance between two tracer particles released on different streamlines increases with time. As such, there is no mechanism for tracer particles traveling through periodic porous media under this condition to mix across streamlines in pure tracer convection simulations.

If F is not aligned with a line of media symmetry (Figures 5.24 and 5.26), although streamlines still cannot cross each other under laminar flow conditions, irregular patterns of streamlines seem to provide the possibility for a tracer particle to sample the whole unit cell during the course of a simulation. This results in a mixing process which can be approximated as Fickian. Another mechanism which causes tracer mass to mix across streamlines is molecular diffusion.

5.7 Simulations of Tracer Hydrodynamic Dispersion

Due to computational limitations, extensive simulations of tracer hydrodynamic dispersion through spatially periodic porous media are not presented. As an asymptotic Fickian behavior of pure tracer convection was not found for two-dimensional spatially periodic porous media when F is aligned with a line of media symmetry, the issue of whether tracer hydrodynamic dispersion under this condition can be described as an asymptotic Fickian process is explored in this section.

One-dimensional tracer hydrodynamic dispersion through a periodic square array of circular cylinders ($n = 0.8$ and $R = 0.5\text{ mm}$) was simulated for $\rho = 10^3 \frac{\text{kg}}{\text{m}^3}$, $\nu = 10^{-6} \frac{\text{m}^2}{\text{s}}$, $F = 0.001 \frac{\text{m}}{\text{s}^2}$, and $d_0 = 10^{-10} \frac{\text{m}^2}{\text{s}}$, $10^{-9} \frac{\text{m}^2}{\text{s}}$, and $10^{-8} \frac{\text{m}^2}{\text{s}}$. The body force F was applied in the positive x direction, i.e., $\gamma = 0^\circ$, and the induced steady state seepage velocity v_s was $9.30 \times 10^{-5} \frac{\text{m}}{\text{s}}$. For the simulations, $Re = \frac{v_s R}{\nu} = 0.0465$, $Pe = \frac{v_s R}{d_0} = 465$ for $d_0 = 10^{-10} \frac{\text{m}^2}{\text{s}}$, $Pe = 46.5$ for $d_0 = 10^{-9} \frac{\text{m}^2}{\text{s}}$, and $Pe = 4.65$ for $d_0 = 10^{-8} \frac{\text{m}^2}{\text{s}}$. Figures 5.39 and 5.40 show the tracer concentration fields at four times for the simulations with $d_0 = 10^{-10} \frac{\text{m}^2}{\text{s}}$ and $d_0 = 10^{-8} \frac{\text{m}^2}{\text{s}}$. The plots were generated directly using discrete SPH data with the grey-scale representing the value

of concentration. The tracer plume front becomes obscure and the concentration field becomes more uniform as d_0 increases.

Figure 5.41 is a plot of M_{2L} as a function of time. Values of M_{2L} were computed by subtracting the centered second moment at time $t = 0$ from that at time t . Figure 5.41 shows that, at any given time, tracer spreading about its center increases as d_0 decreases. Values of hydrodynamic dispersion coefficient in the L direction D_L were calculated using Equation 5.6 and are shown in Figure 5.42. An asymptotic dispersion coefficient was found for the simulation with $d_0 = 10^{-8} \frac{m^2}{s}$. However, the curve corresponding to $d_0 = 10^{-10} \frac{m^2}{s}$ differs little from the one for pure tracer convection. The curve corresponding to $d_0 = 10^{-9} \frac{m^2}{s}$ lies between the curves for $d_0 = 10^{-10} \frac{m^2}{s}$ and $d_0 = 10^{-8} \frac{m^2}{s}$, as expected.

Tracer hydrodynamic dispersion in two-dimensional spatially periodic porous media can be fundamentally different from pure tracer convection when F is aligned with a line of media symmetry. An asymptotic Fickian behavior exists for tracer hydrodynamic dispersion under this condition. However, Fickian behavior appears some time after the tracer is introduced into the flow. A characteristic time t_c defined as (Equation 2.139),

$$t_c = \frac{\mathcal{L}_D^2}{d_0}, \quad (5.19)$$

is needed for tracer to sample interstitial space of the unit cells. The mechanism of molecular diffusion, which provides the possibility for tracer to sample all pore space, is absent in pure tracer convection. The value of t_c is a direct function of the coefficient of molecular diffusion. For the simulation with $d_0 = 10^{-8} \frac{m^2}{s}$, $t_c = 25 s$ if using $\mathcal{L}_D = R = 0.5 mm$, which is approximately the time when D_L becomes essentially constant in Figure 5.42. However, $t_c = 2500 s$ for $d_0 = 10^{-10} \frac{m^2}{s}$ and $t_c = 250 s$ for $d_0 = 10^{-9} \frac{m^2}{s}$. These simulations were not run long enough to reach t_c .

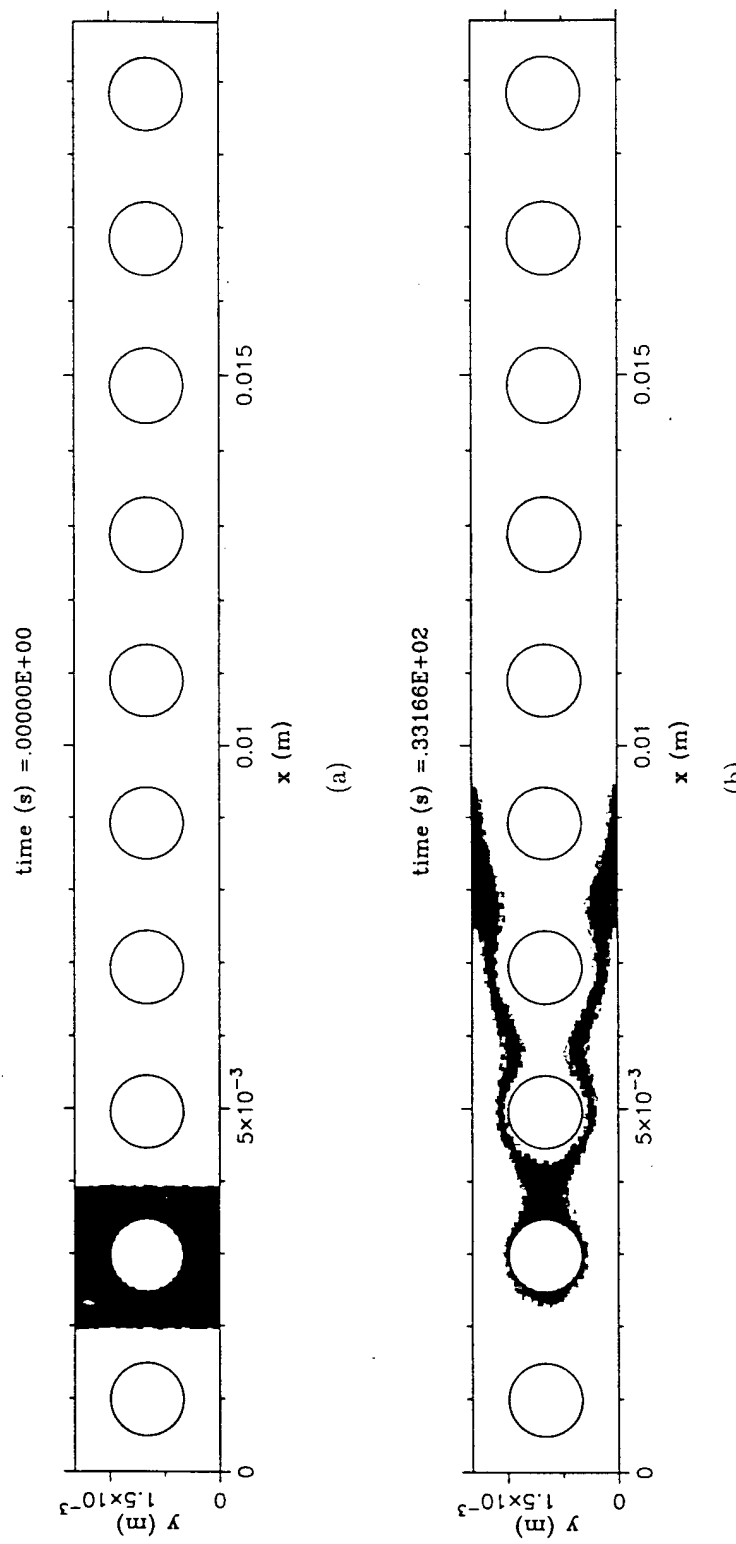


Figure 5.39: Tracer concentration fields for dispersion through a square array of circular cylinders ($d_0 = 10^{-10} \frac{m^2}{s}$) at elapsed times of (a) 0 s, (b) 33.166 s, (c) 65.942 s, (d) 94.038 s.

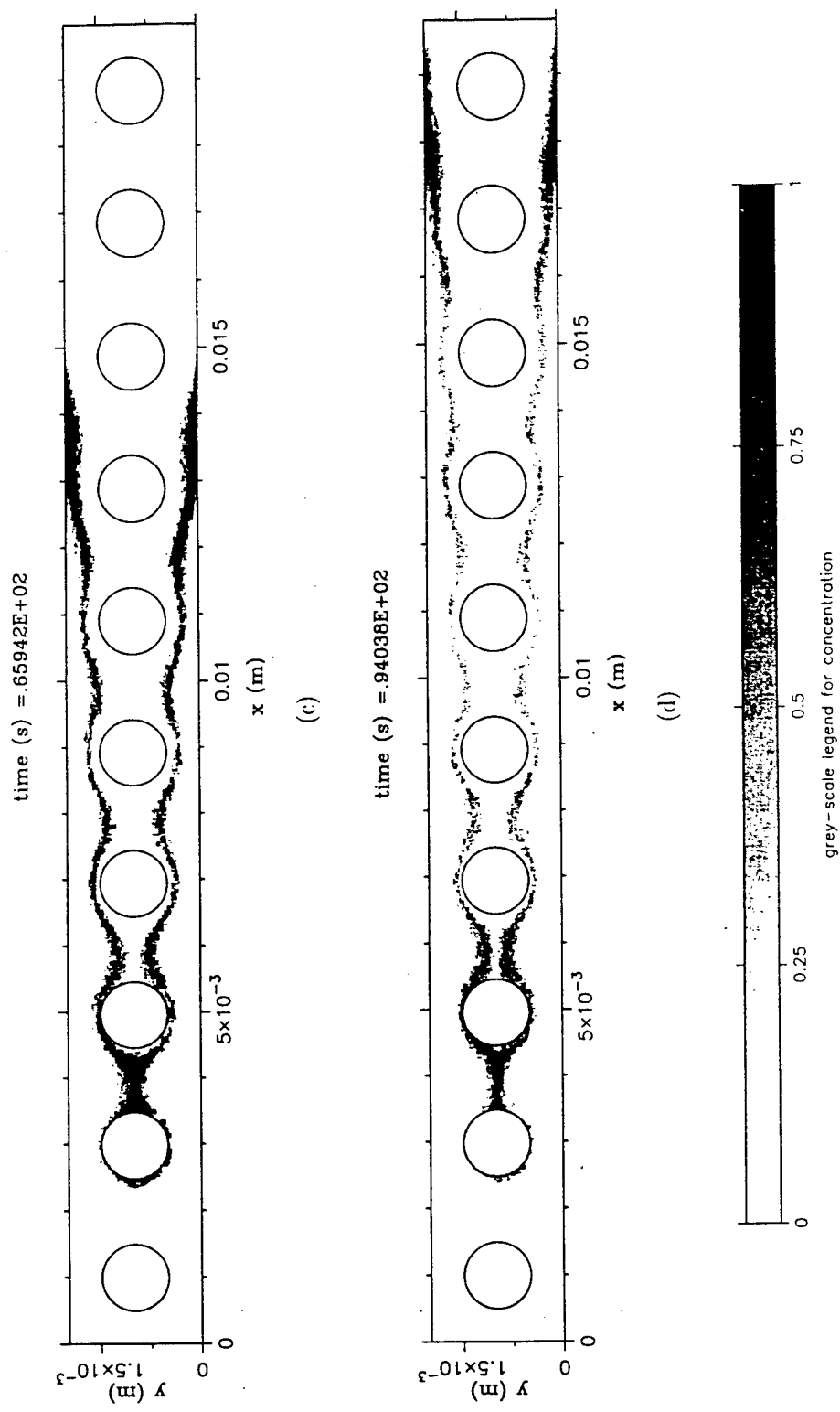


Figure 5.39: Continue.

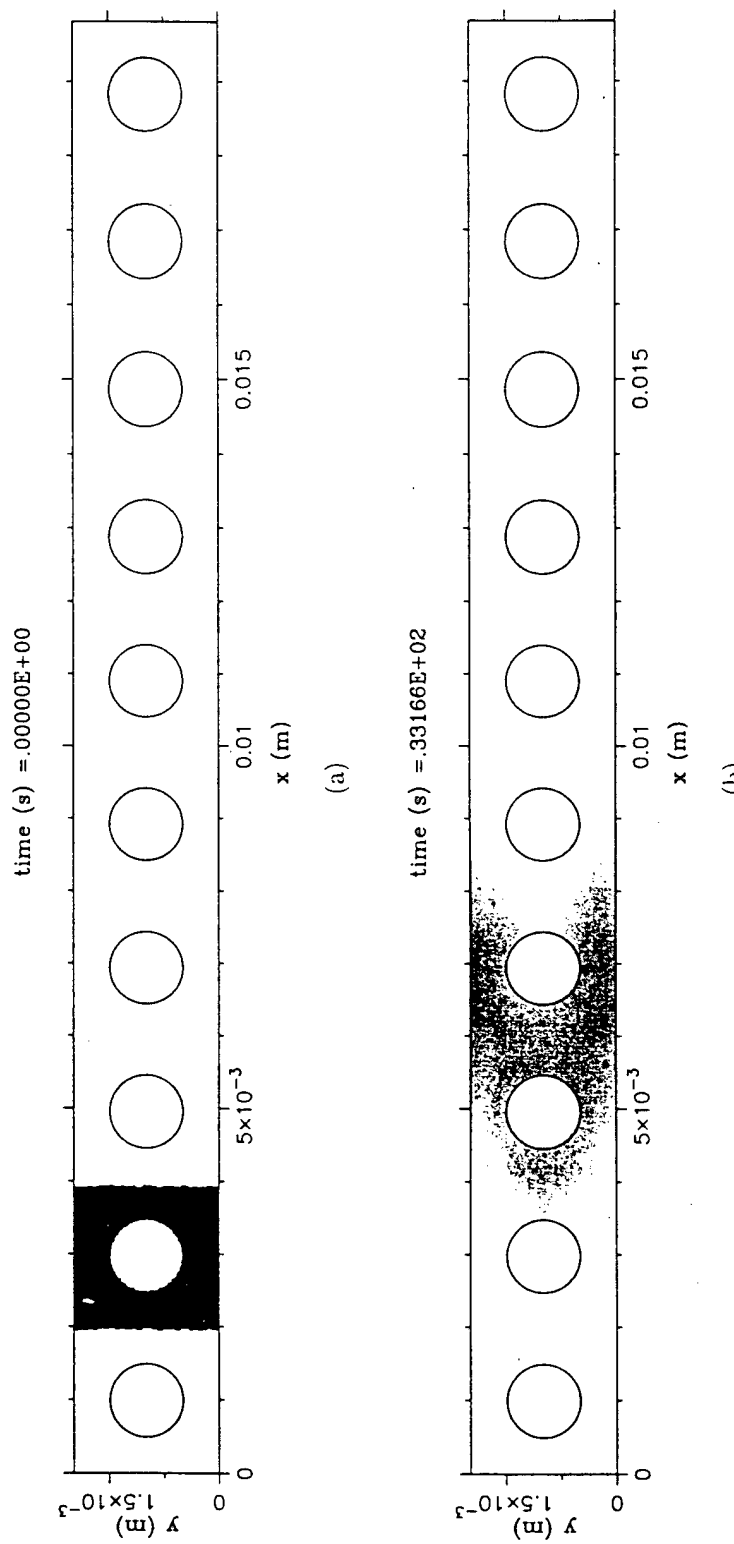


Figure 5.40: Tracer concentration fields for dispersion through a square array of circular cylinders ($d_0 = 10^{-8} \frac{m^2}{s}$) at elapsed times of (a) 0 s, (b) 33.166 s, (c) 65.942 s, (d) 94.038 s.

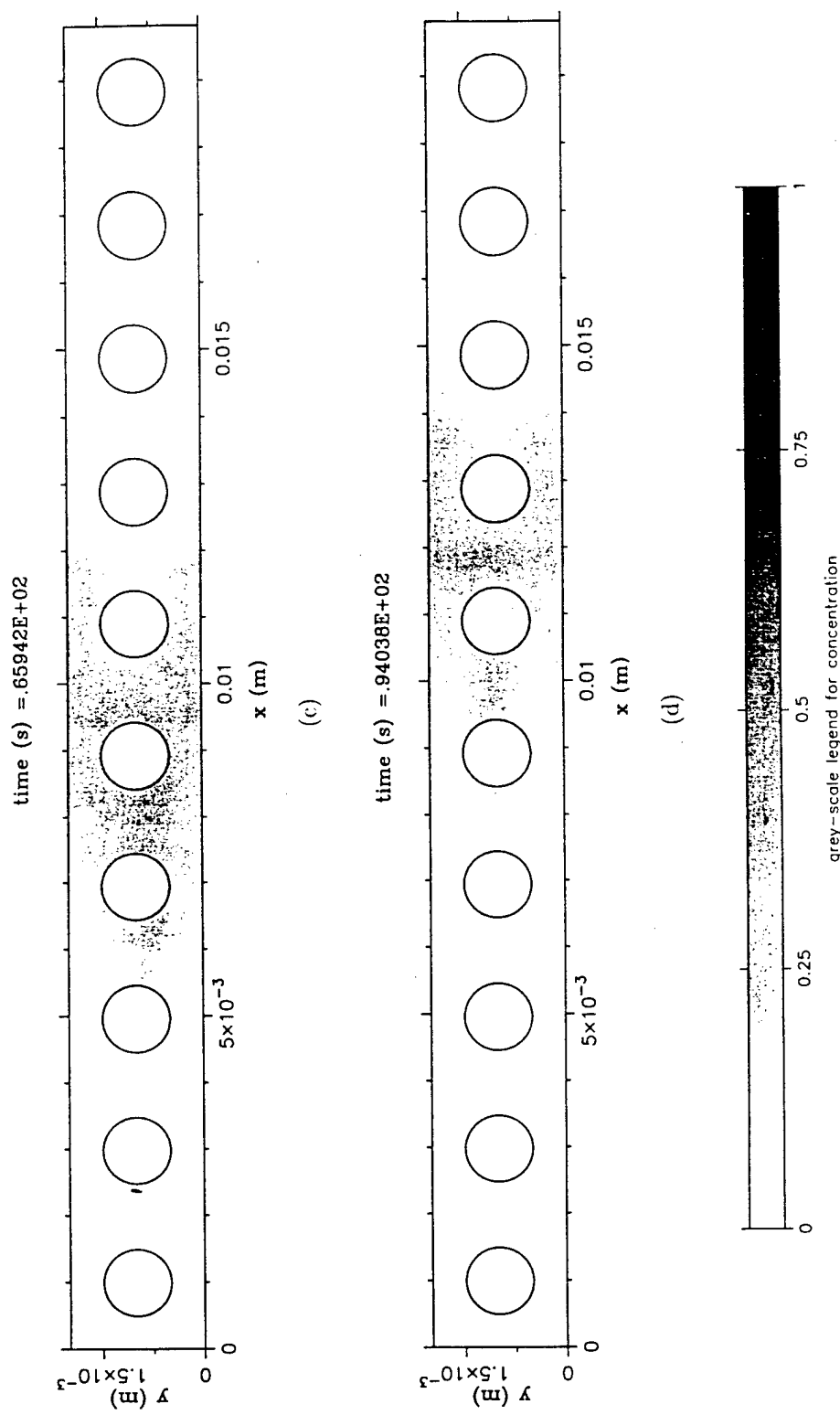


Figure 5.40: Continue.

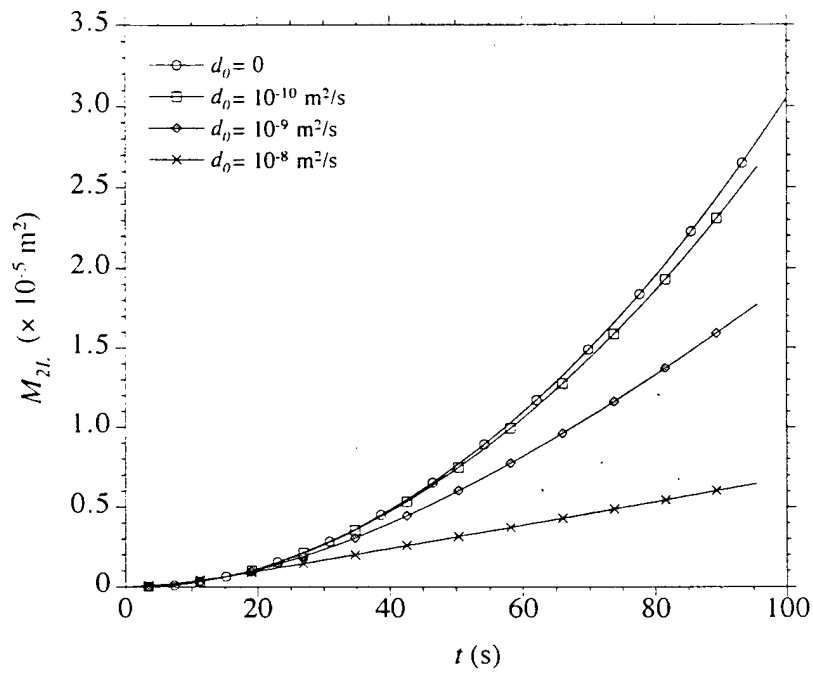


Figure 5.41: Centered second moment in the L direction of tracer distribution versus time for tracer transport through a square array of circular cylinders.

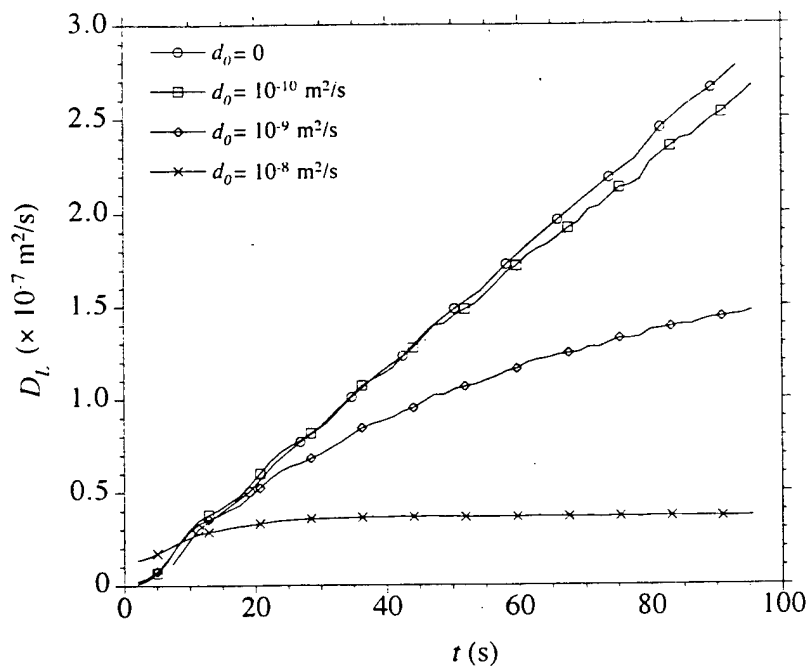


Figure 5.42: Dispersion coefficient in the L direction of tracer distribution versus time for tracer transport through a square array of circular cylinders.

5.8 Summary

Pure tracer convection and hydrodynamic dispersion models were developed using Smoothed Particle Hydrodynamics (SPH). The dispersion model was used to simulate the Taylor dispersion problem and the results were in close agreement with analytical solutions. Simulations using the tracer convection model were used to calculate tortuosity and effective porosity of porous media. It was found that pure tracer convection through two-dimensional spatially periodic porous media cannot be described as an asymptotic Fickian-type process, even for large times, if F is aligned with a line of media symmetry. However, an asymptotic Fickian approximation is valid for tracer hydrodynamic dispersion through two-dimensional spatially periodic porous media. If F is not aligned with a line of media symmetry, Fickian-type mixing is possible for pure tracer convection. Due to the time step constraint for the explicit time integration method and limited computer resources, the SPH model has limitations for simulating tracer dispersion through porous media.

CHAPTER 6 CONCLUSIONS AND RECOMMENDATIONS FOR FUTURE WORK

6.1 Conclusions

1. Necessary extensions have been implemented and tested which allow Smoothed Particle Hydrodynamics (SPH) to model low Reynolds number incompressible flow through porous media;
2. Computed values of permeability and cylinder drag force from simulations of flow through spatially periodic porous media using the SPH model are in accordance with Darcy's law and in close agreement with finite element solutions and other published solutions in the literature;
3. Necessary extensions have been implemented and tested which allow SPH to model diffusion through porous media;
4. Computed values of concentration and effective diffusion coefficient from simulations of diffusion through spatially periodic porous media using the SPH model are in close agreement with finite element solutions and other published solutions in the literature;
5. Nondimensional diffusivities d^* were calculated using the SPH model for spatially periodic porous media with circular and elliptical cylinders arranged in square, staggered, and hexagonal arrays. While specific surface area S_0 does not affect d^* , porosity n and array type were found to be the most and least important parameters, respectively, which influence the values of d^* . Anisotropy of a medium was found to be mainly determined by the aspect ratio $\frac{a}{b}$ of its solid inclusions;

6. Tracer convection and hydrodynamic dispersion models were developed using SPH;
7. Tracer convection simulations were used to calculate tortuosity and effective porosity of porous media. Values of tortuosity calculated using SPH were less than $\sqrt{2} = 1.414$ as proposed originally by Carman (1937) for unconsolidated porous aggregates. Tortuosity was found to be a function of media geometry and the body force F direction. Values of effective porosity calculated using SPH were close to the nominal porosity values for the media type considered in this work;
8. Solutions for Taylor dispersion between infinite plates using hydrodynamic dispersion model were in close agreement with analytical solutions;
9. Simulations using SPH indicated that pure tracer convection through two-dimensional spatially periodic porous media cannot be described as an asymptotic Fickian-type process, even for large times, if F is aligned with a line of media symmetry. However, an asymptotic Fickian approximation is valid for tracer hydrodynamic dispersion through spatially periodic porous media. If F is not aligned with a line of media symmetry, Fickian-type mixing is possible for pure tracer convection;
10. Due to the time step constraint for the explicit time integration method and limited computer resources, the SPH model has limitations for simulating tracer dispersion through porous media.

6.2 Recommendations for Future Work

1. An advanced parallel algorithm is needed for the SPH model to improve its efficiency such that mass transport through porous media can be simulated;
2. A systematic study of media dispersivity as a function of media properties and flow conditions can be conducted using the SPH model;

3. Extension of the SPH model to three-dimensional problems is needed to simulate real random porous media;
4. Incorporation of progressively more complicated physics, such as surface tension, is needed to model multiphase transport, fluid-solid sorption/desorption processes, solute reactions, and decay;
5. A discrete model for fluid-solid systems can be achieved by coupling a three-dimensional SPH model with the discrete element method (DEM), which models the solid phase. DEM will allow modeling of a deformable solid matrix. It is possible to study the generation of pore pressure within porous media subjected to both static and dynamic loadings using this coupled SPH-DEM model. The study may then lead to important findings regarding to liquefaction behavior of loose saturated sand.

LIST OF REFERENCES

LIST OF REFERENCES

- Adler, P. M. (1992). *Porous media: geometry and transports*. Stoneham, MA: Butterworth-Heinemann.
- Al-Khafaji, A. W. and J. R. Tooley (1986). *Numerical Methods in Engineering Practice*. New York: Holt, Rinehart, and Winston, Inc.
- Aris, R. (1956). On the dispersion of a solute in a fluid flowing through a tube. *Phil. Trans. R. Soc. Lond. A235*, 67-77.
- Artymowicz, P. and S. H. Lubow (1994). Dynamics of binary-disk interaction. I. resonances and disk gap sizes. *The Astrophysical Journal* 421, 651-667.
- Avnir, D., D. Farin, and P. Pfeifer (1985). Surface geometric irregularity of particulate materials: the fractal approach. *Journal of Colloid and Interface Science* 103(1), 112-123.
- Balsara, D. S. (1995). von Neumann stability analysis of Smoothed Particle Hydrodynamics-suggestions for optimal algorithms. *Journal of Computational Physics* 121, 357-372.
- Batchelor, G. K. (1967). *An introduction to fluid dynamics*. Cambridge, UK: Cambridge University Press.
- Baudet, C., J. P. Hulin, P. Lallemand, and D. d'Humieres (1989). Lattice-gas automata: a model for the simulation of dispersion phenomena. *Phys. Fluids A* 1(3), 507-512.
- Baveye, P. and G. Sposito (1984). The operational significance of the continuum hypothesis in the theory of water movement through soils and aquifers. *Water Resources Research* 20(5), 521-530.
- Bear, J. (1961). On the tensor form of dispersion in porous media. *Journal of Geophysical Research* 66(4), 1185-1197.
- Bear, J. (1972). *Dynamics of fluids in porous media*. New York: American Elsevier Publishing Company.
- Bedient, P. B., H. S. Rifai, and C. J. Newell (1994). *Ground water contamination: transport and remediation*. Englewood Cliffs, NJ: Prentice Hall.
- Belytschko, T., Y. Krongauz, D. Organ, M. Fleming, and P. Krysl (1996). Meshless methods: an overview and recent developments. *Comput. Methods Appl. Mech. Eng.* 139, 3-47.

- Benz, W. (1990). Smooth particle hydrodynamics: a review. In J. R. Buchler (Ed.), *The numerical modelling of nonlinear stellar pulsations*, pp. 269–288. Kluwer Academic Publishers.
- Benz, W. and E. Asphaug (1995). Simulations of brittle solids using smooth particle hydrodynamics. *Computer Physics Communications* 87, 253–265.
- Bhattacharya, R. and V. K. Gupta (1990). *Dynamics of fluids in hierarchical porous media*, Chapter IV, pp. 61–96. London: Academic Press.
- Bhattacharya, R. N. and V. K. Gupta (1983). A theoretical explanation of solute dispersion in saturated porous media at the Darcy scale. *Water Resources Research* 19(4), 938–944.
- Brenner, H. (1980a). Dispersion resulting from flow through spatially periodic porous media. *Phil. Trans. R. Soc. Lond. A297*, 81–133.
- Brenner, H. (1980b). A general theory of Taylor dispersion phenomena. *Physico-Chemical Hydrodynamics* 1, 91–123.
- Brenner, H. (1981). Taylor dispersion in systems of sedimenting nonspherical Brownian particles. II. homogeneous ellipsoidal particles. *Journal of Colloid and Interface Science* 80(2), 548–588.
- Brenner, H. (1982). A general theory of Taylor dispersion phenomena. II. an extension. *PhysicoChemical Hydrodynamics* 3(2), 139–157.
- Brenner, H. and P. M. Adler (1982). Dispersion resulting from flow through spatially periodic porous media, II. surface and intraparticle transport. *Phil. Trans. R. Soc. Lond. A307*, 149–200.
- Brinkman, H. C. (1947). A calculation of the viscous force exerted by a flowing fluid on a dense swarm of particles. *Applied Scientific Research A1*, 27–34.
- Brinkman, H. C. (1948). On the permeability of media consisting of closely packed porous particles. *Applied Scientific Research A1*, 81–86.
- Broadwell, J. E. (1964). Shock structure in a simple discrete velocity gas. *Phys. Fluids* 7(8), 1243–1247.
- Brosa, U. and D. Stauffer (1989). Vectorized multisite coding for hydrodynamic cellular automata. *Journal of Statistical Physics* 57(1/2), 399–403.
- Brosa, U. and D. Stauffer (1991). Simulation of flow through a two-dimensional random porous medium. *Journal of Statistical Physics* 63(1/2), 405–409.
- Bruschke, M. V. and S. G. Advani (1993). Flow of generalized Newtonian fluids across a periodic array of cylinders. *J. Rheol.* 37(3), 479–498.
- Bryant, S. L., P. R. King, and D. W. Mellor (1993). Network model evaluation of permeability and spatial correlation in a real random sphere packing. *Transport in porous media* 11, 53–70.

- Cancelliere, A., C. Chang, E. Foti, D. H. Rothman, and S. Succi (1990). The permeability of a random medium: comparison of simulation with theory. *Phys. Fluids A 2*(12), 2085–2088.
- Carbonell, R. G. and S. Whitaker (1983). Dispersion in pulsed systems-II theoretical developments for passive dispersion in porous media. *Chemical Engineering Science 38*(11), 1795–1802.
- Carman, P. C. (1937). Fluid flow through granular beds. *Trans. Inst. Chem. Eng. 15*, 150–166.
- Carman, P. C. (1938a). The determination of the specific surface of powders, I. *J. Soc. Chem. Ind. 57*, 225–234.
- Carman, P. C. (1938b). Fundamental principles of industrial filtration. *Trans. Inst. Chem. Eng. 16*, 168–188.
- Carman, P. C. (1939). Determination of the specific surface of powders, II. *J. Soc. Chem. Ind. 58*, 1–7.
- Carman, P. C. (1956). *Flow of gases through porous media*. London: Butterworths.
- Carslaw, H. S. and J. C. Jaeger (1959). *Conduction of heat in solids*. Oxford: Clarendon Press.
- Case, C. M. (1971). Projections of Darcy's law as related to the ellipse of direction. *Water Resources Research 7*(5), 1354–1356.
- Case, C. M. and G. F. Cochran (1972). Transformation of the tensor form of Darcy's law in inhomogeneous and anisotropic soils. *Water Resources Research 8*(3), 728–733.
- Chatzis, I. and F. A. L. Dullien (1977). Modeling pore structures by 2D and 3D networks with application to sandstone. *J. Can. Pet. Technol. 16*, 97–108.
- Chorin, A. J. (1967). A numerical method for solving incompressible viscous flow problems. *Journal of Computational Physics 2*, 12–26.
- Courant, R., K. Friedrichs, and H. Lewy (1928). Über die partiellen differenzengleichungen der mathematischen physik. *Mathematische Annalen 100*, 32–74.
- Crank, J. (1975). *The mathematics of diffusion*. Oxford: Oxford University Press.
- Cushman, J. H. (1984). On unifying the concepts of scale, instrumentation, and stochastics in the development of multiphase transport theory. *Water Resources Research 20*(11), 1668–1676.
- Cushman, J. H. (1986). On measurement, scale, and scaling. *Water Resources Research 22*(2), 129–134.
- Cushman, J. H. (1990). *Dynamics of fluids in hierarchical porous media*. London: Academic Press.
- Cushman, J. H. (1997). *The physics of fluids in hierarchical porous media: angstroms to miles*. Boston: Kluwer Academic Publishers.

- Cushman, J. H. and T. R. Ginn (1993). Nonlocal dispersion in media with continuously evolving scales of heterogeneity. *Transport in Porous Media* 13, 123–138.
- Cushman, J. H., X. Hu, and T. R. Ginn (1994). Nonequilibrium statistical mechanics of preasymptotic dispersion. *Journal of Statistical Physics* 75(5/6), 859–878.
- De Josselin de Jong, G. (1958). Longitudinal and transverse diffusion in granular deposits. *Trans. Amer. Geophys. Un.* 39(1), 67–74.
- d'Humieres, D., P. Lallemand, and U. Frisch (1986). Lattice gas models for 3D hydrodynamics. *Europhysical Letters* 2(4), 291–297.
- Drummond, J. E. and M. I. Tahir (1984). Laminar viscous flow through regular arrays of parallel solid cylinders. *Int. J. Multiphase Flow* 10(5), 515–540.
- Dullien, F. A. L. (1992). *Porous media: fluid transport and pore structure*. San Diego: Academic Press.
- Edwards, D. A., M. Shapiro, P. Bar-Yoseph, and M. Shapira (1990). The influence of Reynolds number upon the apparent permeability of spatially periodic arrays of cylinders. *Phys. Fluids A* 2(1), 45–55.
- Edwards, D. A., M. Shapiro, H. Brenner, and M. Shapira (1991). Dispersion of inert solutes in spatially periodic, two-dimensional model porous media. *Transport in Porous Media* 6, 337–358.
- Eidsath, A., R. G. Carbonell, S. Whitaker, and L. R. Herrmann (1983). Dispersion in pulsed systems-III comparison between theory and experiments for packed beds. *Chemical Engineering Science* 38(11), 1803–1816.
- Einstein, A. (1956). *Investigations on the theory of Brownian movement*. New York: Dover.
- Fatt, I. (1956). The network model of porous media. *Trans. Am. Inst. Min. Metall. Pet. Eng.* 207, 144–177.
- Ferrand, L. A. and M. A. Celia (1992). The effect of heterogeneity on the drainage capillary pressure-saturation relation. *Water Resources Research* 28(3), 859–870.
- Fetter, C. W. (1993). *Contaminant Hydrogeology*. New York: Macmillan Publishing Company.
- Flebbe, O., S. Münzel, H. Herold, H. Riffert, and H. Ruder (1994). Smoothed particle hydrodynamics: physical viscosity and the simulation of accretion disks. *The Astrophysical Journal* 431, 754–760.
- Freeze, R. A. and J. A. Cherry (1979). *Groundwater*. Englewood Cliffs, NJ: Prentice Hall.
- Fried, J. J. (1975). *Groundwater Pollution*. New York: American Elsevier.
- Fried, J. J. and M. A. Combarous (1971). Dispersion in porous media. *Adv. Hydroscl.* 7, 169–282.

- Frisch, U. (1991). Relation between the lattice Boltzmann equation and the Navier-Stokes equations. *Physica D* 47, 231–232.
- Frisch, U., D. d'Humieres, B. Hasslacher, P. Lallemand, Y. Pomeau, and J.-P. Rivet (1987). Lattice gas hydrodynamics in two and three dimensions. *Complex Systems* 1, 649–707.
- Frisch, U., B. Hasslacher, and Y. Pomeau (1986). Lattice-gas automata for the Navier-Stokes equation. *Physical Review Letters* 56(14), 1505–1508.
- Gelhar, L. W., C. Welty, and K. R. Rehfeldt (1992). A critical review of data on field-scale dispersion in aquifers. *Water Resources Research* 28(7), 1955–1974.
- Ghaddar, C. K. (1995). On the permeability of unidirectional fibrous media: a parallel computational approach. *Phys. Fluids* 7(11), 2563–2586.
- Gingold, R. A. and J. J. Monaghan (1977). Smoothed particle hydrodynamics: theory and application to non-spherical stars. *Mon. Not. R. Astr. Soc.* 181, 375–389.
- Gray, W. G. (1975). A derivation of the equations for multi-phase transport. *Chemical Engineering Science* 30, 229–233.
- Greenkorn, R. A. and D. P. Kessler (1969). Dispersion in heterogeneous nonuniform anisotropic porous media. *Industrial and Engineering Chemistry* 61(9), 14–32.
- Guin, J. A., D. P. Kessler, and R. A. Greenkorn (1971). The permeability tensor for anisotropic nonuniform porous media. *Chemical Engineering Science* 26, 1475–1478.
- Gunstensen, A. K. and D. H. Rothman (1991). A lattice-gas model for three immiscible fluids. *Physica D* 47, 47–52.
- Gunstensen, A. K. and D. H. Rothman (1992). Microscopic modeling of immiscible fluids in three dimensions by a lattice Boltzmann method. *Europhysics Letters* 18(2), 157–161.
- Gunstensen, A. K. and D. H. Rothman (1993). Lattice-Boltzmann studies of immiscible two-phase flow through porous media. *Journal of Geophysical Research* 98(B4), 6431–6441.
- Happel, J. (1959). Viscous flow relative to arrays of cylinders. *AICHE Journal* 5(2), 174–177.
- Happel, J. and H. Brenner (1965). *Low Reynolds number hydrodynamics with special applications to particulate media*. Englewood Cliffs, NJ: Prentice-Hall.
- Hardy, J., O. de Pazzis, and Y. Pomeau (1976). Molecular dynamics of a classical lattice gas: transport properties and time correlation functions. *Physical Review A* 13(5), 1949–1961.
- Haring, R. E. and R. A. Greenkorn (1970). A statistical model of a porous medium with nonuniform pores. *AICHE Journal* 16(3), 477–483.

- Hasimoto, H. (1959). On the periodic fundamental solutions of the Stokes equations and their application to viscous flow past a cubic array of spheres. *J. Fluid Mech.* 5, 317–328.
- Horn, F. J. M. (1971). Calculation of dispersion coefficients by means of moments. *AICHE Journal* 17, 613–620.
- Horne, R. N. and F. Rodriguez (1983). Dispersion of tracer flow in fractured geothermal systems. *Geophysical Research Letters* 10(4), 289–292.
- Hull, L. C., J. D. Miller, and T. M. Clemo (1987). Laboratory and simulation studies of solute transport in fracture networks. *Water Resources Research* 23(8), 1505–1513.
- Iberall, A. S. (1950). Permeability of glass wool and other highly porous media. *J. Res. Nat. Bur. Stand.* 45(5), 398–406.
- Jacquin, C. G. and P. M. Adler (1987). Fractal porous media, II. geometry of porous geological structures. *Transport in Porous Media* 2, 571–596.
- Klotz, D. and H. Moser (1974). Hydrodynamic dispersion as aquifer characteristic: model experiments with radioactive tracers. Technical report, Isotope Techniques in Groundwater Hydrology, Intern. Atomic Energy Agency, Vienna, 2:341–354.
- Klotz, D., K.-P. Seiler, H. Moser, and F. Neumaier (1980). Dispersivity and velocity relationship from laboratory and field experiments. *Journal of Hydrology* 45, 169–184.
- Koch, D. L. and J. F. Brady (1985). Dispersion in fixed beds. *J. Fluid Mech.* 154, 399–427.
- Koch, D. L. and J. F. Brady (1987). A non-local description of advection-diffusion with application to dispersion in porous media. *J. Fluid Mech.* 180, 387–403.
- Koch, D. L., R. G. Cox, H. Brenner, and J. F. Brady (1989). The effect of order on dispersion in porous media. *J. Fluid Mech.* 200, 173–188.
- Koch, D. L. and A. J. C. Ladd (1997). Moderate Reynolds number flows through periodic and random arrays of aligned cylinders. *J. Fluid Mech.* 349, 31–66.
- Kohring, G. A. (1991). Calculation of the permeability of porous media using hydrodynamic cellular automata. *Journal of Statistical Physics* 63(1/2), 411–418.
- Koplik, J., C. Lin, and M. Vermette (1984). Conductivity and permeability from microgeometry. *J. Appl. Phys.* 56(11), 3127–3131.
- Kozeny, J. (1927). Über kapillare leitung des wassers in boden. *Sitzungsber. Akad. Wiss. Wien* 136, 271–306.
- Ladd, A. J. C. (1994a). Numerical simulations of particulate suspensions via a discretized Boltzmann equation. part 1. theoretical foundation. *J. Fluid Mech.* 271, 285–309.

- Ladd, A. J. C. (1994b). Numerical simulations of particulate suspensions via a discretized Boltzmann equation. part 2. numerical results. *J. Fluid Mech.* 271, 311–339.
- Lallemand-Barres, A. and P. Peauduc erf (1978). Recherche des relations entre les valeurs mesurées de la dispersivité macroscopique d'un milieu aquifère, ses autres caractéristiques et les conditions de mesure. *Bull. Bur. Rech. Geol. Min. (BRGM), Ser. 2, Sec. III* 4, 277–284.
- Larson, R. E. and J. J. L. Higdon (1986). Microscopic flow near the surface of two-dimensional porous media. part 1. axial flow. *J. Fluid Mech.* 166, 449–472.
- Larson, R. E. and J. J. L. Higdon (1987). Microscopic flow near the surface of two-dimensional porous media. part 1. transverse flow. *J. Fluid Mech.* 178, 119–136.
- Larson, R. G., L. E. Scriven, and H. T. Davis (1981). Percolation theory of two-phase flow in porous media. *Chemical Engineering Science* 36, 57–73.
- Liakopoulos, A. C. (1965). Variation of the permeability tensor ellipsoid in homogeneous anisotropic soils. *Water Resources Research* 1(1), 135–141.
- Libersky, L. D. and A. G. Petschek (1990). Smooth particle hydrodynamics with strength of materials. In H. E. Trease, M. J. Fritts, and W. P. Crowley (Eds.), *Advances in the free-Lagrange method*. New York: Springer-Verlag.
- Libersky, L. D., A. G. Petschek, T. C. Carney, J. R. Hipp, and F. A. Allah-dadi (1993). High strain Lagrangian hydrodynamics. *Journal of Computational Physics* 109, 67–75.
- Liggett, J. A. and P. L.-F. Liu (1983). *The boundary integral equation method for porous media flow*. London: George Allen & Unwin.
- Lucy, L. B. (1977). A numerical approach to the testing of the fission hypothesis. *The Astronomical Journal* 82(12), 1013–1024.
- Lundgren, T. S. (1972). Slow flow through stationary random beds and suspensions of spheres. *J. Fluid Mech.* 51, 273–299.
- Mandelbrot, B. B. (1982). *The fractal geometry of nature*. New York: W. H. Freeman and Company.
- Matheron, G. and G. D. Marsily (1980). Is transport in porous media always diffusive? a counterexample. *Water Resources Research* 16(5), 901–917.
- Mauri, R. (1991). Dispersion, convection, and reaction in porous media. *Phys. Fluids A* 3(5), 743–756.
- Maxwell, J. C. (1873). *A treatise on electricity and magnetism, volume 1*. London: Clarendon Press.
- McNamara, G. R. and G. Zanetti (1988). Use of the Boltzmann equation to simulate lattice-gas automata. *Physical Review Letters* 61(20), 2332–2335.

- Meegoda, N. J., I. P. King, and K. Arulanandan (1989). An expression for the permeability of anisotropic granular media. *International Journal for Numerical and Analytical Methods in Geomechanics* 13, 575–598.
- Mei, C. C. (1992). Method of homogenization applied to dispersion in porous media. *Transport in Porous Media* 9, 261–274.
- Mei, C. C., J.-L. Auriault, and C. Ng (1996). Some applications of the homogenization theory. In J. W. Hutchinson and T. Y. Wu (Eds.), *Advances in applied mechanics*, pp. 277–348. Academic Press.
- Mitchell, J. K. (1993). *Fundamentals of Soil Behavior*. New York: John Wiley & Sons.
- Moltyaner, G. L. (1989). Hydrodynamic dispersion at the local scale of continuum representation. *Water Resources Research* 25(5), 1041–1048.
- Monaghan, J. J. (1989). On the problem of penetration in particle methods. *Journal of Computational Physics* 82, 1–15.
- Monaghan, J. J. (1992). Smoothed particle hydrodynamics. *Annu. Rev. Astron. Astrophys.* 30, 543–574.
- Monaghan, J. J. (1994). Simulating free surface flows with SPH. *Journal of Computational Physics* 110, 399–406.
- Monaghan, J. J. (1995a). Heat conduction with discontinuous conductivity. Applied Mathematics Reports and Preprints, 95/18, Monash University, Australia.
- Monaghan, J. J. (1995b). Simulating gravity currents with SPH: I lock gates. Applied Mathematics Reports and Preprints, 95/5, Monash University, Australia.
- Monaghan, J. J. (1995c). Simulating gravity currents with SPH: III boundary forces. Applied Mathematics Reports and Preprints, 95/11, Monash University, Australia.
- Monaghan, J. J. and J. C. Lattanzio (1985). A refined particle method for astrophysical problems. *Astronomy & Astrophysics* 149, 135–143.
- Morris, J. P. (1994). A study of the stability properties of SPH. Applied Mathematics Reports and Preprints, 94/22, Monash University, Australia.
- Morris, J. P. (1996a). *Analysis of smoothed particle hydrodynamics with applications*. Ph.D. thesis, Monash University, Australia.
- Morris, J. P. (1996b). Stability properties of SPH. *Publ. Astron. Soc. Aust.* 13, 97–102.
- Morris, J. P. (1999). Simulating surface tension with Smoothed Particle Hydrodynamics. *Int. J. Numer. Meth. Fluid Flow*.
- Morris, J. P., P. J. Fox, and Y. Zhu (1997). Modeling low Reynolds number incompressible flows using SPH. *Journal of Computational Physics* 136, 214–226.

- Nutting, P. G. (1930). Physical analysis of oil sands. *Bulletin of the American Association of Petroleum Geologists* 14, 1337–1349.
- Nyer, E. K. (1992). *Groundwater treatment technology*. New York: Van Nostrand Reinhold.
- Ogata, A. (1970). Theory of dispersion in a granular medium. Technical report. U.S. Geological Survey Professional Paper 411-I.
- Perkins, T. K. and O. C. Johnston (1963). A review of diffusion and dispersion in porous media. *Society of Petroleum Engineering Journal* 3, 70–84.
- Perrins, W. T., D. R. McKenzie, and R. C. McPhedran (1979). Transport properties of regular arrays of cylinders. *Phil. Trans. R. Soc. Lond. A369*, 207–225.
- Peyret, R. and T. D. Taylor (1985). *Computational methods for fluid flow*. New York: Springer-Verlag.
- Peyton, R. L., C. J. Gantzer, S. H. Anderson, B. A. Haefner, and P. Pfeifer (1994). Fractal dimension to describe soil macropore structure using X ray computed tomography. *Water Resources Research* 30(3), 691–700.
- Pickens, J. F. and G. E. Grisak (1981). Modeling of scale-dependent dispersion in hydrogeologic systems. *Water Resources Research* 17(6), 1701–1711.
- Plumb, O. A. and S. Whitaker (1988). Dispersion in heterogeneous porous media. *Water Resources Research* 24(7), 913–938.
- Rajaram, H., L. A. Ferrand, and M. A. Celia (1997). Prediction of relative permeabilities for unconsolidated soils using pore-scale network models. *Water Resources Research* 33(1), 43–52.
- Randles, P. W. and L. D. Libersky (1996). Smoothed particle hydrodynamics: some recent improvements and applications. *Comput. Methods Appl. Mech. Eng.* 139, 375–408.
- Ranganathan, S., F. R. Phelan Jr., and S. G. Advani (1996). A generalized model for the transverse fluid permeability in unidirectional fibrous media. *Polymer Composites* 17(2), 222–230.
- Rayleigh, L. (1892). On the influence of obstacles arranged in rectangular order upon the property of a medium. *Phil. Mag.* 34, 481–502.
- Reeves, P. C. and M. A. Celia (1996). A functional relationship between capillary pressure, saturation, and interfacial area as revealed by a pore-scale network model. *Water Resources Research* 32(8), 2345–2358.
- Rivet, J.-P., M. Henon, U. Frisch, and D. d'Humieres (1988). Simulating fully three-dimensional external flow by lattice gas methods. *Europhysical Letters* 7(3), 231–236.
- Rothman, D. H. (1988). Cellular-automaton fluids: a model for flow in porous media. *Geophysics* 53(4), 509–518.

- Rothman, D. H. (1990). Macroscopic laws for immiscible two-phase flow in porous media: results from numerical experiments. *Journal of Geophysical Research* 95(B6), 8663–8674.
- Saffman, P. G. (1959). A theory of dispersion in a porous medium. *J. Fluid Mech.* 6, 321–349.
- Saffman, P. G. (1960). Dispersion due to molecular diffusion and macroscopic mixing in flow through a network of capillaries. *J. Fluid Mech.* 7, 194–208.
- Salles, J., J.-F. Thovert, R. Delannay, L. Prevors, J.-L. Auriault, and P. M. Adler (1993). Taylor dispersion in porous media: determination of the dispersion tensor. *Phys. Fluids A* 5(10), 2348–2376.
- Sangani, A. S. and A. Acrivos (1982a). Slow flow past periodic arrays of cylinders with application to heat transfer. *Int. J. Multiphase Flow* 8(3), 193–206.
- Sangani, A. S. and A. Acrivos (1982b). Slow flow through a periodic array of spheres. *Int. J. Multiphase Flow* 8(4), 343–360.
- Sangani, A. S. and C. Yao (1988b). Transport processes in random arrays of cylinders. I. thermal conduction. *Phys. Fluids* 31(9), 2426–2434.
- Sangani, A. S. and C. Yao (1988a). Transport processes in random arrays of cylinders. II. viscous flow. *Phys. Fluids* 31(9), 2435–2444.
- Scheidegger, A. E. (1954). Statistical hydrodynamics in porous media. *Journal of Applied Physics* 25(8), 994–1001.
- Scheidegger, A. E. (1961). General theory of dispersion in porous media. *Journal of Geophysical Research* 66(10), 3273–3278.
- Scheidegger, A. E. (1974). *The physics of flow through porous media*. Canada: University of Toronto Press.
- Schoenberg, I. J. (1946). Contributions to the problem of approximation of equidistant data by analytic functions. *Q. Appl. Math.* 4(1), 45–99.
- Schwartz, L. M., F. Auzerais, J. Dunsmuir, N. Martys, D. P. Bentz, and S. Torquato (1994). Transport and diffusion in three-dimensional composite media. *Physica A* 207, 28–36.
- Slattery, J. C. (1969). Single-phase flow through porous media. *AICHE Journal* 15(6), 866–872.
- Smith, L. and F. W. Schwartz (1980). Mass transport 1. a stochastic analysis of macroscopic dispersion. *Water Resources Research* 16(2), 303–313.
- Snyder, L. J. and W. E. Stewart (1966). Velocity and pressure profiles for Newtonian creeping flow in regular packed beds of spheres. *AICHE Journal* 12(1), 167–173.
- Sorensen, J. P. and W. E. Stewart (1974). Computation of forced convection in slow flow through ducts and packed beds - II velocity profile in a simple cubic array of spheres. *Chemical Engineering Science* 29, 819–825.

- Spanne, P., J. F. Thovert, C. J. Jacquin, W. B. Lindquist, K. W. Jones, and P. M. Adler (1994). Synchrotron computed microtomography of porous media: topology and transports. *Physical Review Letters* 73(14), 2001–2004.
- Succi, S., R. Benzi, and F. Higuera (1991). The lattice Boltzmann equation: a new tool for computational fluid-dynamics. *Physica D* 47, 219–230.
- Succi, S., E. Foti, and F. Higuera (1989). Three-dimensional flows in complex geometries with the lattice Boltzmann method. *Europhysics Letters* 10(5), 433–438.
- Swegle, J. W., D. L. Hicks, and S. W. Attaway (1995). Smoothed Particle Hydrodynamics stability analysis. *Journal of Computational Physics* 116, 123–134.
- Szabo, B. A. (1968). Permeability of orthotropic porous mediums. *Water Resources Research* 4(4), 801–808.
- Takeda, H., S. M. Miyama, and M. Sekiya (1994). Numerical simulation of viscous flow by smoothed particle hydrodynamics. *Progress of Theoretical Physics* 92(5), 939–960.
- Tamamidis, P., G. Zhang, and D. N. Assanis (1996). Comparison of pressure-based and artificial compressibility methods for solving 3D steady incompressible viscous flows. *Journal of Computational Physics* 124, 1–13.
- Taylor, G. (1953). Dispersion of soluble matter in solvent flowing slowly through a tube. *Phil. Trans. R. Soc. Lond. A219*, 186–203.
- Taylor, G. (1954). Conditions under which dispersion of a solute in a stream of solvent can be used to measure molecular diffusion. *Phil. Trans. R. Soc. Lond. A225*, 473–477.
- Thomasset, F. (1981). *Implementation of finite element methods for Navier-Stokes equations*. New York: Springer-Verlag.
- Thompson, A. H., A. J. Katz, and C. E. Krohn (1987). The microgeometry and transport properties of sedimentary rock. *Ad. Phys.* 36, 625–694.
- Tompson, A. F. B. (1988). On a new functional form for the dispersive flux in porous media. *Water Resources Research* 24(11), 1939–1947.
- Turkel, E. (1987). Preconditioned methods for solving the incompressible and low speed compressible equations. *Journal of Computational Physics* 72, 277–298.
- U.S.EPA (1985). Modeling remedial actions at uncontrolled hazardous waste sites. Technical report, Office of Solid Waste and Emergency Response, EPA/540/2-85/001, Washington, D.C.
- Wan, J., T. K. Tokunaga, C.-F. Tsang, and G. S. Bodvarsson (1996). Improved glass micromodel methods for studies of flow and transport in fractured porous media. *Water Resources Research* 32(7), 1955–1964.

- Wang, H. F. and M. P. Anderson (1982). *Introduction to groundwater modeling: finite difference and finite element methods*. San Francisco: W. H. Freeman and Company.
- Watkins, S. J., A. S. Bhattacharjee, N. Francis, J. A. Turner, and A. P. Whitworth (1996). A new prescription for viscosity in Smoothed Particle Hydrodynamics. *Astronomy & Astrophysics Supplement Series* 119(1), 177–187.
- Whitaker, S. (1969). Advances in theory of fluid motion in porous media. *Industrial and Engineering Chemistry* 61(12), 14–28.
- Whitaker, S. (1973). The transport equations for multi-phase systems. *Chemical Engineering Science* 28, 139–147.
- Whitaker, S. (1986). Flow in porous media I: a theoretical derivation of Darcy's law. *Transport in porous media* 1, 3–25.
- Wolfram, S. (1986). Cellular automaton fluids 1: basic theory. *Journal of Statistical Physics* 45(3/4), 471–526.
- Wong, P.-Z., J. Howard, and J.-S. Lin (1986). Surface roughening and the fractal nature of rocks. *Physical Review Letters* 57(5), 637–640.
- Wyckoff, R. D., H. G. Botset, M. Muskat, and D. W. Reed (1933). The measurement of the permeability of porous media for homogeneous fluids. *Rev. Sci. Instr.* 4, 394–405.
- Wyllie, M. R. J. and A. R. Gregory (1955). Fluid flow through unconsolidated porous aggregates. *Industrial and Engineering Chemistry* 47(7), 1379–1388.
- Wyllie, M. R. J. and M. B. Spangler (1952). Application of electrical resistivity measurements to problem of fluid flow in porous media. *Bulletin of the American Association of Petroleum Geologists* 36(2), 359–403.
- Zhu, Y., P. J. Fox, and J. P. Morris (1997). Smoothed particle hydrodynamics model for flow through porous media. In *Proc., 9th International Conference on Computer Methods and Advances in Geomechanics, Wuhan, P. R. China*, Volume 2, pp. 1041–1046.
- Zhu, Y., P. J. Fox, and J. P. Morris (1999). A pore-scale numerical model for flow through porous media. *International Journal for Numerical and Analytical Methods in Geomechanics*.
- Zick, A. A. and G. M. Homsy (1982). Stokes flow through periodic arrays of spheres. *J. Fluid Mech.* 115, 13–26.